

AFRPL-TR-76-47

EXXON/GRU.2BF.76

EXTERNAL CATALYST BREAKUP PHENOMENA
FINAL REPORT

EXXON RESEARCH AND ENGINEERING COMPANY
WILLIAM F. TAYLOR
LINDEN, NEW JERSEY 07036

TRW SYSTEMS GROUP, INC.
~~JOHN D. KUENZLY~~
ROBERT L. SACKHEIM
REDONDO BEACH, CALIFORNIA 90278

MCDONNELL DOUGLAS ASTRONAUTICS COMPANY
WILLIAM T. WEBBER
HUNTINGTON BEACH, CALIFORNIA 92647

J U N E 1 9 7 6

APPROVED FOR PUBLIC RELEASE
DISTRIBUTION UNLIMITED

AIR FORCE ROCKET PROPULSION LABORATORY
DIRECTOR OF SCIENCE AND TECHNOLOGY
AIR FORCE SYSTEMS COMMAND
EDWARDS AFB, CALIFORNIA 93523



ADA027217

FOREWORD

This report was submitted by Exxon Research & Engineering Company, Government Research Laboratory, Linden, New Jersey 07036, under contract F04611-74-C-0032, job order No. 305811TM with the Air Force Rocket Propulsion Laboratory, Edwards CA 93523.

This report has been reviewed by the Information Office/DOZ and is releasable to the National Technical Information Service (NTIS). At NTIS it will be available to the general public, including foreign nations.

This report is unclassified and suitable for public release.

Steven G. Wax
STEVEN G. WAX, Capt. USAF
Project Engineer

Forrest Forbes
FORREST FORBES, Chief
Propellants Section

FOR THE COMMANDER

Edward E. Stein
EDWARD E. STEIN
Deputy Chief, Liquid Rocket Division

NOTICES

When U.S. Government drawings, specifications, or other data are used for any purpose than a definitely related government procurement operation, the Government thereby incurs no responsibility nor any obligation whatsoever, and the fact that the Government may have formulated, furnished, or in any way supplied the said drawings, specifications or other data, is not to be regarded by implication or otherwise, or in any manner licensing the holder or any other person or corporation, or conveying any rights or permission to manufacture, use or sell any patented invention that may in any way be related thereto.

ACCESSION NO.	
NTIS	✓
DOC	
UNCLASSIFIED	
JUL 1974	
BY	
DISTRIBUTION AVAILABLE TO ALL	
DIA	
A	

UNCLASSIFIED

SECURITY CLASSIFICATION OF THIS PAGE (When Data Entered)

REPORT DOCUMENTATION PAGE		READ INSTRUCTIONS BEFORE COMPLETING FORM	
1. AFRPL 15-471	2. TR-76-47	3. RECIPIENT'S CATALOG NUMBER	
4. TITLE (and Subtitle)		5. PERFORMING ORG. REPORT NUMBER	
EXTERNAL CATALYST BREAKUP PHENOMENA		6. CONTRACT OR GRANT NUMBER(s)	
7. AUTHOR		8. SECURITY CLASS. (of this Report)	
W.F./Taylor, Exxon Research & Eng. Co. J.D./Kuenzly, R.L./Sackheim TRW Systems Group W.T./Webber, McDonnell Douglas Astronautics		9. DATE OF REPORT	Final Report June 74 - January 76
10. PERFORMING ORGANIZATION NAME AND ADDRESS		11. NUMBER OF PAGES	
Exxon Research and Engineering Company Government Research Laboratory Linden, New Jersey 07036		12. SECURITY CLASS. (of this Report)	UNCLASSIFIED
13. CONTROLLING OFFICE NAME AND ADDRESS		14. DECLASSIFICATION/DOWNGRADING SCHEDULE	
Air Force Rocket Propulsion Laboratory Edwards, California 93523		15. DISTRIBUTION STATEMENT (of this Report)	Approved For Public Release, Distribution Unlimited
16. MONITORING AGENCY NAME & ADDRESS (if different from Controlling Office)		17. DISTRIBUTION STATEMENT (of the abstract entered in Block 20, if different from Report)	
18. SUPPLEMENTARY NOTES			
19. KEY WORDS (Continue on reverse side if necessary, and identify by block number)			
Catalyst Catalyst Breakup Hydrazine Monopropellant Hydrazine Catalyst Engine			
20. ABSTRACT (Continue on reverse side if necessary, and identify by block number)			
The overall objective of the work in the program was to investigate the external breakup mechanisms of Shell 405 catalyst so as to establish an understanding of the phenomenon in order to provide monopropellant hydrazine thruster designers with a fundamental technology base which they can use to achieve long life mission requirements. The External Catalyst Breakup Phenomena program involved the joint efforts of Exxon Research and Engineering Company (prime contractor) and McDonnell Douglas Astronautics Company and the Systems Group of TRW, Inc.			

DD FORM 1 JAN 73 1473 EDITION OF 1 NOV 63 IS OBSOLETE

UNCLASSIFIED

SECURITY CLASSIFICATION OF THIS PAGE (When Data Entered)

UNCLASSIFIED

SECURITY CLASSIFICATION OF THIS PAGE (When Data Entered)

Following a review of the literature and other available information, twenty (20) different mechanisms or factors potentially significant to catalyst breakup were investigated either experimentally or analytically or by use of both techniques. Slightly more than half of the mechanisms investigated were found to have a significant influence on the complex phenomena involved in overall catalyst breakup. The significant primary catalyst breakup mechanisms were in general, associated with either pressure crushing forces or with various effects resulting from the presence of liquid hydrazine. A major secondary breakup mechanism is particle to particle abrasion which can occur if the catalyst in a voided bed experiences rapid motion. Another important factor in catalyst breakup is the deterioration as a result of thruster exposure of the ability of a fresh catalyst to resist the various breakup mechanisms. Our results also indicate that the effect of the various mechanisms on the magnitude of breakup can be controlled by adjusting reactor operating variables such as liquid injection velocities, bed temperature, bed gas linear velocity and pressure drop, bed preload and catalyst selection for the various sections of a thruster and point to a number of variables or factors involved in thruster operation where operating envelopes or procedures could be developed to enhance catalyst life.

In a number of areas both experimental and analytical modeling studies were carried out. Results of studies in these areas were examined in order to assess the agreement between analytical modeling results and experimental measurements. The agreement between modeling results and experimental results was outstanding.

Excellent progress has been made with a difficult and complex problem and we feel our work has greatly expanded the state-of-the-art of Shell 405 catalyst breakup technology. However, it is clear in spite of this progress that the ultimate goal of elucidating the overall catalyst breakup phenomena has not been achieved. Our results have led us to reach the conclusion that it is possible to develop an analytical tool to design long life hydrazine mono-propellant thrusters from first principles as opposed to solely using "cut and try" or empirical design approaches. The development of such an engine design optimization model is contingent upon first completing (1) the necessary additional experimental work (2) the development of a global scientific model which would "put together" all prior experimental and analytical results and (3) a model verification test effort involving actual thruster firing tests. We feel that our results strongly suggest that the development of such an advanced technology base is warranted.

SECURITY CLASSIFICATION OF THIS PAGE (When Data Entered)

SUMMARY AND RECOMMENDATIONS

The overall objective of the work in the program was to investigate the external breakup mechanisms of Shell 405 catalyst so as to establish an understanding of the phenomenon in order to provide monopropellant hydrazine thruster designers with a fundamental technology base which they can use to achieve long life mission requirements. The External Catalyst Breakup Phenomena program involved the joint efforts of Exxon Research and Engineering Company (prime contractor) and McDonnell Douglas Astronautics Company and the Systems Group of TRW, Inc. A study of Internal Catalyst Breakup Phenomena was carried out separately by United Technologies Research Company (UTRC) under a different contract (FO4611-74-C-0031). The overall effort was coordinated by the Air Force with the assistance of a Scientific Advisory Board.

Following a review of the literature and other available information, twenty (20) different mechanisms or factors potentially significant to catalyst breakup were investigated either experimentally or analytically or by use of both techniques. Slightly more than half of the mechanisms investigated were found to have a significant influence on the complex phenomena involved in overall catalyst breakup. The significant catalyst breakup mechanisms were, in general, associated with either pressure crushing forces or with various effects resulting from the presence of liquid hydrazine. Mechanisms in the pressure crushing area include the effects of static pressure crushing forces from sources such as steady state gas flow ΔP , bed preload and differential thermal expansions and the effect of dynamic "pop shocks" crushing forces. The wide range of individual catalyst particle crush strengths, particularly on a batch to batch basis, also contributes to pressure crushing problems since the percent of very weak catalyst particles is strongly dependent on this factor. Mechanisms associated with the influence of liquid hydrazine include pulsed liquid stream erosion, liquid quench thermal shock and liquid imbibition where our results corroborate the findings of UTRC that liquid hydrazine imbibed within a catalyst particle can cause high internal pressures which result in particle destruction. Analytical results suggest that erosion effects from solid particles present in the liquid hydrazine is also a possible mechanism but this must be confirmed experimentally. Another important factor in catalyst breakup is the deterioration as a result of thruster exposure of the ability of a fresh catalyst to resist the various breakup mechanisms. Our data to date indicates that liquid hydrazine exposure appears to be responsible for particle crush strength deterioration, however, the situation regarding how various environmental exposures effect the other important properties of the catalyst is not completely clear at present. All of these mechanisms are primary breakup mechanisms in that they are not dependent on the prior occurrence of another mechanism. A major secondary breakup mechanism is particle to particle abrasion which can occur if the catalyst in a voided bed experiences rapid motion. If the bed undergoes catalyst loss from primary breakup mechanisms

our data indicates that the bed can reorient itself, for example, as a result of thermal cycling, and thus generate a significant void space. Bed gas velocities are, in general, well above that required for incipient particle motion. However, this appears to be a necessary but not sufficient cause for particle motion, and at present the fluid dynamic criteria controlling potential particle motion in a voided bed are not defined. Our results also indicate that the effect of the various mechanisms on the magnitude of breakup can be controlled by adjusting reactor operating variables such as liquid injection velocities, bed temperature, bed gas linear velocity and pressure drop, bed preload and catalyst selection for the various sections of a thruster. It may also be possible to mitigate the effects of thruster exposure on catalyst property deterioration or to reduce the probability that a voided bed will experience rapid particle motion by controlling reactor operating variables, but this is not entirely clear at present.

In a number of areas both experimental and analytical modeling studies were carried out. Results of studies in these areas were examined in order to assess the agreement between analytical modeling results and experimental measurements. The agreement between modeling results and experimental results was outstanding. Particularly significant was the fact that modeling results correctly predicted a number of physical results prior to actual experimental work being carried out. This excellent agreement between model results and experimental results in the complex hydrazine monopropellant thruster environment clearly demonstrates that catalyst breakup phenomena can indeed be successfully analytically modeled.

Our results point to a number of variables or factors involved in thruster operation where operating envelopes or procedures could be developed to enhance catalyst life.

- Catalyst Selection. Results suggest that catalyst selection procedures could be developed to maximize the resistant of the catalyst to various breakup mechanisms.

- Pressure Forces. High G loadings and bed pressure drops should be avoided. Bed pre-loads should be kept at a minimum value. Thruster configuration and other design variables should be optimized to minimize catalyst crushing from differential thermal expansion effects.

- Catalyst Bed Heating. Increasing the bed temperature will at some point essentially eliminate the possibility of destruction by the imbibition of liquid hydrazine or by liquid quench thermal shock. Also, this aspect may become important later in life as catalyst activity decreases and where bed heating may well overcome this loss in activity. Overpressure ignition spikes have been a common occurrence during ambient and cold starts. Thus, bed heating should help prevent destructive bed crushing spikes.

- Propellant Dispersion at Injection. Minimum liquid injection velocities via a uniform propellant injection technique will minimize localized bed destruction from pulsed liquid erosion.

• Mesh Size Selection. Mesh size groups degrade to different extents depending upon the mechanism. For example, 14-18 mesh appears stronger to liquid imbibition breakup whereas, 25-30 mesh appears stronger to "pop shock" and liquid quench thermal shock breakup. The particular mission, requirements and design philosophy will dictate the extent of mesh size use.

• Contaminants. Propellant contaminants may reduce catalyst activity or possibly cause fluid dynamic erosion from solid particles in the flowing gases and should be carefully eliminated from system sources. Propellants having low non-volatile residues (NVR) should be used.

Excellent progress has been made with a difficult and complex problem and we feel our work has greatly expanded the state-of-the-art of Shell 405 catalyst breakup technology. However, it is clear in spite of this progress that the ultimate goal of elucidating the overall catalyst breakup phenomena has not been achieved. Twenty mechanisms have been investigated and a number identified as significant contributors to catalyst bed breakup. Some have been sufficiently investigated so that no further work will be needed. However, additional experimental work is needed to quantify a number of mechanisms.

Our results have led us to reach the conclusion that it is possible to develop an analytical tool to design long life hydrazine monopropellant thrusters from first principles as opposed to solely using "cut and try" or empirical design approaches. The development of such an engine design optimization model is contingent upon first completing (1) the necessary additional experimental work (2) the development of a global scientific model which would "put together" all prior experimental and analytical results and (3) a model verification test effort involving actual thruster firing tests. We feel that our results strongly suggest that the development of such an advanced technology base is warranted.

PREFACE

This Final Report describes work carried out under Contract No. FO4611-74-C-0032 during the period from June 1974 to January 1976. It was principally written by Dr. W. F. Taylor, Program Manager, Exxon Research and Engineering Company (ER&E), Mr. W. T. Webber, McDonnell Douglas Astronautics Company (MDAC), and Dr. J. D. Kuenzly and Mr. R. L. Sackheim, TRW Systems Group. Contributions were also made by the following individuals:

Dr. M. Boudart, Stanford University

Dr. W. D. English, MDAC

Mr. A. R. Garabrant, ER&E

Dr. D. P. H. Hasselman, Lehigh University

Mr. R. J. Hoffman, MDAC

Mr. M. Lieberman, ER&E

Dr. E. M. Magee, ER&E

Mr. D. D. Quan, MDAC

Lt. S. G. Wax, AFRPL

Mr. S. A. Schechter, MDAC

The Project monitor on this program was 1st Lieutenant S. G. Wax,

AFRPL.

TABLE OF CONTENTS

	<u>Page</u>
LIST OF ILLUSTRATIONS.....	10
LIST OF TABLES.....	18
1. INTRODUCTION.....	22
2. APPROACH.....	24
2.1 Objective.....	24
2.2 Program Organization.....	24
3. TASK I - PHENOMENOLOGICAL SURVEY.....	24
3.1 Literature Review.....	27
3.2 Sensitivity Testing.....	37
3.2.1 Gas Fluid Dynamic Erosion.....	38
3.2.2 Particle Static Pressure Crushing.....	50
3.2.3 Particle Fluidization.....	65
3.2.4 Liquid Fluid Dynamic Erosion.....	74
3.3 Estimation of Catalyst Strength of Material Properties.....	92
4. TASK II - SELECTED MECHANISM AND BED TESTING.....	94
4.1 Studies Carried Out By TRW Systems Group.....	94
4.1.1 Mechanism Identification.....	94
4.1.1.1 Selected Mechanism Studies.....	95
4.1.1.2 Interaction Studies.....	97
4.1.2 Experimental Techniques.....	100
4.1.2.1 Laboratory Reactor Design and Fabrication...	100
4.1.2.1.1 Design Objectives.....	100
4.1.2.1.2 Description of Design.....	101
4.1.2.1.3 Reactor Components.....	101
4.1.2.1.4 Reactor Fabrication.....	101
4.1.2.2 Mechanism Evaluation Methods.....	105
4.1.2.2.1 Catalyst Handling and Measurement Techniques.....	105
4.1.2.2.2 Parameter Measurement.....	107

TABLE OF CONTENTS (Cont'd)

	<u>Page</u>
4.1.2.3 Test Program.....	110
4.1.2.3.1 Dynamic Pop-Shock Pressure Crushing.....	110
4.1.2.3.2 Hot Gas Thermal Fatigue.....	110
4.1.2.3.3 Hot Gas Thermal Aging.....	110
4.1.2.3.4 Liquid Quench Thermal Shock.....	115
4.1.2.3.5 Void-Volume Abrasion.....	115
4.1.2.3.6 Cold Gas Pressure Crushing.....	115
4.1.2.3.7 Isothermal Catalyst Activity Reactor.....	115
4.1.3 Selected Mechanism Test Results.....	118
4.1.3.1 Dynamic Pop-Shock Pressure Crushing.....	118
4.1.3.2 Hot Gas Thermal Fatigue.....	126
4.1.3.3 Hot Gas Thermal Aging.....	126
4.1.3.4 Liquid Quench Thermal Shock.....	126
4.1.3.5 Void-Volume Abrasion.....	139
4.1.3.6 Cold Gas Pressure Crushing.....	139
4.1.3.7 Isothermal Catalyst Activity Reactor.....	143
4.1.4 Output Data Correlation.....	143
4.1.4.1 Mechanism Analysis.....	145
4.1.4.1.1 Pressure Crushing.....	145
4.1.4.1.2 Thermally Induced Phenomena.....	146
4.1.4.1.3 Voided Bed Abrasion.....	147
4.1.4.2 Catalyst Size Effects.....	148
4.1.4.3 Complex Phenomena.....	149
4.1.4.3.1 Interaction Study I.....	149
4.1.4.3.2 Interaction Study II.....	149
4.1.4.4 Parametric Degradation and Inhibition Criteria.....	152
4.2 Studies Carried Out By Exxon Research and Engineering Company.....	155
4.2.1 Bed Static Pressure Crushing.....	155
4.2.2 The Effect of Particle to Particle Abrasion in a Moving Bed.....	164
4.2.3 Effect of Use Exposure on Catalyst Physical Properties.....	168

TABLE OF CONTENTS (Cont'd)

	<u>Page</u>
4.2.3.1 Effect of Thruster Exposure.....	168
4.2.3.1.1 Effect on Particle Crush Strength Distribution.....	168
4.2.3.1.2 Resistance to Bed Static Pressure Crushing.....	177
4.2.3.1.3 Resistance to Pulsed, Liquid Stream Erosion.....	182
4.2.3.1.4 Resistance to Liquid Quench Thermal Shock.....	187
4.2.3.2 Effect of Exposure in Various Controlled Environments.....	187
4.2.3.2.1 Effect on Particle Crush Strength Distribution.....	187
4.2.3.2.2 Effect of Pulsed Liquid.....	189
4.2.3.2.3 Summary of Results.....	194
5. TASK III - ANALYTICAL MODELING.....	196
5.1 Introduction.....	196
5.1.1 Organization of the Effect.....	196
5.1.2 Overall Purpose and Limitations.....	196
5.1.3 General Description.....	196
5.2 Structures Analyses.....	199
5.2.1 Stress Failure Model.....	199
5.2.2 Temperature Profiles Developed Inside a Catalyst Particle by External Heating or Cooling....	205
5.2.3 Particle Stress Resulting from Thermal Shock.....	211
5.2.4 Pressure Profiles Developed Inside a Catalyst Particle by External Pressurization.....	218
5.2.5 Particle Stress Resulting from Internal Pressure....	220
5.2.6 Particle Stress Resulting from Bed Compression.....	223
5.2.6.1 Particle to Particle Forces Resulting from Bed Compression.....	226
5.2.6.2 Stress Produced in the Particle From Point to Point Contact.....	228
5.2.6.3 Relationship Between Bed Volume and Bed Compaction Change.....	241

TABLE OF CONTENTS (Cont'd)

	<u>Page</u>
5.2.7 Mass Loss Resulting From Bed Compression.....	243
5.2.7.1 Failure Theories.....	243
5.2.7.2 Maximum Tension Stress Criterion.....	244
5.2.7.3 Distortion Energy Approach.....	244
5.2.7.4 Strength Tension Approach.....	247
5.2.7.5 Comparison of Failure Theories With Experimental Data.....	248
5.2.7.6 Results of Sample Calculations.....	249
5.3 Internal Particle Model.....	249
5.3.1 Flow Through a Porous Media.....	257
5.3.2 Klinkenberg Effect, Non-Continuous Flow of Gases.....	258
5.3.3 Imbibition Pressure.....	259
5.3.4 Thermal Effects.....	262
5.3.5 Finite Difference Model.....	265
5.3.6 Results from the Operation of the Internal Particle Model.....	270
5.3.6.1 Initial Results Using an Estimated Permeability Constant.....	270
5.3.6.2 Measurement of the Permeability Constant by Imbibition.....	272
5.3.6.3 Internal Particle Process Model Variation Study Using the Measured Permeability Constant.....	277
5.3.6.3.1 Effect of Variation in Particle Permeability.....	280
5.3.6.3.2 Effect of Variation in Particle Size.....	280
5.3.6.3.3 Effect of Variation in Initial Temperature.....	280
5.3.6.3.4 Initial Saturation Effects.....	285
5.4 Differential Thermal Expansion.....	286
5.4.1 Method of Calculation.....	286
5.4.2 Results from Calculations.....	289
5.4.2.1 Effect of Bed Cooling.....	292
5.4.2.2 Effect of Chamber Inlet Pressure.....	292

TABLE OF CONTENTS (Cont'd)

	<u>Page</u>
5.4.2.3 Effect of Thrust.....	301
5.4.2.4 Effect of Case Material.....	301
5.4.3 Effects of Differential Thermal Expansion/Contraction on the Catalyst.....	301
5.4.4 Differential Thermal Expansion Calculations Carried Out by AFRPL.....	304
5.4.4.1 General Approach.....	304
5.4.4.2 Continuous Operation Calculations.....	306
5.4.4.3 Pulsed Mode Calculations.....	306
5.4.4.4 Conclusions.....	312
5.5 Fluid Erosion.....	312
5.5.1 Program Development.....	312
5.5.1.1 Catalyst Bed Configuration Assumptions.....	315
5.5.1.2 Effect of Temperatures on Fatigue Wear Coefficient.....	315
5.5.1.3 Threshold Velocity for Fatigue Wear.....	315
5.5.2 Method of Calculation.....	318
5.5.3 Results.....	323
5.5.3.1 Parametric Variation Study.....	323
5.5.3.2 Additional Calculations and Discussion.....	329
5.6 Pressure Shocks.....	330
5.6.1 Catalyst Bed Flow Numerical Model.....	330
5.6.2 Sample Calculation.....	330
5.6.3 Mechanical Response of the Bed to Rapid Loading.....	338
5.6.4 Other Conclusions from the Catalyst Bed Mass and Heat Transport Model.....	339
6. CRITICAL ASSESSMENT OF RESULTS AND CONCLUSIONS.....	341
7. REFERENCES.....	355
APPENDICES.....	366

LIST OF FIGURES

<u>No.</u>		<u>Page</u>
3-1	High Severity Gas Erosion Tester (HSGET)	39
3-2	HSGET Particle Envelope Assembly	40
3-3	HSGET Cylindrical Pellet Holder Assembly	41
3-4	Gas Erosion Test: Fresh Shell 405, 1/8" x 1/8" Cylinders at 250 Feet/Second	45
3-5	Gas Erosion Test: Fresh Shell 405, 8 to 12 Mesh Particles at 250 Feet/Second	45
3-6	Gas Erosion Test: Fresh Shell 405, 14 to 18 Mesh Particles at 250 Feet/Second	46
3-7	Gas Erosion Test: Fresh Shell 405, 20 to 25 Mesh Particles at 250 Feet/Second	47
3-8	Gas Erosion Test: Fresh Shell 405, 25 to 30 Mesh Particles at 250 Feet/Second	48
3-9	Gas Erosion Test: Fresh Shell 405, 20 to 30 Mesh Particles at 250 Feet/Second	49
3-10	Instron Testing Instrument (ITI)	51
3-11	Modified LLBN Apparatus for Incipient Particle Movement Velocity Measurement	66
3-12	Maximum Surface Vapor Velocity for Impinging Jets	71
3-13	Correlation of Incipient Particle Movement Velocity	73
3-14	Pulsed Liquid Particle Erosion Tester (PLPET)	75
3-15	PLPET Catalyst Holder Assembly	76

LIST OF FIGURES (Cont'd)

<u>No.</u>		<u>Page</u>
3-16	Liquid Erosion Test: Fresh Shell 405 1/8" x 1/8" Cylinders at 100 Feet per Second and 8,200 Pulses	78
3-17	Liquid Erosion Test: Fresh Shell 405 1/8" x 1/8" Cylinders at 100 Feet per Second and 100,000 Pulses	79
3-18	Liquid Erosion Test: Fresh Shell 405 1/8" x 1/8" Cylinders at 100 Feet per Second and 500,000 Pulses	80
3-19	Liquid Erosion Test: Fresh Shell 405 1/8" x 1/8" Cylinders at 55 Feet per Second and 8,200 Pulses	83
3-20	Liquid Erosion Test: Fresh Shell 405 1/8" x 1/8" Cylinders at 55 Feet per Second and 100,000 Pulses	84
3-21	Liquid Erosion Test: Fresh Shell 405 8 to 12 Mesh Particles at 55 Feet per Second and 8,200 Pulses	85
3-22	Liquid Erosion Test: Fresh Shell 405 8 to 12 Mesh Particles at 55 Feet per Second and 100,000 Pulses	86
3-23	Liquid Erosion Test: Fresh Shell 405 8 to 12 Mesh Particles at 100 Feet per Second and 8,200 Pulses	87
3-24	Liquid Erosion Test: Fresh Shell 405 8 to 12 Mesh Particles at 100 Feet per Second and 100,000 Pulses	88
3-25	Liquid Dynamic Erosion of Fresh Shell 405 1/8" x 1/8" Cylinders	89
3-26	Liquid Dynamic Erosion of Fresh Shell 405 8 to 12 Mesh Particles	90
4-1	Laboratory Reactor for Catalyst Breakup Phenomena Testing	102
4-2	Laboratory Reactor Components	103
4-3	Assembled Laboratory Reactor	104
4-4	Laboratory Reactor Test Cell	108
4-5	Liquid Quench Thermal Shock Test Configuration	109

LIST OF FIGURES (Cont'd)

<u>No.</u>		<u>Page</u>
4-6	Catalyst Bed Pressure Drop as a Function of Peak Upstream Pressure	121
4-7	Cumulative Damage of 14-18 Mesh Catalyst Exposed to Successive Pops	122
4-8	Cumulative Damage of 25-30 Mesh Catalyst Exposed to Successive Pops	123
4-9	Post Pop-Shock Appearance of 14-18 Mesh Catalyst (Magnification 10 x)	124
4-10	Post Pop-Shock Appearance of 25-30 Mesh Catalyst (Magnification 10 x)	125
4-11	Pre and Post-test Appearances of 14-18 Mesh Catalyst Subjected to 100 Thermal Fatigue Cycles (Magnification 10 x)	129
4-12	Pre and Post-test Appearances of 25-30 Mesh Catalyst Subjected to 100 Thermal Fatigue Cycles (Magnification 10 x)	130
4-13	Injector Geometry for Liquid Quench Thermal Shock Studies	132
4-14	Cumulative Fines Generation for Liquid Quench Thermal Shock	136
4-15	Pre and Post-test Appearance of 14-18 Mesh Catalyst Subjected to 200 LQTS Cycles (Magnification 10 x)	137
4-16	Pre and Post-test Appearance of 25-30 Mesh Catalyst Subjected to 200 LQTS Cycles (Magnification 10 x)	138
4-17	Pre and Post-test Appearances of 14-18 Mesh Subjected to Void-Volume Abrasion (Magnification 10 x)	141
4-18	Pre and Post-test Appearances of 25-30 Mesh Catalyst Subject to Void-Volume Abrasion (Magnification 10 x)	142
4-19	Summary of Results of Interaction Study II for 14-18 Mesh Catalysts	156

LIST OF FIGURES (Cont'd)

<u>No.</u>		<u>Page</u>
4-20	Sequential Mini-Bed Crushing of 8-12 Mesh Fresh Shell 405 Catalyst	157
4-21	Sequential Mini-Bed Crushing of 8-12 Mesh Fresh Shell 405 Catalyst	158
4-22	Sequential Mini-Bed Crushing of 14-18 Mesh Fresh Shell 405 Catalyst	159
4-23	Sequential Mini-Bed Crushing of 20-25 Mesh Fresh Shell 405 Catalyst	160
4-24	Sequential Mini-Bed Crushing of 20-25 Mesh Fresh Shell 405 Catalyst	161
4-25	Sequential Mini-Bed Crushing of Fresh 25-30 Mesh Shell 405 Catalyst	162
4-26	Sequential Mini-Bed Crushing of Fresh 20-30 Mesh Shell 405 Catalyst	163
4-27	Effect on the Percent of Weak Particles of a Simultaneous Reduction in Mean Value and Increase in Standard Deviation	178
4-28	Sequential Mini-Bed Crushing of Used 25-30 Mesh Shell Catalyst: Percent Through 30 Mesh	179
4-29	Sequential Mini-Bed Crushing of Used 25-30 Mesh Shell 405 Catalyst: Percent Through 35 Mesh	180
4-30	Comparison of Particle Crush Strength Distributions of 25-30 Mesh Fresh Shell 405 and Used Samples S/N001 and S/N002	181
4-31	Liquid Erosion Test: 14-18 Mesh Shell 405 Catalyst From the Air Force Rocket Propulsion Laboratory After Use in Lower Bed of 5 lbs Thruster at 100 Feet Per Second and 100,000 Pulses	183
4-32	Liquid Erosion Test: 14-18 Mesh Shell 405 Catalyst From Rocket Research Corporation After Use in Outer Bed of APU Gas Generator at 100 Feet Per Second and 100,000 Pulses	184

LIST OF FIGURES (Cont'd)

<u>No.</u>		<u>Page</u>
4-33	Liquid Erosion Test: 14-18 Mesh Shell 405 Catalyst From TRW After 250 Seconds of Steady State Firing Spread of 51 Cold Starts at 100 Feet Per Second and 100,000 Pulses	185
5-1	Failure in a Brittle Porous Material	200
5-2	The Stress Distribution Around a Cylindrical Hole in Biaxial Stress	202
5-3	Failure Surface for Biaxial Loading - Fresh Shell 405	203
5-4	Failure Surface for Biaxial Loading - Used Shell 405	204
5-5	Temperature Profiles in Externally Heated Pellet	209
5-6	Temperature Profiles in Externally Cooled Pellet	210
5-7	Temperature Profile for Estimating Effect of Thermal Stress	213
5-8	Radial Stress as a Function of Time - Heating	214
5-9	Transverse Stress as a Function of Time - Heating	215
5-10	Radial Stress as a Function of Time - Cooldown	216
5-11	Transverse Stress as a Function of Time - Cooldown	217
5-12	Worst-Case Pressure Profiles	221
5-13	Stresses Produced by Pressurization and Blowdown	222
5-14	Pressure and Temperature Profiles	224
5-15	Radial and Transverse Stresses	225
5-16	Unit Cube from a Force Centered Cubic Array	227
5-17	Contact Problem	229
5-18	Maximum Contact Stress	233
5-19	Effect of Poisson's Ratio on Transverse Stresses	234
5-20	Effect of Poissons's Ratio on Tensile Stress	235

LIST OF FIGURES (Cont'd)

<u>No.</u>		<u>Page</u>
5-21	Stress Distribution on the Surface of Two Spheres of Shell 405	236
5-22	Failure Surface - Fresh Shell 405	237
5-23	Failure Surface - Used Shell 405	239
5-24	Bed Pressure Required to Product Failure	240
5-25	Stress Components Acting on Material Element	245
5-26	Comparison of Failure Theories With Experimental Data	250
5-27	Crater Shape - 25 psi Bed Pressure	251
5-28	Crater Shape - 50 psi Bed Pressure	252
5-29	Crater Shape - 100 psi Bed Pressure	253
5-30	Crater Shape - 200 psi Bed Pressure	254
5-31	Crater Shape - 300 psi Bed Pressure	255
5-32	Bed Damage Versus Bed Pressure	256
5-33	Related Permeability Versus Saturation	260
5-34	Related Permeability Versus Saturation	260
5-35	Permeability Versus Pressure	260
5-36	Klinkenberg Factor	260
5-37	Capillary Pressure Versus Saturation	261
5-38	Capillary Pressure J-Function Versus Saturation	261
5-39	Pore Size Distribution for Shell 405	263
5-40	Capillary Pressure Versus Saturation for Shell 405	264
5-41	Nodal Model of a Pellet	266
5-42	Conceptual Model of Nodal Behavior	266
5-43	Internal Particle Model Illustrative Case	271

LIST OF FIGURES (Cont'd)

<u>No.</u>		<u>Page</u>
5-44	Frontal Advance Rate of Water	278
5-45	J-Function Value	279
5-46	Pressure Versus Permeability	282
5-47	Effect of Particle Size	283
5-48	Effect of Initial Temperature	284
5-49	Pressure Versus Initial Saturation	287
5-50	Start-Up Temperature Response	290
5-51	Bed and Chamber Expansion Histories	291
5-52	Cooldown History	293
5-53	Contraction During Cooldown	294
5-54	Effect of Bed Loading on Differential Expansion	295
5-55	Effect of Loading Near Steady State	296
5-56	Effect of Bed Loading During Cooldown	297
5-57	Effect of Pressure on Start-Up Expansion	298
5-58	Effect of Pressure on Cooldown	299
5-59	Effect of Thrust on Start-Up	302
5-60	Mass Loss vs. Pressure - 25-30 Mesh	305
5-61	Bed Compression vs. Time	308
5-62	Temperature vs. Time	309
5-63	Bed Compression vs. Time	310
5-64	Bed Compression vs. Time (0.1 lbf)	311
5-65	Bed Compression vs. Time (5.0 lbf BAC)	313

LIST OF FIGURES (Cont'd)

<u>No.</u>		<u>Page</u>
5-66	Pellet Configuration	314
5-67	Multi-Layer Configuration	316
5-68	Impingement Focusing	317
5-69	Wear Versus Velocity	319
5-70	Catalyst Bed Model	321
5-71	Erosion Versus Particle Contamination	325
5-72	Erosion Versus Flow Rate	327
5-73	Erosion Versus Pressure	328
5-74	Conceptual Model of Hydrazine Rocket	331
5-75	Friction Factor Correlation	332
5-76	Pressure Profile 0.35 milliseconds	333
5-77	Pressure Profile 1.0 milliseconds	334
5-78	Pressure Profile 2.0 milliseconds	335
5-79	Pressure Versus Time	336
5-80	Bed Compression Versus Time	337
5-81	Peak Compressive Stress Versus Rise Time	337

LIST OF TABLES

<u>No.</u>		<u>Page</u>
2-1	Overall Summary of Experimental and Analytical Work	26
3-1	Physical Properties of Iridium and Porous Alumina	32
3-2	MIL-P-26536C	33
3-4	Summary of Sensitivity Tests in the Gas Fluid Dynamic Erosion Tester	42
3-5	Summary of Sensitivity Tests in the Gas Fluid Dynamic Erosion Area	43
3-6	Investigation of the Possible Effect of Specimen Water Content on ITI Crush Strength Measurement	53
3-7	Particle Compressive Crushing Strength of Fresh Shell 405 Catalyst in the ITI	55
3-8	Particle Compressive Strength of Alumina Support Before Attrition	56
3-9	Particle Compressive Strength of Alumina Support After 50% Attrition	57
3-10	Effect of Catalyst Preparation Steps on Particle Average Compressive Crushing Strength	58
3-11	Effect of Iridium Addition on Average Compressive Crushing Strength of 1/8" x 1/8" Cylinders	59
3-12	Summary of Statistical Tests on the Significance of Differences Between Particle Average Compressive Crushing Strength	60
3-13	Effect of Catalyst Preparation Steps on the Scatter in Individual Particle Compressive Crushing Strengths	62
3-14	Particle Crush Strength of Fresh 20-25 Mesh Shell 405 Catalyst or Substrate	63
3-15	Effect of Multiple Loading on Compressive Crushing Strength of Fresh Shell 405 1/8" x 1/8" Cylinders	64

LIST OF TABLES (Cont'd)

<u>No.</u>		<u>Page</u>
3-16	Comparison of Scaling Parameters Used in Incipient Particle Movement Study	67
3-17	Particle Fluidization: Effect of Particle Size and Gas Density on Minimum Inlet Superficial Velocity for Particle Movement	69
3-18	Summary of Particle Fluidization Parameters	72
3-19	Effect of the Number of Pulses at a Fixed Velocity	77
3-20	Effect of Velocity, Number of Pulses and Catalyst Selection on Liquid Erosion in PLPET	82
3-21	Analysis of Variance (ANOVA) Summary	91
4-1	Interaction Study I	98
4-2	Interaction Study II	99
4-3	Original "Pop" Shock Dynamic Pressure Crushing Test Matrix	111
4-4	Expanded "Pop" Shock Dynamic Pressure Crushing Test Matrix	112
4-5	Hot Gas Thermal Fatigue Test Matrix	113
4-6	Hot Gas Thermal Aging Test Matrix	114
4-7	Liquid Quench Thermal Shock Test Matrix	116
4-8	Void-Volume Abrasion Test Matrix	117
4-9	Pop-Shock Data for 14-18 Mesh Catalyst	119
4-10	Pop-Shock Data for 25-30 Mesh Catalyst	120
4-11	Hot Gas Thermal Fatigue Test Results for 14-18 Mesh Catalyst	127
4-12	Hot Gas Thermal Fatigue Test Results for 25-30 Mesh Catalyst	128
4-13	Hot Gas Thermal Aging Test Results	131

LIST OF TABLES (Cont'd)

<u>No.</u>		<u>Page</u>
4-14	Liquid Quench Thermal Shock Data for 14-18 Mesh Catalyst	134
4-15	Liquid Quench Thermal Shock Data for 25-30 Mesh Catalyst	135
4-16	Void-Volume Abrasion Test Data	140
4-17	Isothermal Catalyst Activity Reactor Test Results	144
4-18	Summary of Results for Interaction Study I	150
4-19	Summary of Results for Interaction Study II For 14-18 Mesh Catalysts	151
4-20	Engine Exposed Catalyst Degradation	153
4-21	Comparison of the Resistance of Various Fresh Shell 405 Mesh Sizes to Bed Pressure Crushing	165
4-22	Evaluation of Fresh Shell 405 Catalyst in the Particle to Particle Abrasion Resistance Apparatus (PPARA)	167
4-23	Size Distribution of Fresh Shell 405 Catalyst After Exposure in PPARA	169
4-24	Particle Crushing Strength of Used 18-20 Mesh Shell 405 Catalysts From TRW	170
4-25	Particle Crushing Strength of Used Shell 405 Catalyst From TRW	171
4-26	Particle Crushing Strength of Used Shell 405 Catalyst From the Air Force Rocket Propulsion Laboratory	172
4-27	Particle Crush Strength of Used Shell 405 Catalyst From the Air Force Rocket Propulsion Laboratory	173
4-28	Particle Crushing Strength of Used Shell 405 Catalyst From the Rocket Research Corporation	174
4-29	Particle Crushing Strength of Used Shell 405 Catalyst From the Rocket Research Corporation	175

LIST OF TABLES (Cont'd)

<u>No.</u>		<u>Page</u>
4-30	Some Shell 405 Samples Show Deterioration of Crush Strength Following Thruster Exposure	176
4-31	Comparison of Ability of Fresh Versus Used Shell 405 14-18 Mesh Granules to Resist Pulsed, Liquid Erosion	186
4-32	Particle Crush Strength Distribution of 25-30 Mesh Shell 405 Catalysts Used in TRW "Pop Shock" Studies	188
4-33	Particle Crush Strength Distribution of Samples After Liquid Quench Thermal Shock Tests	190
4-34	Particle Crush Strength Distribution of Samples After Void Volume Abrasion Tests	191
4-35	Particle Crush Strength Distribution of Samples After Exposure to Liquid Hydrazine	192
4-36	Pulsed, Liquid Erosion Resistance of 14-18 Mesh Shell 405 Catalysts Used in TRW "Pop Shock" Studies	193
4-37	Summary of Results of Tests on Catalyst Samples Exposed to Controlled Environments	195
5-1	Supporting Analyses	198
5-2	Internal Particle Processes Variation Study	281
5-3	Conditions Used in Differential Thermal Expansion Calculation	300
5-4	Thruster Characteristics	307
6-1	Analytical Modeling Results Versus Experimental Results	351
6-2	Summary of Significant Mechanisms or Factors	353
6-3	Summary of Insignificant Mechanisms or Factors	354

1. INTRODUCTION

Monopropellant hydrazine is widely regarded as the established standard for unmanned spacecraft auxiliary propulsion systems. To date, there are over 30 United States flight programs that use hydrazine propulsion systems with Shell 405 catalyst as the means for spontaneously initiating the decomposition reaction. These programs have occurred over the last decade. Even with this experience, it is evident that there is still much that is not understood about the fundamental processes involved in heterogeneous hydrazine catalytic reactors.

The Shell 405 catalyst was developed to satisfy the requirements for a simple, reliable, lightweight, nonpower draining and relatively low cost means of spontaneously decomposing hydrazine. The potential use of hydrazine as a monopropellant was first studied extensively in the USA by JPL during the late 1940's and 1950's. It was found that homogeneous, thermal decomposition of hydrazine proceeded slowly, requiring residence times too large to be practical in most rocket engine applications. Subsequent work evolved several catalysts that could effectively sustain decomposition of liquid hydrazine if the initial reactor bed temperature was maintained in the 600° to 800°F range. For these catalyst systems, however, it was necessary to employ techniques that preheated the bed to initiate and sustain decomposition. The complications of using these methods seriously impaired the early acceptance of monopropellant hydrazine for spacecraft propulsion systems. Over the years, efforts were expanded in search for improved spontaneous catalyst with success finally being achieved by the Shell Development Company in what must be considered a true technological breakthrough for that period (1964). The availability of Shell 405 catalyst greatly expanded interest in the application of monopropellant hydrazine propulsion systems, not only because it was a truly spontaneous catalyst, but also because it appeared to be capable of a great many starts.

Coincidentally, the occurrence of the spontaneous catalyst capability was paralleled by a proliferation of unmanned spacecraft missions requiring the use of attitude control and station keeping propulsion systems. The use of Shell 405 catalyst hydrazine systems accelerated, therefore, from the first hurried application in November of 1967 to the number of flight systems in operation at the present time. Because hydrazine thruster technology grew so rapidly, many potential problem areas were bypassed or explored in only enough detail to satisfy specific requirements for a given application. In addition, rapid changes have occurred in thruster performance and life requirements over the last few years. The original specifications for spinning satellites and short-life upper stages required relatively rapid firing rates (on the order of 1 Hz), only a few ambient starts (typically 20 to 50), and only 2,000 to 5,000 pulses. These requirements are simple when compared to the

present needs of three exit stabilized long-life missions that require hundreds of ambient starts (40° to 70°F) and hundreds of thousands of "hot" pulses at varying frequencies. The use of hydrazine thrusters employing Shell 405 catalyst for extended life missions is currently limited by the physical degradation of the catalyst. This program is one part of an extended effort being carried out by AFRPL to improve the life of Shell 405 catalytic hydrazine thrusters.

2. APPROACH

2.1 Objective

The performance of the Shell 405 catalyst deteriorates during its use for hydrazine decomposition in monopropellant thruster operation. The overall objective of work under this contract was to investigate external catalyst breakup mechanisms so as to establish an understanding of this phenomena which can aid in extending catalyst life during use.

2.2 Program Organization

The External Catalyst Breakup Phenomena program involves the joint efforts of Exxon Research and Engineering Company (prime contractor) and McDonnell Douglas Astronautics Company and the Systems Group of TRW, Inc. A study of Internal Catalyst Breakup Phenomena was carried out separately by United Technologies Research Laboratories under a different contract (F04611-74-C-0031). The overall effort (i.e., both internal and external catalyst breakup phenomena work) was coordinated by the Air Force with the assistance of a Scientific Advisory Board (SAB). The SAB consists of appropriate Air Force and contractor members plus the following additional members:

- Mr. S. DeBrock, Lockheed Missiles and Space Corp.
- Mr. M. J. Russi, Aerospace Corp.
- Mr. V. A. Mosely, Bell Aerospace Company
- Dr. J. D. Rockenfeller, Rocket Research Corp.
- Dr. M. Boudart(a), Stanford University
- Dr. D. P. H. Hasselman(a), Lehigh University

Mr. F. S. Forbes, AFRPL, is chairman of the SAB.

The External Catalyst Breakup Phenomena program consisted of three tasks as follows.

Task I - Phenomenological Survey

In Task I a phenomenological survey was performed to identify and describe the more important mechanisms of the external catalyst breakup process. The objective of this work was to establish the foundations for the more extended experimental program in Task II, and to generate an understanding of the catalyst breakup process.

(a) Consultant to Exxon Research and Engineering Company.

Three areas of effort were carried out in Task I. First, a review and analysis of the literature, second, a series of experimental sensitivity tests to screen the breakup hypotheses, and third, a comprehensive assessment of the results of the sensitivity tests, literature review and analytical modeling results so as to select and rank the breakup mechanisms for additional study in Task II.

Task II - Selected Mechanisms Testing

More intensive laboratory testing was performed in Task II. This involved (a) additional investigation of mechanisms or factors which have been shown to be important, and (b) investigation of phenomena occurring in a complex bed environment, rather than just occurring in a single particle. Also the effects of synergisms or interactions were investigated.

Task III - Supporting Analyses

Concurrently with the other tasks, analytical studies were conducted to support the experimental activities and also to aid in the assessment of breakup mechanisms by exploring areas not experimentally investigated. The development of a complete catalytic bed design analysis was beyond the scope of this program. However, governing equations and analytical descriptions of phenomena expected during catalyst breakup in simplified situations, were developed so as to generate an understanding of driving mechanisms that will form a basis for such a design analysis mode. This work was to provide an assessment of the important factors involved in catalyst fracture.

Task I and Task II efforts were carried out in sequence, and primarily involved work by Exxon Research and TRW. Task III was carried out concurrently with Tasks I and II and involved work by McDonnell Douglas Astronautics. An overall summary of experimental and analytical work carried out is shown in Table 2-1.

Table 2-1

Overall Summary of Experimental and Analytical Work

General Area	Specific Mechanisms	Experimental		Analytical
		Task I	Task II	Task III
Fluid Dynamic Erosion	Pure Gas per se	X		
	Liquid Droplets in Gas			X
	Pulsed Liquid Streams	X		
	Solid Particles in Gas			X
Pressure Crushing	Static Individual Particle	X		
	Static Bed		X	
	Bed Cold Gas Cycling		X	
	Dynamic - Normal Transient Pressure Buildup			X
	Dynamic - "Pop" Shock		X	
Differential Thermal Expansion	Compressive Crushing During Heating and Cooling			X
Particle Movement	Incipient Movement Velocity	X		
	Abrasion in "Fluidized" Bed		X	
	Void Volume Hot Gas Flow Abrasion		X	
Thermal Effects	Hot Gas		X	X
	Thermal Shock		X	
	Thermal Aging		X	
	Thermal Fatigue		X	
Internal Pore Pressure Gradients	Liquid Quench of Hot Bed		X	X
	Rapid External Pressurization or Depressurization (no liquid)			X
	Pore Pressure Build-Up as a Result of Imbibed Liquid			X
Effect of Use on Fresh Catalyst Physical Properties	Thruster Exposure		X	
	Controlled Physical Environments		X	
Interactions or Synergisms	Liquid Exposure - Thermal Cycling - Gas Pressure Cycling - Thermal Aging		X	

3. TASK I - PHENOMENOLOGICAL SURVEY

3.1 Literature Search

A literature search relative to catalyst breakup phenomena was made by Exxon Research and Engineering Company and TRW Systems Group. The search included a review of both government and non-government pertinent literature and was primarily based on:

- Lockheed Information Retrieval Service
- APILIT National Retrieval Service
- Reports and Abstracts Furnished by TRW.

The literature was reviewed to examine the available information on possible mechanisms which may contribute to the degradation of Shell 405 hydrazine monopropellant catalytic engines. These encompass both internal (within catalyst particles) and external (particle to particle) phenomena. The results, presented below, include information derived from hydrazine monopropellant engine studies and from other studies which are relevant to the catalyst degradation problem.

3.1.1 Internal Phenomena

3.1.1.1 Reduced Catalyst Internal Porosity

The internal porosity of a catalyst pellet can affect the magnitude of the temperatures and pressures built up during reaction, which in turn, can produce stresses and strains that exceed the tolerable limits of the catalyst structure. This is particularly true if the reaction taking place within the catalyst is exothermic. Prater (47) has shown that significantly higher temperatures can occur inside a catalyst particle relative to the surface bulk fluid temperature during an exothermic reaction. Kesten (32) has applied the Prater equation to the development of a specific model for hydrazine decomposition in Shell 405. The temperature and pressure gradients predicted by these analyses can cause considerable internal stresses within the catalyst structure. Furthermore, extensive thermal and pressure gradients resulting from pore transport limitations during start-up may be considerably higher. This was shown to be the case in studies conducted by Lee, et al (34) on the stability of exothermic reactions in catalysts with transport limitations.

Reductions in total pore volume and changes in pore volume distribution can impede the transfer of heat and pressure generated in the catalyst interstices. Several references can be found to show how exposure of supported catalysts to elevated temperature causes deleterious changes in available micropore volume and pore distribution.

For example, studies by Levy (35) Shachner (60) and Benesi, (3) show how commercial alumina pellets exposed to high temperatures, undergo a large reduction in number of micropores along with reductions in surface area. Sintering is seen to convert several small pores into fewer larger ones such that the total pore volume is relatively unchanged. Such changes have been shown to increase the overall density of the catalyst particle, cause blockage of available active sites and result in increased thermal and pressure stresses.

Sayer and Southern (75) suggest that the rapid decrease observed in the surface area of a CNESRO-1 hydrazine catalyst substrate at temperatures in excess of 1000°C was due to a phase change from the gamma alumina to the alpha alumina. However, even if such is the case, the CNESRO-1 catalyst is based on a γ -alumina which is prepared from aluminum monohydrate (boehmite) while the γ -alumina used for Shell 405 support is prepared from alpha aluminum trihydrate (gibbsite). Their results are thus not directly applicable to the behavior of Shell 405 at elevated temperature but are nevertheless of interest to the present problem.

Peppmahl and Rose (86) have shown, by microscopic examination how catalyst pores could be clogged with fines formed when portions of the catalyst pellets are crushed or attrited. Such possible clogging of internal catalyst pores could contribute to increased pressure build-up within the Shell 405 catalyst and subsequent accelerated catalyst failure.

In addition, it has been shown that exposure of a supported metal catalyst to rapid and high temperature changes can cause extensive migration and growth of metal crystallites such that micropore blockage can occur. The work of Ruchenstein and Petty (53) has shown this to be the case for alumina supported platinum catalysts. Localized high temperatures, achieved in a catalyst pellet at crystallite sites, were found to cause growth and agglomeration of platinum crystallites. In some cases, the transient temperature spikes were believed to cause possible detachment of clusters of crystallites. These processes could be even more severe in a catalyst such as Shell 405 which has an extensive amount (~ 30 wt. %) of dispersed metal (iridium) throughout the catalyst structure.

3.1.1.2 Presence of Adsorbed Species

The literature contains numerous references showing how the adsorption of certain molecular species, present in the reactive system, can interfere with reaction rates and reduce the activity of heterogeneous catalyzed systems. In most cases, loss of catalyst activity for the intended reaction occurs because active catalyst sites are permanently or temporarily occupied by adsorbed species, thus rendering them unavailable for the intended reaction. However, in certain specific

cases, the adsorbed species can itself participate in processes which destroy the catalyst structure. The classic example of this phenomenon is the adsorption of H_2O on alumina substrates at high temperatures. The adsorbed H_2O is seen to catalyze transformations that rapidly reduces the substrate surface area and micropore volume (35)(55).

Adsorption related processes can have deleterious effects on the performance of Shell 405. Kesten (3) has reported that exposure of Shell 405 catalyst to cold, high pressure decomposition products can result in the adsorption of H_2 and NH_3 . The adsorption of these gases was seen as reducing the start-up activity of the catalyst and contributing to large particle pressure build-up. Pressure build-up within the particle pores results from the interaction of temporary lost catalyst activity (from adsorption of NH_3 and H_2) and liquid hydrazine flooding of catalyst pores. This is considered more fully in the paragraphs discussing blockage of outer pores by liquid hydrazine. Studies by Sayer (59) and Wood and Bryant (71) also support the theory of considerable ammonia and hydrogen adsorption on Shell 405 with subsequent loss of available activity for low temperature starts. Their work also supported the observations that the adsorption was reversible and that once the catalyst temperature was elevated, desorption of NH_3 and H_2 would take place. However, cumulative physical adsorption of reaction products could conceivably reduce catalyst activity to a point where low temperature starts would no longer be possible.

More severe deleterious adsorption effects with Shell 405 can occur with chemical species such as halogens, oxygen and H_2O . McCullough (37) has shown that traces of Cl_2 in the hydrazine reactor system could cause permanent loss of catalyst activity. Chlorine is believed to react with iridium metal to form a volatile product $IrCl_3$ whereby active metal sites are completely lost from the catalyst structure. This same mechanism has been shown to be operable in the loss of activity of alumina supported platinum catalyst, used in reforming reactions in the petroleum industry (41). Cl_2 can result from the presence of trace quantities of halogenated solvents such as freons and perchloro ethylene used to clean hydrazine thruster hardware components (37).

In a similar fashion, oxygen can react with iridium metals under certain conditions resulting in conversion to volatile IrO_3 and IrO_2 . This process can result in both loss of iridium metal from the catalyst structure and iridium crystallite growth both resulting in reduced hydrazine decomposition activity. This mechanism has been shown to be responsible for the loss of supported iridium-ruthenium catalyst activity in automobile catalytic converters, as well as other high temperature applications (38).

As indicated in previous paragraphs, the adsorption of water on alumina surfaces has been found to rapidly accelerate high temperature sintering. Shell 405 utilizes a gamma-alumina substrate as a support for metallic iridium crystallites and would be expected to be susceptible to this deleterious phenomenon. This has been confirmed in Shell 405 life test studies conducted by Boge (67). Rapid loss in catalyst area was found to take place when sintering occurred in a nitrogen atmosphere containing water vapor. Effects of trace water may have similar though lower magnitude effects.

Trace water vapor may enter the hydrazine thruster system by adsorption on the Shell 405 catalyst surface during preparation, from contamination in the hydrazine itself, or by chemical reaction. Brooks (5) has reported that water vapor can be formed by the reaction of adsorbed O_2 with IrH under conditions where chemisorbed hydrogen (formed during reduction of the catalyst during preparation or in subsequent hydrazine decomposition) is left on the catalyst surface. These sources of water could contribute to degradation of Shell 405 catalyst surface area and activity by the above mechanism.

Carlson (70) has conducted experimental investigations relating the low temperature, high vacuum, hydrazine ignition properties of Shell 405 catalyst to the concentration of adsorbed gas species including O_2 , N_2 , H_2 and NH_3 present on the catalyst surface. The results of the study indicated that hydrogen could be adsorbed on Shell 405 under high vacuum conditions if the reactor is cooled rapidly. However, no conclusion was reached about any adverse effect of adsorbed hydrogen on ignition delay and catalyst degradation phenomena.

Smith and Solomon (89) relate the catalyst attrition mechanism in hydrazine engines to the irreversible, dissociative adsorption of hydrazine on catalyst sites at temperatures below 450°K.

Peranskii et al. (88) has shown that the mechanical strength of promoted alumina catalysts and resistance to abrasion of catalyst particles was reduced by the adsorption of water and hydrocarbons on the catalyst surface. Similar effects may be possible from the adsorption of reaction products or hydrazine contaminants during the firing of hydrazine monopropellant thrusters.

Thus, the adsorption processes discussed above can all contribute to loss in special catalyst activity. This loss in activity in turn can contribute to severe internal particle pressure build-up and subsequent fracture by interaction with the liquid hydrazine blockage of pores discussed below.

3.1.1.3 Blockage of Catalyst External Pores by Liquid Hydrazine

Kesten (30) has proposed a mechanism whereby the wetting of liquid hydrazine on the outside of porous Shell 405 catalyst particles can prevent decomposition gases from escaping the structure, thus causing severe internal build-up of pressures. Liquid hydrazine is seen as entering the pores by capillary action and requiring very high gas pressures for expulsion. Where non-uniform hydrazine wetting occurs, severe pressure gradients can exist within the particle structure. Motion picture studies of hydrazine decomposition in a single particle by Sangiovanni and Kesten (58) have supported this theory; so have mathematical analyses conducted by the same authors (57).

The interaction of this mechanism with loss of catalyst specific activity (produced by adsorption or diffusional phenomena discussed above) can be great; particularly in transient conditions. Lowered catalyst activity would permit further penetration of the liquid hydrazine into the catalyst structure, requiring greater internal pressures for expulsion. Further, if the reduction in catalyst activity due to adsorption were not uniform, larger thermal gradients would be expected. These effects would be expected to be particularly pronounced during pulse mode operation, where catalyst particles would be repeatedly subjected to cyclic exposure to cold hydrazine and hot decomposition gases.

These effects are supported by the work of Lee (34) who studied the stability of several exothermic reactions in catalyst particles with external transport limitations. It has also been observed to occur in a number of liquid phase heterogeneous catalytic industrial operations.

Moynihan and Bjorklund (82) have estimated the internal pore pressures in Shell 405 resulting from hydrazine adsorption and decomposition to be of the order of 2000 psi. These high pressures combined with large thermal gradients, were believed to be responsible for catalyst breakup in their 1 lbf. test thrusters.

Greer (84) has studied the low temperature (40°F) start characteristics of hydrazine monopropellant engines using high speed photography and a plexiglass reactor. He concluded that catalyst attrition was primarily caused by high pressures generated within the catalyst rather than from large chamber pressure spikes.

On the other hand, Basmadjian's (87) theoretical analysis of pressures arising in both the macropore and micropore networks of catalyst pellets during the rapid venting of high pressure, fixed bed reactors leads to the conclusion that rapid pressure release should not result in damage to the pellets since the pressure in the pellet closely approaches that of the reactor void space. However, Basmadjian's analysis does not consider gas generation by chemical reaction in the micropores and its applicability to the hydrazine thruster situation is limited.

3.1.1.4 Thermal Stress Fracture

In addition to the phenomena discussed above, the catalyst breakup model includes the effects of thermal stress fracture as a process which itself can contribute to catalyst particles. From this standpoint, it is useful to consider the basic composition of the Shell 405 catalyst from a strength of materials, structural, point of view. Shell 405 consists of a composite structural system of a continuous (though porous) phase of gamma alumina with large amounts of iridium (≈ 30 wt. %) metal located in the pore interstices. Physical properties of these materials are compared in Table 3-1. Alumina is a refractory oxide having a very low thermal conductivity. Iridium is a metal having a high thermal conductivity.

Table 3-1

Physical Properties of Iridium and Sintered Alumina

Property	Iridium	Sintered Alumina
Thermal Conductivity cals/cm-sec	.36	.02-.01
Linear Coefficient of thermal expansion in/in/°F	6.5×10^{-6}	3.9×10^{-6}
Compressive Strength, psi		4×10^5
Tensile strength, psi	3.2×10^3	4×10^4
Youngs modulus, psi	6×10^5	5×10^7

Though the linear thermal coefficients of expansion are not too dissimilar, significant local thermal stresses, resulting from temperature differences at the iridium alumina boundaries during start-up conditions, would be expected. This is due to the fact that the local heat fluxes produced at the catalyst active sites would be transferred more rapidly into the much more thermally conductive iridium than to the alumina. Furthermore, during pulse mode operation, metal active sites would tend to be surrounded

by hot decomposition gases, while exterior alumina pore walls would tend to be in contact with the cold, liquid hydrazine feed. This would further enhance transient differential thermal stresses. Large transient local temperature gradients at metal active sites, in porous alumina substrates, have been predicted by the work of Ruchenstein and Petty (53).

In this connection, it should be acknowledged that the analyses of Prater (47) and Kesten (31) (which predict much lower temperature gradients for exothermic reactions occurring within catalyst particles) are steady-state treatments and do not take into consideration local transient conditions. Ruchenstein and Petty's work (53) show that transient phenomena, such as the propagation velocity of the heat flux, must be taken into account to accurately describe the temperature fields inside a catalyst particle.

In a recent paper, Russi (77) points out that differential thermal expansion was not an important factor in the degradation of Shell 405. However, his conclusions were based on heating catalysts to 1800°F in a quartz cylinder and measuring bed volume shrinkage. The problem of differential thermal expansion and thermal stresses developed within the catalyst particles during the rapid (mil sec) temperature change during start-up was not, however, addressed.

3.1.1.5 Catalyst Contamination

The present MIL-SPEC (MIL-P-26536C, Amendment 1) for monopropellant hydrazine controls a large number of potential contaminants, namely:

<u>Contaminant</u>	<u>Max Allowed (% by Wt)</u>
Water	1.0
Chloride	0.0005
Aniline	0.50
Iron	0.002
Non-Volatile Residue	0.005
Carbon Dioxide	0.02
Other Volatile Carbonaceous Material	0.02

The required hydrazine purity must be at least 98.5 percent by weight, There is also a particulate limit of 1 milligram/liter.

Several of the above contaminants can potentially interfere with the hydrazine decomposition reaction. However, no conclusive results are presently available as to the deleterious role of specific contaminants. A process has been developed to purify propellant grade hydrazine as part of the current Mars Lander Program. However, no specific evidence is available which would indicate that use of such a propellant would extend the service life of Shell 405 catalyst.

Christopher and Russell (81) have also studied the effects of adsorbed hydrazine contaminants on catalyst life. Basically, they found that the low volatile metal contaminants such as iron, chromium and zinc appear to deposit on the catalyst, filling the interstitial spaces around the catalyst grains and/or forming a coating over the surface of individual particles. This second mode of deposition may result in reduced catalyst activity and degradation in bed performance.

Chloride contamination of hydrazine, results in formation of ammonium chloride. This compound has a relatively high vapor pressure at the reactor operating temperatures and is not believed to reduce catalyst performance per se (though condensation of NH_4Cl at the orifice of a test flow reactor has caused orifice clogging).

Marked degradation on catalyst performance, due to the presence of MMH and water in combination was believed to have been a result of carbon monoxide adsorption. However, this has not been firmly established. The authors conclude that further work on the effects of hydrazine contaminants on catalyst degradation is required to more fully understand their role.

Barclay (83) reports that Shell 405 catalyst can be deactivated by large quantities of UDMH. This contamination results in the formation of carbon which deposits on the catalyst surface. However, his tests require further work to fully assess the problem of carbon deposition.

Fredrickson (72) reported observing the performance degradation of Shell 405 in two lbf. engines subjected to 86,000 firings of static tests. Though the propellant used in the test program was found to be contaminated with about 1% UDMH, no conclusions were presented as to any adverse effect of the contaminants upon the catalyst.

3.1.2 External Phenomena

3.1.2.1 Poor Fuel Distribution - Bed "Drilling," Hydrazine Puddling

Poor fuel distribution can result from the above catalyst particle degradation sources which in turn lead to uneven pressure drop throughout the bed. Local formation of voids in one part of the bed, and blocking by fines in another, lead to maldistribution of the fuel, which in turn leads to uneven distribution of pressure and stresses in the catalyst beds. This phenomenon has been shown to contribute to catalyst bed degradation in several studies. In addition, Kesten (33) has shown that non-uniform distribution of hydrazine in catalyst beds can produce high temperature gradients under steady state conditions. More severe thermal gradients can result from poor fuel distribution during transient (start-up) conditions in highly exothermic reaction systems. This was shown by the work of Ruchenstein and Petty (53) and Lee (34).

The concept of local hydrazine "puddling" would contribute to high temperature and pressure gradients during start-up. In this concept, liquid hydrazine is seen accumulating in catalyst bed pockets where specific activity has been impaired (by any of the above discussed mechanisms). When the catalyst temperature is sufficiently elevated to activate these bed pockets, excess hydrazine is available and transient surges in pressure and temperature (pressure and temperature shocks) occur which are frequently above bed steady state conditions. Furthermore, the fact that temperature and pressure increases (spiking) occur very rapidly (msecs) means that the catalyst particles are subjected to severe impact loads which intensifies the bed breakdown process.

3.1.2.2 Bed Channeling, Churning and Settling

These phenomena are largely a function of catalyst particle break-down which leads to loss of material and creation of a "loose" bed. In-house studies at Exxon have shown how local fluid flow eddies can produce a "churning" action leading to increased particle to particle abrasion. The settling of small catalyst fragments ("fines") in the interstices of the bed have been observed to cause the channeling of reactants in a number of fixed bed catalytic systems. It is particularly important for systems operating under high pressures and high gas velocities.

Fredrickson (72) reported on the performance of two 5 lbf. engines subjected to 86,000 static firings. Engine degradation was indicated by excessive chamber pressure oscillations, and depressed pressure pulse shape. Post test observations revealed that 80% and 50% of the upper bed catalyst was lost from the two engines respectively. Failure was attributed to inadequate catalyst bed retention, which in turn could cause bed churning and catalyst attrition.

Fredrickson (74) reported that the loss in thrust of an S/N 002 monopropellant hydrazine thrust engine developed by Marquardt was apparently caused by the formation of excessive fines which decreased catalyst bed porosity. However, no conclusions are presented as to the actual formation of the fines during the testing.

3.1.2.3 Bed Erosion

Erosion of the Shell 405 catalyst bed by high velocity liquid or gaseous hydrazine is also considered to be a possible source of Shell 405 degradation.

However, preliminary high pressure gas attrition tests at Aerospace by King et al. (78) and at Rocket Research (79) indicate that this may have only a secondary contribution to the overall catalyst degradation mechanism.

3.1.3 Other Factors

Other possible phenomena that could contribute to the degradation process, include:

- Catalyst preparation history
- Crystal structure
- Particle geometry

All can effect and interact with most of the above mechanisms as indicated below.

3.1.3.1 Catalyst Preparation History

Clearly, the way in which the catalyst is prepared and the quality control over the preparation processes can be most important. Incomplete removal of halides could result in iridium crystallite growth and migration as well as loss through volatilization; incomplete removal of H₂O can result in accelerated alumina substrate desurfacing as well as destruction of the micropore structure; incomplete catalyst reduction to impaired activity for start-up. In addition, improper pre-attrition techniques can result in producing residual stresses in the final material which could act as built in latent sources of mechanical failure. A few examples cited in the literature illustrate some of the catalyst preparation.

Neuton (73) et al reports that pre-attrition of Shell 405 catalyst at the 90% level appeared to improve the cold start stability of the catalyst and recommended further evaluation of the technique. Pre-attrition is believed to remove the weak or stressed, portions of catalyst particles prior to firing.

Traina and Pernicono (85) have shown that the strength of alumina supported catalysts, as well as other catalytic properties, were very dependent on the methods of preparation of the catalyst including thermal treatments such as drying and calcination and forming treatments such as grinding, extrusion and tableting, etc.

3.1.3.2 Crystal Structure

With regard to crystal structure, possible alumina substrate phase changes during operation could weaken the basic catalyst structure. However, in this connection, most of the references reviewed in this preliminary literature study indicate that gamma alumina undergoes a transformation to the alpha phase via a theta phase (54,55). Transformation of the basic Shell 405 substrate gamma alumina to the alpha phase can occur rapidly in the presence of certain contaminants (such as H_2O , halides and alkaline earth metals).

3.1.3.3 Particle Geometry

The effect of catalyst particle geometry on its structural stability has also been shown to be important. Paranski et al (45) has described how particles of nearly spherical geometry tend to resist fracture from abrasion and other external forces better than granules which are irregular and have a high "aspect ratio" (large l/r). Similar dependence of the susceptibility of fracture to size and shape are predicted by the work of Chaplin (11) who analyzed fundamental stress-strain patterns in granular material.

3.2 Sensitivity Testing

As a result of the literature search and other considerations, a number of areas were chosen for experimental investigation. Work was carried out by Exxon Research and Engineering Company in the areas of:

- Gas Fluid Dynamic Erosion
- Particle Static Pressure Crushing
- Particle Incipient Movement Velocity
- Liquid Fluid Dynamic Erosion

3.2.1 Sensitivity Testing in the Gas Fluid Dynamic Erosion Area

The effect of gas fluid dynamic erosion was evaluated using single catalyst particles. This work was done using the High Severity Gas Erosion Tester (HSGET) shown in Figure 3-1. The unit consists of a 11-vi-Duty oven with three separate temperature controlled furnaces. The first two sections serve as a pre-heater for the flowing gas. The specimens are held in the third zone. Nitrogen was used as the flowing gas. Individual particles and pellets were held in specially constructed holder assemblies fabricated from 325 mesh type 304 stainless steel screen (see Figures 3-2 and 3-3). Individual particles were photomicrographed, vacuum dried overnight and weighed both before and after exposure to hot flowing gas in the HSGET apparatus. Five replicate samples were used in each run. Total exposure to nitrogen at 1700°F in the HSGET, which is preheated to operating temperatures, was one hour. Variables investigated included superficial gas velocity and catalyst selection parameters.

Tests were conducted at 50, 110 and 250 feet per second superficial gas velocity. All standard sizes of fresh Shell 405 catalyst were tested at 250 feet per second; the 1/8" cylinders, 14 to 18 mesh granules and 25 to 30 mesh granules were also tested at lower velocities. Five replicate runs with individual particles were made in each case. Detailed data is shown in the Appendix. In Table 3-4 is shown the average absolute weight loss for each test and in Table 3-5 the same results are reported on an average percent weight loss basis. Standard deviations calculated from the replicate data on a percentage change in weight basis are also shown in the Appendix. Photomicrographs of representative particles (two out of five) for each catalyst size before and after exposure to the hot flowing gas at 250 feet per second are shown in Figures 3-4 to 3-9.

An examination of the weight data indicates that none of the granular Shell 405 gas erosion tests showed a statistically significant average percentage weight loss at any of the gas velocities employed. This was corroborated by an examination of photomicrographs of particles before and after exposure to hot flowing gas, which did not indicate any obvious change in particle morphology. In contrast, the 1/8" x 1/8" cylindrical pellets exhibited a statistically significant (t-test at the 95% confidence limit) average percentage weight loss at all the gas velocities employed. The overall average weight loss with the cylinders was 3.1%. The differences in the weight losses at the different gas velocities was not statistically significant at the 95% confidence level (t-test).

A statistical Analysis of Variance was also performed on results from gas fluid dynamic erosion tests. The calculations were performed using the IBM three star analysis of variance (ANOVA) program.

Figure 3-1

High Severity Gas Erosion Tester (HSGET)

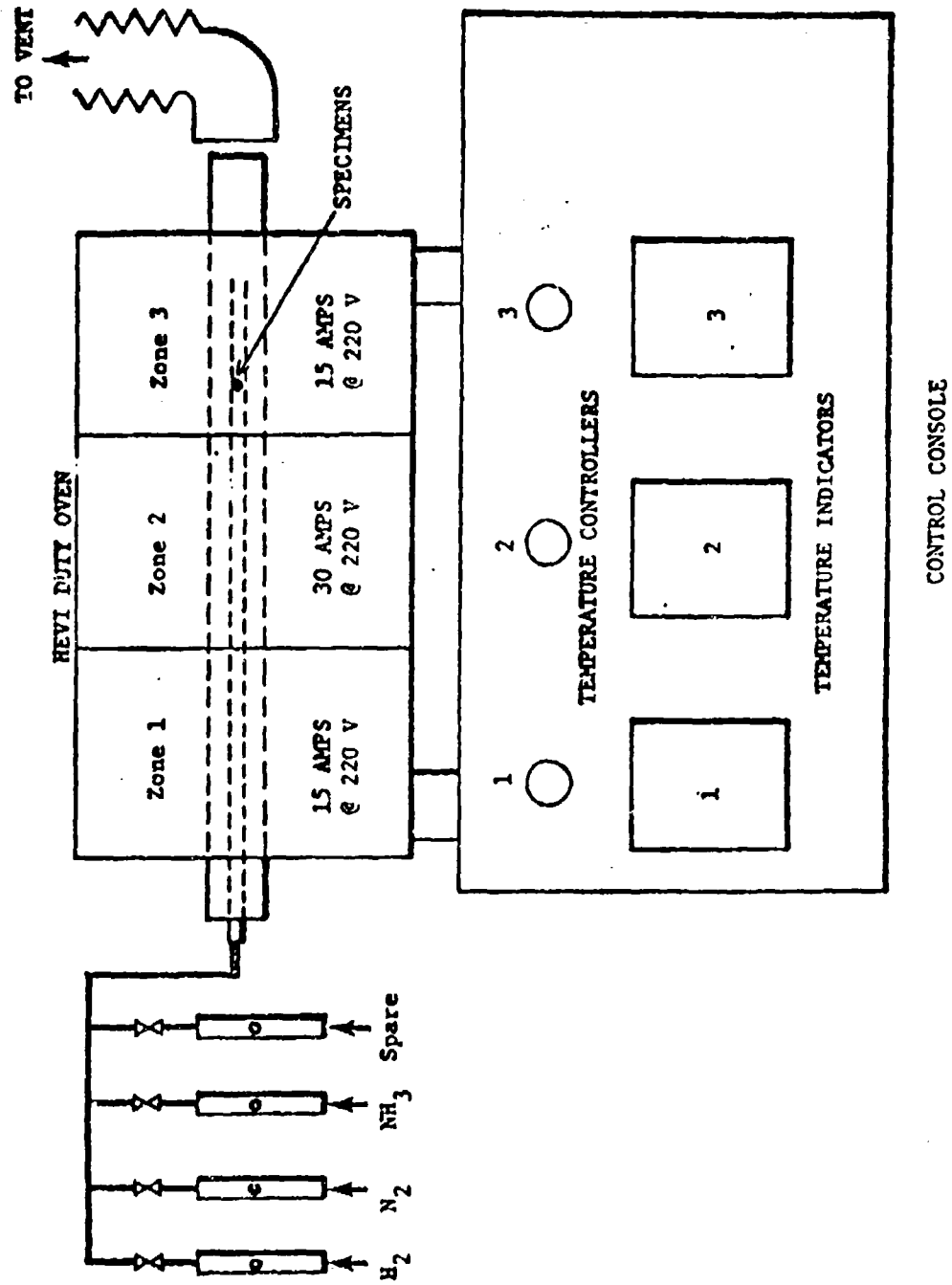
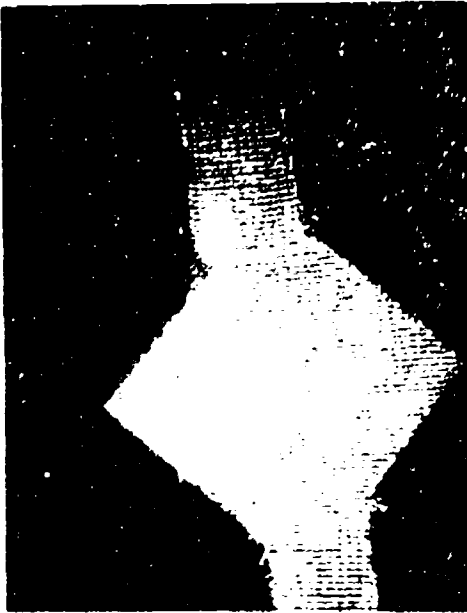


Figure 3-2

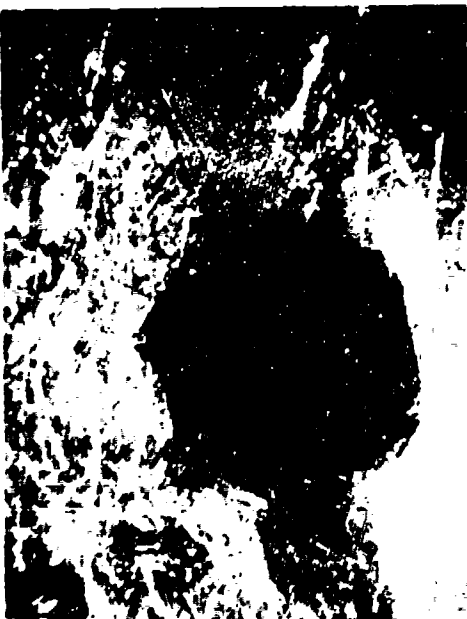
HSGET Particle Envelope Assembly



Lower Assembly With Support Tabs



Upper Assembly Superimposed
on Lower Assembly



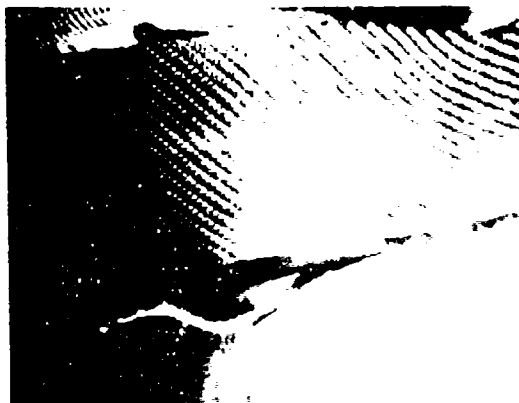
Face View--Folded Envelope



Side View--Folded Envelope
Enclosing Particle

Figure 3-3

HSGET Cylindrical Pellet Holder Assembly



1/8" x 1/8" Pellet in Assembly Strips



Nichrome Holder Wire



Assembly with 1/8" x 1/8" Pellet

Table 3-4

Summary of Sensitivity Tests in the Gas
Fluid Dynamic Erosion Tester

Average Weight Loss in 10^{-5} Grams (a)

Fresh Shell 405 Catalyst Size	Superficial Gas Velocity, feet per second		
	50	110	250
1/8" x 1/8" cylinders	166	137	160
8-12 Mesh	-	-	19
14-18 Mesh	-	0	1
20-25 Mesh	-	-	0
25-30 Mesh	0	0	0
20-30 Mesh	-	-	0

(a) Total weight loss for all specimens in each category divided by the number of specimens. Weight loss after exposure to flowing nitrogen at 1700°F for one hour.

Table 3-5

Summary of Sensitivity Tests in the Gas
Fluid Dynamic Erosion Area

Fresh Shell 405 Catalyst Size	Average Percent Weight Loss		
	Superficial Gas Velocity, feet per second		
	50	110	250
1/8" x 1/8" Cylinders	3.28	2.68	3.22
8-12 Mesh	-	-	1.04
14-18 Mesh	-	0	0
20-25 Mesh	-	-	0
25-30 Mesh	0	0	0
20-30 Mesh	-	-	0

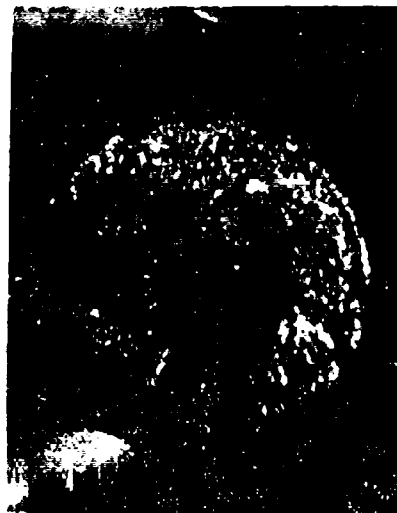
- Weight loss after exposure to flowing nitrogen at 1700°F for one hour.

Figure 3-4

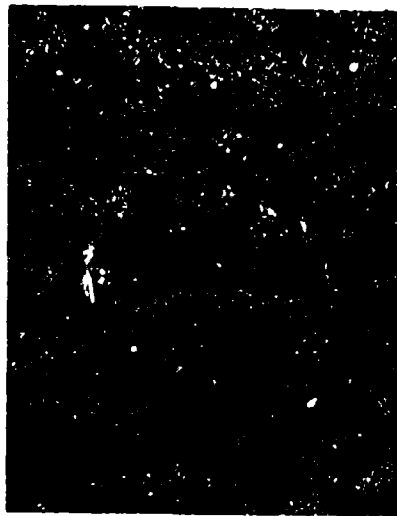
Gas Erosion Test: Fresh Shell 405, 1/8" x 1/8"
Cylinders at 250 feet/second



Pellet 1 - Before



Pellet 1 - After



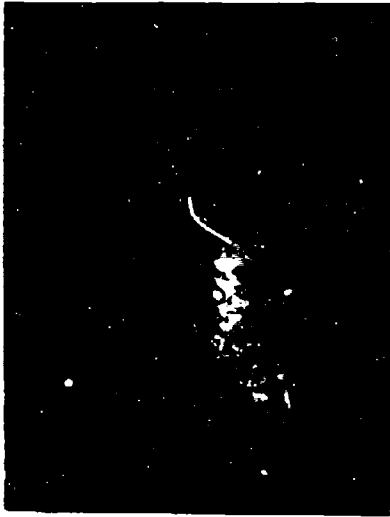
Pellet 2 - Before



Pellet 2 - After

Figure 3-5

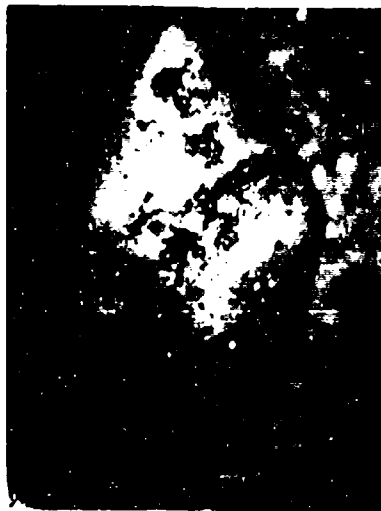
Gas Erosion Test: Fresh Shell 405, 8 to 12
Mesh Particles at 250 Feet/Second



Particle 1 - Before



Particle 1 - After



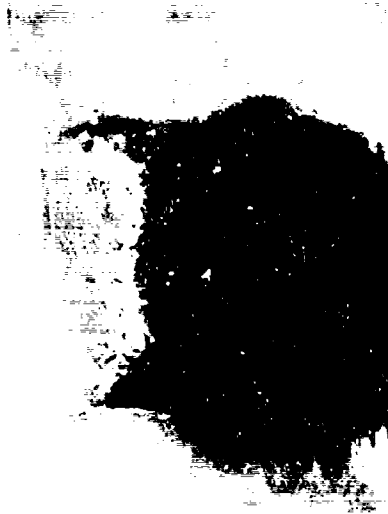
Particle 4 - Before



Particle 4 - After

Figure 3-6

Gas Erosion Test: Fresh Shell 405, 14 to 18 Mesh
Particles at 250 feet/second



Particle 1 - Before



Particle 1 - After



Particle 2 - Before



Particle 2 - After

Figure 3-7

Gas Erosion Test: Fresh Shell 405, 20 to 25 Mesh
Particles at 250 feet/second



Particle 1 - Before



Particle 1 - After



Particle 3 - Before



Particle 3 - After

Figure 3-8

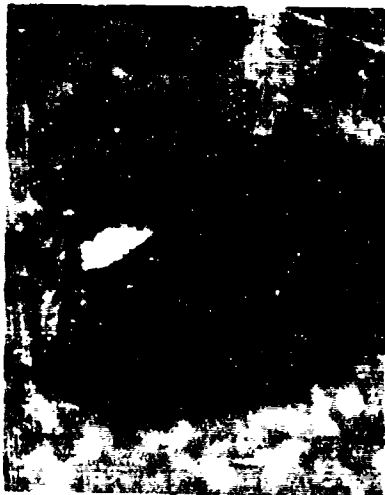
Gas Erosion Test: Fresh Shell 405, 25 to 30 Mesh
Particles at 250 Feet/second



Particle 1 - Before



Particle 1 - After



Particle 4 - Before



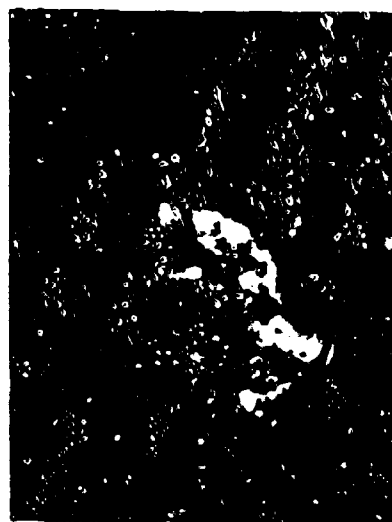
Particle 4 - After

Figure 3-9

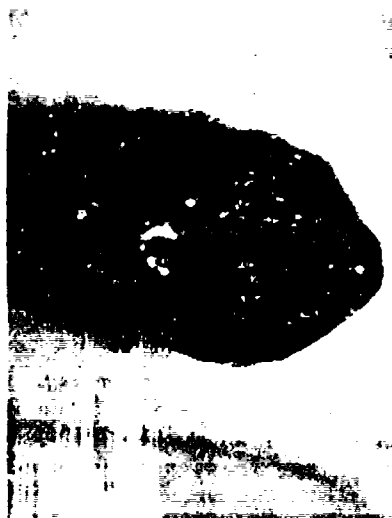
Gas Erosion Test: Fresh Shell 40's, 20 to 30 Mesh
Particles at 250 feet/second



Particle 1 - before



Particle 1 - After



Particle 2 - Before



Particle 2 - After

The input data and results are shown in the Appendix. The row variables tested were 1/8" pellets versus 25-30 mesh particles and the column variable tested was superficial velocity at three levels for the two catalyst sizes. Five replicates at each condition was included. F-tests on the mean squares using the replicate sum of squares results for the denominator term indicates that only the row effect is significant at better than the 95% confidence level. Other factors and interactions were not significant using this criteria. This analysis agrees with the conclusion based on t-tests of the individual sets of data that the 1/8" pellets exhibited a significant weight loss whereas the granular material did not and that this weight loss did not vary significantly with gas velocity.

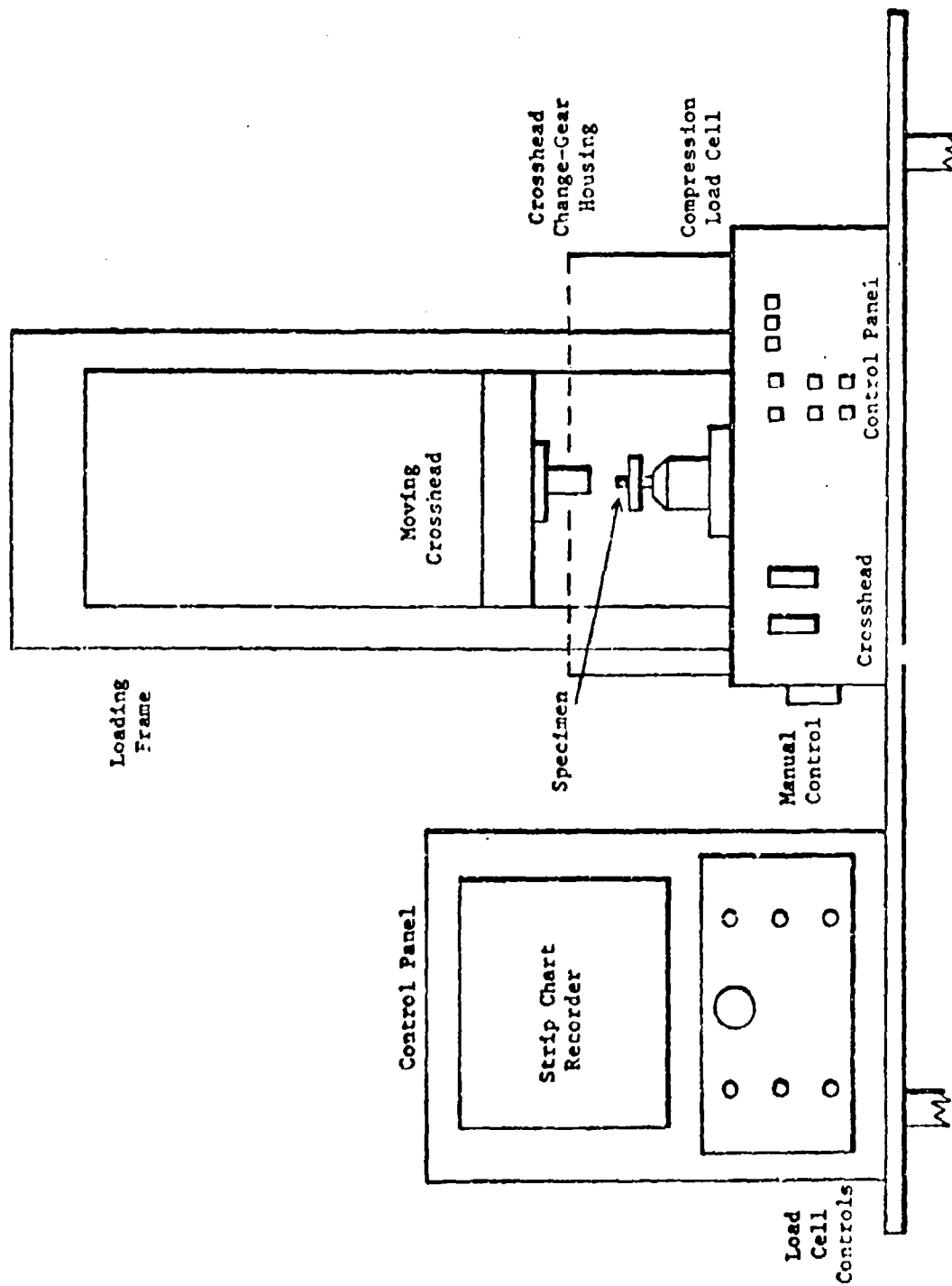
Although it is not clear why only the cylindrical pellets exhibited a weight loss, it is interesting to speculate on possible causes. The granular Shell 405 catalyst is smaller in size than the 1/8" x 1/8" cylinders and has a "rounded" geometry resulting from the attrition procedure. The granules are also prepared from a different alumina source than the cylinders. Thus, the weight loss may not be the result of gas erosion per se, but simply reflect a loss of volatile material peculiar to the cylindrical catalyst as a result of heating to 1700°F in nitrogen. This volatile loss would involve a non-water material as the pellets are adjusted to a common water level before weighting both before and after exposure to hot flowing gas. Many commercial pelletized catalysts exhibit a weight loss upon heating to temperatures in the range of 1700°F (9). The fact that the weight loss did not vary with gas velocity over the range of 50 to 250 feet per second would tend to corroborate this interpretation. It is also possible that this difference resulted from the geometry of the pellets and particles themselves. In the HSGET test with the cylindrical pellets, the flowing gas impinged on the face of the cylinder, rather than on its side. This suggests the possibility that the cylindrical pellets experienced some erosion as a result of the formation of a turbulent wake, which did not develop to the same extent with the more streamlined, smaller granular particles.

Most important, however, is the fact that the granular Shell 405 catalysts did not exhibit any significant weight loss even after exposure to gas velocities as high as 250 feet per second for one hour. These results indicate that gas fluid dynamic erosion per se is not a major contributor to the degradation of individual catalyst particles.

3.2.2 Sensitivity Testing in the Particle Static Pressure Crushing Area

Particle pressure crushing studies were carried out in the Instron Testing Instrument (ITI) shown in a schematic form in Figure 10. Individual catalyst particles were tested in the ITI on an as-is-basis so as not to alter their characteristics. Results, thus, are to be

Figure 3-10
Instron Testing Instrument (ITI)



considered as a crushing strength rather than a compressive strength and have merit on a relative rather than an absolute basis. This is particularly true of the granular mesh size catalyst specimens since they have a non-cylindrical geometry and thus do not provide parallel loading forces when tested in the ITI. The use of replicate testing and statistical techniques were employed in order to provide as firm a basis for analyzing the data as possible.

Work on the following factors was carried out with fresh Shell 405 catalyst:

- Distribution of individual particle crush strength as a function of catalyst selection parameters, i.e., different catalyst sizes.
- Effect of attrition.
- Effect of water level.
- Effect of repeated loading.

Prior to carrying out the catalyst selection parameters work, a study was made of a possible effect of catalyst moisture content on the average crushing strength. Consultant discussions indicated that such an effect might either (1) be an artifact affecting the measurement (e.g., by causing particles to move horizontally during the test), or (2) could reflect an effect of the strongly bound water in the small angstrom size pores of the alumina. A small effect of water content on the crushing strength of alumina based hydrotreating catalysts were recently reported in the literature (92). Thus, in addition to a possible variable influencing ITI measurement results, such an effect could have significant bearing on interpreting crush strength results since a catalyst after its initial firing in a space environment would be expected to have a very low moisture content. For this study, Fresh Shell 405 1/8" cylinders and 14-18 mesh catalyst were employed along with Harshaw AL1602 alumina 1/8" cylinders. The specimens were tested (1) as-is, (2) after drying in a vacuum oven and (3) after saturation by water vapor at 80°F. Replicate tests with sample sizes of up to 15 tests were employed. Results of this study are shown in Table 3-6. Detailed data are contained in the Appendix.

An examination of the average crushing strengths in Table 3-6 indicated no obvious effect of water level on both the Shell 405 catalyst cylinders and mesh granules and the Harshaw alumina cylinders. Statistical t-tests on the variations of means for each material indicated they were not statistically different. An examination of the standard deviations indicates that the vacuum oven dried material in all three cases had a higher standard deviation than the as-is and water saturated samples. Statistical F-tests on these differences in variances indicated that none of these differences were significant at the 95% confidence level).

Table 3-6

Investigation of the Possible Effect of Specimen
Water Content on ITI Crush Strength Measurement

		"As Is"(a)	Dried in Vacuum Oven(b)	Water Saturated(c)
Fresh Shell 405 1/8 x 1/8 Cylinders	Average Crush Strength lbs	34.4	34.9	35.0
	Sample Size	10	15	15
	Standard Deviation, lbs	6.08	7.54	6.43
Fresh Shell 405 14-18 Mesh	Average Crush Strength, lbs	1.99	1.59	1.17
	Sample Size	5	10	10
	Standard Deviation, lbs	.85	.98	.61
Harshaw Alumina AL 1602 1/8 x 1/8 cylinders	Average Crush Strength, lbs	26.6	28.8	24.6
	Sample Size	10	10	9
	Standard Deviation, lbs	5.65	9.42	5.64

(a) Tested as is after removal from their containers.

(b) Tested after drying in a vacuum oven overnight at 110°C and 120 mm Hg total pressure.

(c) Tested after being saturated with water vapor at 80°F and 1 atm total pressure.

The data obtained with the 1/8" cylinders and 14-18 mesh fresh Shell 405 at various water levels was pooled into a single set of data and an average crushing strength and standard deviation calculated for the resultant sample size of 40 and 25 replicate measurements, respectively. Twenty-five replicate measurements were also made on other mesh size Shell 405 catalyst. Results of these tests are shown in Table 3-7. As would be expected because of geometric effects, the standard deviations of the granular specimens are much larger compared to their mean value. This is shown below:

<u>Specimen</u>	<u>Standard Deviation as % of Average Crushing Strength</u>
• 1/8" x 1/8" cylinders	
Fresh Shell 405	19.0
Al 1602 Alumina	26.0
• Fresh Shell 405 granules	
8-12 Mesh	40.1
14-18 Mesh	56.6
20-25 Mesh	65.1
25-30 Mesh	48.2
20-30 Mesh	65.0

In Table 3-8 are shown the results of tests with the various mesh size of alumina support before attrition, while in Table 3-9 are shown the results on the corresponding material after 50% attrition. In Table 3-10 is shown a comparison of the effect of catalyst preparation steps on particle average compressive crushing strength of the various sizes of granular material. In Table 3-11 is shown a comparison of the cylindrical alumina pellets before and after iridium addition. The difference between the average crushing strengths within a given size of material were subjected to statistical analysis (t-tests at the 95% confidence level) to see if these differences are statistically significant. A summary of these statistical tests are shown in Table 3-12.

Table 3-7

Particle Compressive Crushing Strength of Fresh Shell 405
Catalyst in the III

	1/8" x 1/8" Cylinder	8-12 Mesh	14-18 Mesh	20-25 Mesh	25-30 Mesh	20-30 Mesh
Average Crushing Strength, lbs	34.8	4.26	1.50	0.74	0.56	0.61
Sample Size	40	25	25	25	25	25
Standard Deviation, lbs	6.62	1.75	0.85	0.48	0.27	0.40
Cumulative Distribution of Crushing Strength, lbs (a)						
1%	19.4	0.30	-	-	-	-
5%	24.0	1.45	0.11	-	.11	-
10%	26.3	2.12	0.41	.12	.22	0.10
50%	34.8	4.36	1.50	.74	.56	0.61
90%	43.3	6.60	2.59	1.35	.90	1.12
95%	45.6	7.25	2.89	1.52	1.00	1.27
99%	50.2	8.42	3.48	1.85	1.18	1.54

(a) - Calculated from measured mean and standard deviation assuming a normal distribution.

Table 3-8

Particle Compressive Strength of Alumina Support Before Attrition

	Mesh Size				
	8-12	14-18	20-25	25-30	20-30
Average Crushing Strength, lbs.	2.26	1.09	0.39	0.40	0.45
Sample size	25	25	25	25	25
Standard Deviation, lbs.	1.37	0.68	0.26	0.17	0.20
Distribution of Crushing Strength, lbs. (a)					
1%	-	-	-	-	-
5%	0.02	-	-	0.12	0.12
10%	0.51	0.17	.06	0.18	0.20
50%	2.26	1.09	0.39	0.40	0.45
90%	4.01	1.96	0.72	0.62	0.70
95%	4.50	2.20	0.81	0.68	0.78
99%	5.44	2.38	1.00	0.80	0.91

(a) Calculated from measured mean and standard deviation assuming a normal distribution.

Table 3-9

Particle Compressive Strength of Alumina Support After 50% Attrition

	Mesh Size				
	8-12	14-18	20-25	25-30	20-30
Average Crushing Strength, lbs.	3.16	1.86	0.72	0.50	0.46
Sample size	25	25	25	25	25
Standard Deviation, lbs.	1.17	0.86	0.39	.26	.28
Distribution of Crushing Strength, lbs. (a)					
1%	0.39	-	-	-	-
5%	1.20	0.45	0.08	0.07	-
10%	1.62	0.76	0.22	0.17	0.10
50%	3.12	1.86	0.72	0.50	0.46
90%	4.62	2.96	1.22	0.83	0.82
95%	5.04	3.27	1.36	0.93	0.92
99%	5.85	3.87	1.63	1.11	1.11

(a) calculated from measured mean and standard deviation assuming a normal distribution

Table 3-10
Effect of Catalyst Preparation Steps on
Particle Average Compressive Crushing Strength

Material	Average Crushing Strength - lbs. (a)				
	Mesh Size				
	8-12	14-18	20-25	25-30	20-30
Alumina Support before attrition	2.26	1.09	0.39	0.40	0.45
Alumina Support after 50% attrition	3.16	1.86	0.72	0.50	0.46
Attrited Support after Iridium addition (fresh Shell 405)	4.26	1.50	0.74	0.56	0.61

(a) average crushing strength based on 25 replicate measurements

Table 3-11

Effect of Iridium Addition on Average
Compressive Crushing Strength of 1/8" x 1/8" Cylinders

Material	Average Compressive Crushing Strength, lbs.	Sample Size	Standard Deviation, lbs.
1/8" x 1/8" alumina support	34.6	25	9.89
1/8" x 1/8" alumina support after iridium addition (fresh Shell 405)	34.8	40	6.62

Table 3-12

Summary of Statistical Tests on the
Significance of Differences Between Particle
Average Compressive Crushing Strength

Size	Is the Difference Statistically Significant? (a)	
	Comparison of Material Before and After 50% Attrition	Comparison of Material Before and After Metal Addition
1/8" x 1/8" cylinders	-	No
8-12 Mesh	Yes	Yes
14-18 Mesh	Yes	No
20-25 Mesh	Yes	No
25-30 Mesh	No	No
20-30 Mesh	No	No

(a) Based on a t-test using the measured means and standard deviations at the 95% confidence level (single sided t-test at .025).

It can be seen from examining Tables 3-10, 11 and 12 that the addition of the iridium metal to the alumina support in general did not result in any significant increase in particle crushing strength. In contrast, the use of the attrition procedure during the preparation of the catalyst support in general improves the average crushing strength, with the improvement with the larger granular sizes (i.e., 8-12, 14-18, and 20-25 mesh) being statistically significant.

<u>Mesh Size</u>	<u>Increase in Crushing Strength of 50% Attrited Support over Support Before Attrition</u>
8-12	38%
14-18	70%
20-25	84%
25-30	25%
20-30	22%

These latter two effects presumably reflect the loss of the weaker granular material during both the grinding process involved in the initial mesh size selection and in the attrition procedure where at least 50% of the weaker material is rejected. In contrast to the improvement in average crush strength, as shown in Table 3-13, the attrition procedure did not improve the scatter in the individual values (i.e., reduce the standard deviation), so that both the attrited supported and the corresponding metal loaded catalyst still have a relatively wide variation in individual particle crushing strengths. A wide variation in individual crushing strengths is deleterious since it means (as shown in Table 3-7) that an aggregate bed of individual particles will contain an appreciable number of particles with individual crushing strengths much lower than that represented by the average crushing strength (50% value). These results suggest that preparation techniques that would reduce the standard deviation or variation in individual crushing strengths could offer the possibility of significant improvements in aggregate or bed performance.

Particle crush strength measurements were made on a sample of 90% attrited 20-25 Mesh fresh Shell 405 catalyst from that used by Bell Aerospace Company in the Long Life Monopropellant Design Criteria Program. The results of these measurements are shown in Table 3-14, along with previously obtained results with the standard 50% attrited catalyst and attrited and unattrited support of the same mesh size. The 90% attrited catalyst had an average crush strength 45% higher than the standard 50% attrited catalyst. Tests indicate this increase is statistically significant, whereas the difference in standard deviation between the two materials was not significant. It can also be seen that the 90% attrited catalyst is markedly better in average crush strength than the unattrited support. Since the addition of the iridium metal to the support had no significant effect on average crush strength, this improvement would appear to reflect entirely the effect of the use of the attriting procedure.

Table 3-13

Effect of Catalyst Preparation Steps on the
Scatter in Individual Particle Compressive Crushing Strengths

Standard Deviation of Individual
Crushing Strength - lbs.

Material	Mesh Size				
	8-12	14-18	20-25	25-30	20-30
Alumina support before attrition	1.37	0.68	0.26	0.17	0.20
Alumina support after 50% attrition	1.17	0.86	0.39	0.26	0.28
Attrited support after iridium addition (fresh Shell 405)	1.75	0.85	0.48	0.27	0.40

Table 3-14

Particle Crush Strength of Fresh 20-25 Mesh
Shell 405 Catalyst or Substrate

	90% attrited catalyst (a)	50% attrited catalyst	50% attrited support	Unattrited support
Average Crush Strength, lbs	1.07	0.74	0.72	0.39
Sample Size	25	25	25	25
Standard Deviation, lbs	0.38	0.48	0.39	0.26

(a) Sample from that used by Bell Aerospace Company in the Long Life Monopropellant Design Criteria Program.

Table 3-15

Effect of Multiple Loading on Compressive Crushing
Strength of Fresh Shell 405 1/8" x 1/8" Cylinders

<u>Number of repeated compressive loadings (a)</u>	<u>Compressive Crushing Strength, lbs.</u>
0	34.8
10	34.9 (b)
25	42.0 (b)
50	35.8 (b)

(a) Cylindrical pellet axially loaded repeatedly to 50% of average failure compressive crushing strength followed by complete pressure release, then loaded to failure to measure crushing strength.

(b) Not statistically different from mean value for no repeated loading based on a t-test at the 95% confidence limit using the measured standard deviation value for fresh Shell 405 1/8" x 1/8" cylinders.

A short study was also made of the effect of repeated loading on the crushing strength of fresh Shell 405 catalyst. This was done by repeated axial loading of the 1/8" x 1/8" cylindrical Shell 405 catalyst to 50% of the average compressive crushing strength. Specimens were exposed to 10, 25, and 50 repeated loadings and then loaded to failure so as to measure the crushing strength. Results of these tests are shown in Table 3-15. Statistical t-tests at the 95% confidence level indicated that none of these values are statistically different from the mean value for the catalyst which had not been subjected to repeated loadings.

3.2.3 Sensitivity Testing in the Particle Fluidization Area

Sensitivity tests in the particle fluidization area were carried out. In the terminology used by engineers who design fixed bed catalytic reactors, bed fluidization simply implies any movement of catalyst particles as a result of gas flow either in void spaces inadvertently formed within the bed or in a contiguous volume such as the inlet sections above the catalyst bed where either catalyst particles or the ceramic distributor balls which are used could experience movement. Commercial experience with fixed beds indicate that once bed fluidization begins catalyst degradation by impact fracture and particle to particle abrasion is generally quite serious and often catastrophic. Thus, design practice is aimed at identifying conditions to avoid bed fluidization via control of injector design and flow rates to avoid incipient bed fluidization velocities.

Incipient particle movement velocities of various granular Shell 405 catalyst were measured in the modified ILBET apparatus shown in a schematic in Figure 3-11. This unit employs a simple right angle, center axis, cylindrical pipe gas inlet. The scaling parameters (i.e., the ratio of the dimensions of the vessel, pipe gas inlet, catalyst particles, separation distance between bed and inlet, and bed depth) employed are listed in Table 3-16, along with typical values employed in larger equipment used to establish commercial design criteria. It can be seen that, in general, the scaling parameters are quite similar. The top of the catalyst bed is visually observed and the incipient fluidization velocity was defined as the lowest velocity at which any particle on the top of the bed first experienced movement, as the gas velocity is progressively increased. Replicate measurements were made at each set of conditions.

Figure 3-11

Modified ILBET Apparatus for
Incipient Particle Movement
Velocity Measurement

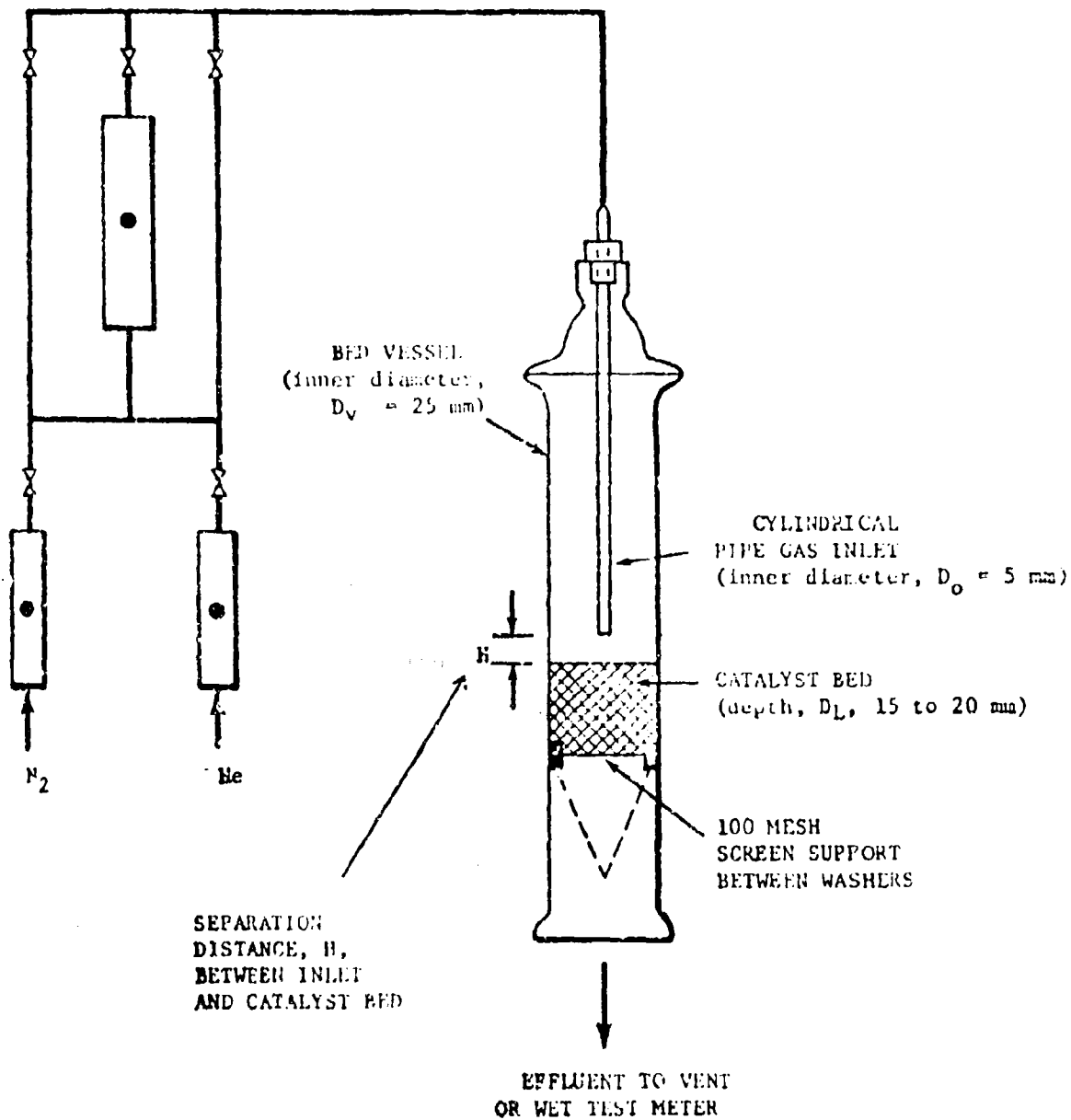


Table 3-16
Comparison of Scaling Parameters Used
In Incipient Particle Movement Study

Scaling Parameter	Range of Values	
	ILBET Used For Particle Fluidization	Typical Lab Vessel Used to Establish Commercial Design Practice
D_v/D_o	5	~ 6
D_o/D_p	2.5 to 7	3 to 12
D_L/D_p	10 to 20	15 to 30
H/D_o	2	~ 2

Terminology: D_v = inner diameter of bed vessel
 D_o = inner diameter of pipe type inlet
 D_L = catalyst bed depth
 H = separation distance between bed and inlet
 D_p = particle diameter

Pure nitrogen, pure helium and helium-nitrogen blends were used to provide data on the effect of gas density. In addition to the effect of gas density, catalyst selection parameters were also investigated.

The minimum inlet distributor superficial velocity for particle movement was measured for fresh Shell 405 particles of 8 to 12 mesh, 14 to 18 mesh and 20 to 30 mesh size. The detailed data obtained with pure helium, pure nitrogen, and helium-nitrogen blends are shown in the Appendix. In Table 3-17 is summarized the average inlet velocity and standard deviation of the velocity determined from the replicate measurements with pure nitrogen and helium. These values were determined from a sample size of ten replicate measurements. Statistically significant (t-tests at the 95% confidence level) differences exist between the average velocities found for the various mesh sizes and the two gases employed.

A correlation of incipient fluidization data was made employing the following equation:

$$V_g = K \left[g D_p \frac{(\rho_p - \rho_g)}{\rho_g} \right]^{1/2} \quad (3-1)$$

where: V_g = incipient movement velocity

g = gravity constant

D_p = diameter of particle

ρ_g = vapor density

ρ_p = particle density

K = empirical correlating constant to be derived from the data.

Since the density for gases is much lower than the particle density, the equation was simplified as follows:

$$V_g = K' \left(\frac{D_p}{\rho_g} \right)^{1/2} \quad (3-2)$$

where $K' = K(g\rho_p)^{1/2}$

Table 3-17

**Particle Fluidization: Effect of Particle Size
and Gas Density on Minimum Inlet Superficial
Velocity for Particle Movement**

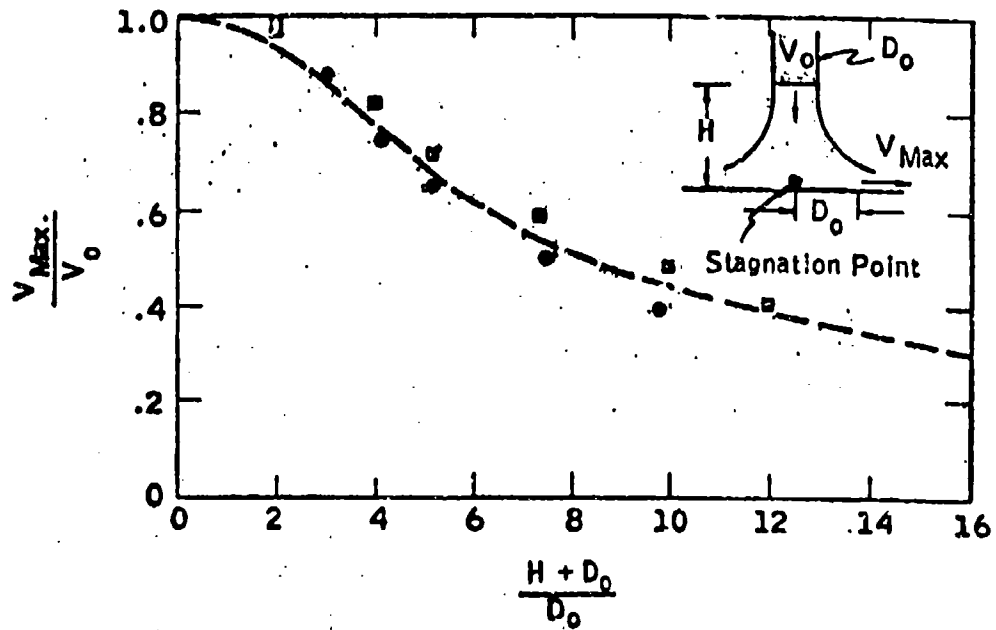
		Fresh Shell 403 Particle Size		
		8-12 Mesh	14-18 Mesh	20-30 Mesh
Pure Nitrogen	Average Velocity M/sec (a)	5.49	4.03	2.28
	Sample Size	10	10	10
	Standard Deviation M/sec	1.49	0.47	0.47
Pure Helium	Average Velocity M/sec (a)	12.18	9.61	6.72
	Sample Size	10	10	10
	Standard Deviation M/sec	1.22	1.51	1.30

(a) Average minimum superficial velocity in the inlet distributor tube which causes any particle movement, meters per second.

The incipient movement velocity was estimated in terms of a horizontal or surface velocity from the superficial inlet velocity using a literature correlation of maximum surface vapor velocity or a function of inlet velocity and inlet geometry. This correlation is shown in Figure 3-12. For the conditions employed in the present study, this correlation predicts that the horizontal or surface velocity will be 85% of the inlet superficial velocity. Average incipient movement velocities calculated from this correlation are shown in Table 3-18, and both the pure nitrogen and helium results and the results from the helium-nitrogen blends. Also shown in Table 3-18, are average gas compositions and an average catalyst particle diameter for the mesh sizes employed. The average incipient particle movement velocity in terms of feet per second was then plotted as a function of $(D_p/\rho_g)^{1/2}$. This correlation is shown in Figure 3-13, and is applicable to a unit value g gravity environment.

It could appear that, in general, thruster gas velocities will be above the incipient particle movement velocity. As an example, a hydrogen-nitrogen gas mixture (67% H_2 - 33% N_2) at 10 atmospheres and 925°C will have an approximate 1.1 g/liter density. For the largest granular size employed, i.e., 8-12 mesh, this would yield an $(D_p/\rho_g)^{1/2}$ value of approximately 1.35. From Figure 3-13, which assumes a unit gravitational field, this would correspond to a incipient movement velocity of approximately 12 feet/second. The highest anticipated satellite gravitational field is 5.0 G, for an on-orbit spinner, and this higher gravity would raise this incipient particle movement velocity to approximately 28 feet per second. Lower gravitational fields, smaller catalyst particle sizes, and higher gas densities at higher pressures will all directionally lower the incipient fluidization velocity. Assuming that a thruster gas velocity of 110 feet per second is representative, it can be seen that Shell 405 granules are exposed to velocities much higher than the incipient particle movement velocity, and that particle movement is not precluded by lack of sufficient gas velocity once sufficient void space occurs in the catalyst bed. In addition, because of the great difference between actual gas velocities and incipient particle movement velocities, the limitation of gas velocities to preclude the possibility of particle movement in a voided bed would not appear to be a practical in hydrazine monopropellant thrusters.

Figure 3-12
Maximum Surface Vapor
Velocity for Impinging Jets



Legend

- Impingement Jet Data From A 16" Ducted Fan
- Impingement Jet Data From A 4" Uniform Jet

Source: R. E. Kuhn, NASA TN D-56,
 September, 1959.

Table 3-18

Summary of Particle Fluidization Parameters

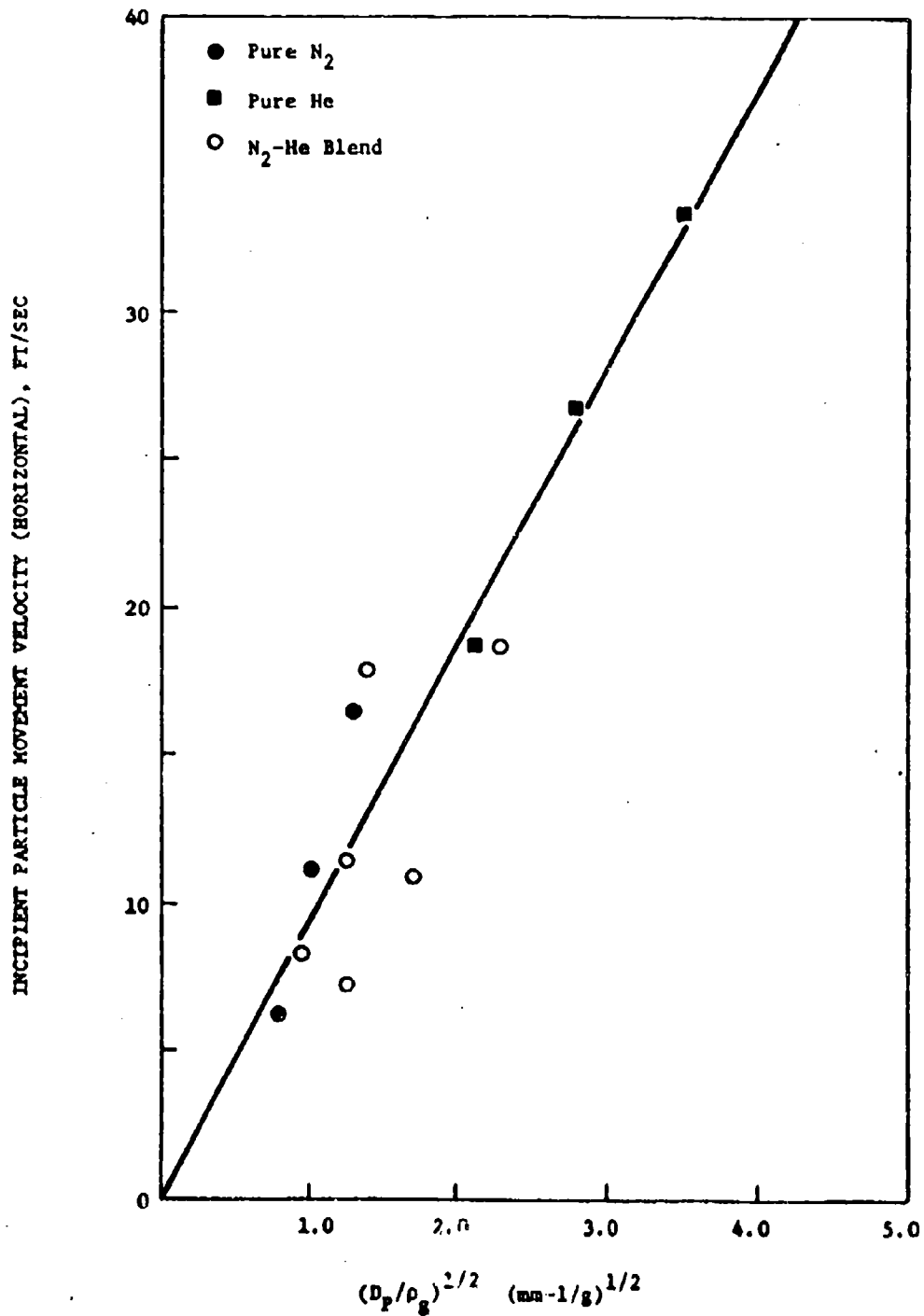
Fresh Shell 405 Particle Size	Average Gas Comp. % N ₂ in N ₂ -He	Average Particle Diameter D _p , mm (a)	Gas Density g/l	Average Incipient Particle Movement Velocity, ft/sec (b)	$(\rho_p/\rho_g)^{1/2}$ $(\text{mm-l/g})^{1/2}$
8-12	100	2.00	1.16	16.57	1.31
14-18	100	1.19	1.16	11.24	1.01
20-30	100	0.71	1.16	6.36	0.78
8-12	0	2.00	0.16	33.98	3.54
14-18	0	1.19	0.16	26.81	2.73
20-30	0	0.71	0.16	18.75	2.11
8-12	85.0	2.00	1.01	17.94	1.41
14-18	63.0	1.19	0.78	11.52	1.24
20-30	63.3	0.71	0.78	8.26	0.95
8-12	22.3	2.00	0.38	18.83	2.29
14-18	26.2	1.19	0.42	10.99	1.68
20-30	30.2	0.71	0.46	7.37	1.24

(a) Average D_p for 8-12 mesh assumed as 2.00 mm (10 mesh opening), for 14-18 mesh as 1.19 mm (16 mesh opening), for 20-30 mesh as 0.71 mm (25 mesh opening).

(b) A horizontal velocity which is assumed to be 85% of average inlet distribution superficial gas velocity for $H+D_o/D_o = 3$.

Figure 3-13

Correlation of Incipient Particle Movement Velocity



3.2.4 Sensitivity Testing in the Liquid Fluid Dynamic Erosion Area

Sensitivity tests in the liquid fluid dynamic erosion area were carried out. A test involving individual catalyst particles subjected to a pulsed, liquid flow was carried out in the Pulsed Liquid Particle Erosion Test (PLPET) apparatus shown in Figure 3-14. In this test, individual catalyst particles were passed through a stream of flowing liquids at a speed which could be varied by changing the stirrer speed. A flat nozzle was employed so as to produce as near a rectangular flow of liquid as possible. The stream angle was adjusted so that the catalyst particle struck the liquid stream at a right angle. The velocity of the liquid stream was maintained high enough to insure that the stream geometry was restored before the next impact of the particle (the stream advanced a minimum of 7 cm in the time required to complete a revolution of the arm which was 1 cm in diameter).

The 1/8" x 1/8" cylindrical particles were held in a small clamp which was attached to the moving arm. Granular 8-12 mesh catalyst particles were first attached to a small wooden dowel via the use of glue, and the dowel held in a small clamp attached to the moving arm. In Figure 3-15 are shown photomicrographs of the catalyst holder assembly. In the case of the 8-12 mesh catalyst particles, the glue was removed from the catalyst particles via a combustion technique prior to making the final weight measurement. This combustion technique consisted of burning off the glue and a small portion of the dowel attached to the glue (the major portion of the dowel was simply cut off) in a laboratory furnace with flowing air at 1300°F. Blank measurements of dowel glued particles indicated this technique was capable of effecting complete glue and dowel removal. In order to eliminate any thermal effects, the catalyst particles were pre-exposed to 1300°F air before being exposed in the PLPET apparatus, and its water level held constant before any weight measurement was made. Initial runs using 1-methylnaphthalene as the liquid indicated this fluid had some solvent power relative to the glues tried, which tended to loosen the particles from the dowel at high speeds. In order to solve this problem, water was substituted as the fluid. Similarly, early runs with the combustion furnace at 1700°F indicated that Shell 405 catalyst exhibited some spontaneous weight loss simply from exposure to flowing air at this temperature, necessitating a reduction of the combustion temperature to 1300°F. This loss presumably resulted from the volatility of iridium oxide at this temperature (94 to 97). Glue and dowel removal was still effected at this lower temperature. Replicate experiments were made in all cases.

Figure 3-14

Pulsed Liquid Particle Erosion Tester (PLPET)

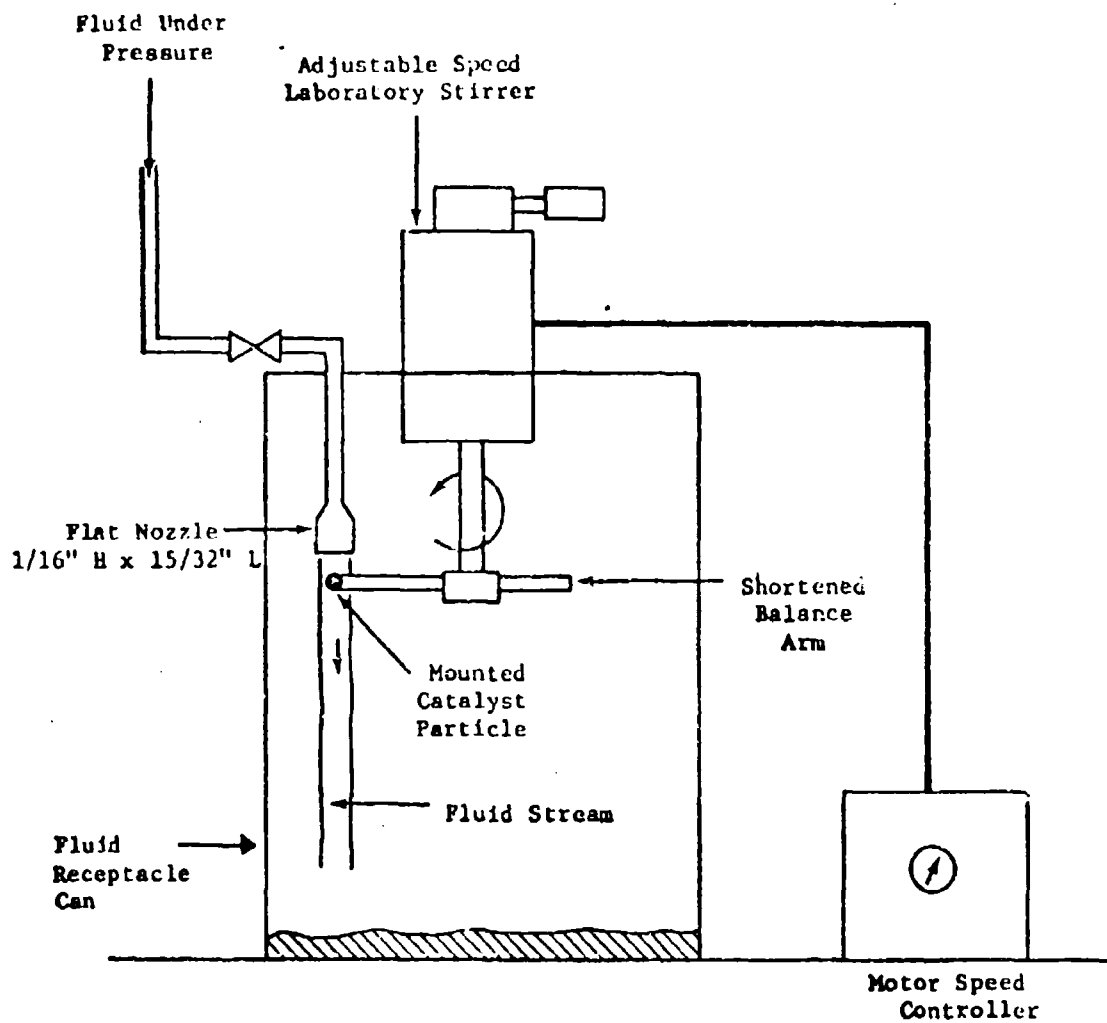


Figure 3-15

PLPET Catalyst Holder Assembly



8-12 Mesh Fresh
Shell 405 Catalyst
Particle Glued to Dowel



Catalyst Particle--
Dowel Assembly
Held in Clamp



Fresh Shell 405
1/8" x 1/8" Cylinder
Held in Plastic
Coated Clamp

The effect of the number of pulses up to 500,000 pulses was investigated using Fresh Shell 405 1/8" x 1/8" cylinders at 100 feet per second liquid velocity. Results of these tests are shown in Table 3-19. Individual data is tabulated in the Appendix. In general, the average weight loss increased with increasing number of pulses, although the difference between the average weight loss at 100,000 and 500,000 pulses was not statistically significant, principally because of the rather large variation in individual pellet results after exposure to 500,000 pulses (see detailed data in the Appendix). Photomicrographs of representative pellets taken before and after exposure to pulsed liquid flow are shown in Figures 3-16 to 3-18. Evidence of the effects of liquid erosion on the face of the pellets exposed to 100,000 and 500,000 pulses can be clearly seen.

Table 3-19

Effect of the Number of Pulses at a Fixed Velocity (a,b)

	Number of Pulses		
	8,200	100,000	500,000
Average Weight Loss, %	0.30	0.90	1.06
Sample Size	5	5	5
Standard Deviation, wt % loss	0.17	0.08	1.09

(a) Fresh Shell 405 1/8" x 1/8" cylinders

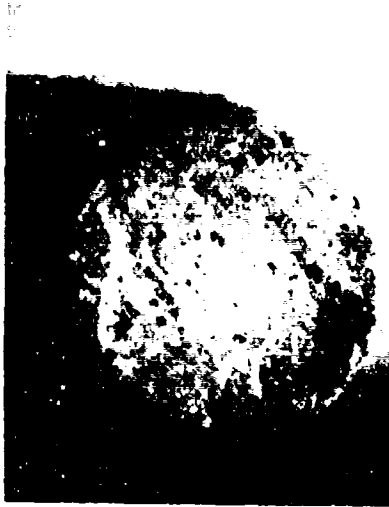
(b) Velocity of liquid relative to particle,
100 feet per second

The effect of pulsed liquid erosion was investigated further in the PLPET apparatus using the following variables:

- Liquid velocity
- Number of pulses
- Catalyst selection parameters

Figure 3-16

Liquid Erosion Test: Fresh Shell 405 1/8" x 1/8"
Cylinders at 500 Feet per Second and 8,200 Pulses



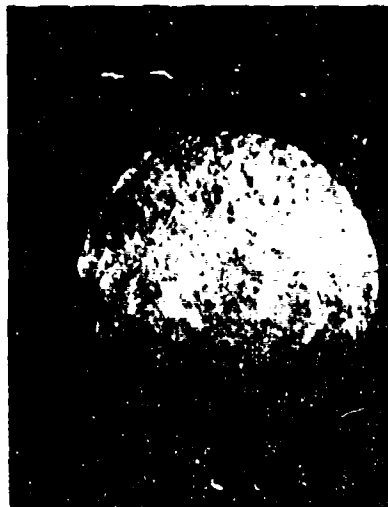
Pellet 1 - Before



Pellet 1 - After



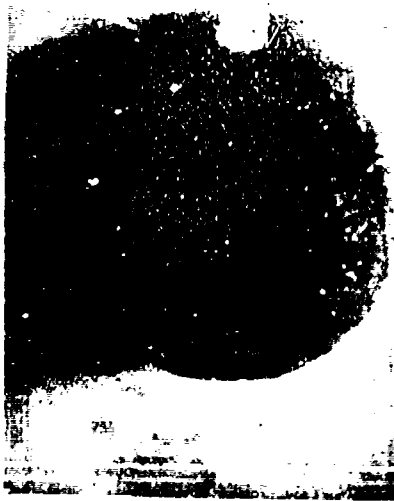
Pellet 5 - Before



Pellet 5 - After

Figure 3-17

Liquid Erosion Test: Fresh Shell 405 1/8" x 1/8"
Cylinders at 100 Feet per Second and 100,000 Pulses



Pellet 3 - Before



Pellet 3 - After



Pellet 5 - Before



Pellet 5 - After

Figure 3-18

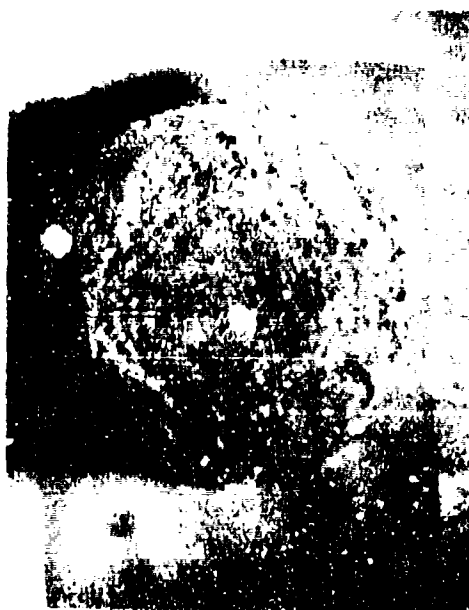
Liquid Erosion Test: Fresh Shell 405 1/8" x 1/8"
Cylinders at 100 Feet per Second and 500,000 Pulses



Pellet 3 - Before



Pellet 3 - After



Pellet 5 - Before



Pellet 5 - After

Each variable was tested at two levels i.e. 55 and 100 feet per second liquid velocity, 8,200 and 100,000 pulses and 1/8" x 1/8" cylinders and 8-12 mesh particles. Individual tests were replicated. The program was planned thus as a 2^3 full factorial statistically designed experiment with replication. This experimental design made possible a statistical analysis for all main effects and two and three factor interactions. A summary of average weight losses for each condition tested is shown in Table 3-20. Photomicrographs of representative catalyst pellets or particles both before and after exposure to the pulsed liquid flow at 55 feet per second are shown in Figures 3-19 to 3-24. Detailed data are tabulated in the Appendix. The average weight loss data as a function of velocity is plotted in Figure 3-25 for the 1/8" cylinders and in Figure 3-26 for the 8-12 mesh granules. Examination of the data indicates that the weight loss for the 8-12 mesh granules was greater than for the 1/8" cylinders at a fixed velocity and number of pulses, and that the weight loss increased with velocity and number of pulses as would be expected.

As indicated previously, photomicrographs of the 1/8" x 1/8" cylinders exposed to a liquid velocity of 100 feet per second and 100,000 and high pulses clearly show signs of pronounced "pitting" on the pellet face exposed to the liquid stream. Photomicrographs of the 8 to 12 mesh granules similarly exposed to a liquid velocity of 100 feet per second and 100,000 pulses do not show evidence of pronounced "pitting", although weight measurements indicate the weight loss at equivalent conditions for the granules was at least as great as for the pellets. Similarly, photomicrographs of both pellets and granules exposed to lower velocities and numbers of pulses do not show signs of pronounced "pitting", although small weight losses were observed.

A statistical Analysis of Variance (ANOVA) was performed on the data (93). The individual data used in the ANOVA is shown in the Appendix, along with the means associated with the three main effects. In Table 3-21 is shown a summary of the ANOVA calculations. Variance ratio tests (F-distribution) were performed on the resultant mean squares using the replicate mean square to determine the residual error. All three main effects (i.e., effect of number of pulses, velocity, and catalyst type) were significant at the 95% confidence level. None of the interactions (i.e., the three two-factor interactions and the one three-factor interaction) were significant at this confidence level.

Table 3-20
Effect of Velocity, Number of Pulses and Catalyst Selection
on Liquid Erosion in PIPE

Number of Pulses		Velocity of Liquid Relative To Particle		
		55 Feet per Second	100 Feet per Second	
		1/8" x 1/8" Cylinders	8-12 Mesh Granules	1/8" x 1/8" Cylinders
				8-12 Mesh Granules
8,200	Avg. Weight Loss %	0.12	0.25	0.30
	Sample Size	5	4	5
	Standard Deviation	0.06	0.40	0.17
				0.28
100,000	Avg. Weight Loss %	0.61	0.79	0.90
	Sample Size	4	5	5
	Standard Deviation	1.08	0.32	0.08
				0.22

Figure 3-19

Liquid Erosion Test: Fresh Shell 405 1/8" x 1/8"
Cylinders at 55 Feet per Second and 8,200 Pulses



Pellet 1 - Before



Pellet 1 - After



Pellet 5 - Before



Pellet 5 - After

Figure 3-20

Liquid Erosion Test: Fresh Shell 405 1/8" x 1/8"
Cylinders at 55 Feet per Second and 100,000 Pulses



Pellet 1 - Before



Pellet 1 - After



Pellet 4 - Before



Pellet 4 - After

Figure 3-21

Liquid Erosion Test: Fresh Shell 405 8 to 12 Mesh
Particles at 55 Feet per Second and 8,200 Pulses



Particle 4 - Before



Particle 4 - After



Particle 5 - Before



Particle 5 - After

Figure 3-22

Liquid Erosion Test: Fresh Shell 405 8 to 12 Mesh
Particles at 55 Feet per Second and 100,000 Pulses



Particle 4 - Before



Particle 4 - After



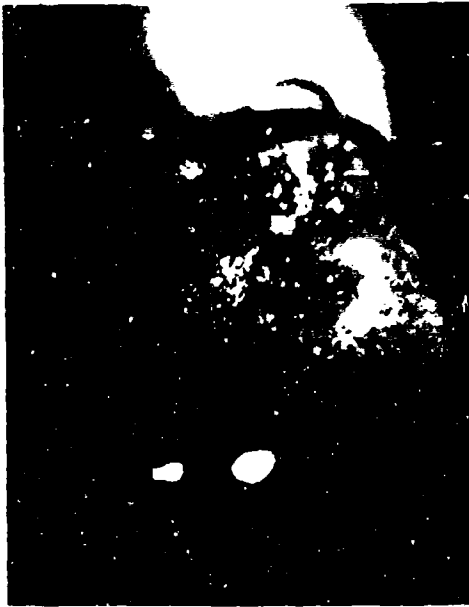
Particle 5 - Before



Particle 5 - After

Figure 3-23

Liquid Erosion Test: Fresh Shell 405 8 to 12 Mesh
Particles at 100 Feet per Second and 8,200 Pulses



Particle 3 - Before



Particle 3 - After



Particle 4 - Before



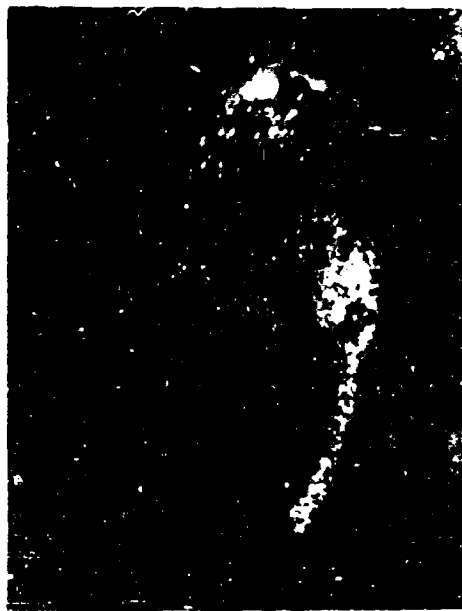
Particle 4 - After

Figure 3-24

Liquid Erosion Test: Fresh Shell 405 8 to 12 Mesh
Particles at 100 Feet per Second and 100,000 Pulses



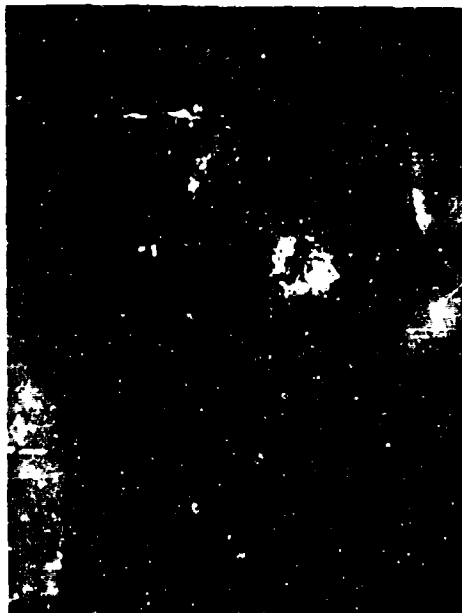
Particle 1 - Before



Particle 1 - After



Particle 3 - Before



Particle 3 - After

Figure 3-25
Liquid Dynamic Erosion of Fresh Shell 405
1/8" x 1/8" Cylinders

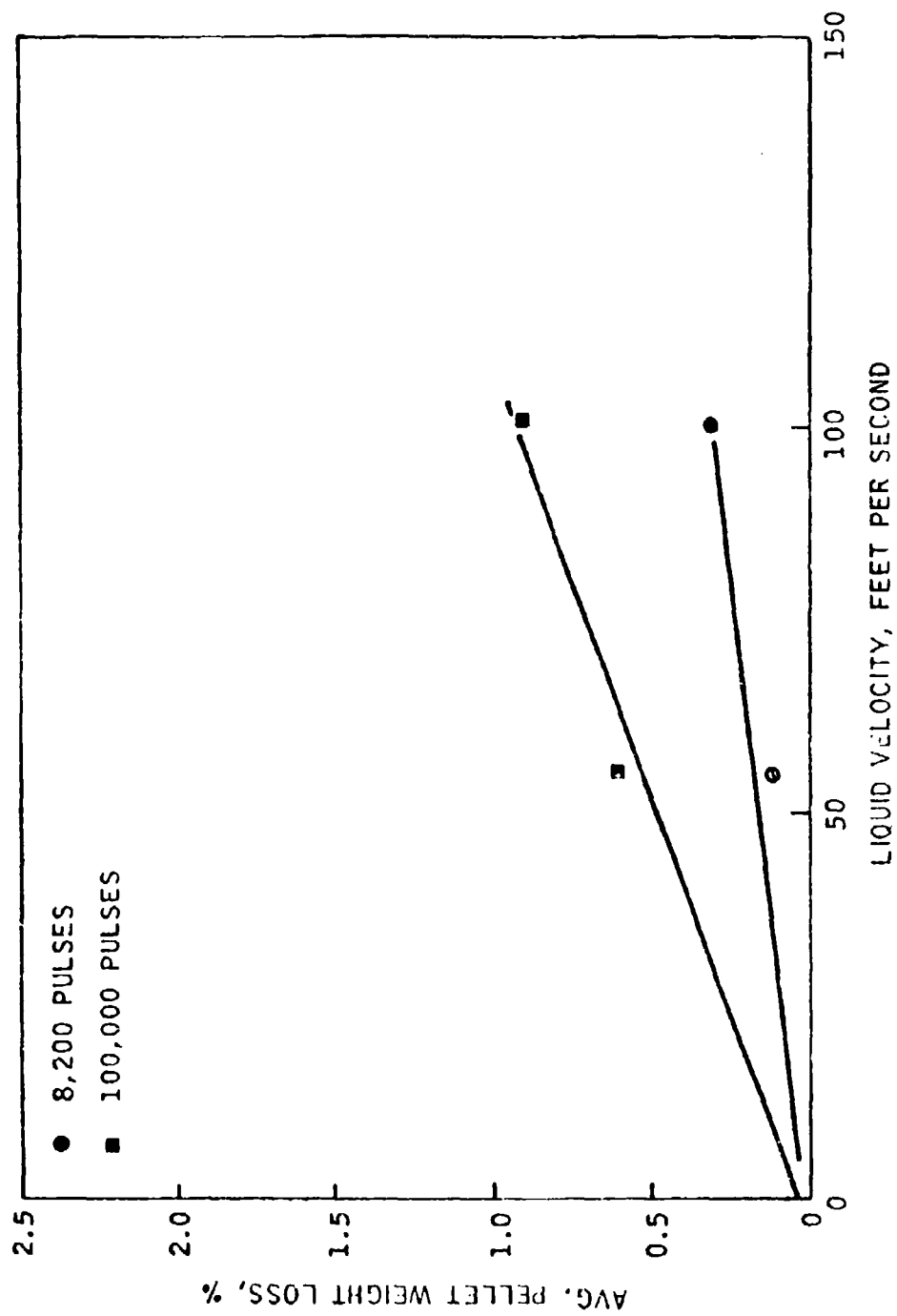


Figure 3-26

Liquid Dynamic Erosion of Fresh Shell 405
8 to 12 Mesh Particles

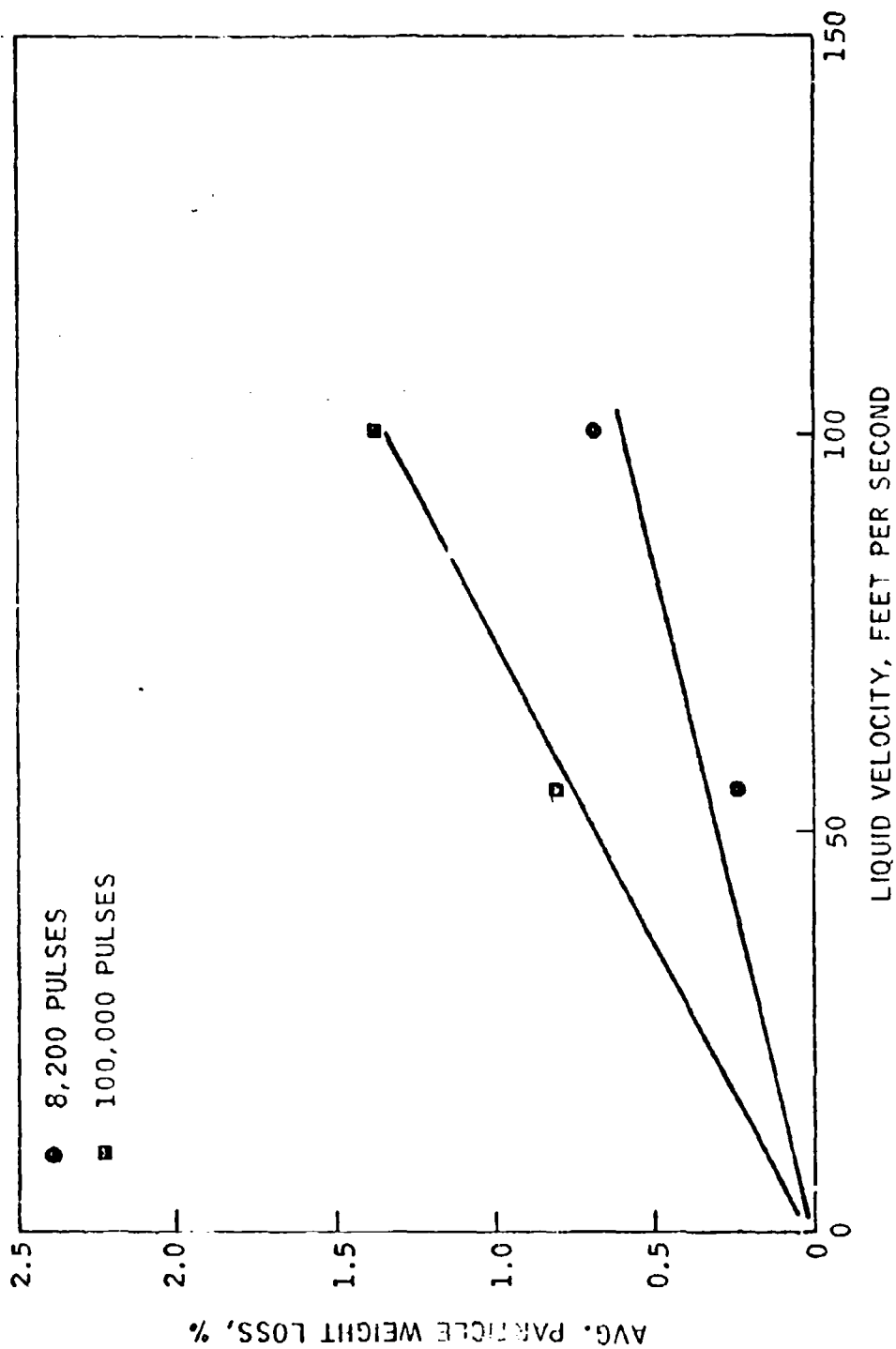


Table 3-21
Analysis of Variance (ANOVA) Summary
Pulsed Liquid Erosion Data

<u>Source of Variation</u>	<u>Sum of Squares</u>	<u>Degrees of Freedom</u>	<u>Mean Square</u>
Pulse Number	3.26041	1	3.26041
Velocity	1.35424	1	1.35424
Catalyst Type	0.82944	1	0.82944
Pulse Number x Velocity Interaction	0.03025	1	0.03025
Pulse Number x Catalyst Type Interaction	0.00961	1	0.00961
Velocity x Catalyst Type Interaction	0.16900	1	0.16900
Pulse Number x Catalyst Type x Velocity Interaction	0.00009	1	0.00009
Replicates	<u>4.98215</u>	<u>32</u>	<u>0.15569</u>
TOTAL	10.63518	39	--

Pulsed, liquid erosion tests were also extended to 14 to 18 mesh fresh Shell 405 catalyst to see if other mesh size of granular catalysts exhibited higher weight losses. Use of smaller than 14 to 18 mesh size catalyst in these tests was impractical because of the difficulty of making meaningful weight change measurements. Photomicrographs of 14 to 18 mesh particles selected from the sample of five particles after exposure to 100,000 pulses at 100 feet per second are shown in Figure 3-22. The fresh 14 to 18 mesh material showed an average weight loss of 1.08% with a standard deviation of 1.08 wt. %. By comparison data obtained with 8 to 12 mesh fresh granules showed an average weight loss of 1.35% with a standard deviation of 0.22 wt. % after a similar exposure. A t-test on these results indicates that the difference between the two values is not statistically significant. Thus, it is concluded that there is no difference between the ability of fresh 8-12 mesh and 14-18 mesh material to resist pulsed, liquid erosion. The fresh 14-18 mesh material exhibited a significantly higher standard deviation than the fresh 8-12 mesh material; and it is felt that this difference simply reflects the greater difficulty in making weight change measurements with smaller particles.

In general, although pulsed liquid stream erosion was shown to effect particle weight loss, the magnitude of the loss was low with the fresh catalysts. For example, with a granular catalyst exposed to 100,000 pulses, the average weight loss can be held to only 0.7 wt % if the linear velocity is restricted to a maximum of 50 feet per second. Thus, if liquid injection velocities are held below 50 feet per second, the weight losses experienced by fresh granular catalysts at the bed inlet during a cold start attributable to pulsed, liquid stream erosion per se will be small. The effect of pulsed liquid stream erosion on granular catalysts exposed to aging in a thruster environment, is discussed later in this report.

3.3 Estimation of Catalyst Strength of Material Properties

Strength of material properties are important parameters in interpreting both experimental and analytical results. Determination of the true strength of material properties of the small, irregularly shaped Shell 405 catalyst particles is a difficult task. To help overcome this difficulty, Dr. D. P. H. Hasselman, Director of the Ceramics Research Laboratory, Lehigh University was retained to (1) provide expert opinion and advice in this area, and (2) to estimate a number of material properties of individual catalyst particles. Dr. Hasselman's reports describing this effort are contained in the Interim Technical Report (100).

Experimental measurements were also made using the ITI to help estimate Shell 405 catalyst properties. Stress-strain measurements were made on Shell 405 1/8" x 1/8" cylinders in compression. Blank measurements were also made. These measurements yielded a Youngs Modulus of approximately 300,000 psi. A measurement was also made using the PCMB/ITI to determine a bed modulus using 20 to 25 mesh Shell 405 catalyst at pressures up to 1,000 psi. This experiment yielded a bed modulus of approximately 25,000 psi. A modulus of this magnitude indicates that a bed subjected to a 100 psi load will compact approximately 0.4%.

Figure 3-22

Liquid Erosion Test: Fresh Shell 405 14-18 Mesh
Catalyst at 100 Feet Per Second and 121,000 Pulses



Pellet 1 - Before



Pellet 1 - After



Pellet 2 - Before



Pellet 2 - After

4. TASK II - SELECTED MECHANISM AND BED TESTING

Following completion of Task I, more intensive laboratory testing was carried out both by TRW Systems Group and Exxon Research and Engineering Company. In general, this experimental work involved (a) additional investigation of mechanisms or factors which were shown in Task I to be important and (b) investigation of phenomena occurring in a complex bed environment, rather than just occurring in a single particle. Also the effect of synerisms or interactions was investigated and output data correlations were made.

4.1 Studies Carried Out by TRW Systems Group

Shell type 405 catalyst is currently the industrial standard for catalytic hydrazine reaction engines. Advances in satellite technology have placed extended life requirements on propulsion systems using Shell 405 in hydrazine thrusters. Excessive physical degradation of the catalyst limits the propulsion system's ability to efficiently perform on long life missions. The "External Catalyst Breakup Phenomena" program was undertaken to identify, evaluate and correlate specific catalyst breakup mechanisms in order to provide catalyst users with a fundamental technology base to meet long life mission requirements.

TRW's participation in the overall program included efforts involving the literature review, sensitivity test design and assessment, selected mechanism tests, synergistic effects, output data correlation and systems safety study.

Engine operating data and design considerations were provided for a phenomenological survey and literature review to assist analytical modeling efforts (MDAC) and sensitivity test designs. Sensitivity test assessment combined with analytical modeling results provided the necessary data to conduct extensive selected mechanism testing. A unique laboratory reactor was designed and fabricated to quantify important external breakup mechanisms identified during the phenomenological survey. Interaction study matrices were evaluated to determine the effects of synergism. An output data correlation phase indicated the extent of catalyst degradation that could be expected under various thruster operating conditions. A systems safety study was performed to indicate the precautions necessary to minimize unintentional catastrophic failure of hardware and physical harm to uninvolved bystanders.

This section of the report centers around TRW's major contributions to the overall program: Selected Mechanism Testing and Output Data Correlation.

4.1.1 Mechanism Identification

A comprehensive literature survey described in Section 3.1 identified numerous specific breakup mechanisms from the general areas of fluid dynamic erosion, pressure crushing, differential thermal expansion,

particle movement, thermal shock and internal pore pressure gradients. Analytical modeling techniques using strength failure criterion were performed (see Section 5) to discriminate the relative destructive potential of each specific mechanism and to act as a guide in formulating and correlating the experimental studies (100).

Correlation of the analytical and experimental phases of the phenomenological survey revealed areas of major, significant and insignificant breakup mechanisms:

Major Breakup Mechanisms

1. Particle-to-particle crushing from static forces such as flowing gas ΔP , differential thermal expansion effects or pressure shocks.
2. Pore pressure buildup from imbibed liquid hydrazine.
3. Particle movement in a voided bed.

Significant Breakup Mechanisms

1. Fluid dynamic erosion from a pulsed liquid stream.
2. Abrasion from particulates in a flowing gas.
3. Thermal shock during liquid quench cooldown.

Insignificant Breakup Mechanisms

1. Gas and liquid droplet fluid dynamic erosion.
2. Pore pressure gradients during rapid gas pressurization or depressurization.
3. Hot gas thermal shock.
4. Transient effects in pressure shocks.

4.1.1.1 Selected Mechanism Studies

Specific breakup mechanisms were selected for extensive testing with catalyst beds in modified laboratory reactors. The selected mechanism studies were undertaken to:

1. Quantify the more important breakup mechanisms.
2. Assess the effects of multiparticle interactions.
3. Investigate the effects of synergism.

4. Permit application of the results to catalyst bed operation in general.
5. Verify and strengthen the analytical models.

The mechanisms that were selected for extensive study are described below with reference to their occurrence in hydrazine thruster operation and analytical model predictions. A unique feature of these test studies is the exclusion of hydrazine interference for all catalyst bed tests. The techniques for producing and isolating the described phenomena are discussed in Section 4.1.2.

1. "Pop" Shock Dynamic Pressure Crushing

An orderly procedure occurs during the normal start of a catalytic hydrazine engine: propellant injection into the reaction chamber, vaporization and controlled decomposition kinetics which produces a transient chamber pressure buildup to a final steady-state value. The particle-to-particle crushing forces resulting from the dynamic pressure transient were analytically determined to be less than a failure criterion level. Common start transient times for chamber pressure build-up are in the ten to fifteen millisecond range. The natural bed oscillation period (response time) was determined at 0.6 ms. The catalyst bed would therefore respond faster than the pressure buildup transient and be subjected only to a normal steady-state pressure drop. Abnormal start transients, caused by design deficiencies or catalyst activity decreases, produce pressure amplitudes which are much higher than normal and occur in a reduced time period. This phenomenon, termed "pop" shock, results in hydrazine detonations caused from uncontrolled decomposition kinetics. The dynamic "pop" shock degradation mechanism effectively bounds the upper limit of pressure amplitudes encountered in catalytic hydrazine engine operation.

2. Hot Gas Thermal Fatigue (and thermal aging)

The thermal stresses developed from gaseous flow over catalyst particles during a cold start heatup transient or from cool-down were analytically determined to be below the failure criterion level for new catalyst. Physically degraded catalyst (severely used condition) was predicted to incur some failure on cooling. This mechanism was investigated to determine if repeated hot gas cycling (fatigue) would degrade new catalyst and if hot gas cycling was a significant contribution to the degradation of used catalyst. Thermal aging or prolonged exposure to hot, hydrazine decomposition gases was included to complete the study of thermal effects and serves as a reference point of comparison for the hot gas thermal fatigue studies, even though it was not expected to be a major degradation mechanism.

3. Liquid Quench Thermal Shock

This mechanism produces thermal stresses when cold liquid hydrazine impinges onto a hot catalyst bed. The heat transfer characteristics of a liquid medium allow more severe tensile stresses to be developed on the

outer catalyst particle surfaces. The analytical model predicted some failures from liquid quench thermal shock which suggested that this was a borderline degradation mechanism. The analytical predictions were based on boiling heat transfer considerations that were extremely difficult to characterize for the hydrazine thruster environment. This mechanism, guided by the analytical model, was studied to elucidate the quench shock effect, and hence to provide an insight into the dominant boiling heat transfer mode.

4. Void-Volume Abrasion

Sensitivity tests revealed that a significant amount of particle-to-particle abrasion could be possible in catalyst beds that had been voided by some other breakup mechanism. Void volume abrasion tests were performed to investigate this effect in a catalytic engine environment.

5. Cold Gas Pressure Crushing

Particle-to-particle crushing from the forces generated by hot flowing gas contains two additive variables, pressure crushing and thermal effects. Tests with cold gas removed the thermal effects and enabled isolation of "pure" pressure crushing mechanism.

6. Isothermal Catalyst Activity Reactor

Limited tests were performed by immersing catalyst particles in an isothermal hydrazine bath. The nature of imbibition pressure effects could be studied without the generation of copious quantities of hot gas (thermal effects) and the subsequent catalyst bed pressure crushing forces.

4.1.1.2 Interaction Studies

The simultaneous action of separate factors, which acting together have a greater effect than the arithmetic sum of their individual effects is often termed either a synergism or an interaction. The experimental identification of potential synergisms is important not only to catalyst users, but also for the preparation of a realistic analytical model. The principle of superimposition is most commonly used to determine the total effect from the sum of individual parts. A system failure criteria may be developed where by the degradation forces resulting from liquid imbibition, pressure crushing, thermal effects, etc., are added and compared to the strength failure criteria. An overall model, based on the principle of superimposition, would be very unrealistic should a potential synergism go undetected.

Two interaction studies were evaluated as statistically designed experiments. The studies were planned around the selected mechanism testing and are presented in Tables 4-1 and 4-2 as parametric logic matrices. The Interaction Study I independent variables were:

Table 4-1

Interaction Study I

Is Catalyst Exposed To High Temperature Flowing Gas?	Is Catalyst Exposed to Repeated Bed Pressure Loads?			
	NO		YES	
NO	14-18 Mesh	25-30 Mesh	14-18 Mesh	25-30 Mesh
	Fresh Shell 405	Fresh Shell 405	Cold Gas Pressure Crushing	Cold Gas Pressure Crushing
YES	Thermal Aging (Full and Voided Beds)	Thermal Aging (Full and Voided Beds)	Hot Gas Thermal Fatigue	Hot Gas Thermal Fatigue

Table 4-2

Interaction Study II

Is Catalyst Exposed To Thermal Fatigue Heat Up Cycling?	Is Catalyst Exposed to Liquid Hydrazine?			
	NO		YES	
	14-18 Mesh	25-30 Mesh	14-18 Mesh	25-30 Mesh
NO	Fresh Shell 405	Fresh Shell 405	Isothermal Activity Reactor	Isothermal Activity Reactor
YES	Hot Gas Thermal Fatigue	Hot Gas Thermal Fatigue	Catalytic Hydrazine Thruster	Catalytic Hydrazine Thruster

1. Catalyst selection parameters.
2. Exposure to high temperature flow gas.
3. Exposure to repeated bed pressure loads.

Submatrix elements are indicated to allow evaluation of void-volume abrasion and used catalyst.

The Interaction Study II independent variables were:

1. Catalyst selection parameters
2. Exposure to thermal fatigue heat up cycling
3. Exposure to liquid hydrazine

4.1.2 Experimental Techniques

4.1.2.1 Laboratory Reactor Design and Fabrication

4.1.2.1.1 Design Objectives

Objectives for the experimental investigation of catalyst bed degradation induced from external effects were that the operating characteristics of a normal catalytic hydrazine engine be reproduced without allowing liquid hydrazine to contact any portion of the catalyst bed. The following parameters and ranges were identified as typical for catalytic hydrazine engines:

1. Catalyst sizes: 14-18 mesh
25-30 mesh
2. Bed temperature extremes: ambient to $\approx 1600^{\circ}\text{F}$
3. Gas composition: Nitrogen, Hydrogen and ammonia corresponding to approximately 60 percent dissociated ammonia.
4. Chamber pressures: 75 psia to 250 psia
5. Catalyst bed pressure drop: 50 psi nominal
6. G loading (flow rate divided by bed cross-sectional area):
0.01 to 0.03 lb/in.²-sec

A valid comparison of the destructive potential of each mechanism under investigation would not be possible unless the design could accommodate all tests and their associated variables. A single design was therefore highly desired which would allow easy catalyst bed installation, test, removal and analysis.

4.1.2.1.2 Description of Design

A unique laboratory reactor was designed to meet all anticipated parametric and test requirements. This reactor is shown as an assembly drawing in Figure 4-1. An electrothermal hydrazine decomposition device was placed up-stream of a catalyst bed chamber. The decomposition device was derived from a flight model electrothermal hydrazine thruster (109) and produces hot gases from decomposed hydrazine nearly identical in composition and temperature to those encountered in catalytic hydrazine engines. An isolation plenum was placed between the decomposition device and catalyst bed container to allow various catalyst bed "start" temperatures. The laboratory reactor design provided for

1. Elimination of liquid hydrazine impingement for all catalyst bed tests,
2. Simulation of catalytic hydrazine engine environments,
3. Geometric equivalence for all catalyst bed tests,
4. Operational parameter measurement,
5. Catalyst bed accessibility for installation and removal.

4.1.2.1.3 Reactor Components

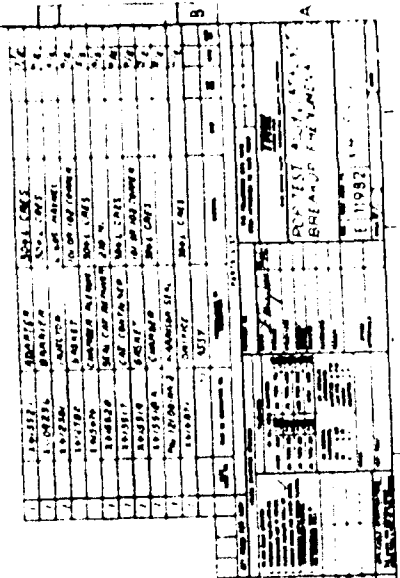
The electrothermal decomposition chamber consisted of a single stream liquid hydrazine injector, 0.2 inch diameter decomposition chamber, and an external heater to elevate the temperature of sixty platinum screens to a point where hydrazine decomposition could be initiated and sustained. The decomposition device was threaded into the plenum chamber and sealed by a nickel gasket. The plenum chamber had provisions for external cooling and a pressure tap. The plenum was modified later in the program by incorporating an injector for the Liquid Quench Thermal Shock tests. The decomposition device and plenum was flange mated to a lower chamber which accepted a 0.2 inch diameter by 0.2 inch (or 0.4 inch) long catalyst bed container. The plenum-lower chamber and catalyst bed container seals were of nickel. A pressure tap and thermocouple probe were incorporated beneath the catalyst bed container. A plug containing a 0.022 inch orifice sealed the lower chamber.

Laboratory reactor drawings are included in Appendix.

4.1.2.1.4 Reactor Fabrication

Reactor components were fabricated from 300 series stainless steels wherever possible to reduce material and machine costs. Exceptions to this were the Haynes 25 liquid hydrazine injector, nickel gasket seals, platinum screens and Haynes 25 upper and lower catalyst bed retainer screens. The fabricated components are illustrated in Figure 4-2 (disassembled) and

Figure 4-1



→

Figure 4-2

Laboratory Reactor Components

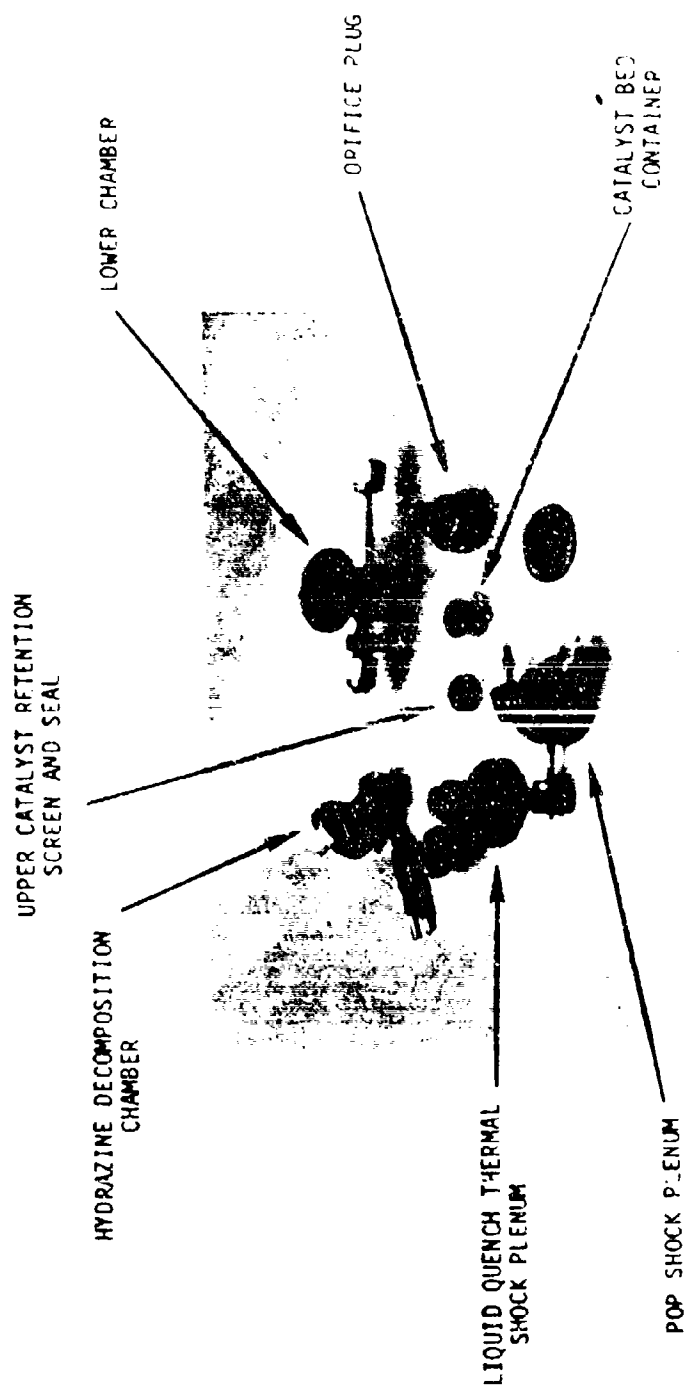


Figure 4-3

Assembled Laboratory Reactor

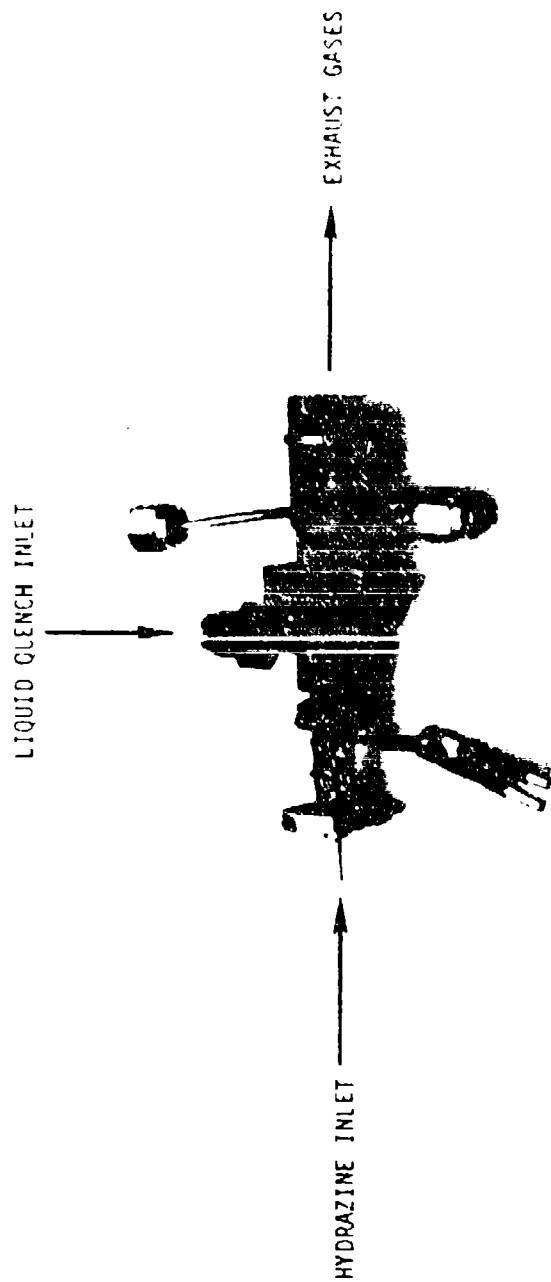


Figure 4-3 (assembled) in the as-tested condition. Two plenums are shown in Figure 4-2; the original Pop Shock plenum, and a similar plenum modified for the Liquid Quench Thermal Shock Studies. The fully assembly reactor in Figure 4-3 is shown with the Liquid Quench injection plenum.

4.1.2.2 Mechanism Evaluation Methods

4.1.2.2.1 Catalyst Handling and Measurement Techniques

All catalyst tested in the as received condition was drawn from the same mesh size lot. The two lots of nominal 14-18 mesh and nominal 25-30 mesh were prescreened to 14-18 mesh and 25-30 mesh in order to increase test-to-test catalyst size uniformity. The handling and measurement procedures used during the test program are described below:

1. Pre-Nitridation of Catalyst Containers

Materials of construction for hydrazine engines readily absorb nitrogen and form external nitride layers. The extent of this process is most rapid during the initial exposure of bare metal surfaces to the high temperature environment. Failure to account for this process could severely influence pre- and post-test catalyst bed container weight measurements. All catalyst bed containers, upper and lower retainer screens and the upper bed gasket were pre-conditioned by extended steady-state firings in the laboratory reactor. The impact of subsequent nitridation was minimal.

2. Catalyst Conditioning

Catalyst for all bed tests was stabilized to the atmospheric laboratory environment for a period of twenty-four hours prior to and after test. A series of weight measurements established that this time period was sufficient for the moisture adsorption and desorption processes to equilibrate.

3. Catalyst Loading and Unloading

Catalyst and catalyst bed containers were weighed to the nearest 0.1 mg on Mettler analytical balances:

- a. Weigh catalyst bed container and lower 40 mesh Haynes 25 retaining screen.
- b. Weigh upper retaining screen and gasket.
- c. Load catalyst into bed container. Catalyst pre-compaction of settling techniques were not employed.
- d. Weigh catalyst and bed container assembly.
- e. Photograph top of catalyst bed.
- f. Stabilize catalyst for 24 hours.
- g. Reweigh catalyst and bed container and install into laboratory reactor.
- h. TEST
- i. Remove catalyst and bed container from laboratory reactor and weigh catalyst bed container assembly. *J*

- j. Photograph top of catalyst bed.
- k. Stabilize catalyst for 24 hours.
- l. Reweigh catalyst and bed container.
- m. Remove catalyst from container and weigh.
- n. Weigh catalyst bed container and retainer screens.

At this point the amount, if any, of catalyst "lost" during test and or handling was ascertained. Catalyst lost during test was defined as that less than the 40 mesh retaining screens. Weight difference measurements based on catalyst alone and on catalyst plus bed container revealed that any catalyst "lost" during handling was within measurement accuracy.

4. Catalyst Mesh Size Separation

Two mesh size separations were performed for each starting size catalyst. Catalyst weights were made according to the following schemes:

Original 14-18

14-18	Catalyst remaining on 18 mesh.
18-20	Catalyst through 18 mesh and remaining on 20 mesh.
<20>40	Catalyst through 20 mesh and remaining on 40 mesh.
<40	Sum of catalyst through 40 mesh plus catalyst lost during test, i.e., that which escaped through the retaining screen.

Original 25-30

25-30	Catalyst remaining on 30 mesh.
30-35	Catalyst through 30 mesh and remaining on 35 mesh.
<35>40	Catalyst through 35 mesh and remaining on 40 mesh.
40	Sum of catalyst through 40 mesh plus catalyst lost during test, i.e., that which escaped through the retaining screen.

The weights in each mesh size category were expressed as a percentage of the initial, pre-test catalyst weight. A material balance was calculated by summing the mesh size category percentages. The average material balance for all tests taken as a whole was 99.55 percent initial with a standard deviation of 1.13 percent initial. These results indicated that the handling and measurement techniques did not introduce an experimental uncertainty variable.

Selected samples of tested catalyst were carefully packaged to minimize catalyst movement and sent to Exxon Research and Engineering Company for further evaluation. The results of those tests are discussed in Section 4.2.3.

4.1.2.2.2 Parameter Measurement

Laboratory reactor tests with catalyst beds were performed in test facilities normally used for monopropellant hydrazine reaction engines. The test facilities were equipped with vacuum chambers to simulate high altitude operation and data acquisition equipment to measure operating variables. Thus, all variables reported were obtained in the same manner as for catalytic hydrazine engines.

The Liquid Quench Thermal Shock configuration is shown within the test chamber in Figure 4-4. Closer details appear in Figure 4-5. The liquid, anhydrous ammonia cylinder and associated valve is revealed in the background. Nominal instrumentation for the reactor tests consisted of

Temperatures

- Decomposition device
- Plenum
- Catalyst bed chamber
- Gas stream

Pressures

- Hydrazine supply
- Ammonia supply
- Vacuum chamber
- Plenum (above bed)
- Catalyst chamber (below bed)

Miscellaneous

- Hydrazine flowrate
- Valve voltage and current
- Heater voltage and current

Figure 4-4

Laboratory Reactor Test Cell

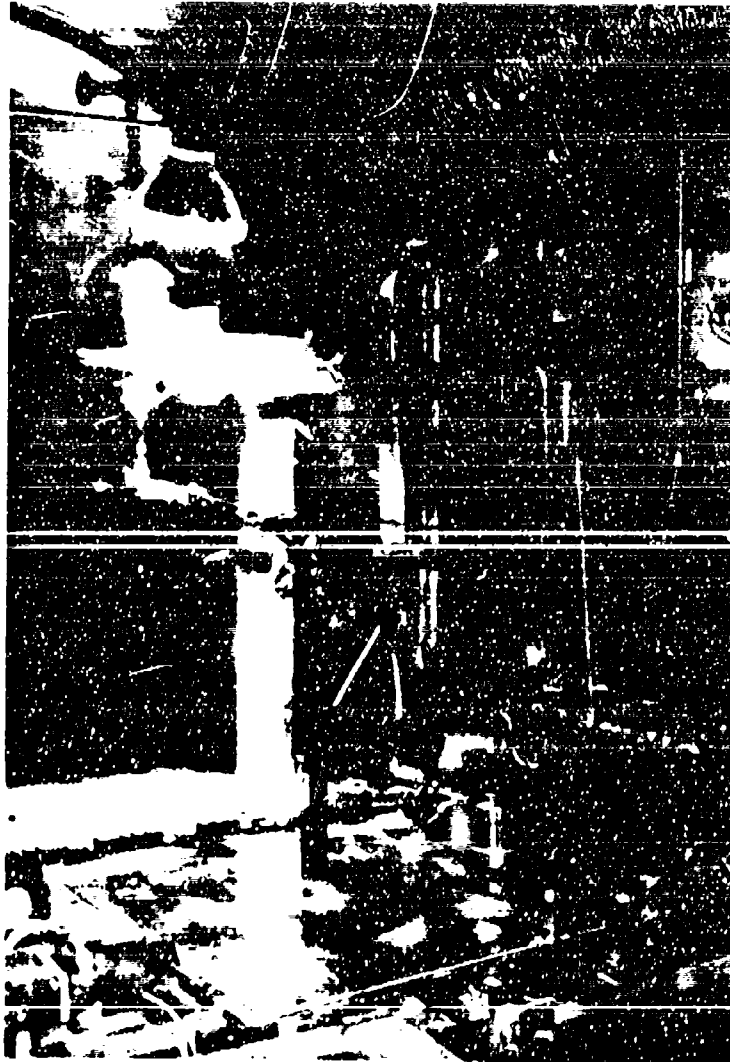
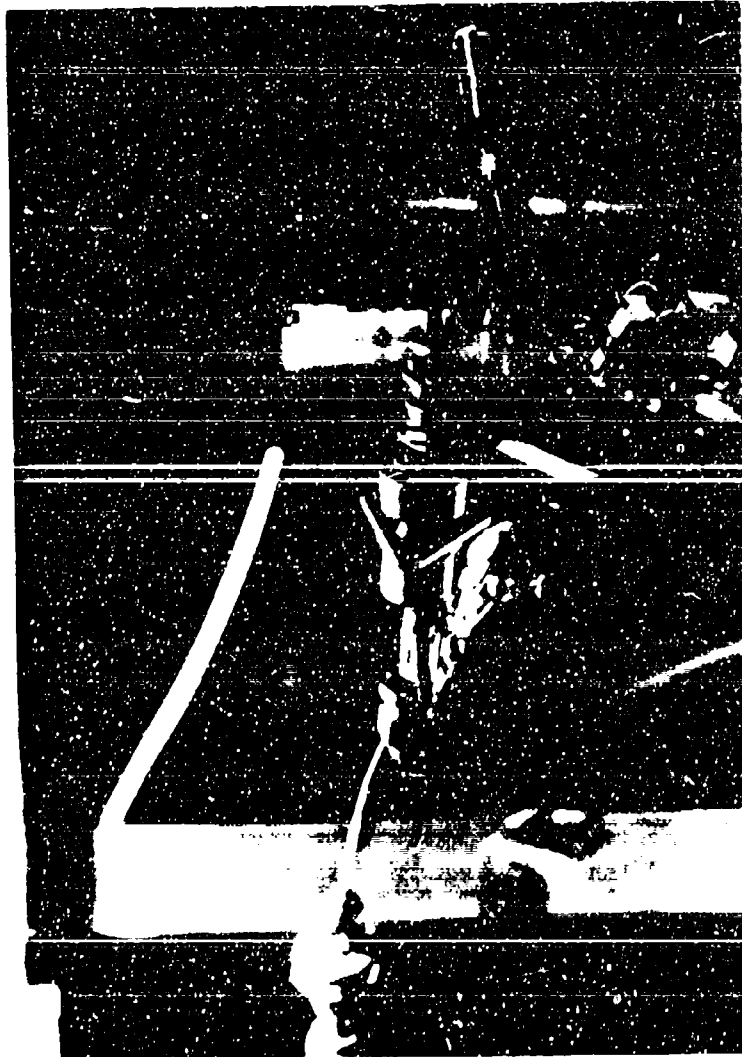


Figure 4-5

Liquid quench thermal shock test configuration



Duty cycles were controlled by preprogrammed function generators. The data were recorded on conventional stripcharts, digital readout or on high speed oscillographs when the need arose to measure the rapid pressure transients encountered during the Pop-Shock tests.

4.1.2.3 TEST Program

This section presents the Selected Mechanism test matrices in final form used during the program. Several of the original matrices were greatly expanded after initial test data were analyzed. The expansion of these matrices and the information derived from the data was responsible for understanding the destructive potential of the various mechanisms.

4.1.2.3.1 Dynamic Pop-Shock Pressure Crushing

Primary variables included catalyst selection parameters and number of "pop" shocks. The threshold level of an overpressure ignition spike was thought to be in the neighborhood of 1500 psia. The original matrix included an undetermined low number and high number of "pops" for each mesh size catalyst. The original test matrix is illustrated in Table 4-3. Evaluation of this four-element matrix indicated that parametric damage curves could not be presented because:

1. Threshold amplitude not defined.
2. Decomposition device could not be operated to reproduce decomposition detonations above 1000 psia every time.
3. Low and high numbers required further definition.

The above uncertainties required matrix expansion to define the threshold amplitude and ascertain the cumulative damage below, at and above the suspected threshold. This expanded matrix is presented in Table 4-4.

4.1.2.3.2 Hot Gas Thermal Fatigue

The Hot Gas Thermal Fatigue (HGTF) matrix is shown in Table 4-5. The laboratory reactor was operated in a stable, controlled decomposition mode for the HGTF tests. A ten percent duty cycle consisting of 6 sec on, 54 sec off was used for all tests. The 200 tests were performed only at the higher bed pressure drop.

4.1.2.3.3 Hot Gas Thermal Aging

Four tests were performed to match the cumulative on-time of the hot gas thermal fatigue tests. These tests consisted of 600 and 1200 seconds of steady-state operation which corresponded to the 100 and 200 HGTF tests, respectively. The hot gas thermal aging test matrix is presented in Table 4-6.

Table 4-3
Original "Pop" Shock Dynamic Pressure Crushing Test Matrix

Number of "Pop" Shocks	Fresh Shell 405 Catalyst Size	
	14-18 Mesh	25-30 Mesh
Low	X	X
High	X	X

- Bed holding temperature near ambient
- Threshold "pop" amplitude > 1500 psia

Table 4-4

Expanded "Pop" Shock Dynamic Pressure Crushing Test Matrix

Number of "Pop" Shocks	Fresh Shell 405 Catalyst Size	
	14-18 Mesh	25-30 Mesh
Amplitude P_{s1} Low \downarrow High	X	X
Amplitude P_{s2} Low \downarrow High	X	X
Amplitude P_{s3} Low \downarrow High	X	X

- Actual threshold between P_{s1} and P_{s2}

Table 4-5

Hot Gas Thermal Fatigue Test Matrix

Bed Pressure Drop	Fresh Shell 405 Catalyst Size	
	14-18 Mesh	25-30 Mesh
20 PSI	100 Cycles	100 Cycles
50 PSI	100 Cycles 200 Cycles	100 Cycles 200 Cycles

● Cycle: ambient (~200°F) to 1500°F

Table 4-6
Hot Gas Thermal Aging Test Matrix

Steady-State Exposure Duration, Sec	Fresh Shell 405 Catalyst Size	
	14-18 Mesh	25-30 Mesh
600	X	X
1200	X	X

4.1.2.3.4 Liquid Quench Thermal Shock

Liquid Quench Thermal Shock (LQTS) tests were performed on catalyst in three conditions: (1) Fresh Shell 405; (2) Thermally Fatigued Shell 405; and (3) Used Shell 405. The original test matrix was expanded to a lower number of quench cycles in order to aid in test technique and obtain more information. The intermediate plenum was modified by placing a 0.008 inch ID, single stream injector in axial alignment above the catalyst bed. Liquid, anhydrous ammonia was selected as the quench medium after consideration of the influence water might have on desurfacing the alumina substrate.

The ammonia injection flow rate was calibrated by measuring the flow characteristics of the injector at the saturation pressure ($\approx 70^{\circ}\text{F}$). The equivalent G loading for all tests was $0.032 \text{ lbs/inc}^2\text{-sec}$. Various ammonia injection pulse widths were investigated. The most reproducible pulses were from five to nine seconds duration.

The final form of the LQTS test matrix is shown in Table 4-7. The used catalyst was obtained from a TRW XMRE-5 five pound thruster. This catalyst, nominal 18-20, was subjected to the following hydrazine exposure:

566	Ambient starts (70°F)
210,098	Pulses
2,646	Seconds steady-state
431	Pounds propellant thrust

The catalyst recovered from the engine was separated into upper bed and lower bed lots. Catalyst from each bed location was further meshed to obtain reasonable uniformity for quench shock testing. The surviving 18 mesh catalyst from each bed was subjected to 200 quench cycles as was meshed 25-30 catalyst.

4.1.2.3.5 Void-Volume Abrasion

Partially voided catalyst beds were subjected to 600 seconds steady-state hot gas flow according to the test matrix appearing in Table 4-8. The void-volume was determined as the volume percent of the bed obtained by partial bed loads.

4.1.2.3.6 Cold Gas Pressure Crushing

Each catalyst size was subjected to 200 cold gas cycles (dry filtered nitrogen). The duty cycle was identical to that used for the hot gas thermal fatigue studies.

4.1.2.3.7 Isothermal Catalyst Activity Reactor

A limited number of tests were performed with 14-18 mesh catalyst in an isothermal hydrazine bath at 40°F . These tests were performed to provide the Interaction Study II with baseline information. Immersion times of 30 seconds were used and multiple immersions were also included. This test series was not expanded to include all potential variables. Extended isothermal immersion tests do not simulate the true environment of a catalytic hydrazine engine. Recent work by United Technologies Research Laboratories concentrating on internal breakup mechanisms was referenced for the Interaction Studies II Matrix where appropriate.

Table 4-7

Liquid Quench Thermal Shock Test Matrix

Catalyst Condition	Number of Quench Cycles	Shell 405 Catalyst Size	
		14-18 Mesh	25-30 Mesh
New	5	X	X
	25	X	X
New Plus 100 Fatigue* Cycles	5	X	X
	25	X	X
New Plus 100 Fatigue Cycles	100	X	X
	200	X	X
Used Upper Bed**	200	X	X
Used Lower Bed	200	X	X

*Fatigued - 100 Thermal Fatigue Cycles Prior to Quench Cycles

**Used - 566 Cold Starts (70°F); 210,098 Pulses; 2,646 Seconds Steady-State
431 Pounds Propellant Thruput

Table 4-8

Void-Volume Abrasion Test Matrix

G Loading, lbs/sec-in ²	Void Volume, %	Fresh Shell 405 Catalyst Size	
		14-18 Mesh	25-30 Mesh
0.01	10	X	X
	20	X	X
0.015	20	X	X

4.1.3 Selected Mechanism Test Results

4.1.3.1 Dynamic Pop-Shock Pressure Crushing

The original Pop-Shock test matrix (Table 4-3) was expanded in order to determine the threshold amplitude of damage and cumulative effect of successive "pops". The nature of uncontrolled decomposition kinetics responsible for the high magnitude spikes resulted in unpredictable pop intensities. Several tests were therefore performed to gather enough data to provide a basis for interpretation.

Data for the two catalyst sizes are presented in Tables 4-9 and 4-10 for 14-18 mesh and 25-30 mesh catalyst, respectively. The rise time to maximum detonation intensity above the catalyst bed was generally two to four milliseconds. The catalyst bed response was considerably faster; a pressure drop across the bed was established and maintained a near constant value throughout the transient pressure profile. The pressure drop across the bed was a function of peak upstream pressure intensity. This behavior is illustrated in Figure 4-6. The data for both catalyst sizes (14-18 and 25-30) are consistent with some bias for the 25-30 mesh catalyst at intensity levels up to 1500 psia. This behavior is in accordance with the observation that the smaller mesh size has a higher packing fraction and would be expected to create a higher pressure drop at equivalent peak intensities.

The data indicate that micro-detonation which produce less than approximately 150 psi bed pressure drop did not cause severe degradation. This level corresponded to a peak detonation intensity of approximately 1000 psia. Threshold levels for significant, single pop damage appeared to be in the 1700 to 2000 psia range, bed pressure drops between 300 and 450 psi, respectively. Cumulative damage occurred below the single "pop" threshold. The cumulative damage from successive pops is illustrated in Figure 4-7 for 14-18 mesh and in Figure 4-8 for 25-30 mesh catalyst. The cumulative damage is expressed as total fines generation as a function of number of "pops" above a cumulative damage threshold. Two damage thresholds were identified for the 14-18 mesh catalyst, whereas, only one threshold level could be deduced from the data for 25-30 mesh. The lower 14-18 mesh damage threshold of 1000 psia produced 23% fines generation after 8 pops (on curve). Eight successive pops above 1500 psia produced 76% fines generation, a factor of three higher than that observed at the lower threshold. A comparison of similar cumulative damage thresholds for both mesh size catalysts suggested that the 14-18 catalyst was twice as susceptible to dynamic pressure crushing than was the 25-30 catalyst.

Typical post-test appearances of the in-situ catalyst beds are shown in Figure 4-9 (14-18 mesh) and Figure 4-10 (25-30 mesh) (The photographs appearing in Figures 4-9 and 4-10 are of the top portion of the catalyst bed where the pressure crushing forces would be least). No visible damage can be observed in Figure 4-9a (1 pop at 1725 psia). Exposure to two pops at 1800 psia caused fracture of two particles (Figure 4-9b). Extensively damaged catalyst, Figures 4-9c and 4-9d, is readily observed (16 pops above 1000 psia). The upper flange area, Figure 4-9c, contains a substantial amount

Table 4-9

Pop-Shock Data for 14-18 Mesh Catalyst

Identification	Number of Pops in Range, psia		Fines Generation (%Initial)	Total Fines, %	Material Balance %				
	≥1500	1499-1000							
16-23	4	1	3(>750)	82.4	2.4	6.8	7.2	16.4	98.8
41-52	0	0	1(850)	96.3	0	1.7	1.6	3.3	99.9
53-55	0	2(1425)	1(850)	92.8	2.0	1.9	3.4	7.3	100.1
57-104	8	8	11	23.2	8.8	13.3	54.2	76.3	99.5
105-107	1(1725)	0	0	94.7	2.0	0	0.8	2.8	97.5
108-125	4	3	7	81.1	7.1	6.9	3.9	17.9	99.0
125-156	2(1800)	0	11	95.9	2.3	1.0	1.6	4.9	100.8

Average material balance = 99.37%

Standard deviation = 1.07%

Table 4-10

Pop Shock Data for 25-30 Mesh Catalyst

Identification	Number of Pops in Range, psia		Fines Generation (% Initial)		Total Fines, %	Material Balance, %
	≥1500	1499-1000	<999	25-30 30-35 <35>40 <40		
259-271	2(1900)	5	4	88.4 4.7 2.5 4.3	11.5	99.9
272-291	0	0	8	96.5 2.1 0 1.3	3.4	99.9
292-321	0	1	2	93.6 4.2 0 2.3	6.5	100.1
322-354	0	0	21	95.4 0.8 0 4.3	5.1	100.5
356-377	3(1500)	0	21	92.6 3.8 0.2 3.9	7.9	100.5
378-386	3(2000)	0	4	94.7 1.8 0.8 3.3	5.9	100.6

Average material balance = 100.25%

Standard deviation = 0.32%

Figure 4-6

Catalyst Bed Pressure Drop As a Function of Peak Upstream Pressure

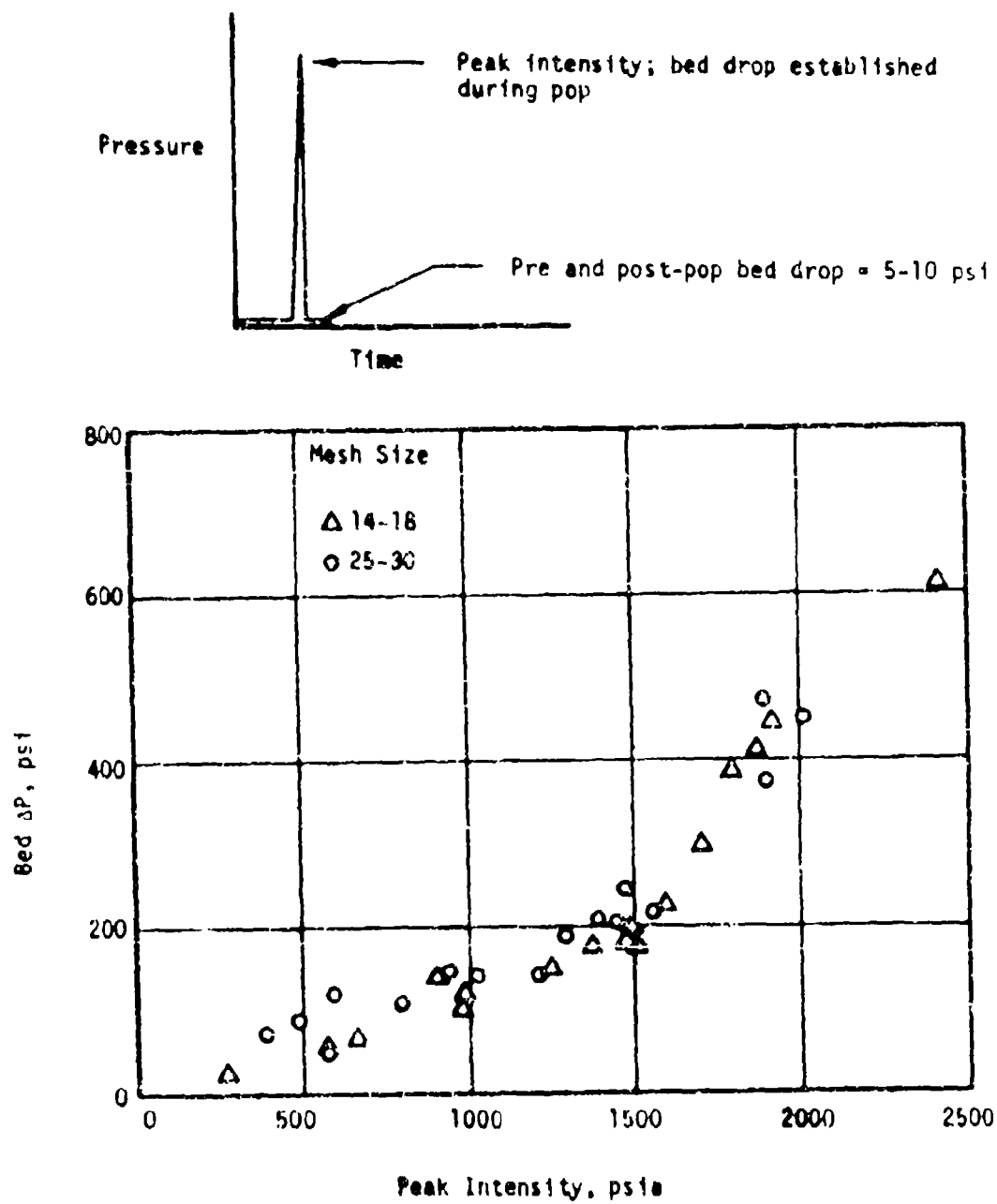


Figure A-7
Cumulative Damage of 14-18 Mesh Catalyst Exposed to Successive Pops

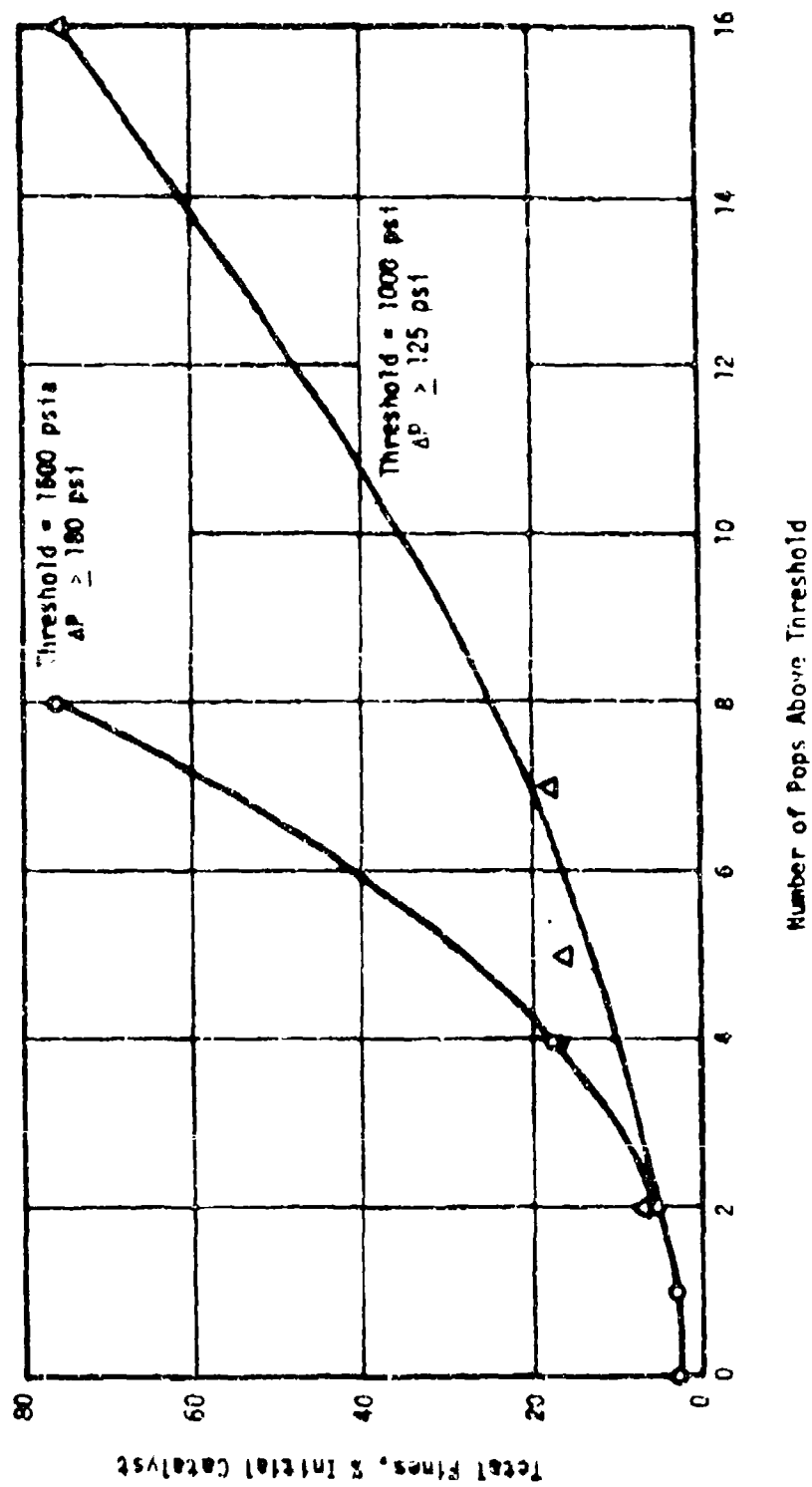


Figure 4-8

Cumulative Damage of 25-30 Mesh Catalyst Exposed to Successive Pops

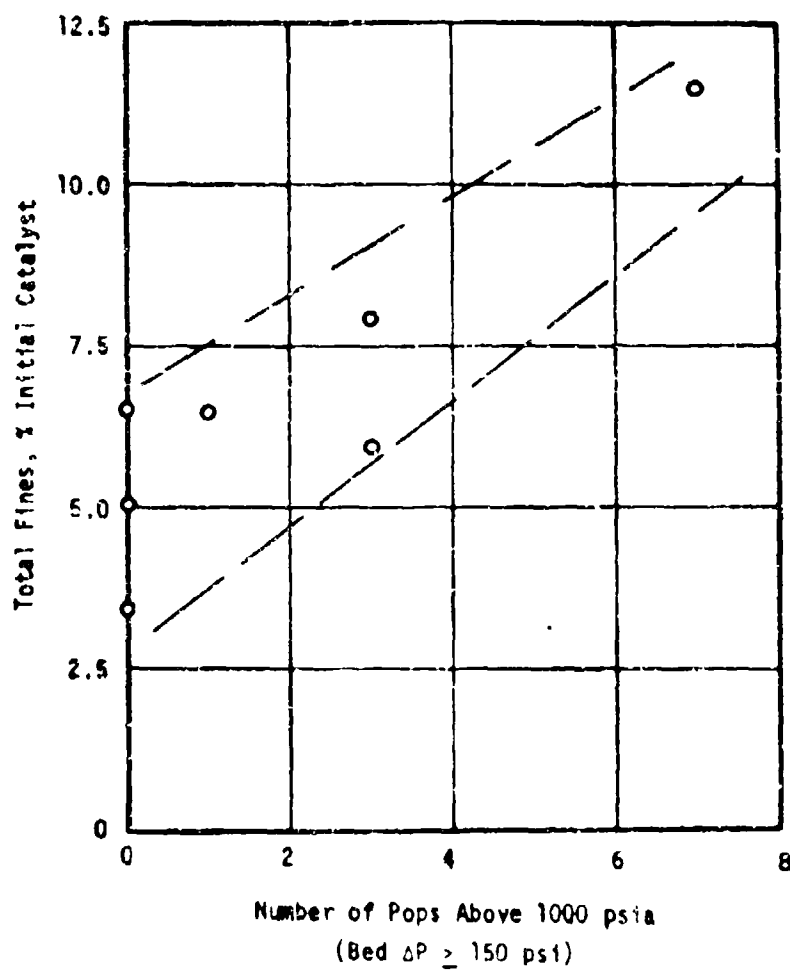
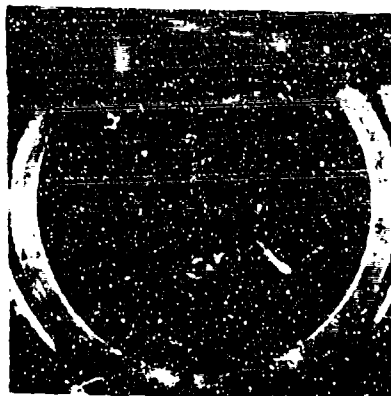


Figure 4-9

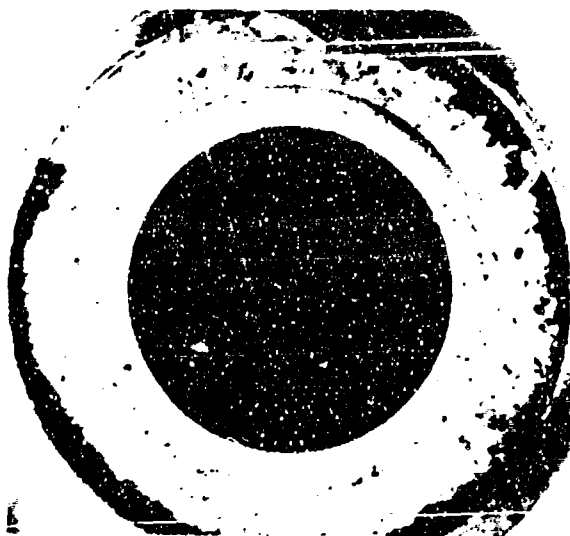
Post Pop-Shock Appearance of 14-18 Mesh Catalyst (Magnification 10X)



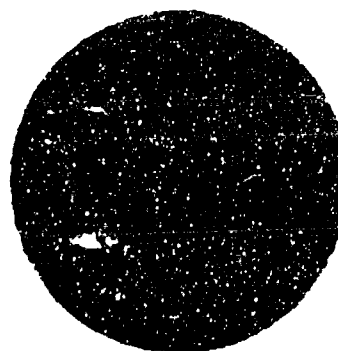
(a) 1 @ 1725 psia



(b) 2 @ 1800 psia
11 < 999 psia



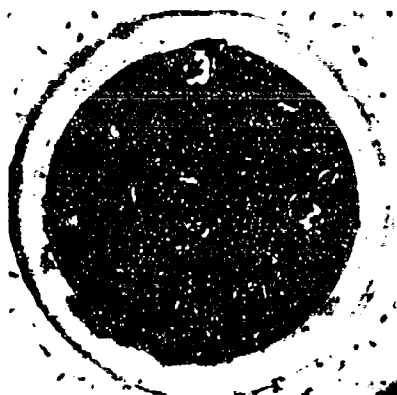
8 ≥ 1500 psia
8 @ 1499-100 psia
11 < 999 psia
(Illustrating Fines)



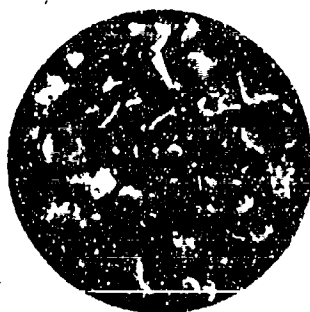
(d) Same as (c)
(Catalyst Remaining in Bed)

Figure 4-10

Post Pop-Shock Appearance of 25-30 Mesh
Catalyst (Magnification 10X)



(a) 21.99 psia



(b) 2 @ 1900 psia,
5 @ 1499-100 psia,
4 <999 psia

of extremely fine particulate. Catalyst remaining in the container covers a wide spectrum of mesh sizes. Numerous particles are observed to have spherical symmetry which strongly suggested that an interaction was present. The post-test appearances of the 25-30 mesh catalyst revealed little degradation on the top portion of the bed. One and possibly two individual particles have fractured, as seen in Figure 4-10b.

Individual particle crush strength measurements were performed at ER&EC on the 25-30 mesh catalyst used in the pop-shock studies. That data, discussed in Section 4.2.3.2.1 revealed variations in mean crush strength without indicating an obvious trend. Pulsed, liquid erosion resistance measurements were obtained in the PLPET apparatus at ER&EC on the 14-18 mesh pop-shock catalyst. These data are discussed in Section 4.2.3.2. Variations in the mean weight loss are noticeable, with a higher mean weight loss for particles that were subjected to intensities above 1500 psia.

4.1.3.2 Hot Gas Thermal Fatigue

Hot gas thermal fatigue cycling revealed some catalyst degradation. The fines generation data are presented in Table 4-11 (14-18 mesh) and Table 4-12 (25-30 mesh). Exposure to a 10% duty cycle (6 sec. on, 54 sec. off) which cycled the catalyst from approximately 300°F to 1500°F produce the same relative amount of degradation for both mesh size catalysts which was independent of the bed pressure drop (to 50 psi) and number of cycles between 100 and 200. The average fines generation was 4.67% for the 14-18 mesh catalyst and 4.52% for the 25-30 mesh catalyst. It was apparent that the same mechanism was responsible for the observed degradation. Pre- and post-test photomicrographs failed to reveal any fractured particles on the top of the catalyst bed. However, the pre- and post-test appearances did reveal considerable catalyst rearrangement as is observed in Figures 4-11 and 4-12.

4.1.3.3 Hot Gas Thermal Aging

The amount of degradation during 600 and 1200 seconds steady-state exposure was similar to that encountered during the hot gas thermal fatigue studies. The thermal aging fines generation data appears in Table 4-13. The level of degradation suggested that the same thermal and pressure crushing mechanisms were responsible for the fines generation in both hot gas thermal fatigue and thermal aging.

4.1.3.4 Liquid Quench Thermal Shock

The LQTS test matrix (Table 4-7) was performed after numerous operational difficulties were resolved. The ammonia injector was sized to produce an equivalent G loading of 0.03 lbs/in²-sec at an injection pressure of 128.8 psia (corresponds to the vapor pressure of saturated liquid at 70°F). Use of the ammonia's vapor pressure to expel the liquid precluded incorporation of auxiliary pressurization manifolds. The injector placement within the upper plenum is illustrated in Figure 4-13.

Table 4-11

Hot Gas Thermal Fatigue Test Results for 14-18 Mesh Catalyst

Bed Pressure Drop, psi	Number of Cycles	Fines Generation		Total Fines, %	Material Balance, %
		14-18	(% Initial) <20>40 18-20		
20	100	93.7	1.1	3.3	98.1
50	100	93.9	0.6	4.0	98.5
50	200	94.0	1.9	3.1	99.0

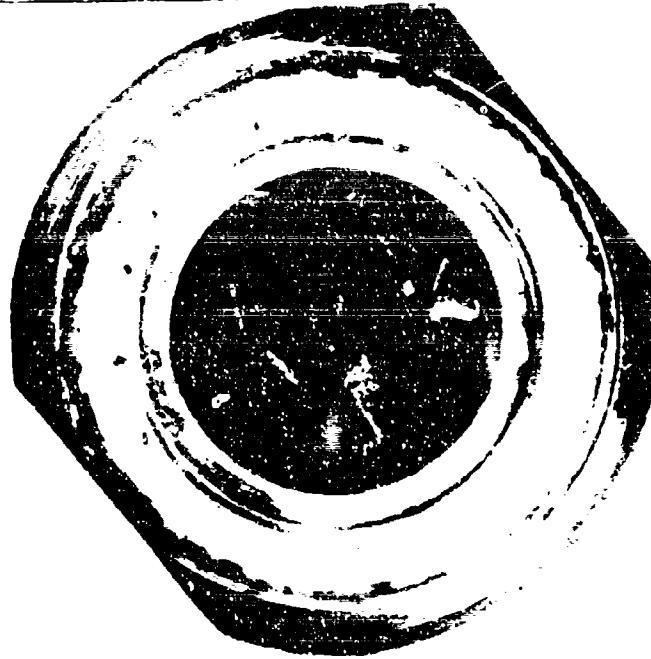
Table 4-12

Hot Gas Thermal Fatigue Test Results for 25-30 Mesh Catalyst

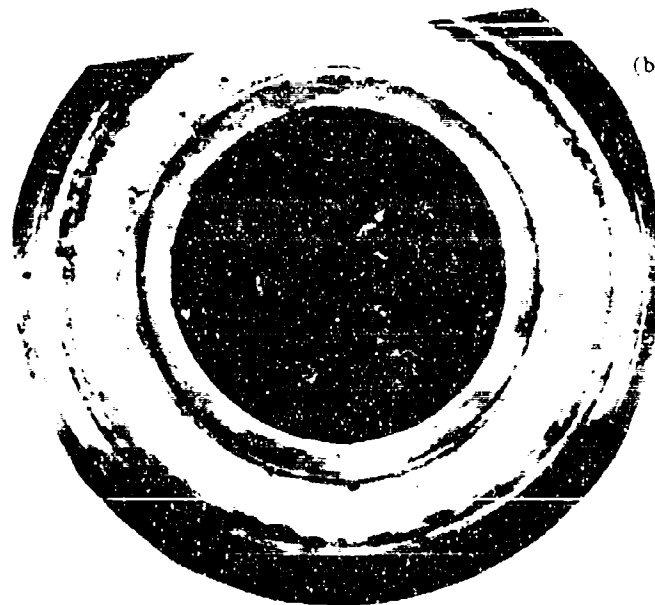
Applied Pressure Drop, psi	Number of Cycles	Fines Generation (% Initial)		Total Fines, %	Material Balance, %
		25-30	30-35 <35>40		
20	100	94.8	2.1	3.0	99.9
50	100	94.1	1.1	4.2	99.4
50	200	95.8	2.8	1.4	100.0

Figure 4-11

Pre- and Post-Test Appearances of 14-18 Mesh Catalyst Subjected to
100 Thermal Fatigue Cycles (Magnification 10X)



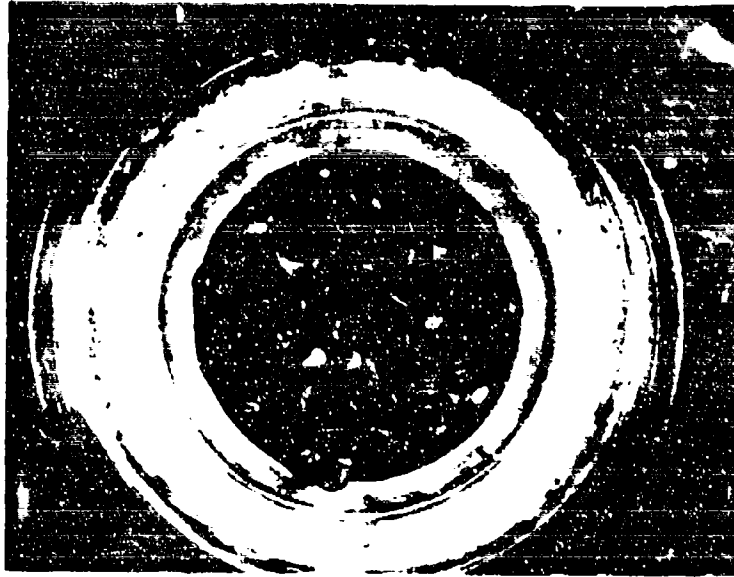
(a) PRE-TEST



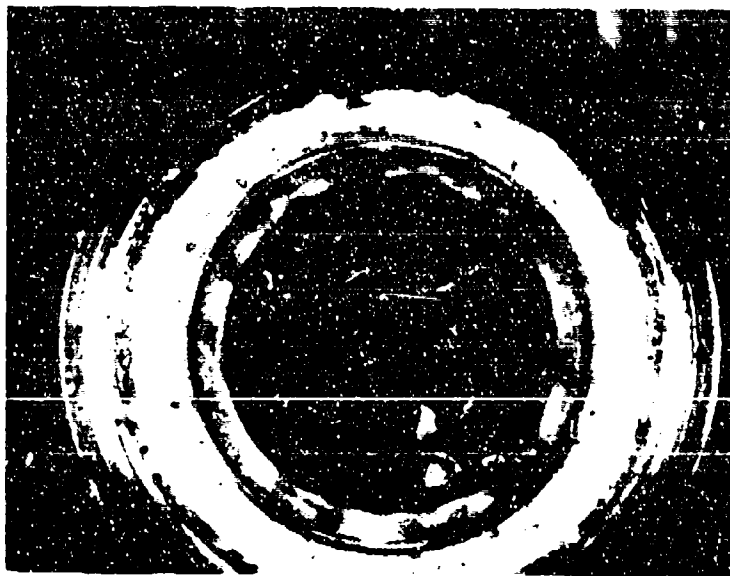
(b) POST-TEST

Figure 4-12

Pre- and Post-Test Appearances of 25-30 Mesh Catalyst Subjected to
100 Thermal Fatigue Cycles (Magnification 10X)



(a) PRE-TEST

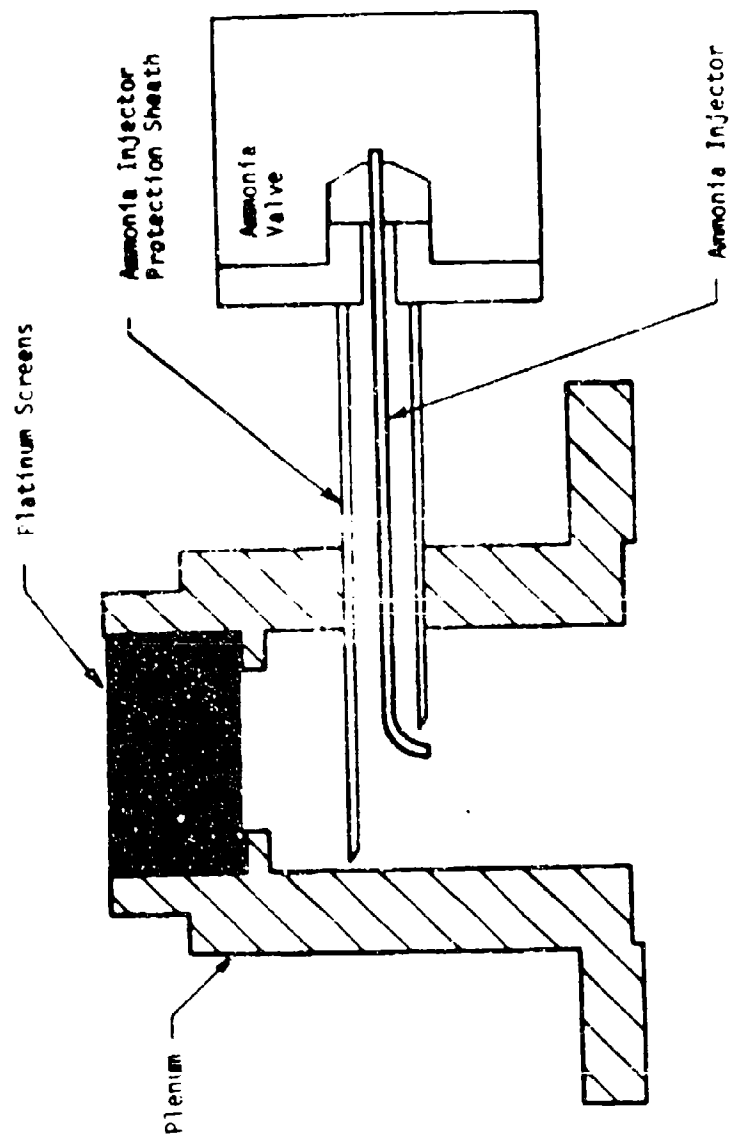


(b) POST-TEST

Table 4-13
Hot Gas Thermal Aging Test Results

Fresh Shell 405 Catalyst Size				
14-18 Mesh Fines Generation (% Initial)		25-30 Mesh Fines Generation (% Initial)		
	600 Sec	1200 Sec		600 Sec
14-18	94.3	94.5	25-30	93.8
18-20	0	0.8	30-35	2.2
<20>40	0	0	<35>40	0
<40	3.7	3.9	<40	4.4
Total Fines, %	3.7	4.7	Total Fines, %	6.6
Material Balance, %	98.0	99.2	Material Balance, %	100.4
				1200 Sec
				94.6
				2.1
				0
				3.3
				5.4
				100.0

Figure 4-13
Injector Geometry for Liquid Quench Thermal Shock Studies



The LQTS test procedure was straight forward; catalyst bed heating to a uniform temperature by the hot decomposition gases, closure of the hydrazine propellant valve, a delay to allow the chamber pressure to reach an approximate zero value and actuation of the liquid ammonia propellant valve. Short quench pulses of 100 to 200 milliseconds were initially used. However, chamber pressure and temperature traces indicated that the ammonia was vaporizing in the injector and only vapor was being expelled. A common soakback problem was identified; too much heat was transferred to the injector during the heat up cycle. This problem was circumvented by cooling a portion of the ammonia injector protection sheath and using longer ammonia valve actuation times (several seconds). Evidence of liquid ammonia expulsion was a sustained chamber pressure during the quench cycle and rapid temperature decreases of the catalyst bed chamber components. Cycles were repeated when the downstream thermocouple probe indicated 100°F or below.

Catalyst beds subjected to 5 and 25 quench cycles were run in the new and thermally fatigued condition; those which had 100 quench cycles were fatigued first; and the 200 quench cycle tests were run with new and thruster used catalyst without any prior fatigue conditioning. Hot gas thermal fatigue cycles prior to LQTS were performed on the catalyst bed in-situ using the LQTS laboratory reactor configuration. LQTS was initiated immediately after the designated number of fatigue cycles were accumulated.

The LQTS data for 14-18 mesh and 25-30 mesh catalysts are shown in Table 4-14 and Table 4-15, respectively. The data for new or new plus fatigue cycles indicate degradation only for the 14-18 mesh catalyst. The fines generation of the 25-30 mesh catalyst was not significantly different than that obtained for hot gas thermal fatigue only (4.6%-100 LQTS, 5.1%-200 LQTS versus 5.2%-100 HGTF, 3.2%-200 HGTF). Data for the 14-18 mesh catalyst project cumulative quench shock degradation above 50 quench cycles. Two hundred thermal fatigue cycles produced about 5% total fines generation, whereas, 200 quench cycles produced 10% total fines generation. The total fines generation as a function of number of quench cycles is shown in Figure 4-14 for both mesh size catalysts.

Individual particle crush strength measurements were made at ER&EC for catalyst subjected to 5 and 25 quench cycles. These test results are discussed in Section 4.2.3.2. All samples exhibited an increase in mean crush strength. However, increases below about 20% of the baseline measurements were not judged to be statistically significant. A rough correlation was apparent between the crush strength increase in the samples of surviving material and the percent fines generation in the LQTS tests. This suggested that at least a part of the mean crush strength increase resulted from a selective removal of the weaker particles during LQTS exposure.

Differences in the behavior of 14-18 mesh and 25-30 mesh catalyst is readily seen by a comparison of the pre and post-test photomicrographs appearing in Figures 4-15 and 4-16, respectively. These catalyst beds were exposed to 200 LQTS cycles. Numerous 14-18 mesh particles in the top portion of the bed fractured, whereas, fracturing of the 25-30 mesh particles was not observed. The fines generation data for the used catalyst subjected

Table 4-14

Liquid Quench Thermal Shock Data for 14-18 Mesh Catalyst

Identification	Catalyst Condition	No. Quench Cycles	Fines Generation (%)		Total Fines, %	Material Balance, %
			14-18	18-20 <20>40		
Lots 1	New	5	96.5	0	3.1	99.6
Lots 2	New	25	94.6	0	3.7	98.3
Lots 3	Fatigued*	5	95.1	0	3.0	98.1
Lots 4	Fatigued	25	97.3	1.7	4.6	101.9
Lots 11	Fatigued	100	90.4	2.2	7.8	98.1
F3	New	200	89.8	2.6	10.2	100.0
Lots 13	Used** Upper Bed	200	40.5	57.4	58.4	98.8
Lots 15	Used Lower Bed	200	39.3	42.7	55.9	95.2

*Fatigues -- 100 Thermal Fatigue Cycles Prior to Quench Cycles

**Used -- 566 Cold Starts (70°F); 210, 098 Pulses; 2,646 Second Steady-State; 431 Pounds Propellant Thruput

Average material balance = 98.75%

Standard deviation = 1.92%

Table 4-15

Liquid Quench Thermal Shock Data for 25-30 Mesh Catalyst

<u>Identification</u>	<u>Catalyst Condition</u>	<u>No. Quench Cycles</u>	<u>Fines Generation (% Initial)</u>			<u>Total Fines, %</u>	<u>Material Balance, %</u>
			<u>25-30</u>	<u>30-35</u>	<u><35>40</u>		
Lots 5	New	5	97.6	1.0	0	2.2	99.8
Lots 6	New	25	94.8	2.5	0	5.0	99.8
Lots 7	Fatigued*	5	95.2	2.2	0	3.9	99.1
Lots 8	Fatigued	25	94.6	3.3	0	5.8	100.4
Lots 12	Fatigued	100	95.7	0.4	0.7	4.6	100.3
F4	New	200	95.4	2.6	0.3	5.1	100.5
Lots 14	Used** Upper Bed	200	88.8	10.6	0.6	11.2	100.0
Lots 16	Used Lower Bed	200	88.2	7.5	2.6	11.8	100.0

*Fatigued — 100 Thermal Fatigue Cycles Prior to Quench Cycles.

**Used — 566 Cold Starts (70°F); 210, 098 Pulses; 2,646 Seconds Steady-State; 431 Pounds Propellant Thruput.

Average material balance = 99.99%

Standard deviation = 0.45%

Figure 4-14

Cumulative Fines Generation for Liquid Quench Thermal Shock

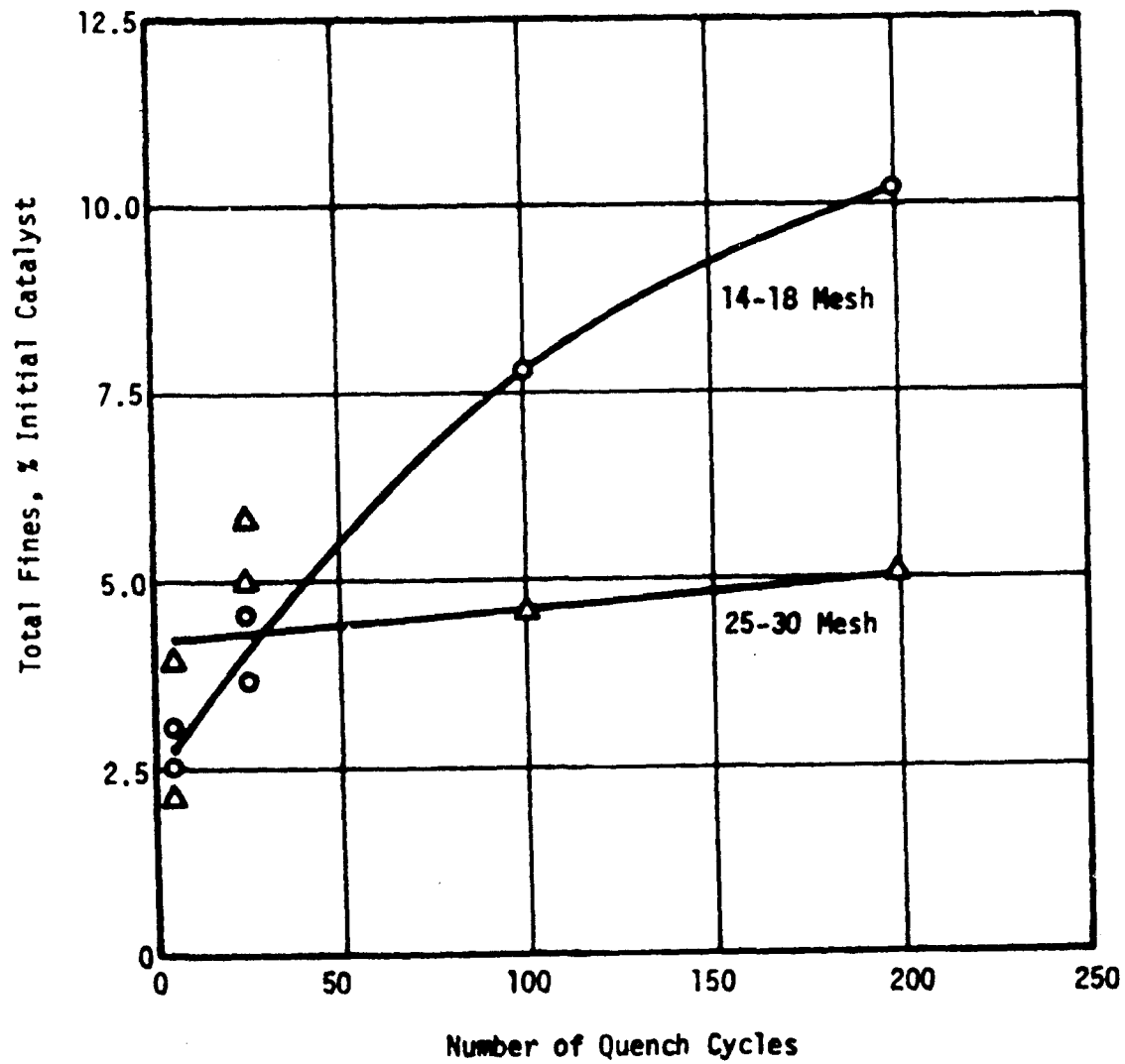
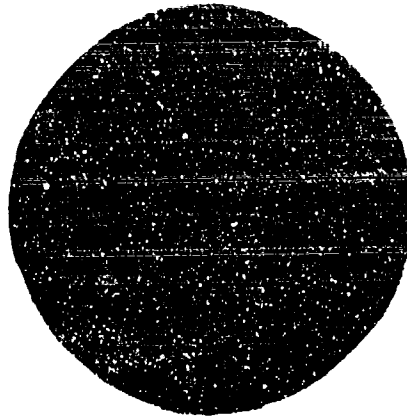
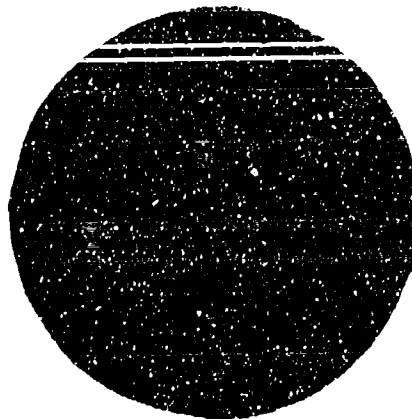


Figure 4-15

Pre and Post-test Appearance of 14-18 Mesh Catalyst Subjected to
200 LOTS Catalytic Conversion (10X)



(a) PRE-TEST



(b) POST-TEST



Figure 4-16

Pre and Post-Test Appearance of 25-30
Mesh Catalytic Subjected to 200 LOTS Cycles (Magnification 10X)

(a) PRE-TEST



(b) POST-TEST

to 200 LQTS cycles should be viewed with some scrutiny. The original catalyst was nominal 18-20 mesh. The post-thruster test separation revealed that some catalyst was within the 14-18 mesh range with a bias towards the 18 mesh size. The amount of fines generation reported as 18-20 most likely resulted from very small geometrical changes during the LQTS exposure. A significant finding was the large difference in less than 40 mesh fines for the upper and lower portions of the original thruster bed. Particles in the upper portion of the bed experienced direct hydrazine impingement during thruster firings. Those particles which remained in the 14-18 mesh size category were most likely the strongest particles in the upper bed. Particles from the lower bed experienced the most pressure crushing forces. A weakening of these particles would result in a higher degree of degradation from the quench shock environment. A similar trend is noticed for the 25-30 mesh catalyst which had fractured from the thruster exposure. The overall level of degradation, however, is significantly different from the 14-18 mesh catalyst. These observations are in good correlation with the LQTS data for new catalyst.

4.1.3.5 Void-Volume Abrasion

The Void-Volume Abrasion test data (Table 4-16) did not indicate a high sensitivity to the tests performed. Statistical significance could not be placed on the relative amount of fines generation. A comparison of the pre and post-test appearances revealed that particle rearrangement and/or movement took place. These photographs are shown in Figures 4-17 and 4-18 for 14-18 mesh and 25-30 mesh catalyst, respectively. Several factors may have prevented the measurement of any significant abrasion:

- Recirculation effects over the top portion of the bed may have been insufficient to cause a superficial exit velocity to be below the particles terminal settling velocity.
- Geometrical size factors and void volume percentages may have prevented free movement.
- The inlet gas velocity may have been too low to notice abrasion within the time period studied.

4.1.3.6 Cold Gas Pressure Crushing

Each catalyst mesh size was subjected to 200 cold gas cycles using dry filtered nitrogen at inlet pressures sufficient to cause a bed pressure drop of approximately 50 psi. The LQTS apparatus was used with the decomposition device removed. The results, shown on the following page, revealed negligible degradation.

Table 4-16

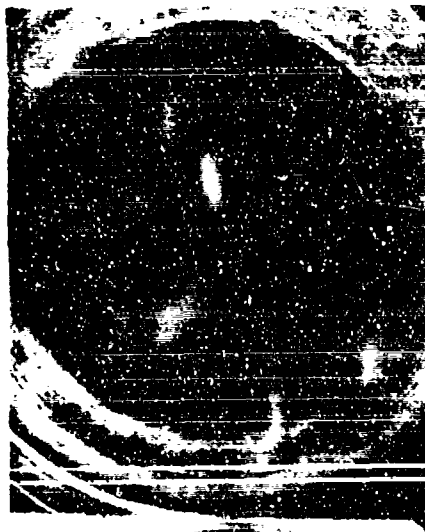
Void-Volume Abrasion Test Data

CATALYST SIZE	SEPARATION CATEGORY	G LOADING = 0.01 lb/sec-in ²		G LOADING = 0.015 lb/sec-in ²
14-18		10% VOID	20% VOID	20% VOID
	14-18	= 98.1	98.4	94.7
	18-20	= 0	0	0
	<20>40	= 0	0	0.5
	<40	= 0.8	1.6	3.8
	Fines, %	= 0.8	1.6	4.3
	Mat'l Balance, %	= 98.9	100.0	99.0
25-30		93.6	92.9	95.1
	25-30	=		
	30-35	= 2.7	4.0	1.0
	<35>40	= 0	0	0
	<40	= 3.2	2.7	2.7
	Fines, %	= 5.9	6.7	3.7
	Mat'l Balance, %	= 99.5	99.6	98.8

Figure 4-17

Pre and Post-Test Appearances of 14-18 Mesh Subjected
to Void-Volume Abrasion (Magnification 10X)

(a) PRE-TEST

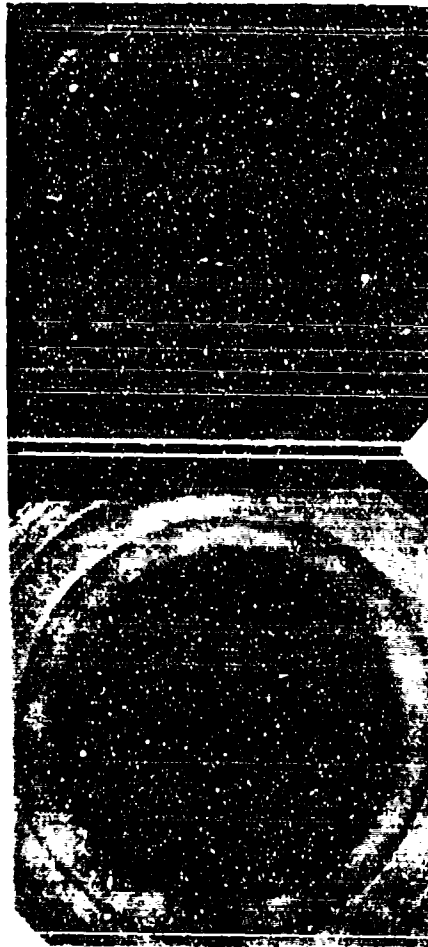


(b) POST-TEST

Figure 4-18

Pre and Post-Test Appearances of 25-30 Mesh Catalyst Subject
to Void-Volume Abrasion (Magnification 10X)

(a) PRE-TEST



(b) POST-TEST

<u>14-18 Mesh Catalyst</u>		<u>25-30 Mesh Catalyst</u>	
14-18	98.5	25-30	97.5
18-20	1.2	31-35	2.1
<20>40	0.2	<35>40	0
<40	0.7	<40	0.5
Total Fines, %	2.2	Total Fines, %	2.6
Material Balance, %	100.6	Material Balance, %	100.1

4.1.3.7 Isothermal Catalyst Activity Reactor

A limited number of tests were performed by immersing catalyst in liquid hydrazine at 40°F. These tests were undertaken in order to provide information for the Interaction Study II matrix. No attempt was made to quantify all the possible immersion test variables. Fourteen-eighteen mesh catalyst from three separate lots was prescreened and separated into six batches, each batch consisting of 100 particles. One batch from each lot was consecutively immersed ten times in hydrazine maintained at 40°F. Each immersion cycle was of thirty seconds duration every five minutes. The liquid hydrazine was kept at the desired temperature by a water and ice cooled jacket. A screened holder contained the catalyst which allowed vigorous agitation while the catalyst was immersed. The hydrazine bath was protected by a blanket of gaseous nitrogen. The catalyst was subjected to a high rate gaseous nitrogen purge immediately upon removal from the hydrazine bath and prior to reimmersion. The catalyst was inspected under a microscope following all testing to determine the number of broken particles. The three tested samples and the three unexposed samples were sent to Exxon Research and Engineering Company for post and fresh mean crush strength testing. Results are discussed in Section 4.2.3.2. The immersion and strength test results are compared in Table 4-17. No correlation was observed between the fresh particle crush strength and the percent which fractured as a result of liquid immersion. A rough correlation was observed between the number of particles which fractured during immersion testing and the post-test mean crush strength. The meaning of this correlation was not apparent. These results, however, indicate that internal pore pressure buildup resulting from liquid exposure is a major breakup mechanism, corroborating extensive test data on the internal catalyst breakup phenomena made available by UTRL (110).

4.1.4 Output Data Correlation

This section presents a definitive analysis of the Selected Mechanism Test Results. Mechanisms responsible for the observed degradation are identified, described and compared to the analytical predictions, synergisms are deduced from the parametric Interaction Study Matrices, and the extent of degradation anticipated during engine operation is discussed. Methods that may be employed to inhibit catalyst breakup are suggested.

Table 4-17

Isothermal Catalyst Activity Reactor Test Results

	LOT A			LOT B			LOT C		
	% Fractured	\bar{L} , (1) lbs.	S, (2) lbs.	% Fractured	\bar{L} , lbs.	S, lbs.	% Fractured	\bar{L} lbs.	S, lbs.
Immersed	27	1.056	0.58	30	1.147	0.60	49	1.219	0.67
Fresh Shell 405	--	1.611	0.76	--	1.331	0.74	--	1.901	0.68

(1) \bar{L} = mean crush strength

(2) S = standard deviation

4.1.4.1 Mechanism Analysis

4.1.4.1.1 Pressure Crushing

Catalyst degradation from the forces generated by flowing gas was experimentally verified as a major breakup mechanism. The mechanism caused localized and gross catalyst failure which depended on the magnitude of the force developed by the flowing gas. The pressure crushing mechanism manifests itself by brittle fracture due to stresses created at the particle-to-particle contact points. The irregular particle shape causes a wide range of stress distribution at the contact points of catalyst in a bed. Localized failure occurs at very low bed pressure drops due to the nature of contact point stress distributions. A sharp contact (small contact area) or areas of the catalyst surface which are below a mean strength level will fail at a stress loading which is considerably below a bulk value. Localized failures produce very small fines. An equilibrium situation is reached when the contact area has increased to a value where the catalyst can now support the pressure loading. The localized failure mode due to pressure loading should occur early in the catalyst bed life with little to no further degradation in the absence of other factors. This aspect was supported by the fines generation data for cold gas pressure crushing, hot gas thermal fatigue and thermal aging.

The stress levels generated by large pressure drops, as in the case of pop-shock, causes localized and gross failures. Gross failures are identified with the complete fracturing of an entire particle. The process by which this occurs begins much in the same way as for localized failure. Small fines are initially produced at the contact points in order to relieve the stress. The increase in bearing area is insufficient to support the load, fines become trapped between the contact points and a crack is initiated at the surface. The alumina substrate cannot deform plastically to blunt the crack tip and fracture proceeds throughout the particle. Each subsequent high level loading would appear to have the same effect as the first one. Catalyst in the bed is no longer in a preferred position and fines generation will continue as long as gross fracturing occurs.

Observations of the post-test catalyst bed condition from cold gas pressure crushing, hot gas thermal fatigue, thermal aging and pop-shock revealed a phenomena which has not been reported. The relative degree of post-test bed compaction for the four test series is listed below:

<u>Test Series</u>	<u>Bed Compaction</u>
Hot Gas Cycling (Thermal Fatigue)	Tightest
Cold Gas Cycling (Pressure Crushing)	Moderately tight
Constant Hot Gas Exposure (Thermal Aging)	Moderately loose
Pop-Shock, low level	Moderately loose
Pop-Shock, high level	Loose

The degree of bed compaction has been identified with a preferred reorientation mechanism. Loosely packed catalyst at the beginning of a test will have a tendency to orient itself under the presence of disturbing forces. Cyclic operation allows multiple relaxations to occur within the bed. The catalyst bed achieves a high degree of preferred reorientation during low stress level, cyclic operation. (The thermally cycled beds achieved a higher degree of compaction than the cold gas cycled beds which indicated a thermal influence). Preferred reorientation during steady-state operation would appear to occur only when the localized pressure induced perturbations can overcome the inter-particle frictional forces. The magnitude of these perturbations depends on the relative chamber pressure roughness, but will in any event be smaller than that for cyclic relaxations. Low level pop-shock bed compaction was similar to that for thermal aging. Preferred reorientation was only partial, as the larger amount of fines generation and fractured particles caused constant interruptions in the reorientation process. High level pop-shock tests destroyed any tendency of the bed reorientation process by constantly fracturing individual catalyst particles.)

The analytical modeling predictions were strongly supported by the selected mechanism test results in the area of pressure crushing. Localized failures were predicted at very low bed pressure drops (about 5 psi). Although tests were not performed at these low levels, it is entirely conceivable that breakup could occur due to the wide stress distributions encountered in a catalyst bed. The most significant correlation between analytical modeling and experimental effort was in the area of dynamic pressure crushing, i.e., pop-shock. An analysis of the shock wave dynamics indicated that the catalyst bed would act to establish a pressure differential prior to the full impact of maximum shock intensity in a catalytic engine environment. Catalyst degradation was predicted to increase with the level of established pressure drop. The pop-shock test data were in complete agreement with the analytical predictions. The catalyst bed response was much faster than the generated pressure wave. A pressure drop was established at the onset of the simulated overpressure ignition spike. Damage to the catalyst bed increased with increasing pressure drop. Dynamic pressure crushing was fully equivalent to pressure effects encountered during the steady-state flow of gases.

4.1.4.1.2 Thermally Induced Phenomena

Three types of thermally induced phenomena were present during the selected mechanism tests:

1. Thermal shock during hot gas heatup
2. Thermal shock during liquid quench cooldown
3. Particle-to-particle crushing from differential thermal expansion effects

Hot gas thermal shock was identified as an insignificant breakup mechanism during the phenomenological survey. The heat transfer rates were calculated to be insufficient to cause breakup. The effect of fatigue cycling was, therefore, investigated. The hot gas thermal fatigue data revealed that the catalyst was immune to fatigue and subsequent breakup for at least 200 cycles of 6 seconds duration each. The thermal fatigue and thermal aging data taken as a whole suggested that the effects of hot gas exposure either in a cyclic or steady-state mode would not degrade the catalyst for extended exposure times typically of several thousand pulses or seconds of steady-state. The hot gas thermal phenomena data did not indicate significant particle-to-particle crushing from due to thermal expansion differences between the catalyst and catalyst bed container. Thermal expansion difference effects are highly singular to the thrust chamber design and the absence or possible presence of this mechanism cannot be inferred from the present data for other user design applications.

The thermal shock effects during liquid quench cooldown were analytically modeled using the best available heat transfer analogy. This was classified as a borderline breakup mechanism. The liquid quench thermal shock data supported the analytical predictions: new catalyst should be relatively unaffected, whereas, thruster exposed catalyst should experience modest degradation depending on the relative decrease in strength.

The liquid quench thermal shock tests provided an insight into the boiling heat transfer mode. The thermally induced stresses required to effect breakup in a boiling heat transfer regime must come from high rates of heat transfer. These rates can be achieved only in the nucleate boiling regime. The time period in which the maximum tensile stress would be developed on the catalyst surface was predicted to be ten milliseconds after quench initiation. The quench shock test data revealed degradation above that observed for thermal fatigue. Pressure crushing forces were minimal during the quench cycle. These factors strongly suggest that nucleate boiling was present and persisted over a time period sufficient to generate thermal stresses at or close to the failure level. The transition from nucleate to film boiling would have occurred after the time period during which the maximum stresses were generated. The nucleate boiling heat transfer coefficients would appear to be higher than that which was approximated for the analytical model.

4.1.4.1.3 Voided Bed Abrasion

Sensitivity tests performed during the mechanism assessment phase indicated that abrasion from particle movement was a significant factor in the overall catalyst degradation. Selected mechanism tests with pre-voided bed volumes of 10% and 20% did not indicate a statistically

significant contribution to degradation as measured by fines production. Test results from the particle-to-particle abrasion resistance apparatus (see Section 4.2.2) revealed that a two hour test at ambient temperature resulted in the generation of 14.6% fines at a superficial inlet nitrogen gas velocity of 250 ft/sec and 2.4% fines at an inlet velocity of 160 ft/sec (data are for 14-18 mesh catalyst). The laboratory reactor was operated at a G loading of .015 lbs./in²/sec; the gas temperature was approximately 1600°F. The gas velocity corresponding to this G loading and temperature at an ammonia dissociation fraction of 0.5 and chamber pressure of 200 psia is 18.4 ft/sec. A typical five pound thruster operating at a G loading of 0.03 lbs./in²-sec and chamber pressure of 100 psia with similar gas composition and temperature would have a chamber gas velocity of 70 ft/sec. Although the velocity in the void-volume abrasion tests was close to the terminal settling velocity, significant G loading increases would have to be made in order to approach velocities where abrasion could be measurable in a reasonable test time.

One series of the pop-shock tests indicated that void-volume abrasion took place. A large void was formed, fines were observed on the upper bed container flange, numerous particles had spherical symmetry. It is now apparent that a violent fluidization process occurred once the bed became voided. The equivalent G loading during a large spike is difficult to estimate. That G loading could have been between one and two orders of magnitude over the nominal value. The violent disturbance caused particles to be accelerated with subsequent impact with other particles and the container restraining surfaces.

All of the voided bed abrasion results show that situations are possible wherein the abrasion mechanism can be a major degradation factor once a catalyst bed has become voided from other causes.

4.1.4.2 Catalyst Size Effects

The question of which mesh size catalyst is better able to withstand the hydrazine thruster environment has been debated since the inception of catalytic engines. The present study has indicated that the degree of varying mesh size catalyst breakup is a strong mechanistic function. Statistical differences in breakup were noticed for the mechanisms dynamic pressure crushing (pop-shock) and liquid quench thermal shock. Comparative pop-shock data are listed below:

Cumulative Damage After 7 Pops at a Bed Pressure Drops \geq 150 psi Fines Generation, % Initial		Mesh Size
35		14-18
11.5		25-30

Best Available Copy

Best Available Copy

This behavior suggests that the irregular catalyst shape prevents the 14-18 mesh from achieving a preferred bed packing. Under situations of high pressure loading, 14-18 mesh catalyst is subjected to higher stress per contact point than is the 25-30 mesh catalyst. There is no implication in the data that the 14-18 mesh catalyst is inherently weaker than is the 25-30 mesh catalyst.

The liquid quench thermal shock data (Figure 4-14) are again statistically different for 14-18 and 25-30 mesh catalyst. Ten percent fines generation (14-18) versus 5% for the 25-30 mesh after 200 quench cycles. The 5% fines generation for 25-30 mesh was nominal degradation in the absence of LQTS, i.e., hot gas thermal fatigue. This difference, once more, does not involve any inherent weakness in the catalyst size; but, rather the thermal stresses generated during quench cycling are greater for the 14-18 mesh by virtue of the larger mean diameter. This aspect was predicted by the analytical modeling effort.

4.1.4.3 Complex Phenomena

4.1.4.3.1 Interaction Study I

A summary of results for Interaction Study I is shown in Table 4-18. All of the breakup levels are quite low, however, exposure to high temperature gases appears to be slightly deleterious. Although the magnitude of the effects shown in Table 4-18 are not large, from a statistical point of view there is an interaction in the data, as the average effect of going from "no flowing gas" to "flowing gas" increased the % fines 5.1% in the absence of a bed pressure load, and only 2.2% in the presence of a bed pressure load. More important, however, is the potentially dangerous effect that was identified for exposure to high temperature flowing gas and abnormal or pop-shock bed pressure loads IN a voided bed. The rate of fines generated for 14-18 mesh with repeated pop-shock (first derivative) increased abruptly between 2 and 4 "pops" above a bed pressure drop of 180 psi. A pure pressure crushing mechanism would be expected to produce a monotonic increasing functional relationship between fines generation and successive loads. Post-test observations of the bed, i.e., spherically symmetric catalyst and particulate forced upwards, indicated that a void-volume abrasion interaction was present. No interaction was found at lesser bed loadings. It is doubtful that the sum of void-volume abrasion and pressure crushing, taken singularly, could account for the extensive damage. A similar interaction for 25-30 mesh catalyst was not noticed, however, the occurrence should not be ruled out at higher bed loadings after a voided condition exists.

4.1.4.3.2 Interaction Study II

A summary of results of Interaction Study II for 14-18 Mesh catalyst is shown in Table 4-19. The deleterious effect of exposure to liquid hydrazine is clearly evident. Selected mechanism test results did not reveal synergisms present in the Interaction Study II matrix. The

Table 4-18

Summary of Results For Interaction Study I

Is Catalyst Exposed To High Temperature Flowing Gas	Total % Fines			
	Is Catalyst Exposed To Repeated Bed Pressure Loads?			
	NO		YES	
NO	14-18 Mesh	25-30 Mesh	14-18 Mesh	25-30 Mesh
	Fresh Shell 405	Fresh Shell 405	2.2%	2.6%
	4.2% (a)	6.0% (a)	4.7% (a)	4.4% (a)
YES				

(a) Average of all data obtained.

Table 4-19

Summary of Results of Interaction Study II For 14-18 Mesh Catalysts

Is Catalyst Exposed To Thermal Fatigue Heat Up Cycling?	Total % Fines	
	NO	YES
NO	Fresh Shell 405	35% (a)
YES	4.7%	30.5% (b)

(a) Average isothermal activity reactor results.

(b) Average of TRW XMRE 5 lbf thruster results for top screen and upper bed.

areas where synergisms may be present are in actual thruster firings. Catalyst recovered from a TRW XMRE-5 five pound thruster (cf. Section 4.1.2.3.4) was separated into three bed position lots and separated into surviving mesh sizes. That data is shown in Table 4-20. A comparison of the selected mechanism test results with that of the thruster exposed catalyst clearly indicate two distinctive factors.

1. Catalyst below top screen and upper bed have fines generation significantly in excess of the lower bed largely indicating an effect of the presence of liquid hydrazine.
2. Rough correlation between hot gas thermal aging, hot gas thermal fatigue fines generation with that of the lower bed catalyst.

4.1.4.4 Parametric Degradation and Inhibition Criteria

The selected mechanism test results have been categorically sorted by a deductive rejection method. The absence of normal operating synergisms allows each test series to be broken up into degradation by additive mechanisms. The relative degradation percentages may be used as a guide to implement methods for reducing catalyst degradation.

Pressure Crushing (Normal) Only

Test Data: Cold Gas Flow Degradation = 2.4%
 ≈50 psi bed drop
 200 cycles

Extrapolation: 50 psi bed drop Degradation, little change
 200 + cycles

Reasoning: Degradation established early in life. Monotonic
 decreasing function to asymptote

Extrapolation: 100 psi bed drop Degradation, 10%
 200 + cycles

Extrapolation: 125 + psi bed drop Degradation, >20%
 20 + cycles

Reasoning: Degradation constant. Bed cannot relax to relieve
 stress generation. Based on pop shock data.

Table 4-20

Engine Exposed Catalyst Degradation

AREA OF RECOVERED CATALYST

	1		2	
	Below Top Screen % Recovered		Upper Bed % Recovered	
			Lower Bed % Recovered	
14-18	3.6	72.1	7.6	5.5
18-20	68.5		59.5	83.6
20-25		7.3	12.9	3.5
25-30		3.7	8.3	1.4
30-35		2.4	4.4	0.7
<35		14.5	7.4	5.3
Total		27.9	33.0	10.9

Pressure Crushing (Abnormal)

Ignition overpressure spikes must be eliminated to prevent disastrous bed damage. Severe interaction possible in voided bed.

Thermal Effects Only

Test Data:	Hot Gas Flow	Degradation 3%
	50 psi bed drop	
	200 cycles or	
	1200 seconds steady-state	
Extrapolation:	10^5 cycles	Degradation, little change
	10^4 seconds steady-state	
Reasoning:	Degradation established early in life Monotonic decreasing function to asymptote.	
Test Data:	Liquid Quench Thermal Shock	Degradation, increasing with
	200 cycles	repeated thruster exposure
Extrapolation:	10^5 cycles	5 max
Reasoning:	LQTS tests more severe than in actual practice. Hydrazine impingement on hot bed would most likely not cause severe quench shock. Decomposition energy release would force film binding.	

Breakup due to differences in catalyst and chamber wall coefficients was not noticed in the present study, although analytical predictions indicate this factor should be carefully considered in engine design criteria.

In the absence of synergistic effects or situations where a catalyst bed has been degraded by gross voiding, hydrazine imbibition or other non catalyst failures, results of these selected mechanism tests indicate that catalyst breakup over long lifetimes should not exceed 15% by the combined results of external breakup mechanisms. The effects of hydrazine imbibition and the wetting phenomenon has long been witnessed as severely degraded catalyst beds. A partial understanding of these phenomena has just recently been obtained. At the present point in time, the state-of-the-art is not complete enough to make predictions as to the relative failure rates or amounts that could be experienced in actual engine operation. The empirical data available on catalyst degradation is a very strong function of the particular engine designer's philosophy. However, the analytical and experimental work to date (100,110) have revealed a new understanding of the complex phenomena that may be used as a catalyst breakup inhibition.

4.2 Studies Carried Out By Exxon Research and Engineering Company

4.2.1 Bed Static Pressure Crushing

Results from both pressure crushing tests with individual catalyst particles and analytical modeling calculations indicated that static pressure crushing is a significant catalyst breakup mechanism. Thus, experimental pressure crushing studies were extended from tests with individual particles to tests involving the static pressure crushing of a small bed of granular catalyst. Data was obtained on all the standard mesh sizes of fresh Shell 405 i.e. 8 to 12, 14 to 18, 20 to 25, 25 to 30 and 20 to 30 mesh. For the latter three mesh sizes the data was obtained using the Pressure Crushing Mini-Bed (PCMB) with a bed diameter of 0.25 inches shown in a schematic in Figure 4-19. For these mesh sizes this apparatus provides a ratio of bed diameter to particle diameter ranging from approximately 8 to 10. Sufficient catalyst was employed to yield bed depths ranging from 3/4 to 1 inch, which resulted in ratios of bed length to bed diameter ranging from 3 to 4. For 8 to 12 and 14 to 18 mesh size material a PCMB with a diameter of 0.50 inches (twice the previous diameter) was employed with a bed depth of approximately 0.60 inches. The PCMB was axially loaded in compression using the Instron Instrument (ITI).

The following procedure was adopted in obtaining the data. The fresh Shell 405 catalyst was first screened and any material outside the cited mesh size was rejected. Approximately 1.0 to 2.5 g of proper mesh size catalyst was charged to the reactor, and the reactor tapped until the bed settled to a constant volume. The movable upper assembly was placed in the PCMB and a sequential series of measurements was made with the same sample at progressively higher bed pressures. In general, a series of runs were made at bed pressures of approximately 25, 50, 100, 200 and 350. In the sequential run series the bed is loaded to the lowest bed pressure first and then held under this load for 20 minutes. The load is removed and the bed contents screened and the weight of the resultant fractions determined. The reactor is then repacked with the surviving original mesh size material and tapped to constant volume. The PCMB is first loaded to the initial pressure load and held for ten minutes, then loaded to the second highest bed pressure and held there for 20 minutes. The load is then removed and the bed contents screened and weighed. As the surviving bed material is subjected to higher and higher pressures, it is always loaded in sequence to the previous loads employed and held at these loads for 10 minutes prior to a 20 minute loading time at the higher pressure. Detailed data obtained from the sequential runs are shown in the appendix.

The product from each pressure crushing measurement was characterized as to its size distribution by sieving through progressively smaller sieve openings down to a through 35 mesh size. Material balances were also calculated for each mesh size separation. Excellent material balances were obtained. Results are shown for both individual loading pressure results, and also on a cumulative basis for the sequence of pressures employed. In several instances replicate run sequences were made. Agreement of results, in general, was good. In Figures 4-20 to 4-26 are plotted the cumulative weight percentage of fresh Shell 405 through various mesh sizes for the pressures employed. The exponential increase in the weight of material through a given mesh size as pressure is increased is characteristic of the general experience with catalysts under pressure loading.

Figure 4-19

Pressure Crushing Mini-Bed (PCMB)

Used For Testing Catalysts Less Than 20 Mesh Size

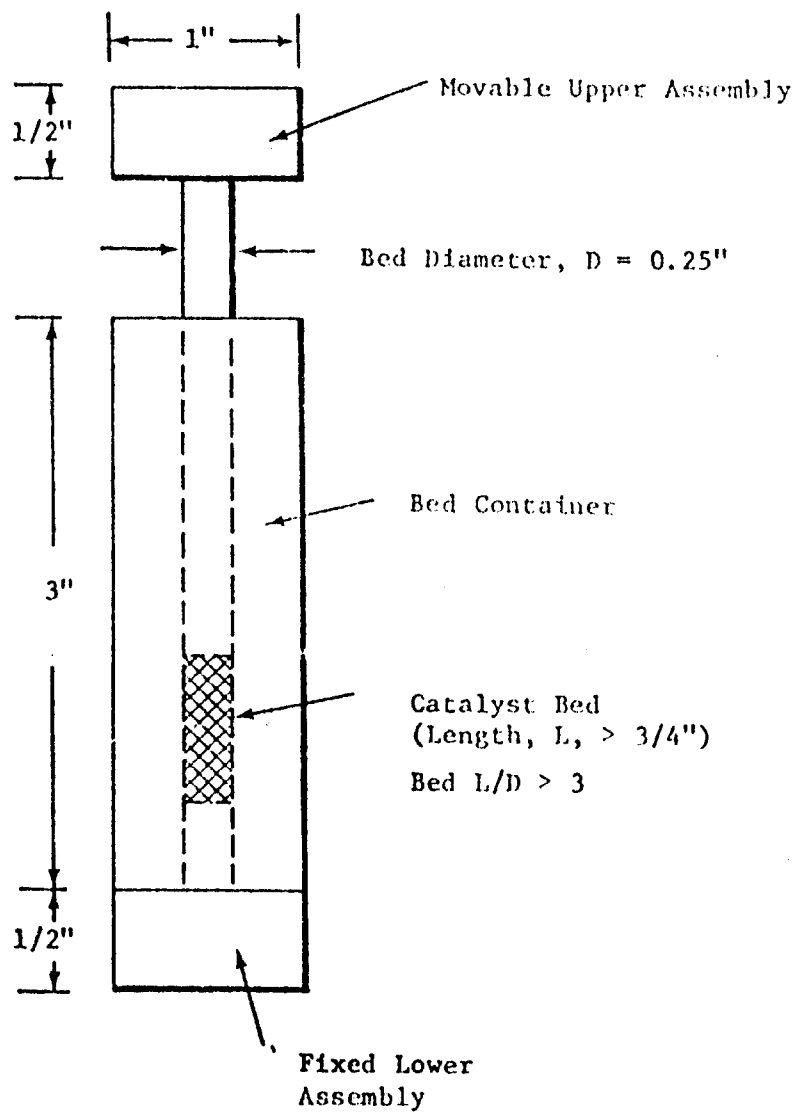


Figure 4-20

Sequential Mini-Bed Crushing of 8-12 Mesh Fresh Shell 405 Catalyst

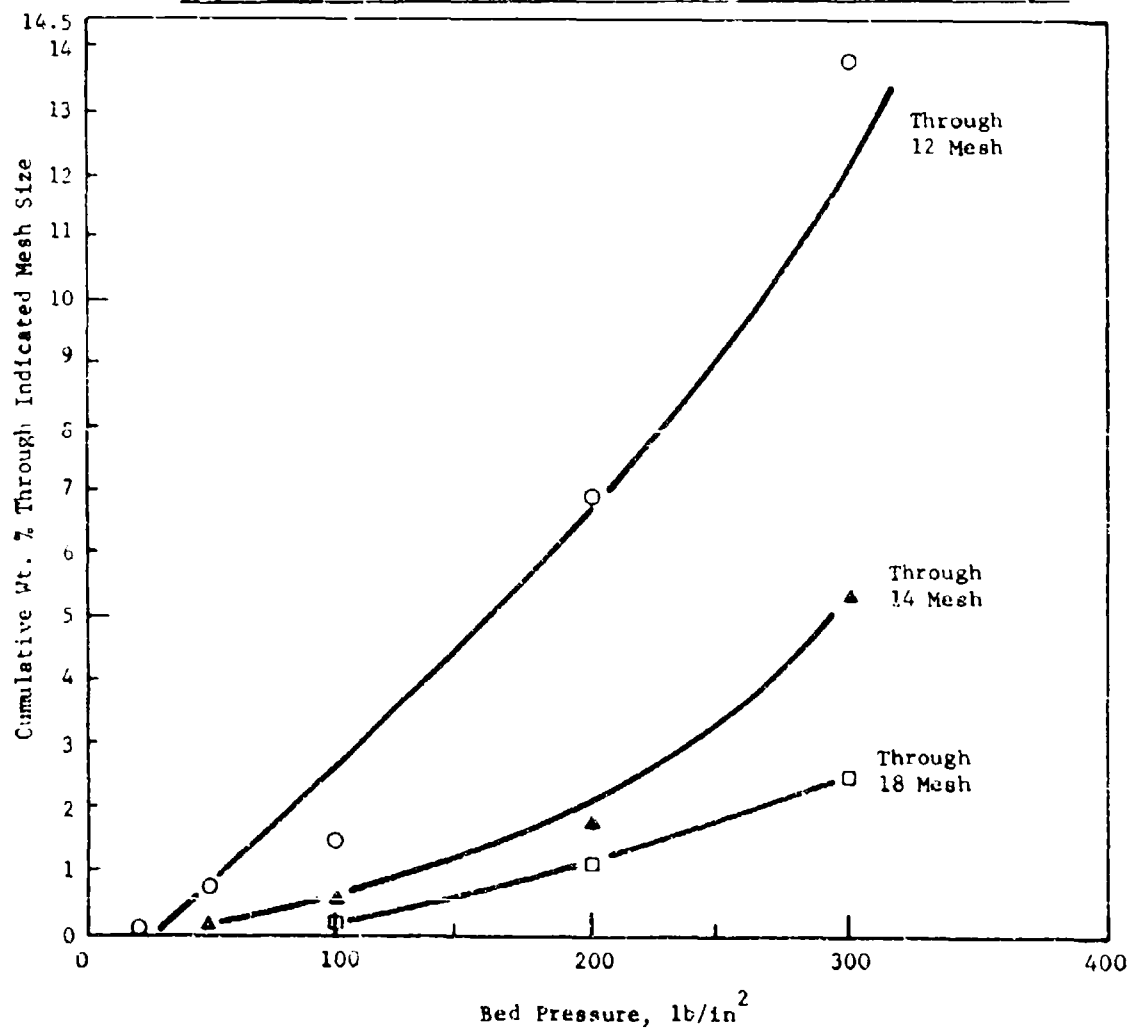


Figure 4-21

Sequential Mini-Bed Crushing of 8-12 Mesh Fresh Shell 405 Catalyst

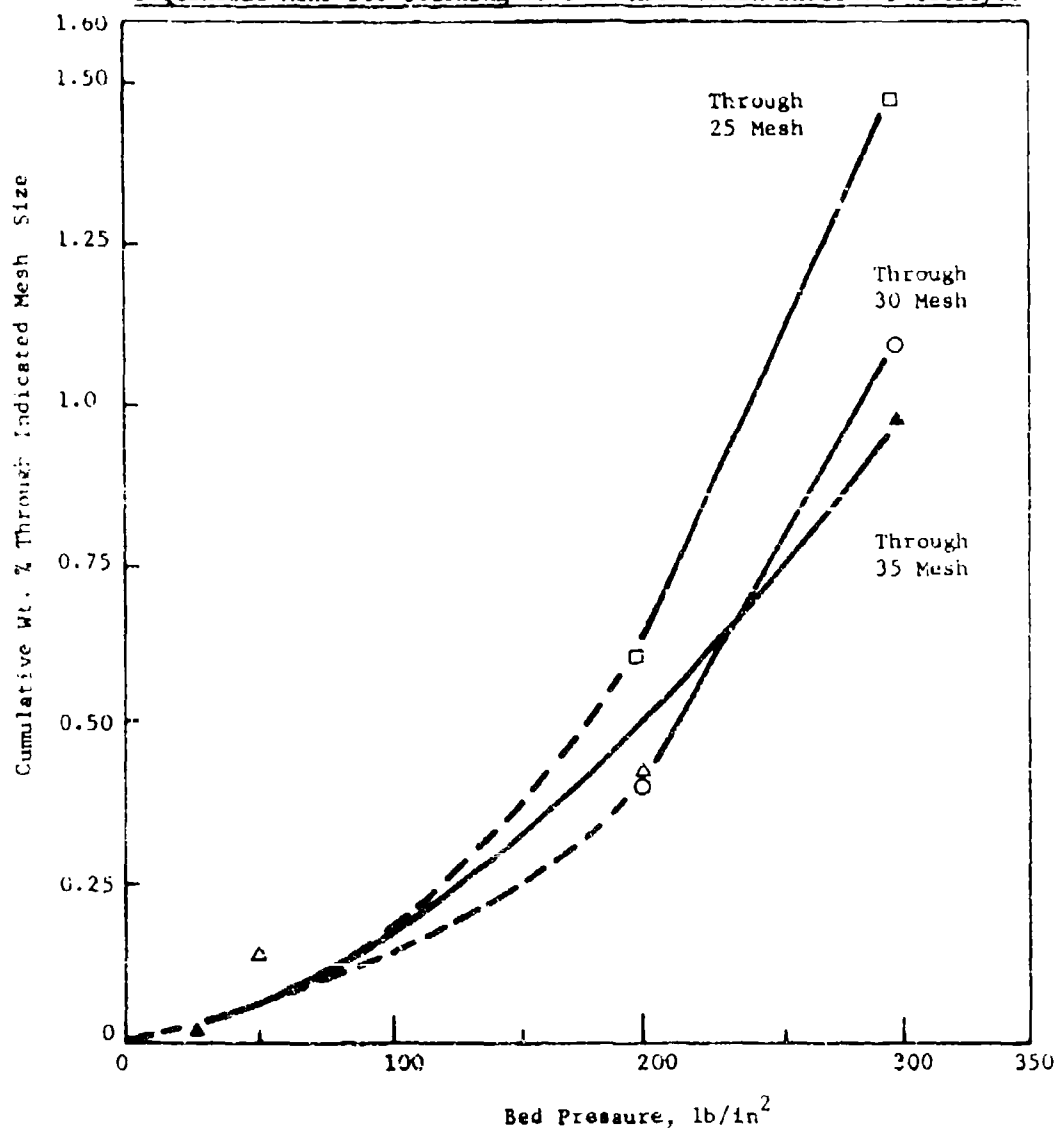


Figure 4-22

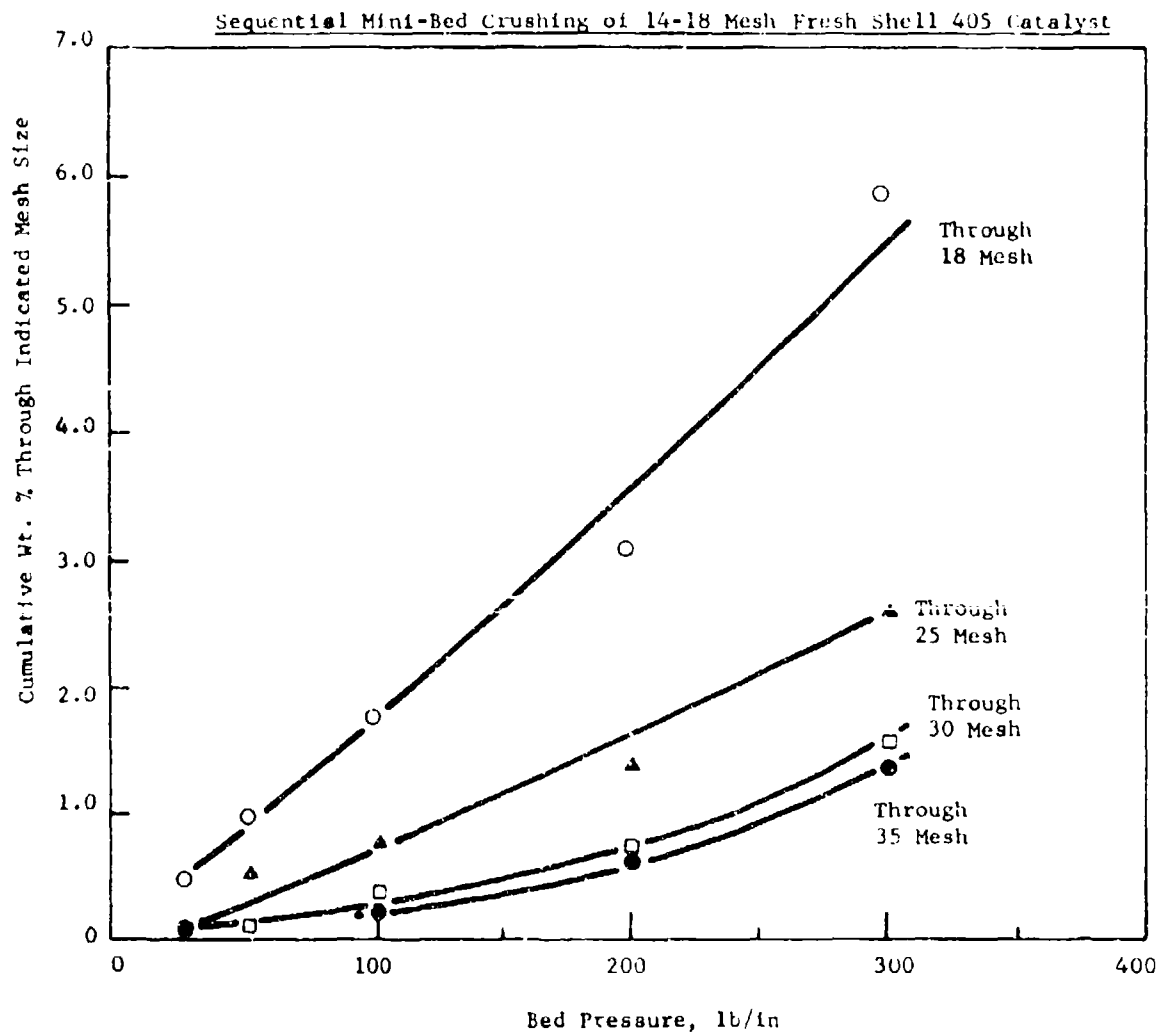


Figure 4-23

Sequential Mini-Fed Crushing of 20-25 Mesh
Fresh Shell 405 Catalyst

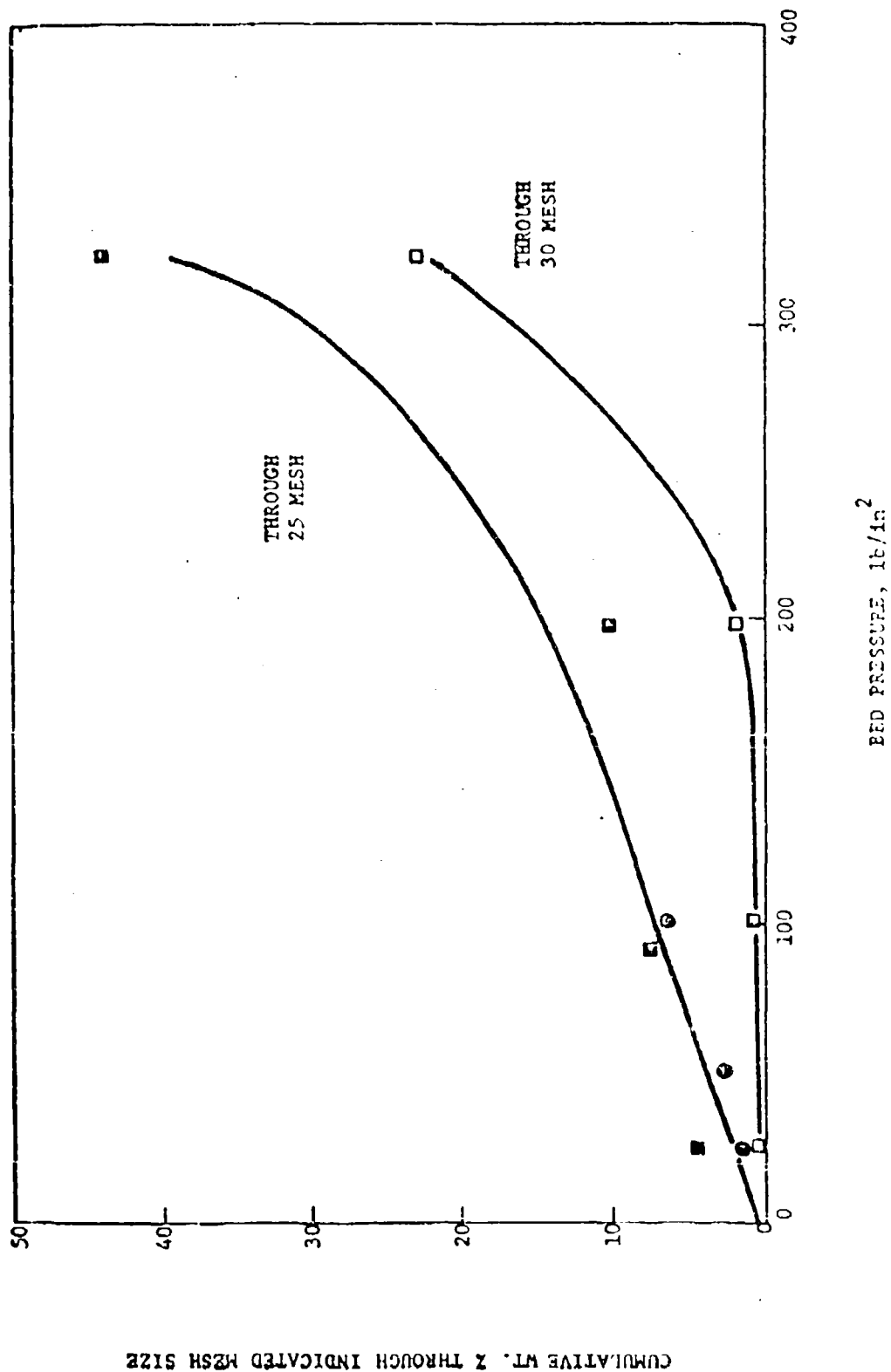


Figure 4-24
 Sequential Mini-Bed Crushing of 20-25 Mesh
 Fresh Shell 405 Catalyst

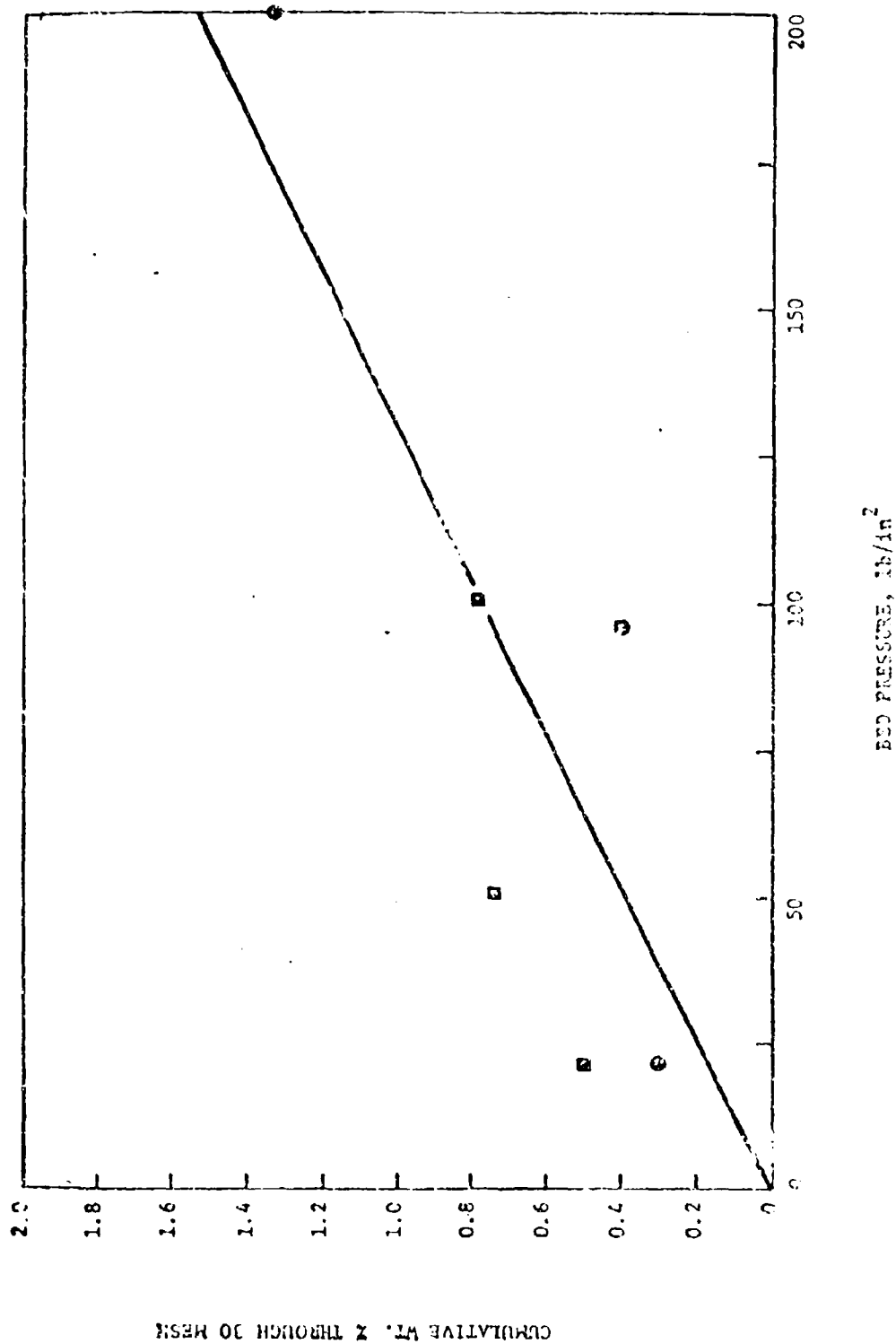


Figure 4-2

Sequential Mini-Bed Crushing of
Fresh 25-30 Mesh Shell 405 Catalyst

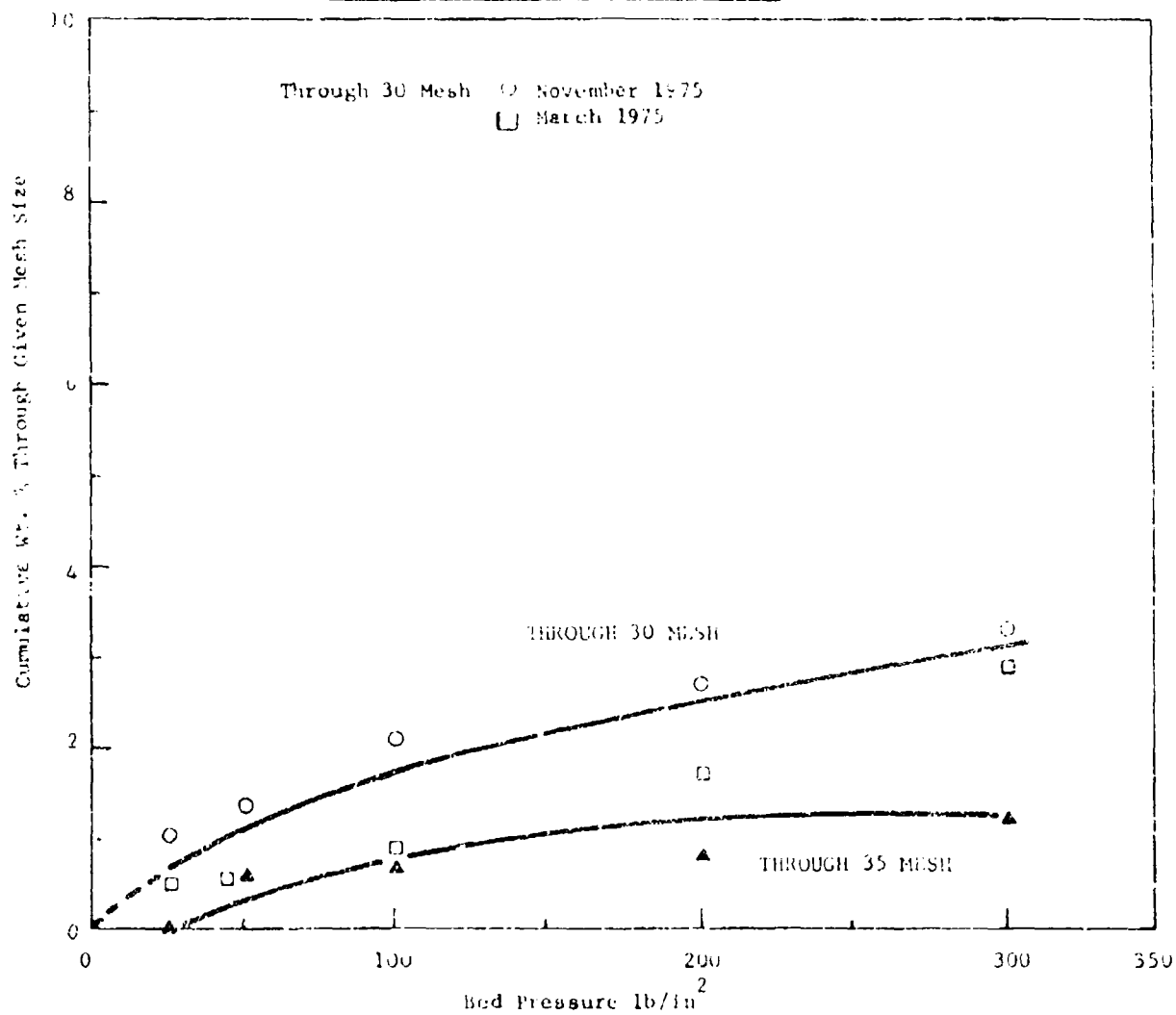
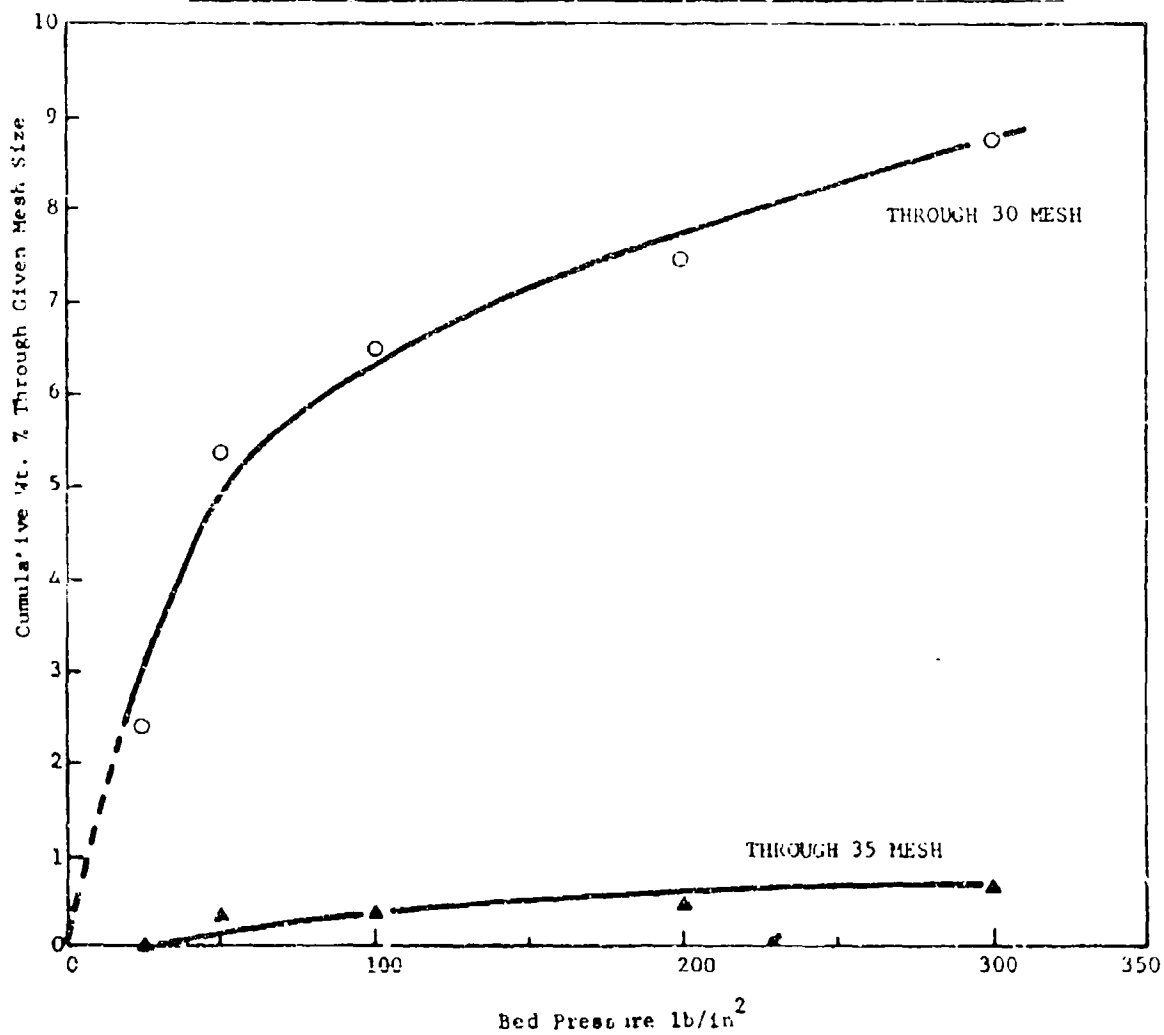


Figure 4-26

Sequential Mini-Bed Crushing of Fresh 20-30 Mesh Shell 405 Catalyst



In Table 4-21 is shown a comparison of the ability of the various fresh Shell 405 catalyst mesh sizes to resist bed pressure crushing. Shown as a function of mesh size at two fixed bed pressures (100 and 200 psi) are the weight percent of material lost from the starting mesh size. Also shown for purposes of analysis are the size characteristics of the mesh sizes involved based on the size of the opening present in each mesh size. Assuming that the particles are spherical in shape, the contact area between particles all of the same size will not depend on the absolute size of the particles. For an actual Shell 405 mesh size material, the contact area, however, will be a function of the distribution of particle sizes with the contact area increasing as the width of the distribution of particle sizes increases. As a rule of thumb, this effect becomes important when the ratio of the largest particle to the smallest particle exceeds the $\sqrt{2}$ (152). Since this is not the case with the standard starting mesh sizes employed with Shell 405, the various mesh sizes should have approximately equivalent contact areas. It does suggest, however, that the small mesh size fines generated as the bed breaks up will tend to increase the particle to particle contact area and thus help to stabilize the bed against pressure crushing forces.

An examination of the data in Table 4-21 indicates that with the exception of the 20 to 25 and 20 to 30 mesh sizes, an equal pressure level produces approximately the same level of material lost from the starting mesh size. Since the 25 to 30 mesh material is much stronger than the 20 to 25 mesh material, it suggests that the weakness of the 20 to 30 mesh material as caused by the presence of significant quantities of 20 to 25 mesh material. However, the unusually weak nature of the 20-25 mesh size material represents an anomaly similar to that suggested by limited bed pressure crushing data previously obtained with this mesh size by Bell Aerospace Corporation and ultimately may result from batch to batch variations in catalyst crush strength.

4.2.2 The Effect of Particle to Particle Abrasion In a Moving Bed

In the Task I work the gas velocities necessary for incipient movement of Shell 405 catalyst particles was measured. This data indicated that in general the gas velocities to which Shell 405 catalyst particles are exposed in a thruster are above the incipient particle movement velocity. A voided thruster bed, thus has sufficient gas velocity for particle movement. In Task III, the possible effect of such movement was assessed on catalyst degradation. In general, the interaction between the flowing fluids and the solid catalyst bed in a hydrazine thruster after a void volume has been introduced must indeed be complex and complete elucidation of such a system is a major task in itself. However, in order to assess the magnitude of possible catalyst losses resulting from particle to particle abrasion when a voided bed is in motion a simplified experimental test was developed and employed.

Table 4-21

Comparison of the Resistance of Various Fresh Shell 405 Mesh
 Sizes to Bed Pressure Crushing

Starting Mesh Size	Size of Particles in Mesh Size, mm	Particle Range, R mm (a)	Particle Ave Diameter, Dave mm (b)	Range x 100 Dave	Wt. % Lost From Starting Mesh Size	
					100 psi	200 psi
8 to 12	$1.68 \leq D \leq 2.38$	0.70	2.030	34%	2.5	6.9
14 to 18	$1.00 \leq D \leq 1.41$	0.41	1.205	34%	1.7	3.3
20 to 25	$0.71 \leq D \leq 0.84$	0.13	0.775	17%	6.0	10.0
25 to 30	$0.59 \leq D \leq 0.71$	0.12	0.650	18%	1.7	2.7
20 to 30	$0.59 \leq D \leq 0.84$	0.25	0.715	35%	6.5	7.6

(a) Particle Range, R_1 = Maximum Diameter - Minimum Diameter

(b) Average Particle Diameter; Dave = Maximum Diameter + Minimum Diameter divided by 2.

In developing a test to assess the possible effect of particle to particle abrasion, a number of configurations were tried using variations of the modified ILBET apparatus, so as to establish a design which produced a constant, vigorous motion of the bed which would insure particle to particle contact of the majority of the particles. Use of the simple modified ILBET apparatus was unsatisfactory in that movement of all of the bed on a relatively constant basis could not be achieved at the inlet velocities of interest. Similarly altering the apparatus so as to reverse the gas flow from a downflow situation to an upflow situation (with the gas exiting at the top) also failed to provide constant motion of all of the bed. A third modification as shown in Figure 4-22 produced an acceptable configuration. This Particle to Particle Abrasion Resistance Apparatus (PPARA) uses a design similar to the modified ILBET apparatus except the bottom of the reactor was converted to a solid surface rather than an exit screen and the gas exited through a screen at the top of the reactor. At a sufficiently high velocity the bed expands and movement occupies essentially the complete reactor volume. Excellent movement of essentially all the particles in the bed can be achieved with the configuration by maintaining the superficial gas exit velocity below the particle's terminal settling velocity. If the exit velocity exceeds the particle's terminal settling velocity then a number of the particles are held stationary against the exit screen. The terminal settling velocity (against gravity in air at 70°F) of particles of Shell 405's density varies from approximately 30 feet per second for an 8 to 12 mesh size particle to 15 feet per second for a 20 to 30 mesh size particles (133). When a superficial inlet velocity of 250 feet per second is used in the PPARA, the superficial exit velocity is approximately 4 feet per second, which is well below the terminal settling velocity of all Shell 405 particle sizes of interest.

A series of runs were made in the PPARA using nitrogen as the gas and employing a two hour test period for exposure to abrasion. Fresh Shell 405 catalyst samples of 8 to 12 mesh, 14 to 18 mesh and 20 to 30 mesh size were employed. The samples were screened to insure the proper size and weighted before the start of the run, and then screened to various mesh sizes and weighted at the end of the run. Two superficial inlet gas velocities were employed, 250 feet per second and 160 feet per second. The latter value was fixed at this level since experimental tests indicated that gas velocities much below the value failed to produce vigorous and complete bed movement. Detailed data are shown in the appendix. A summary of the percent total weight loss of the various fresh Shell 405 catalyst particle sizes after exposure in the PPARA is shown in Table 4-22. It can be seen that the total weight loss ranged for the various particle sizes from 15 to 20% at the 250 feet per second gas inlet velocity. For the lower 160 feet per second gas inlet velocity the total weight loss for the various particle sizes ranged from approximately 3 to 6%, demonstrating a clear effect of velocity on abrasion loss as would be expected. In general, for a given superficial inlet gas velocity, the smaller catalyst particles exhibited a slightly greater average weight loss. This again presumably reflects the effect of particle velocity on abrasion loss, since smaller particles would be expected to reach a higher particle velocity for a given inlet gas velocity.

Table 4-22

EVALUATION OF FRESH SHELL 405 CATALYST IN THE
PARTICLE TO PARTICLE ABRASION RESISTANCE APPARATUS (PPARA)

Percent Total Weight Loss After Two Hours (b)

Superficial Inlet Gas Velocity (a) feet per second	Catalyst Particle Size		
	8-12 Mesh	14-18 Mesh	20-30 Mesh
250	14.6	17.0	19.4
160	4.0	2.4	6.3

- (a) Using nitrogen at ambient conditions.
(b) Total material outside of initial mesh size.

In Table 4-23 is shown data on the size distribution of the fresh catalyst after the two hour exposure in the PPARA. In general, a relatively large fraction of the "lost" catalyst (i.e. the catalyst outside of the starting mesh range) ended up in the smaller than 35 mesh size range. Investigators engaged in studies of size reduction processes (134) state that in general abrasion processes produce greater quantities of smaller particles than do compression or impact processes. Our results in the PPARA fit this general picture of the effect of abrasion i.e., that abrasion produces many more very smaller particles than would compression. Abrasion, thus, is more likely to result in the production of smaller particle which would have a greater tendency to be lost from the reactor itself than the larger particles than could be produced in compression.

Most important, however, the results demonstrate that particle movement in a voided reactor is capable of resulting in significant loss of the catalyst in the reactor.

4.2.3 Effect of Use Exposure on Catalyst Physical Properties

4.2.3.1 Effect of Thruster Exposure

The effect of thruster exposure on catalyst properties is an important question i.e. do critical catalyst material properties deteriorate as a result of thruster exposure. To provide data to help answer this question, samples of catalysts which have been used in thrusters were tested to see if this thruster exposure degraded the material properties of the fresh Shell 405. Material properties which were evaluated included particle crush strength distribution, bed static pressure crushing resistance, resistance to pulsed, liquid stream erosion and resistance to liquid quench thermal shock degradation. Samples of used catalyst were supplied by AFRPL, Rocket Research Corporation and TRW.

4.2.3.1.1 Effect on Particle Crush Strength Distribution

The particle crush strength distribution was characterized by determining the mean and standard deviation. Particle crush strength measurements were made using the ITI. Twenty-five replicate measurements were usually made on each sample. The particles tested were selected via random sampling from the batches provided following sieving, and were then dried in a vacuum oven overnight at 105°C and 25.5" Hg total pressure prior to testing. In Tables 4-24 to 4-29 are shown the results of tests on the samples received. Samples showing a loss in mean crush strength or an increase in scatter (standard deviation) relative to a fresh material of the same mesh size were tested to see if the changes were statistically significant. The means were tested using a single-sided t-distribution test at the 95% confidence level and the standard deviations were tested using an F-distribution test at the 95% confidence level. Conclusions from these tests are summarized in Table 4-30. Although no fresh 18 to 20 mesh Shell 405 particulates were tested, an interpolation of the data on other mesh sizes suggests that such a mesh size would have an average crushing strength of approximately 1 pound. This suggests that the downstream bed samples exposed to 94,000 pulses have suffered a loss in particle

Table 4-23

Size Distribution of Fresh Shell 405
Catalyst After Exposure in PPARA

Starting Mesh Size	Percent of Catalyst Outside of Starting Mesh Size (a)		
	Mesh Size	250 feet per sec Inlet Velocity	160 feet per sec Inlet Velocity
8-12	12-14	6.34	1.81
	14-18	3.06	0.10
	18-25	0.85	0.0
	25-30	0.27	0.0
	30-35	0.16	0.0
	smaller than 35	3.90	2.04
	Total	14.58	3.95
14-18	18-25	7.82	0.75
	25-30	1.41	0.03
	30-35	0.92	0.0
	smaller than 35	6.85	1.64
	Total	17.00	2.42

(a) After two hour exposure in PPARA using nitrogen at indicated inlet superficial gas velocity. Percentages all based on initial weight of fresh catalyst.

Table 4-24

Particle Crushing Strength of
Used 18-20 Mesh Shell 405 Catalysts From TRW

	Sample 1	Sample 2
Sample History	TRW Sample. 84,000 pulses in 5 lbf thruster in November 1972 Sample from downstream end of bed.	TRW Sample. 210,000 pulses in 5 lbf thruster in August 1973. Sample from upper portion of bed near the injector.
Average Crushing Strength, lbs(a)	0.55	1.02
Sample Size	10	10
Standard Deviation lbs.	0.25	0.51

(a) Samples dried in vacuum oven overnight at 110°C and 120 mm Hg
Total pressure.

Table 4-25
Particle Crushing Strength
of Used Shell 405 Catalyst From TRW

		Fresh	Used
1/8" x 1/8"	Average Crushing Strength, lbs.	34.8	21.9 ^(a)
	Sample Size	40	10
	Standard Deviation lbs	6.62	11.5
14-18 Mesh	Average Crushing Strength, lbs	1.50	1.72 ^(b)
	Sample Size	25	10
	Standard Deviation	0.85	0.99

(a) TRW sample. Detailed history not available, however, estimated at a few thousand seconds steady state operation.

(b) TRW sample. Approximately 250 seconds of steady state firing spread over 51 cold starts.

Table 4-26

Particle Crushing Strength of Used Shell 405 Catalyst From the Air Force Rocket Propulsion Laboratory (a)

	20-30 Mesh		14-18 Mesh	
	Upper Bed Sample (U > 30)	Fresh Catalyst	Lower Bed Sample (L > 25)	Fresh Catalyst
Average Crushing Strength, lbs.	0.60	0.61	1.73	1.50
Sample Size	25	25	25	25
Standard Deviation, lbs.	0.35	0.40	0.76	0.85
Statistically Significant	Decrease in Mean (b)	NO	NO	--
	Increase in Scatter (c)	NO	NO	--

(a) Used in Hughes 5 lbf thruster. Test duty cycle of 115,644 total pulses, 264 total starts, 98 starts at 30-40 F, 338 lbs. total fuel.

(b) Single sided S-test. $t_{10.48} \geq 1.30$.(c) F-test. $F_{24,24,.10} \geq 1.70$.

Table 4-27

Particle Crush Strength of Used Shell 405 Catalyst From
The Air Force Rocket Propulsion Laboratory (a)

Catalyst	Mean Crush Strength lbs. (b)	Standard Deviation lb.
Fresh 25-30 mesh (standard 50% attrited)	.56	.27
Used 50% attrited 25-30 Mesh (S/N0001)	.42	.19
Used 90% attrited 25-30 Mesh (S/N0002)	.81	.37

(a) Catalyst used by AFRPL in a Marquardt 5 lbf. thruster, 113,000 pulses, 2,600 seconds total time, 23 cold starts (at approx. 40°F).

(b) Based on a sample size of 25.

Table 4-28

Particle Crushing Strength of Used Shell 405 Catalyst From Rocket Research Corporation (a)

	25-30 Mesh		14-18 Mesh	
	Bed Near Injector	Fresh Catalyst	Outer Catalyst Bed	Fresh Catalyst
Average Crushing Strength, lbs.	0.43	0.56	1.50	1.50
Sample Size	25	25	25	25
Standard Deviation lbs.	0.23	0.27	0.91	0.85
Statistically Significant	Decrease in: Mean (b)	Yes	--	--
	Increase in Scatter (c)	No	--	--

(a) Catalyst used in Space Shuttle APC gas generator life test. Gas generator subjected to over 260,000 pulses and 10 hours total burntime.

(b) Single sided t-test. $t_{.10, 48} \geq 1.30$.(c) F-test. $F_{24, 24, .10} \geq 1.70$.

Table 4-29
Particle Crushing Strength of Used Shell 405 Catalyst From Rocket Research Corporation

25-30 Mesh Catalyst			
	Upper Bed Near Injector in 5 lbf REA (a)	Mid-Bed Location in MJS 0.2 lbf REA (b)	Fresh Catalyst
Average Crushing Strength, lbs.	0.45	0.48	0.56
Sample Size	25	25	25
Standard Deviation, lbs.	0.38	0.23	0.27
Statistically Significant	Decrease in Mean (c)	No	--
	Increase in Scatter (d)	No	--

- (a) Engine accrued 423,000 pulses while delivering 44,000 lbf-sec total impulse. Majority of pulsing operation cycled the catalyst bed between 650 and 1030°F.
- (b) Utilized on the Jet Propulsion Laboratory MJS '77 spacecraft. Engine accrued 380,000 pulses and 30 hours total burntime.
- (c) Single side t-test. $t_{.10, 48} \geq 1.30$.
- (d) F-test. $F_{24, 24, .10} \geq 1.70$.
- (e) Using standard deviation of fresh catalyst for used samples. Use of higher std. dev. of used catalyst results in $t = 1.22$.

Table 4-30

SOME SHELL 405 SAMPLES SHOW DETERIORATION OF CRUSH STRENGTH FOLLOWING THRUSTER EXPOSURE

Source	Sample		Significant Loss of Mean Crush Strength	Significant Increase in Scatter
	Size	Brief History		
AFRPL	14-18	Lower bed, 5 lbf thruster 115,644 total pulses	NO	NO
RRC	14-18	Outer bed, APU gas gen. 260,000 pulses	NO	NO
TRW	14-18	250 sec steady state firing and 51 cold starts	NO	NO
RRC	25-30	Upper bed, 5 lbf REA, 423,000 pulses	YES - 20%	YES - 40%
RRC	25-30	Mid bed, 0.2 lbf REA 380,000 pulses	NO	NO
RRC	25-30	Bed near injector, APU gas gen. 260,000 pulses	YES - 23%	NO
AFRPL	20-30	Upper bed, 5 lbf thruster 115,644 total pulses	NO	NO
TRW	1/8" Cyl.	Few thousand seconds steady state operation	YES - 37%	YES - 74%
AFRPL	25-30	5 lbf, 113,000 pulses 2,600 seconds and 23 cold starts	YES - 25%	NO

crushing strength, whereas the upper bed samples exposed to 210,000 pulses did not. Data for a fresh 90% attrited 25 to 30 mesh catalyst is not available. Previous results with a 90% attrited 20 to 25 mesh catalyst would indicate that its crush strength should be approximated 45% higher than the 50% attrited catalyst, i.e. approximately 0.81 lbs., suggesting no loss of mean crush strength. Thus, it can be seen that in a number of cases a statistical significant loss of mean crush strength occurred. In two cases a simultaneous loss of mean crush strength and increase in standard deviation occurred.

A sharp increase in the percent of weakest particles occurs when both the mean crush strength decreases and the standard deviation increases. An illustrative calculation was made to demonstrate this. Two cases were calculated for the distribution of crush strength using arbitrary units. Case I assumed a mean value of 100 units and a standard deviation of 20 units which was chosen to correspond to the approximate 20% standard deviation we have experienced with fresh cylindrical Shell 405 catalysts. In Case II the mean value was reduced by 20% to 80 units and the standard deviation increased 50% to 30 units to represent a used catalyst material. These distributions are shown in Figure 4-27 and the major increase in weaker particles can be clearly seen. For example, with Case I, crush strengths below 53.4 units represent 1.0% of the total population, while for Case II, crush strengths below 53.4 units represent 18.9% of the total population.

4.2.3.1.2 Resistance to Bed Static Pressure Crushing

Bed pressure crushing tests were made with the 25 to 30 mesh used Shell 405 catalyst samples obtained from AFRPL (samples S/N001 and S/N002). The standard sequential bed pressure crushing procedure was used. All detailed data is shown in the appendix. The data obtained with the used 25 to 30 mesh Shell 405 samples S/N001 and S/N002 are shown in Figures 4-28 and 4-29. It can be seen that the used 50% attrited S/N001 catalyst had a much larger percent leaving the starting mesh size than the fresh catalyst which is the standard 50% attrited preparation. On a through 35 mesh basis, the used 50% attrited S/N001 catalyst exhibited only a slightly higher loss at higher pressures than did the fresh standard 50% attrited catalyst. Interestingly, the used 90% attrited sample S/N002 exhibited a much higher percent through 30 mesh than did the used 50% attrited S/N001 sample, whereas on a through 35 mesh basis this ranking was reversed.

In Figure 4-30 is plotted a distribution of crush strength calculated from the particle mean crush strength (\bar{X}) and standard deviation (σ) measured for fresh 50% attrited Shell 405 and used samples S/N001 and S/N002. The relative rankings obtained from this calculation corresponds to the ranking observed with the sequential bed pressure crushing tests on a percent through 35 mesh basis. This comparison, however, leaves unexplained the larger percent which passed out of the initial mesh size (i.e. through 30 mesh) of used S/N002 sample than used S/N001 or fresh Shell 405 samples. It would appear that the change of particle sizes in a bed under pressure loading as influenced by changes in catalyst strength of material properties from thruster exposure is a complex phenomena.

Figure 4-27

Effect on the Percent of Weak Particles of a Simultaneous
Reduction in Mean Value and Increase in Standard Deviation

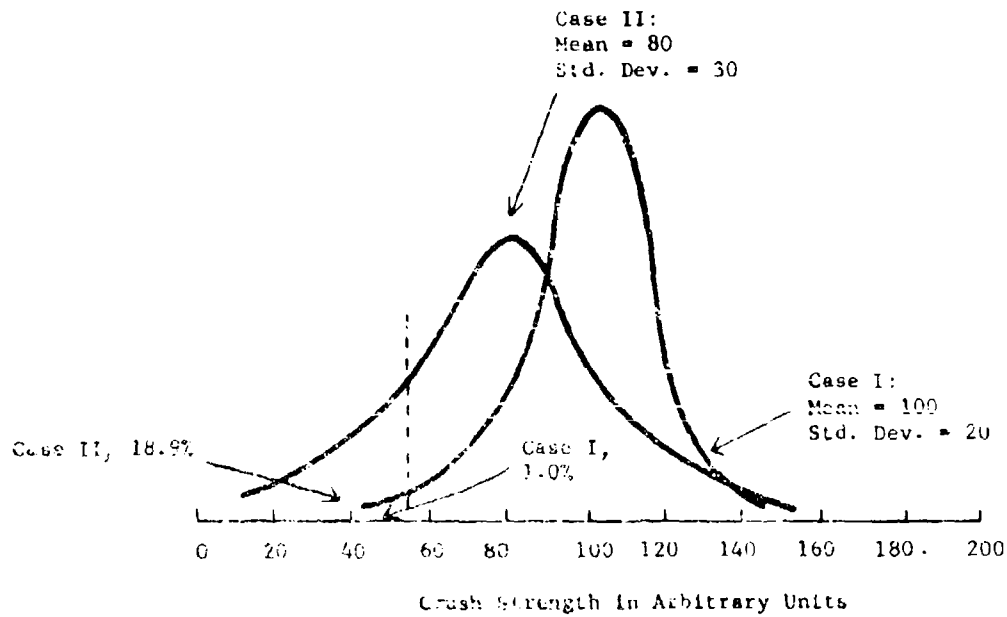


Figure 4-28

Sequential Mini-Bed Crushing of Used 25-30
Mesh Shell 405 Catalyst: Percent Through 30 Mesh

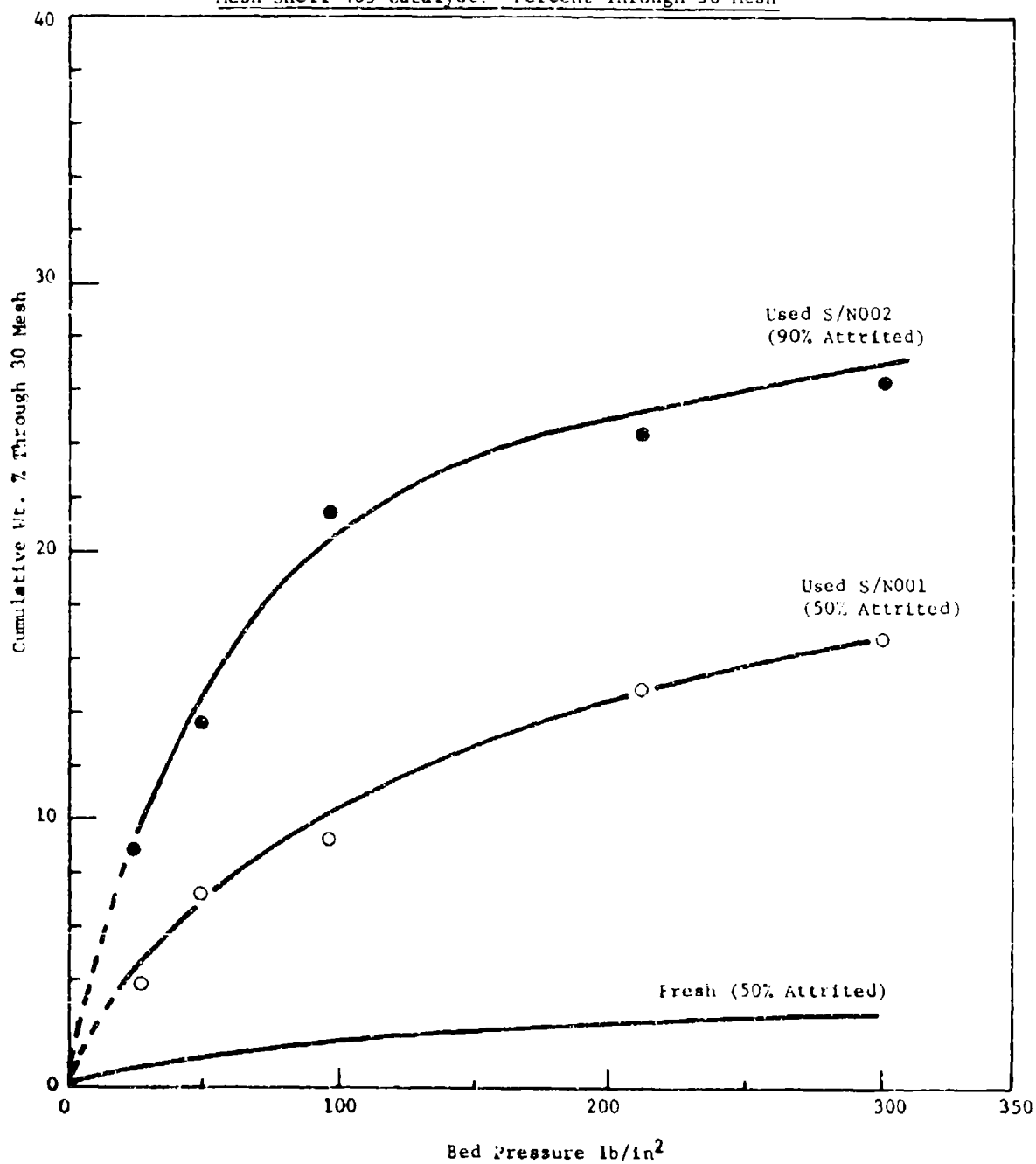


Figure 4-29

Sequential Mini-Bed Crushing of Used 25-30
Mesh Shell 405 Catalyst: Percent Through 35 Mesh

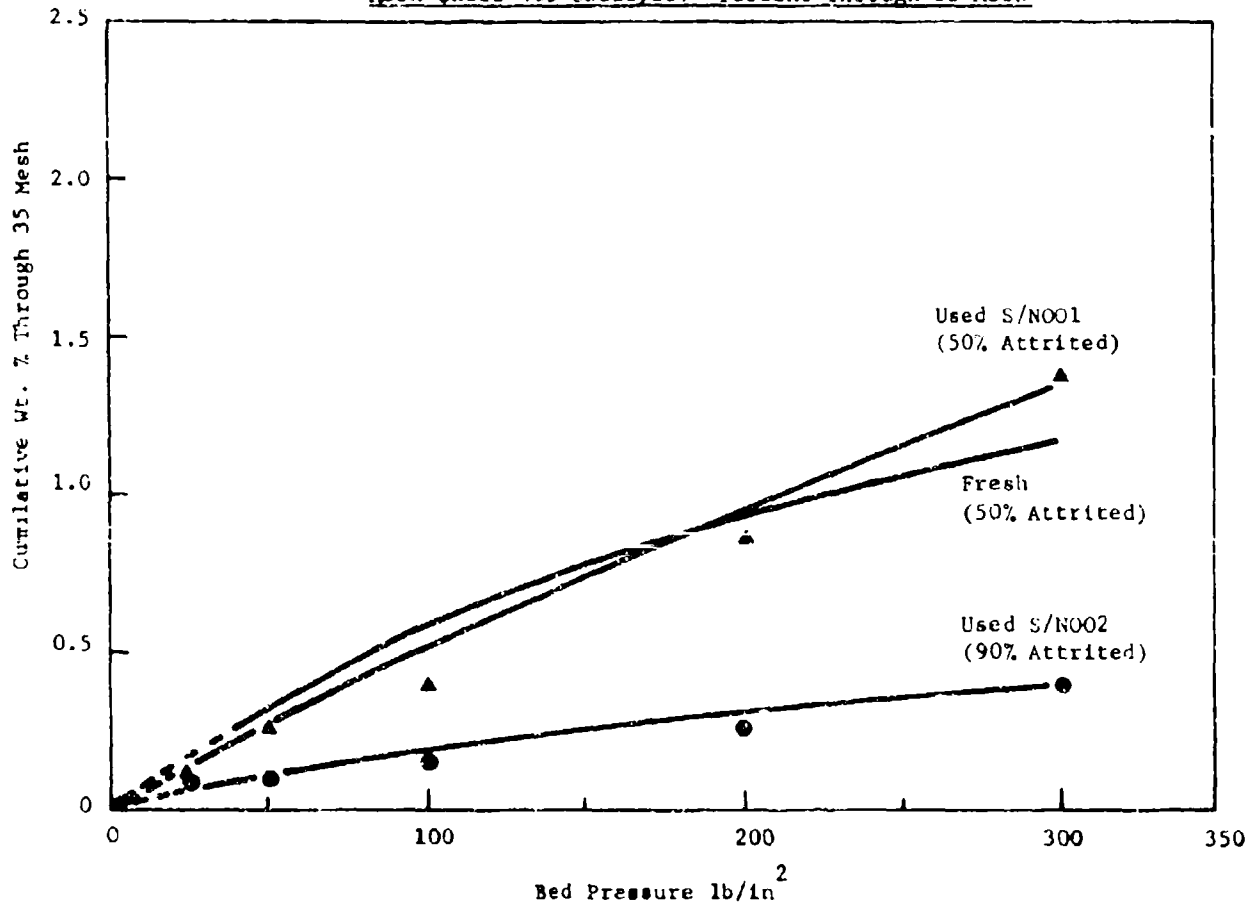
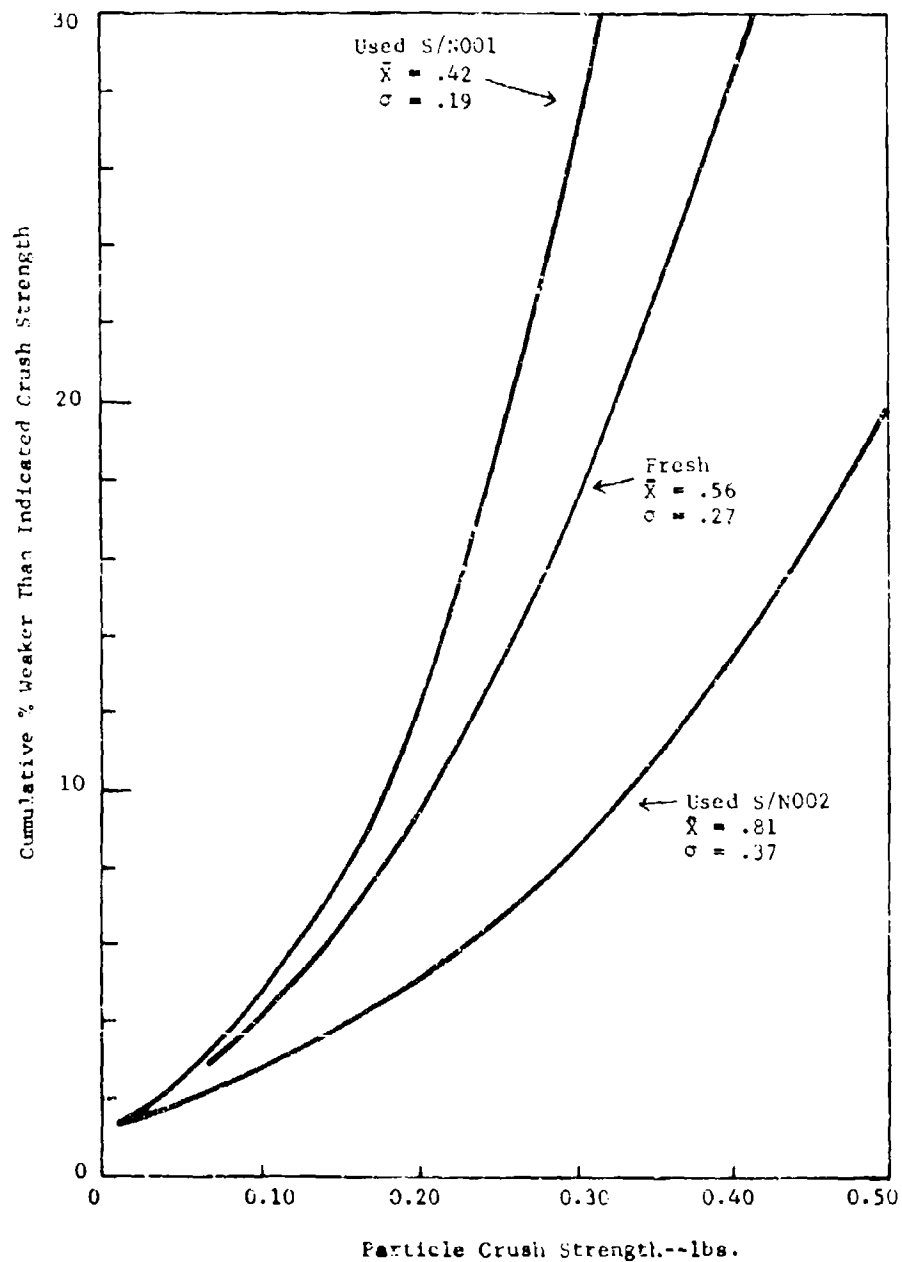


Figure 4-30

Comparison of Particle Crush Strength
Distributions of 25 to 30 Mesh Fresh Shell
405 and Used Samples S/N001 and S/N002



4.2.3.1.3 Resistance to Pulsed, Liquid Steam Erosion

Experimental measurements that was made to determine the ability of fresh Shell 405 catalyst to resist erosion from a pulsed liquid stream at varying velocities indicated that 8-12 mesh granules and 1/8" x 1/8" cylinders experienced weight loss when exposed to liquid erosion and that the magnitude of the loss increased with both increased number of pulses and higher linear velocity. In general, however, the magnitude of this loss with fresh catalyst was low and can be controlled by limiting the magnitude of the velocity to which the catalyst is exposed. For example, with the fresh granular catalyst exposed to 100,000 pulses, the average weight loss can be held to 0.7% if the liquid velocity is restricted to a maximum of 50 feet per second. However, an important question regarding pulsed liquid stream erosion is whether or not catalyst aging caused by thruster exposure will decrease the ability of the granules to resist this erosion.

To answer this question a number of samples of used granular catalyst were tested in the PLPET apparatus. The catalyst samples, all of which were 14-18 mesh material and had previously been evaluated for possible loss of crush strength, were as follows:

- TRW sample with approximately 250 seconds of steady state firing spread over 51 cold starts.
- Rocket Research Corporation sample from outer catalyst bed in APU gas generator life test, with 260,000 pulses and 10 hours total burntime.
- AFRPL sample from lower bed of higher 5 lbf thruster after 115,644 total pulses, 264 total starts, 98 starts at 30-40°F and 308 lbs total fuel.

These tests were carried out in the PLPET apparatus using the procedures previously described. Replicate experiments were made in all cases. As before, photomicrographs were made of each individual particle before and after exposure. All used and the fresh sample of 14-18 mesh catalyst were subjected to 100,000 pulses with a liquid velocity of 100 feet per second.

Detailed data obtained from these PLPET experiments are shown in the appendix. Photomicrographs of selected particles before and after exposure to pulsed liquid flow erosion are shown in Figures 4-31 to 4-33. Results from the experiments are summarized in Table 4-31.

The used samples of 14-18 mesh catalyst all showed higher weight losses than did the fresh material. Examination of the photomicrographs indicated that both in the case of one of the Rocket Research sample particles and one of the TRW sample particles part of the pellet was broken off as a result of PLPET exposure. This observation was corroborated by the weight measurements which showed a 35.6 and 48.7% weight loss for the affected particles respectively. Similar exposure of fresh Shell 405 granules has never indicated either visual or gravimetric evidence of part of a particle breaking off.

Figure 4-31

Liquid Rocket Test: 14-18 Mesh Shell 405 Catalyst From the Air Force
Rocket Propulsion Laboratory After Use in Lower Bed of 5 Thru Thruster
at 100 Feet Per Second and 100,000 Paises



Pellet 2 - Before



Pellet 2 - After



Pellet 5 - Before



Pellet 5 - After

Figure 4-32

Liquid Erosion Test: 14-18 Mesh Shell 405 Catalyst from
Rocket Research Corp. After Use in Outer Bed of AP Gas
Generator at 100 Feet Per Second and 100,000 Pulses



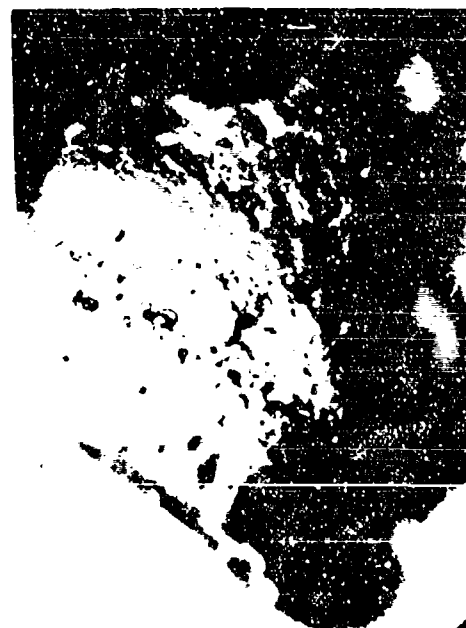
Pellet 3 - Before



Pellet 3 - After



Pellet 4 - Before



Pellet 4 - After

Figure 4-33

Liquid Erosion Test: 14-18 Mesh Shell 405 Catalyst Iron
1% Water 250 seconds of Steady State Firing Speed of 51
Cold Starts at 100 Feet Per Second and 100,000 Pulses



Pellet 3 - Before



Pellet 3 - After



Pellet 5 - Before



Pellet 5 - After

Table 4-31

Comparison of Ability of Fresh Versus Used Shell 405
14-18 Mesh Granules to Resist Pulsed, Liquid Erosion

Catalyst, 14-18 mesh	Average Weight loss, % (a)	Sample Size	Standard Deviation % wt. Loss	Evidence of any pellets experiencing a breaking off during PLPET exposure
Fresh	1.08	5	1.08	NO
Used sample from AFRPL, lower bed 5 lbf thruster after 115,644 total pulses.	2.90	4	1.86	NO
Used sample from Rocket Research Corp., outer bed in APU gas generator after 260,000 pulses.	11.68	5	13.84	YES
Used sample from TRW, after approx. 250 sec. of steady state firing and 51 cold starts	10.88	5	21.17	YES

(a) Exposed in PLPET apparatus to 100,000 pulses at liquid velocity of 100 feet per second.

A statistical t-test indicates that the difference between the average loss of the AFRPL sample and the fresh catalyst of the same mesh size is significant. A similar analysis of the results obtained with the samples of used catalyst from TRW and Rocket Research Corp. is complicated by the fact that these samples incurred not only an erosion weight loss as experienced by fresh and other used samples but also a fracture weight loss resulting from part of the particle breaking off during PLPET exposure. Thus, the individual weight loss values in the samples are not normally distributed about a mean, as would be the result of "normal" or random error, but rather are distributed in a highly skewed manner (see data in the appendix). This effect is basically the cause for the unusually high standard deviations which were calculated for these samples.

In any event, it is clear that exposure in a thruster environment has clearly degraded the ability of the fresh Shell 405 catalyst particles to resist erosion from a pulsed liquid stream. It is also interesting to note that these three used catalyst samples which all showed some evidence of a deleterious effect on the ability to resist liquid erosion showed no decrease in average crush strength in previous tests.

4.2.3.1.4 Resistance to Liquid Quench Thermal Shock Degradation

As described in Section 4.1.3.4 liquid quench thermal shock studies were carried out on samples of both 14 to 18 and 25-30 mesh Shell 405 catalysts which had experienced actual thruster firings (560 cold starts at 70°F, 210,098 pulses and 2,646 seconds of steady state firing). For the identical number of liquid quench cycles (200) the thruster exposed samples experienced a significantly higher total fines generation than did the fresh catalyst of the same mesh size indicating a deleterious effect from thruster exposure on the ability of the catalyst to resist liquid quench thermal shock.

4.2.3.2 Effect of Exposure in Various Controlled Environments

In the course of conducting various experiments fresh Shell 405 catalyst has been exposed to different controlled environments (see Section 4.1). Samples of catalyst from these experiments were tested to see if such exposures changed the distribution of particle crush strengths or resistance to pulsed liquid stream erosion.

4.2.3.2.1 Effect on Particle Crush Strength Distribution

Particle crush strength measurements were made on samples of 25 to 30 mesh catalyst exposed to various types of thruster environment in the "Pop Shock" apparatus. Results of these measurements are summarized in Table 4-32. Detailed data are shown in the Appendix. Also shown is the previous measurements obtained for fresh Shell 405 of the same mesh size. It can be seen that neither 600 seconds of steady state operation or a 100 cycle exposure altered either the average particle crush strength or the standard deviation. In contrast, exposed to "pop shocks" with the exception of sample 292-321 produced significantly different mean crush strengths without producing any obvious pattern in the data.

Table 4-32

Particle Crush Strength Distribution of 25-30 Mesh Shell
405 Catalysts Used in TRW "Pop Shock" Studies

<u>TRW</u> <u>Identification</u>	<u>"Pop Shock" Exposure</u>	<u>Mean Crush</u> <u>Strength lbs. (a)</u>	<u>Standard</u> <u>Deviation</u> <u>lbs. (a)</u>
272-291	8 "pops", <999 psi	0.524	0.28
292-321	1 "pops" at 1000 to 1499 psi	0.549	0.18
	2 "pops" at <999 psi		
322-354	21 "pops" at < 999 psi	0.601	0.27
356-377	3 "pops" at 1500 psi	0.619	0.39
370-386	3 "pops" at 2000 psi	0.529	0.24
100 cycles	--	0.565	0.30
600 seconds steady state	--	0.565	0.30
Fresh Shell 405	--	0.56	0.27

(a) Measurements obtained from a sample of size 25.

Samples of catalysts exposed to controlled environments in the Liquid Quench Thermal Shock Tests (LQTS) and Void Volume Abrasion Tests (VVA) were tested for particle crush strength properties. Results are shown in Tables 4-33 and 4-34. As can be seen, all the samples show at least some modest increase in mean crush strength, although in general increases below approximately 20% are not statistically significant on an individual t-test basis. This result is in contrast to tests with samples which have seen thruster exposure, where often significant decreases are seen in mean strength. An examination of the data indicates a rough correlation between the increase in crush strength and the % fines produced in the original Liquid Quench Thermal Shock and the Void Volume Abrasion Tests, suggesting that at least part of the increase in the mean crush strength of the samples resulted from a selective removal of the weaker particles during LQTS and VVA exposure.

Samples of 14 to 18 mesh fresh Shell 405 catalysts from different lots were immersed 10 times in liquid hydrazine. Particle crush strength measurements made on both the as-received catalyst and the catalyst after immersion in liquid hydrazine are shown in Table 4-35. It can be seen that two of the samples of surviving catalyst after liquid immersion shown a reduced mean crush strength relative to the same batch of fresh catalyst. It is also interesting to note the relatively large lot to lot variation in the mean crush strength of fresh Shell 405. The difference between the mean crush strength of lot C and lot B is statistically significant, whereas the other mean crush strength differences are not significant (lot A versus either lot B or C).

4.2.3.2.2 Effect on Pulsed Liquid Steam Erosion

Pulsed, liquid erosion resistance measurements were made on samples of the 14-18 mesh catalyst exposed to various types of thruster environment in the "Pop Shock" apparatus. These tests were carried out in the PLPET apparatus using the standard run procedure. All used samples of the 14-18 mesh catalyst were subjected to 100,000 pulses with a liquid velocity of 100 feet per second. Results of these measurements are summarized in Table 4-36. Also shown are the previous measurements obtained for fresh Shell 405 catalyst of the same mesh size. Detailed data are shown in the Appendix.

It can be seen exposure to 600 seconds of steady state operation or "pop shocks" under 1500 psi (Samples 41-52 and 53-53) neither resulted in a significantly higher average weight loss or evidence of any granules breaking off in PLPET exposure. In contrast, exposure to 100 cycles or to a "pop shock" of 1725 psi (Sample 105-107) resulted in both a higher mean weight loss and evidence of granules breaking off in PLPET exposure. Other samples with exposure to "pop shocks" over 1000 psi (Samples 108-125 and 126-158) showed a higher average weight loss but no evidence of granules breaking off in the PLPET apparatus.

Table 4-33

Particle Crush Strength Distribution of Samples After Liquid Quench Thermal Shock Tests

Catalyst Condition	Numbers of Quench Cycles	14-18 Mesh			25-30 Mesh		
		Mean Crush Strength lbs. (a)	% Change in Mean	Std. Deviation lbs. (a)	Mean Crush Strength lbs. (a)	% Change in Mean	Std. Deviation lbs. (a)
Fresh	0	1.50	Base	0.85	0.56	Base	0.27
	5	1.68	+11.9	0.79	0.57	+1.8	0.28
	25	1.64	+9.4	0.75	0.73	+30.4	0.30
After 100 Thermal Fatigue Cycles	0	(b)	--	(b)	0.57	Base	0.30
	5	1.47	--	0.85	0.64	+12.3	0.29
	25	1.71	--	0.81	0.70	+22.8	0.33

(a) Based on a sample size of 25.

(b) Insufficient number of particles available for meaningful measurement.

Table 4-34

Particle Crush Strength Distribution of Samples After Void Volume Abrasion Tests

G Loading lb/sec-in ²	Void Volume, %	14-18 Mesh			25-30 Mesh		
		Mean Crush Strength lbs. (a)	% Change in Mean	Std. Deviation lbs. (a)	Mean Crush, Strength lbs. (a)	% Change in Mean	Std. Deviation lbs. (a)
Fresh Catalyst - 0	--	1.50	Base	0.85	0.56	Base	0.27
.01	10	1.65	+10.0	0.82	0.67	+19.6	0.33
.02	20	1.92	+28.0	1.07	0.75	+33.9	0.49

(a) Based on a sample size of 25.

Table 4-35

Particle Crush Strength Distribution (a) of Samples After Exposure to Liquid Hydrazine

Shell 405 14-18 Mesh	Fresh Catalyst As Received		Catalyst Surviving After Immersion in Liquid N ₂ H ₄ (a)		7. Loss in Mean Crush Strength	Statistically Significant (c)
	Mean Crush Strength lbs.	Std. Deviation lbs.	Mean Crush Strength lbs.	Std. Deviation lbs.		
C	1.901	0.68	1.219	0.67	35.9	YES
A	1.611	0.76	1.056	0.58	34.5	YES
B	1.331	0.74	1.147	0.60	13.8	NO

(a) Based on a sample size of 25 particles.

(b) Immersed ten (10) times in 40° hydrazine.

(c) Based on single-sided t-distribution test at the 95% confidence level.

Table 4-36

Pulsed, Liquid Erosion Resistance of 14-18 Mesh Shell 405 Catalysts
Used in TRW "Pop Shock" Studies (a)

TRW Identification	"Pop Shock" Exposure	Sample Size	Mean Weight Loss, %	Standard Deviation, % wt. loss	Evidence of Any Granules Breaking Off in PLPET?
41-52	1 "pop" at 850 psi	4	0.72	0.40	NO
53-55	2 "pops" at 1425, 1 "pop" at 850 psi	3	0.43	0.13	NO
105-107	1 "pop" at 1725 psi	4	2.88	3.12	YES
108-125	4 "pops" at > 1500 psi, 3 "pops" at between 1000 and 1499 psi and 7 "pops" at < 999 psi	4	1.67	0.66	NO
126-156	2 "pops" at 1800 psi, 11 "pops" at < 999 psi	4	1.47	0.58	NO
100 cycles	--	4	16.04	28.04	YES
600 seconds steady state	--	2	1.30	0.23	NO
Fresh Shell 405	--	5	1.08	1.08	NO

(a) All particles exposed to 100,000 pulses at 100 feet per second in PLPET apparatus.

4.2.3.2.3 Summary of Results

A summary of results of tests on samples of catalysts which were survivors from fresh catalysts exposed to controlled, different environments is shown in Table 4-37. Exposure to liquid hydrazine was the only environment from which the surviving catalyst showed a decrease in mean crush strength. However, the fresh catalyst surviving both thermal cycling exposure and "pop" shocks in excess of 1500 psi exposure showed evidence of decreased resistance to pulsed, liquid erosion.

Table 4-37

Summary of Results of Tests on Catalyst
Samples Exposed to Controlled Environments

<u>Nature of Environment</u>	<u>Evidence of Loss of Particle Crush Strength</u>	<u>Evidence of Loss of Resistance to Liquid Erosion</u>
Thermal Cycling (100 cycles)	NO	YES
Steady State Exposure (600 seconds)	NO	NO
Exposure to Liquid Hydrazine (10 immersions in 40° N ₂ H ₄)	YES	--
Liquid Quench Thermal Shock (25 Quench Cycles)	NO	--
"Pop" Shocks in Excess of 1500 psi	NO	YES
Void Volume Abrasion	NO	--

5. TASK III - ANALYTICAL MODELING

5.1 Introduction

5.1.1 Organization of the Effort

Analytical modeling supporting studies were carried out by McDonnell Douglas Astronautics Company (MDAC). The MDAC Study Manager for this project was Mr. R. J. Hoffman, Project Thermodynamics Engineer--Plume Effects, Aero/Thermodynamics and Nuclear Effects Department. Mr. W. T. Webber of the same department acted as Principal Investigator for the study and performed the analyses of the internal particle behavior and of pressure shocks. Mr. S. A. Schechter of the Structures Department performed the analyses of stresses from thermal shock, internal pressure, particle-to-particle contact, and examined the mechanical failure mechanism. Mr. D. Quan of the Propulsion Department performed the analyses related to differential expansion. The analysis of fluid erosion was done by Dr. W. D. English of the Propulsion Department.

5.1.2 The General Purpose and Limitations

Analytical modeling studies in general were conducted both to support experimental activities and to explore areas not investigated experimentally. In order to carry out these supporting analyses a number of assumptions had to be made in regards to (1) the nature of the governing equations and analytical descriptions of the phenomena involved (2) typical values for thruster parameters such as catalyst size, bed loading etc. and (3) the various physical properties of Shell 405 granules, particularly in the strength of materials area. It was recognized a priori (1) that the decisions made in the areas of thruster parameters would not be universally applicable (2) true strength of material properties of granular Shell 405 catalyst were generally not available, and (3) our knowledge of the detailed processes involved in various proposed catalyst breakup mechanisms is often incomplete. Thus, the modeling work described in this report was not intended to provide universal and final answers to all catalyst breakup and thruster design problems but rather to provide appropriate and timely support to the overall effort, and particularly to the phenomenological survey portion of the program.

5.1.3 General Description

The areas involved in analytical modeling are shown in Table 5-1. The interrelationship between the experimental studies and supporting analyses were previously shown in Table 3-21. These studies had a number of objectives. First, they were designed to aid in the discrimination of important highly destructive mech-

anisms from the less important mechanisms, so as to help guide the direction of the concurrent and subsequent experimental tasks in the direction of the most important phenomena. Second, these studies were designed to aid in the interpretation and correlation of the results of the experimental studies. Third, and perhaps most important, the analytical models were to be the means of extending the findings of experimental results to other operating conditions, and to aid in predicting how catalyst failure can be controlled by appropriate choices of engine design and operational parameters.

Although the analyses have been broken into several categories, the majority have a common meeting ground in the limited physical strength of the catalyst. Whenever the local stresses developed in the catalyst material exceed certain values, local failure and loss of material will result.

The stresses at the contact points between two adjoining catalyst particles are amenable to analysis by Hertzian contact theory to determine these local stresses, regardless of whether the contact forces are produced by steady gas pressure drop through the bed, pressure shocks acting upon the bed, differential expansion tending to compact the bed, or even the impact of two colliding particles. Stresses may be generated in the interior of the particle by rapid external heating or cooling, rapid externally applied pressurization or depressurization, or by the local generation of heat or gas pressure interior to the particle, from the decomposition of liquid hydrazine which has flowed into the interior of the particle under the action of surface tension forces or externally applied pressure. In any of these cases, the radial temperature or pressure profile suffices to determine the radial and tangential stress field interior to the particle.

Thermally derived stresses, pressure derived stresses, and point-to-point contact derived stresses may be calculated individually, and then superposed to yield the total stress field, and this will show synergistic effects when several processes act together to exceed a failure stress that would not have been attained by any of the processes acting singly.

The thermally induced free volume changes of the bed and chamber hardware during a startup and shutdown may be calculated from the sequence of time-varying temperature profiles in each. These profiles are obtained from existing computer programs described the thermochemistry and the flow through the bed. To obtain bed compression stress from the volume change requires a bed deformation theory, since loaded granular materials are inherently nonlinear in deflection, and do not have constant elastic moduli. Evaluating the local stresses in the particles at locations of point-to-point contact also requires a structural model.

The erosion by gas-entrained hydrazine droplets or solid particles carried through the bed requires a still different bed model. Mass losses may be calculated by knowledge of the effects of particle velocity and impact angle upon the local mass-loss ratio, the abrasion resistance property of the substrate, and the variation of this property with temperature. These are combined with the calculated gas velocity profile, catalyst temperature profile, and hydrazine quality profiles in the catalyst bed, to give a numerical solution by marching through the bed. Primary and secondary particles are carried along in these calculations in marching from the injector end to the downstream end of the catalyst pack. Impacts are presumed to occur at each new layer of catalyst particles which is encountered.

Table 5-1
Supporting Analyses

1. Thermal Shock Stresses in Individual Catalyst Particles
 - A. Calculate time-dependent temperature profiles in individual catalyst particles.
 - B. Calculate stresses resulting from the temperature profiles.
2. Internal Pressure Stresses in Individual Catalyst Particles
 - A. Calculate time-dependent pressure profiles in individual catalyst particles.
 - B. Calculate stresses resulting from the pressure profiles.
3. Differential Thermal Expansion of Catalyst Bed and Chamber
 - A. Calculate time-dependent temperature, pressure, and velocity distributions in the bed during a smooth start transient.
 - B. Calculate temperature distributions in chamber hardware.
 - C. Calculate time-dependent differential bed compression.
 - D. Calculate stresses in individual particles resulting from bed compression.
4. Fluid Dynamic Erosion
 - A. Calculate time-dependent temperature, pressure, and velocity distribution in the bed during start transients and steady-state operation.
 - B. Calculate erosion rate of catalyst particles based upon impingement of gas carrying entrained droplets and particles.
5. Pressure Shocks in Bed
 - A. Calculate time-dependent flow processes in bed during hard start.
 - B. Calculate bed compression from pressure distribution.
 - C. Calculate particle stresses resulting from bed compression.
6. Mass Loss Resulting from Bed Compression.

5.2 Structures Analyses

5.2.1 Stress Failure Model

The purpose of the stress failure analysis was to develop a failure model for the Shell 405 catalyst, by extending the uniaxial compressive failure value, which was experimentally measured using 1/8" x 1/8" cylinders, to a multiaxial, tension-compression failure surface, suitable for use for other shapes of catalyst particles, and for other modes of stress application.

In the failure tests described in Section 3.2 the 1/8" cylindrical pellets were loaded in uniaxial compression. The failure stress for fresh Shell 405 catalyst was 2836 psi with a standard deviation of 19 percent. The failure level for used material was 1785 psi with a standard deviation of 53 percent. The typical failure was a crack in the direction of the load in each pellet, shown schematically in Figure 5.1. This type of overall (macroscopic) fracture is typical in porous brittle materials (99). The failure is due to the local (micromechanical) tensile stresses which occur at the surface of the internal pores at 90° to the load direction.

In the remaining analyses, a failure criteria is required to assess the severity of the macroscopic or gross stress states produced by the thermal, internal pressure and contact loadings. As only uniaxial compressive failure data were available, the simple local maximum tensile stress around the pores was selected as the failure mode. The pore shape, a cylindrical pore, was selected from a microscopic examination of the material. If more types of failure test data were available, e.g., tensile, biaxial, etc., then a more complicated two or even three dimensional failure model could be developed.

The solution of the stress state in the substrate material around a cylindrical pore in a semi-infinite media in uniaxial stress was obtained from Reference 101. The stress state produced at the pore boundary by biaxial loading of the porous material was obtained by superposition of two stress states produced by uniaxial loading, with one rotated 90 degrees to the other.

For circular cylindrical void in a semi-infinite medium under macroscopic biaxial tensile loads, S_1 and S_2 , the maximum micromechanical tensile stress is circumferential, at the surface of the void. The distribution is easily found from the Reference 101 solutions to be

$$\sigma_\theta = S_1 (1 + 2 \cos 2\theta) + S_2 (1 - 2 \cos 2\theta) \quad (5.2-1)$$

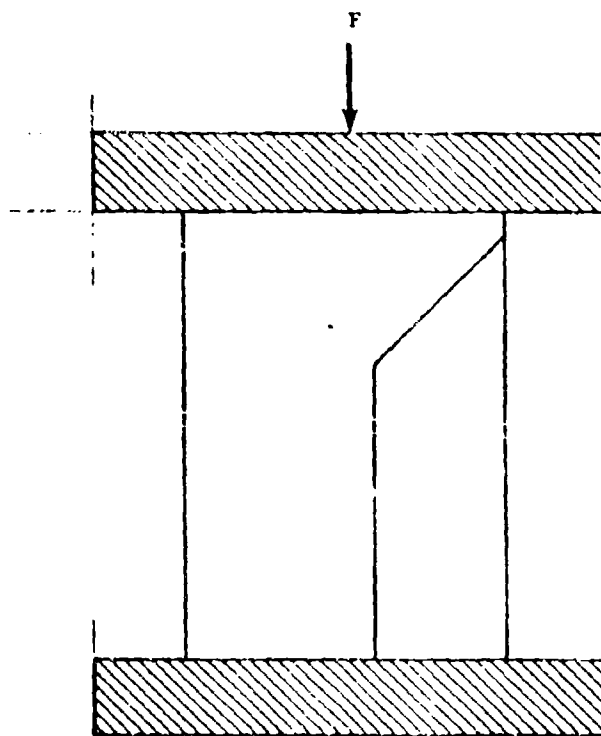


Figure 5-1. Failure in a Brittle Porous Material.

$$\text{and the maxima are } (\sigma_0)_{\max} = \begin{cases} 3 S_1 - S_2, & \text{at } \theta = \pm \frac{\pi}{2}, \text{ for } S_1 > S_2 \\ 3 S_2 - S_1, & \text{at } \theta = 0, \pi, \text{ for } S_2 > S_1 \end{cases} \quad (5.2-2)$$

where θ is the angle around the void, and $\theta = 0$ is aligned with S_1 , as shown in Figure 5.2.

Note that since the radial stress is zero at the surface, the micromechanical stress state is uniaxial at the surface, even though the macroscopic load is biaxial. Thus we can relate the biaxial tension-compression macroscopic failure criterion desired to a micromechanical uniaxial tensile failure.

The macroscopic failure stress measured for the fresh material under uniaxial compression ($S_1 = 2836$ and $S_2 = 0$), shows the micromechanical tensile failure strength (from equation (5.2-2)) $(\sigma_0)_{\max}$ is 945 psi. The macroscopic failure stress measured for the used material under uniaxial compression ($S_1 = 1785$ psia and $S_2 = 0$) shows the micromechanical tensile failure strength (from equation (5.2-2)) is 595 psi. The corresponding biaxial macroscopic failure envelope generated by equation (5.2-2) is shown in figures (5-3 and 5-4). The details of the shape of the envelope will change if different assumptions are made for pore shape but the basic failure envelope shape will remain (102). The complete solution for the arbitrary elliptical void was solved in Reference 102. For an elliptical hole under uniaxial tension with the major axis, a , normal to the load and a minor axis, b , the maximum tension is

$$\sigma = S \left(1 + 2 \frac{a}{b} \right) \quad (5.2-3)$$

Two-dimensional stress distributions caused by stress boundary conditions do not involve the elastic constants. In the general three-dimensional case the solution does depend on the elastic constants, in particular on Poisson's ratio, ν . In the following micromechanical three-dimensional analysis, the Poisson's ratio used is that of the solid material surrounding the pores, denoted ν_s . In the later macroscopic analysis of the stresses produced by thermal, pressure, and contact loadings, the Poisson's ratio used is that of the overall porous medium. The Poisson's ratio, ν_s , of the substrate material is known, 0.32 for temperatures up to 1800°F. The Poisson's ratio of the actual catalyst is not known.

The peak micromechanical σ_{\max} tensile stress for a spherical void in a solid body under uniaxial compression stress S , again from Reference 101, is

$$\sigma_{\max} = \frac{15 \nu_s - 3}{2 (7 - 5 \nu_s)} S \quad (5.2-4)$$

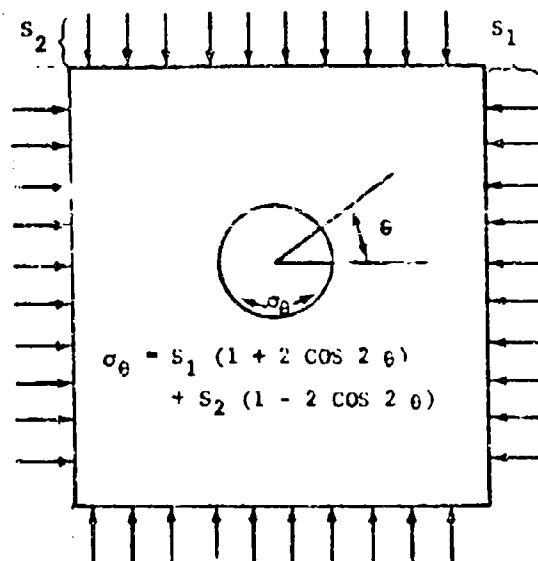


Figure 5-2. The Stress Distribution Around
a Cylindrical Hole in Biaxial Stress.

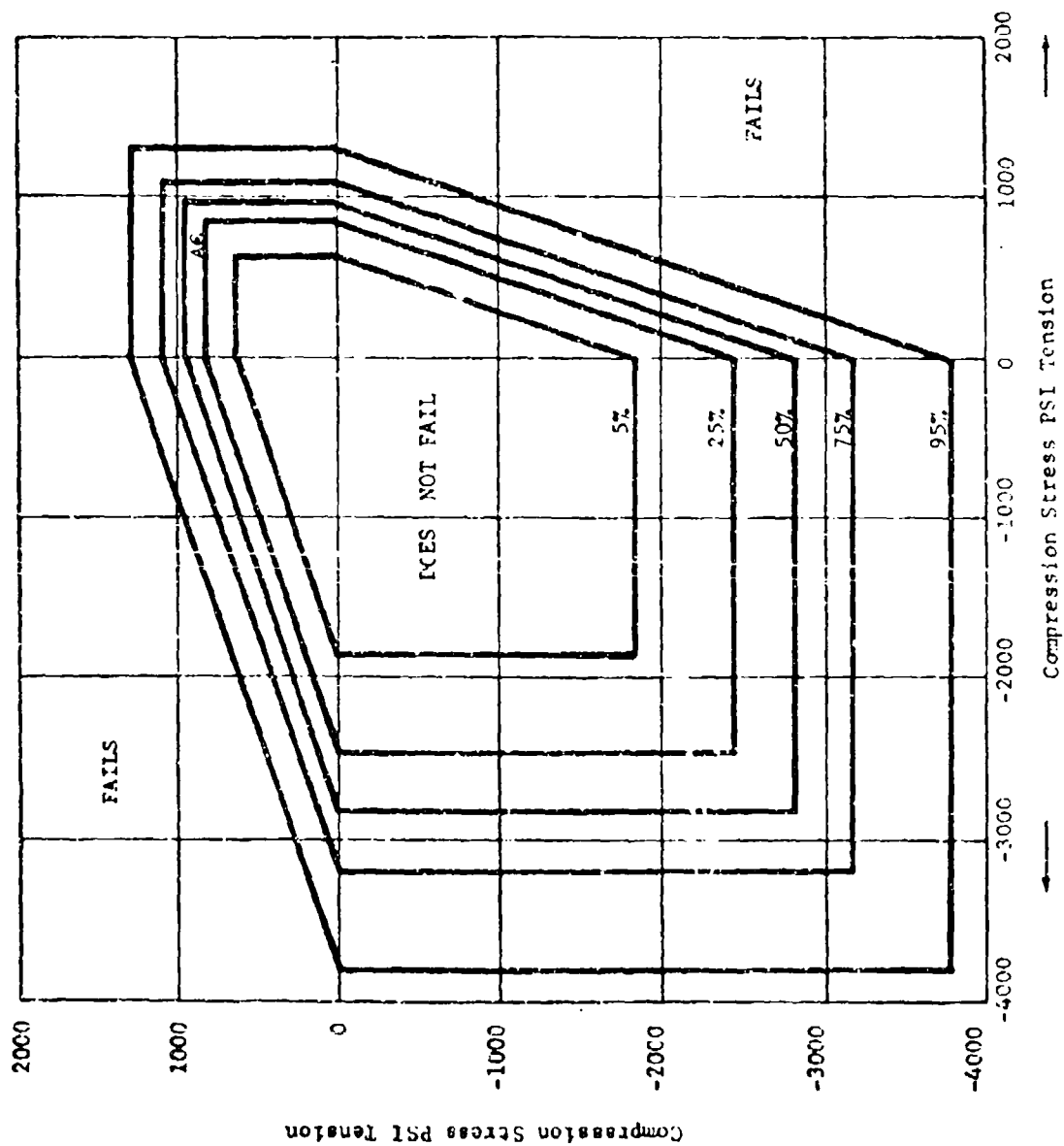


Figure 5-3. Failure Surface for Biaxial Loading - Fresh Shell 405.

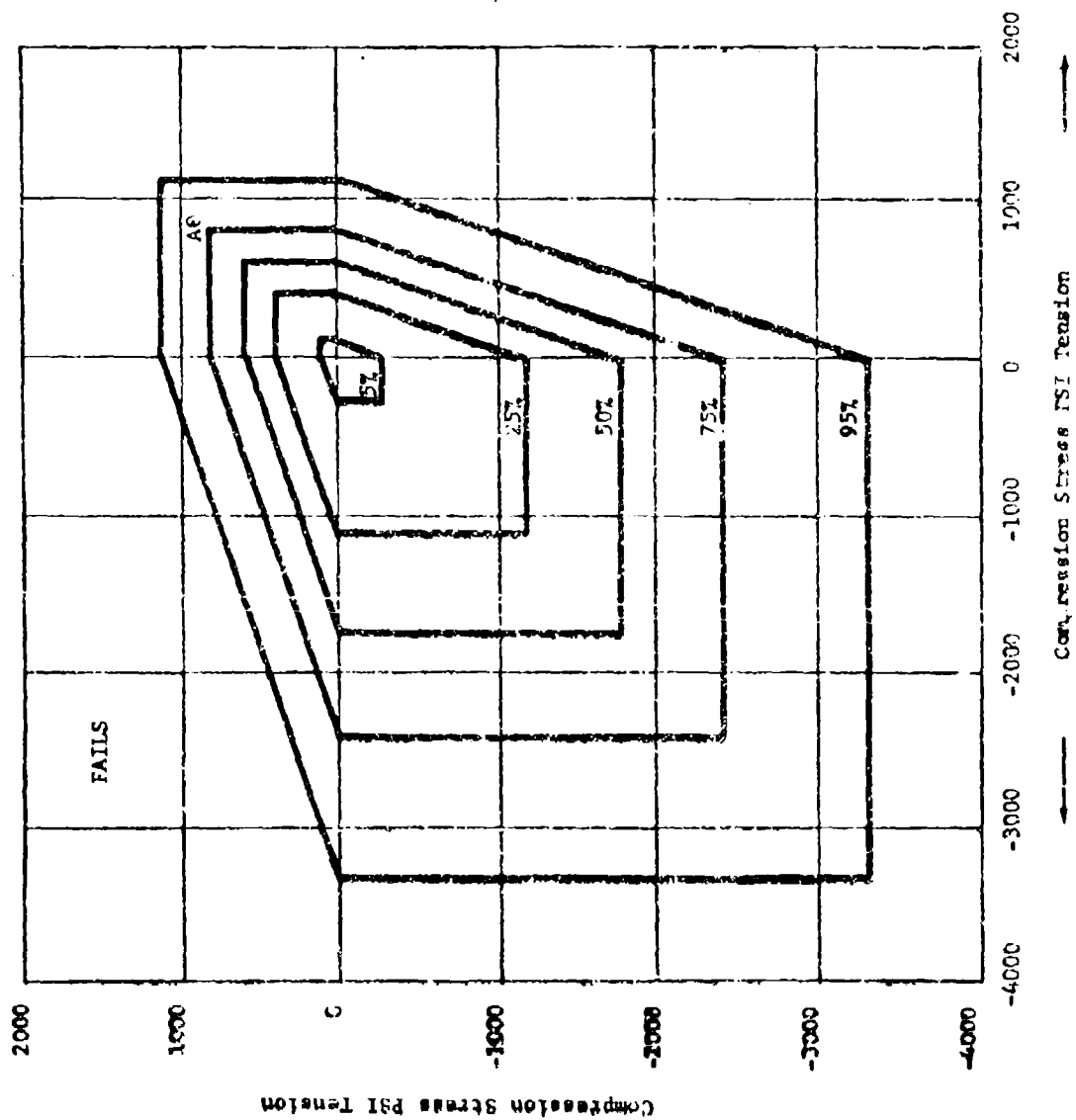


Figure 5-4. Failure Surface for Biaxial Loading - Used Shell 405.

For $\nu_s = 0.32$, $\sigma_{\max} = 0.7225S$. The tensile stress produced by a biaxial load could be obtained by superposition as done for equation 5.2-1. However, the solution for the maxima is somewhat complicated, and has not yet been worked out. The micromechanical tensile failure stress for a spherical void is 2048 psi. This is more than two times the failure stress of a cylindrical void, 945 psi. This difference indicates the dependence of the failure criteria used here on the assumption made regarding pore shape, and points up the need for failure tests using biaxial and, if possible, triaxial, stress states. Even uniaxial tensile failure test data would greatly reduce the uncertainties.

5.2.2 Temperature Profiles Developed Inside a Catalyst Particle by External Heating or Cooling

The temperature profiles developed when an initially cold catalyst particle is externally heated, or when a uniformly hot catalyst particle is externally cooled is a function of two dimensionless moduli, the Biot number and the Fourier number.

The Biot number expresses the effect of the external thermal resistance on the transient temperature profiles which are developed inside the thermally conductive body, and is especially important for the real case where heat is transferred to (from) the body from a hot (cold) fluid flowing past the body. The Biot number is, roughly speaking, the ratio of external thermal conductance to internal thermal conductance. If, for instance, a cold, thermally resistive sphere were exposed to a hot external fluid of infinite conductance, the exterior boundary of the sphere would instantly assume the high external temperature, and the thermal gradient in the outermost lamina of the sphere would be infinite. This would correspond to an infinite Biot number. If, instead, the interior of the sphere had infinite conductance, while the conductance of the hot fluid surrounding it was finite, the sphere would heat up uniformly, with no internal gradients. This would correspond to a Biot number of zero. The Biot number is:

$$Bi = \frac{hr}{k_p} \quad (5.2-5)$$

where r is the radius of the particle

k_p is the thermal conductivity of the particle

h is the heat transfer coefficient for the convected fluid surrounding the particle. h is defined by the equation

$$q/\Delta = h \Delta T \quad (5.2-6)$$

the value of h is generally estimated in terms of a dimensionless Nusselt number:

$$Nu = \frac{hD}{k_F} \quad (5.2-7)$$

where D = diameter of the particle

k_F = thermal conductivity of the fluid flowing around the particle.

The Nusselt number is generally estimated from a correlation involving Reynolds number and Prandtl number. An acceptable correlation for sphere is:

$$Nu = 2 + .6 Re^{1/2} Pr^{1/3} \quad (5.2-8)$$

Reynolds Number is defined:

$$Re = \frac{\rho V D}{\mu} = \frac{GD}{\mu} \quad (5.2-9)$$

where ρ is density of the fluid

V is velocity of the fluid

D is diameter of the particle

μ is viscosity of the fluid

and Prandtl number is:

$$Pr = \frac{C_p \mu}{k_F} \quad (5.2-10)$$

where C_p is specific heat of the fluid at constant pressure

μ is viscosity of the fluid

k_F is thermal conductivity of the fluid

For hydrazine decomposition products the following estimates of physical properties were assumed:

$$C_p = .725 \text{ cal/gram } ^\circ K$$

$$\mu = 6.66 \times 10^{-4} \text{ poise}$$

$$k = 5.56 \times 10^{-4} \text{ cal/cm sec } ^\circ K$$

$$Pr = \frac{.725 \times 6.66 \times 10^{-4}}{5.56 \times 10^{-4}} = .736$$

For a conservative catalyst bed design, the following values were assumed:

$$G = .05 \frac{\text{pounds}}{\text{in}^2 \text{ sec}} = 3.5 \frac{\text{gram}}{\text{cm}^2 \text{ sec}}$$

$$D = .10 \text{ cm (25 mesh)}$$

then,
$$Re = \frac{3.5 \times .10}{6.66 \times 10^{-4}} = 526.$$

The Nusselt Number may now be calculated

$$Nu = 2 + .6(526.)^{1/2}(.736)^{1/3} = 14.4$$

This permits calculation of the heat transfer coefficient:

$$h = \frac{Nu K}{D} = \frac{14.4 \times 6.56 \times 10^{-4}}{.1} = .0944 \frac{\text{cal}}{\text{cm}^2 \text{ } ^\circ\text{K}}$$

To estimate the Biot number it is necessary to have a value for the thermal conductivity of the catalyst. Values may be found in the literature which vary from .005 to .05 $\frac{\text{cal}}{\text{cm sec } ^\circ\text{K}}$ hence the Biot number for the external

heating of the particle will fall within the range:

$$Bi = \frac{.0944 \times .05}{.05} = .0944$$

to

$$Bi = \frac{.0944 \times .05}{.005} = .944$$

Obviously if different values are used for pellet radius or bed loading (chamber pressure or contraction area ratio) then the Biot number will vary correspondingly.

To estimate the Biot number for the cooling of a hot particle being quenched in liquid hydrazine, a value for the maximum heat transfer coefficient for boiling heat transfer to the quench liquid must be obtained. Experimental investigations of boiling heat transfer to water show that the heat transfer rate increases rapidly with temperature difference until a threshold value is reached, whereupon the heat transfer changes from nucleate boiling to film-boiling, and the heat transfer rate decreases enormously. At the maximum value, just before the transition, the temperature difference is approximately 150°F (83°C) and the heat transfer rate is approximately 410,000 BTU/hr-ft² (30.9 cal/cm² sec). The corresponding value for heat transfer coefficient is:

$$h = \frac{30.9}{83} = .37 \text{ cal/cm}^2 \text{ } ^\circ\text{C}$$

If we presume that this same value will be obtained with boiling hydrazine instead of water, then the Biot number may be estimated (using high and low estimates for thermal conductivity of the catalyst):

$$Bi = \frac{.37 \times .05}{.05} = .37$$

$$Bi = \frac{.37 \times .05}{.005} = 3.7$$

Hence external cooling by cold hydrazine results in a Biot number approximately four times higher than external heating by hot product gases.

The Fourier number is the undimensionalized time in which a transient heating or cooling event may be measured. The time required to heat an object is proportional to its heat storage capability:

$$\Delta H = AL\rho C_p \Delta T \quad (5.2-11)$$

where

ΔH is stored heat

A is cross-sectional area of the element

L is the length of the element

ρ is the density of the material

C_p is the specific heat of the material

ΔT is change in temperature

The time required to heat an object is inversely proportional to its heat conduction rate H , where

$$H = \frac{A K_t}{L} \Delta T \quad (5.2-12)$$

where K_t is thermal conductivity

Combining the expressions, and introducing a parameter of proportionality:

$$t = Fo \frac{\rho C_p L^2}{K_t} \quad (5.2-13)$$

The parameter in this expression, Fo , is called the Fourier number, and expresses the extent of completion of the thermal transient.

For a particle of catalyst:

$$\rho = 3.4 \text{ gram/cm}^3$$

$$C_p = .22 \text{ calories/gram } ^\circ K$$

$$L(\text{radius}) = .05 \text{ cm (25 mesh)}$$

$$K = .01 \text{ (median value) calories/cm sec } ^\circ K$$

$$Fo = \frac{Kt}{\rho C_p L^2} = \frac{.01 t}{3.4 \times .22 \times .05^2} = 5.4 t$$

With the Biot number and Fourier number identified, it is easy to look up the solutions for the transient temperature profiles inside the catalyst particles in standard reference texts, (Reference 103). A family of profiles for a Biot number of 1.0 similar to a worst-case for external heating is shown in Figure 5.5. A family of profiles for a Biot number of 4.0, similar to a worst-case for external cooling is shown in Figure 5-6.

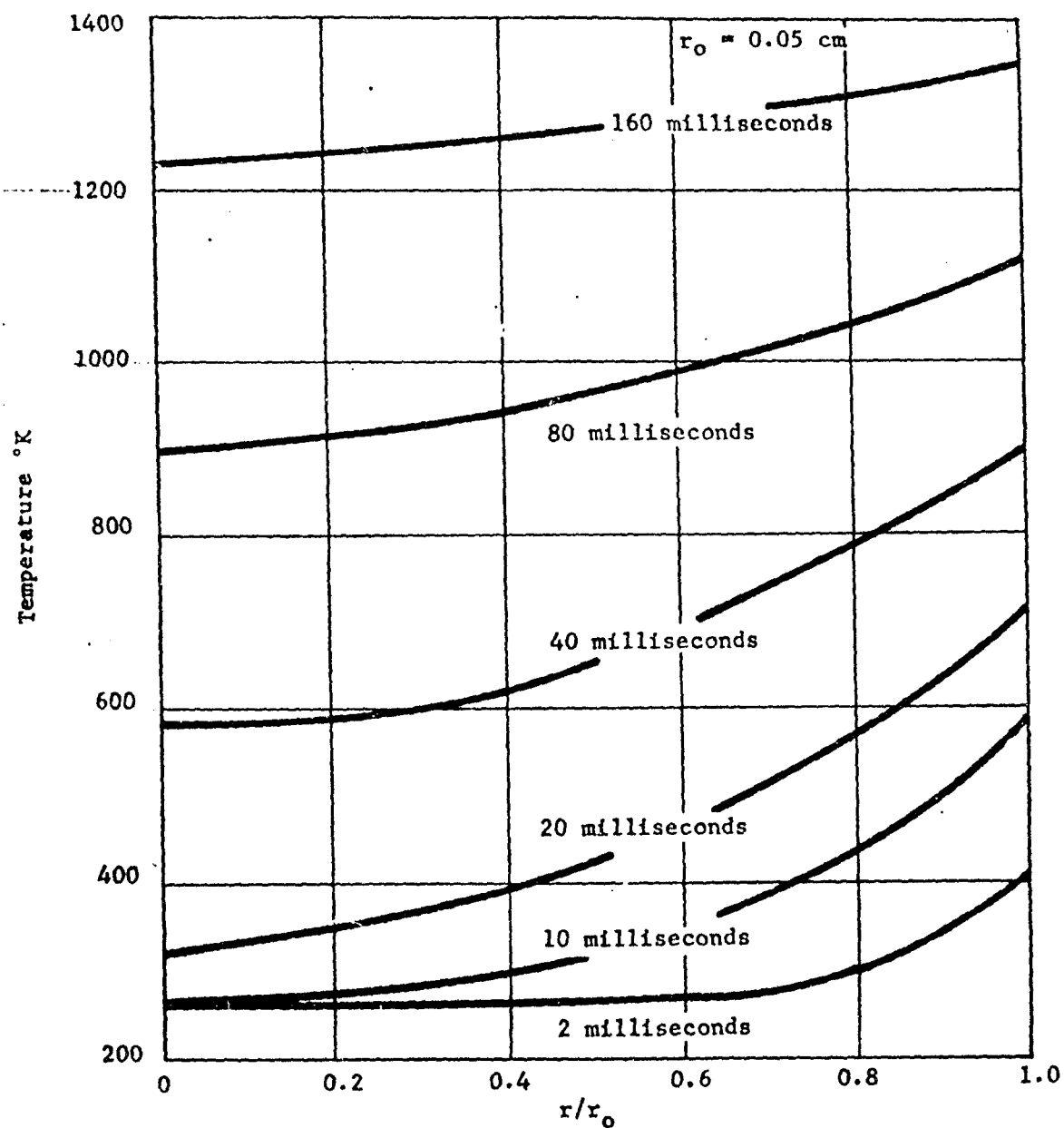


Figure 5-5. Temperature Profiles in an Externally Heated Spherical Pellet as a Function of Time During Heating.

Biot Number = 1.0

Hot Gas Temperature = 1473°K

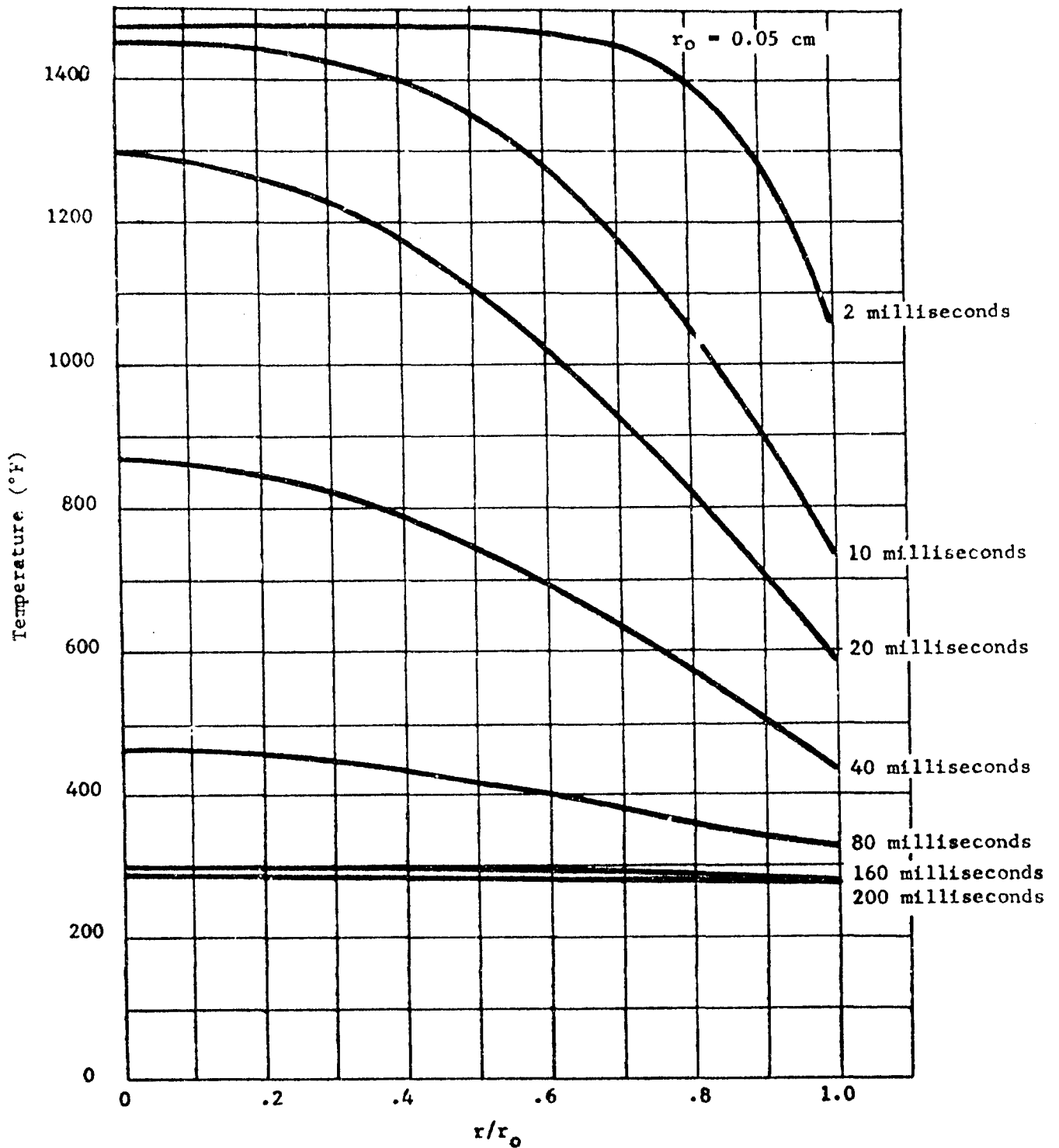


Figure 5-6. Temperature Profiles in an Externally Cooled Spherical Pellet as a Function of Time.

Biot Number = 4.0, corresponding to maximum rate nucleate boiling heat transfer.

5.2.3 Particle Stresses Resulting From Thermal Shock

The stresses which result from internal temperature profiles developed in a catalyst particle may be calculated for spherical, isotropic homogeneous materials. The loads were assumed to be spherically symmetric. Then for an arbitrary temperature profile, $T(r)$, the radial and tangential stresses which are classical elastic solutions from Reference 101 are

$$\sigma_r(r) = \frac{2\alpha E}{1-\nu_p} \left[\frac{1}{r_o^3} \int_0^{r_o} T(r) r^2 dr - \frac{1}{r^3} \int_0^r T(r) r^2 dr \right] \quad (5.2-14)$$

and

$$\sigma_t(r) = \frac{\alpha E}{1-\nu_p} \left[\frac{2}{r_o^3} \int_0^{r_o} T(r) r^2 dr + \frac{1}{r^3} \int_0^r T(r) r^2 dr - T(r) \right] \quad (5.2-15)$$

where

- σ_r = radial stress (psi)
- σ_t = tangential stress (psi)
- α = coefficient of thermal expansion of the porous sphere (in/in °F)
- E_p = Young's modulus of the porous medium (psi)
- ν_p = Poisson's ratio of the porous medium
- r = radius (in)
- r_o = outer radius of the sphere (in)

To show the types of stress distributions and some general results from the above equations, consider the temperature profile

$$T = A \left(\frac{r}{r_o} \right)^n \quad (5.2-16)$$

which allows closed-form solutions. This function is sketched in Figure 5.7. The total temperature difference is always A , while the abruptness of the temperature rise increases as n is increased. Thus the effects of A and n upon thermal stresses calculated using these profiles reveals the effect of total temperature difference in the particle, and the effect of varying temperature gradient in the particle. The above distribution produces a radial stress field which is

$$\sigma_r = \frac{2\alpha EA}{(1-\nu_p)(n+3)} \left[1 - \left(\frac{r}{r_o} \right)^{n+3} \right] \quad (5.2-17)$$

The maximum absolute value of the radial stress which occurs at $r = 0$ is

$$\sigma_r = \frac{2\alpha EA}{(1-\nu_p)(n+3)} \quad (5.2-18)$$

This stress is tensile for $A > 0$ (heating) and compression for $A < 0$ (cooling). The transverse stress σ_t from equation 4.2-15 becomes

$$\sigma_t = \frac{\alpha EA}{(1-\nu_p)(n+3)} \left\{ 2 - (n+2) \left(\frac{r}{r_0} \right)^n \right\} \quad (5.2-19)$$

Therefore, for $A > 0$ this starts as a tensile stress at $r = 0$ of the same magnitude as $\sigma_r(0)$ and reaches a compressive maximum at $r = r_0$ of

$$\sigma_t = \frac{\alpha E A n}{(1-\nu_p)(n+3)} \quad (5.2-20)$$

at the surface. For cooling ($A < 0$) σ_t starts in compression at $r = 0$ and goes to tension at the outer surface. Therefore, the ratio of the maximum tensile stress to maximum compressive stress is, for heating $2/n$.

From equations (18) and (20) it can be seen that the maximum stresses are directly proportional to the temperature difference, A , between the outside and inside of the sphere. For $r = 0$, the center of the sphere, the stress state is hydrostatic ($\sigma_r = \sigma_t$), and when $A > 0$ (heating) tensile stresses are produced. Also, at $r = 0$ the steeper the gradient (the larger n is) the smaller the stress. If $A < 0$ (cooling) this stress state would be compressive. Since it is a hydrostatic compressive stress, no failures occur on cooling. Therefore, at $r = 0$, the heating condition ($A > 0$) is the only one which can produce a failure.

At the surface of the sphere, $r = r_0$, the radial stress, σ_r , is zero. The transverse stress for heating ($A > 0$) is negative (compression). Since this is a uniaxial stress state, a failure can occur. The magnitude of the compression is $\frac{n}{2} \sigma_r$. Near the surface σ_r is small, but tensile,

and thus will reduce the amount of the σ_t compressive stress required to produce a failure, thus a failure could initiate below but near the surface. On cooling ($A < 0$) the surface will be in tension, hence the failure will only occur at the exterior of the sphere and propagate inwards. The magnitude of surface stress is proportional to the temperature difference and the ratio $(n/n+3)$. Since $(n/n+3)$ increases as n increases, the steeper the gradient, the greater the surface stress.

Now consider a specific heatup/cooldown case in a 20-25 mesh catalyst particle. The radial and tangential stress solutions for the typical temperature profiles for heat-up, Figure 5-5 and cooldown, Figure 5-6, are shown in Figures 5-8 to 5-11. These show the greatest temperature difference on heating occurs at 20 milliseconds, which produces the greatest tensile and compressive stress. On cooldown the greatest tensile stress occurs at 10 milliseconds.

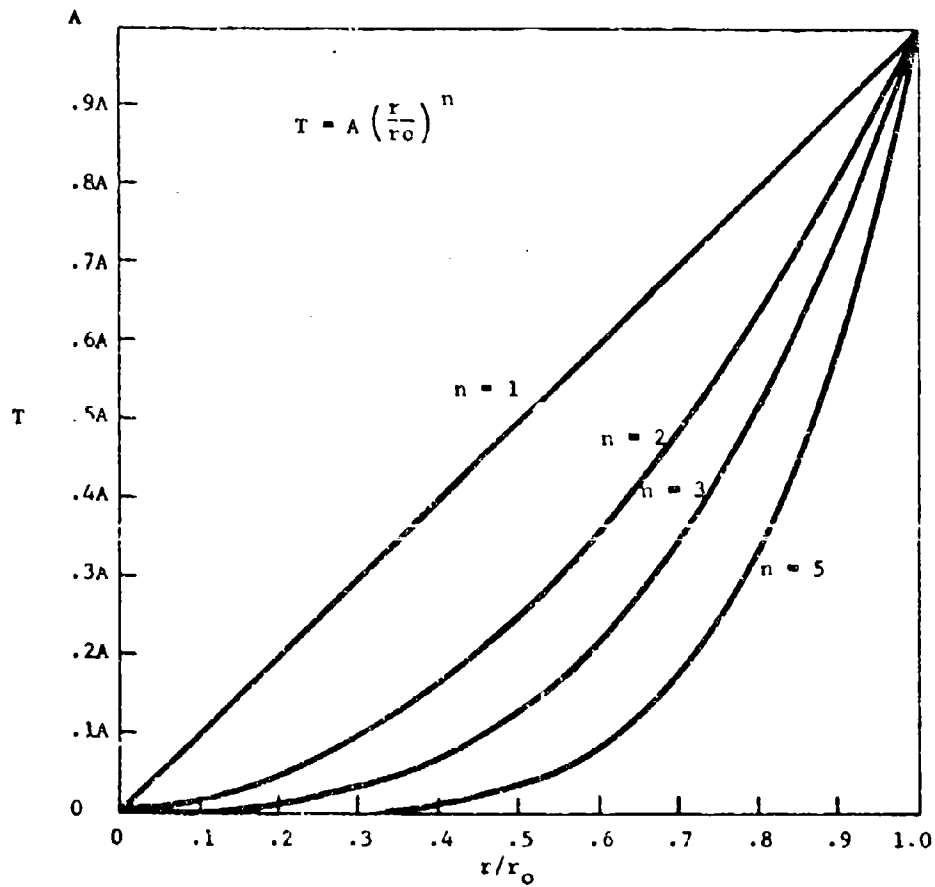


Figure 5-7. Arbitrary Temperature Profiles for Estimating Effects of Thermal Stress.

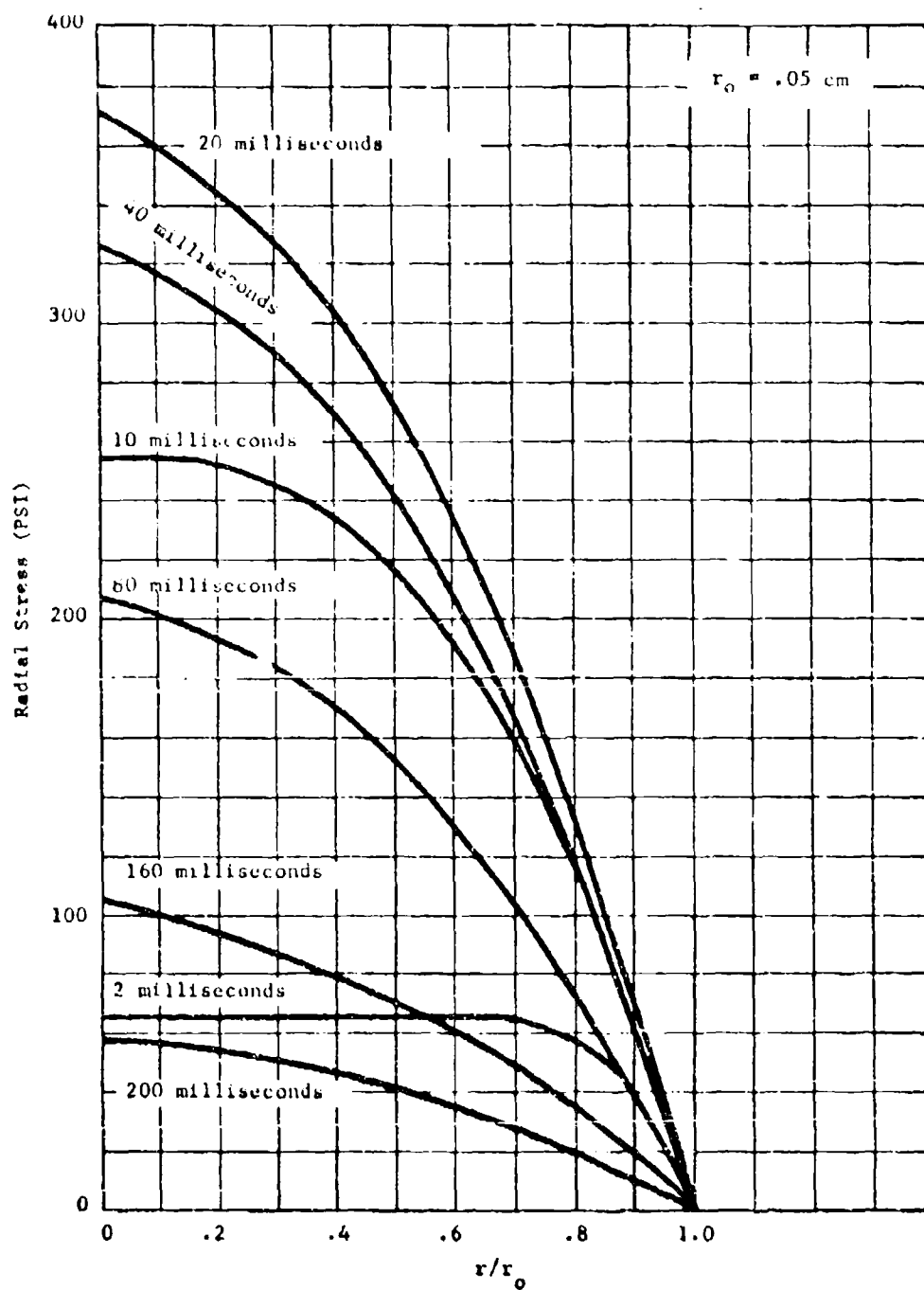


Figure 5-8. Radial Stress As A Function of Time Produced by Heating
 $G = .05 \text{ pounds/in}^2$, Gas Temp. = 1473°K , Particle Temp. = 273°K

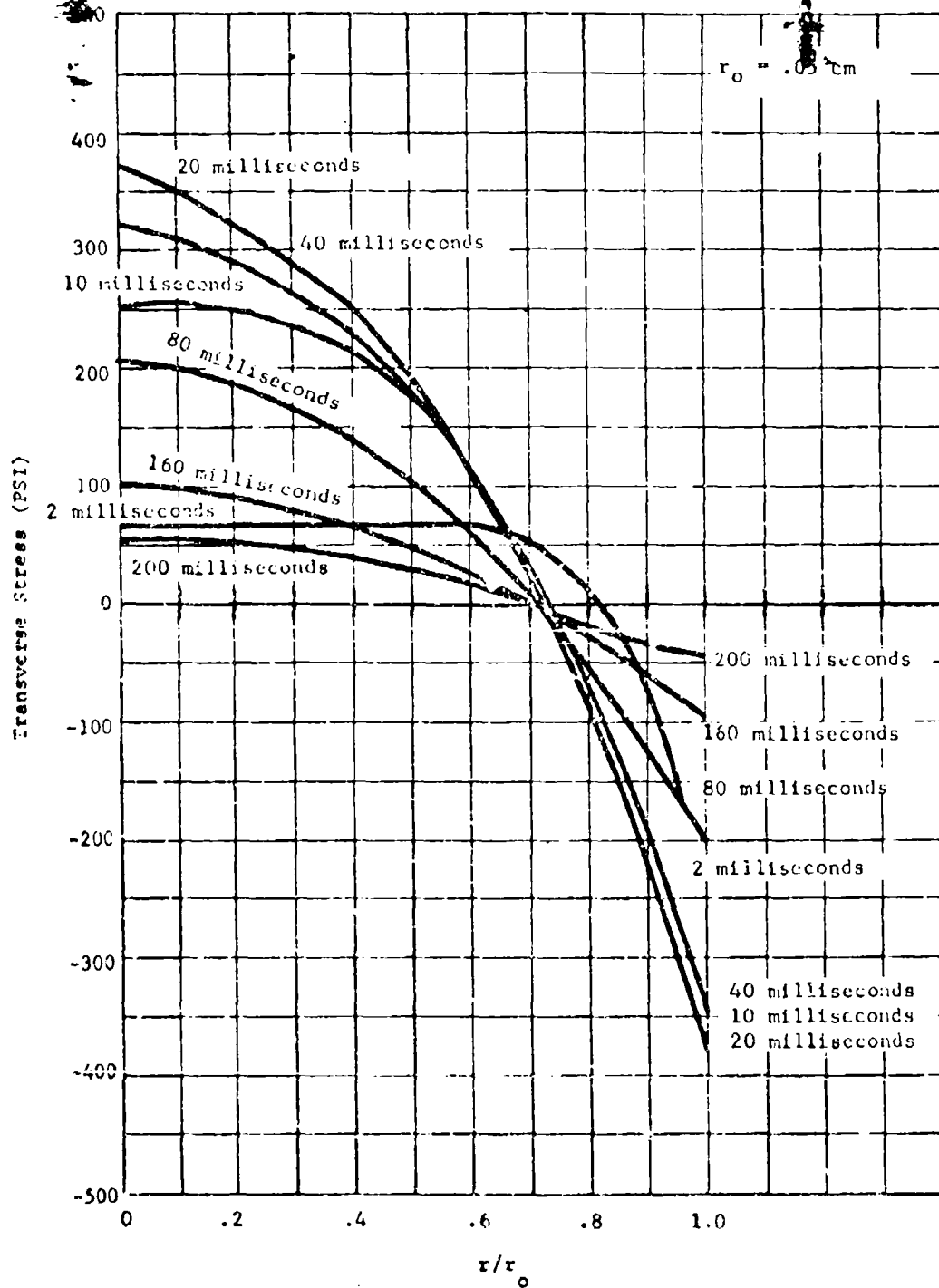


Figure 5-9. Transverse Stress as a Function of Time Produced by Heating.

$G = .05$ pounds/in². sec. Gas Temp. = 1473°K, Particle Temp. = 273

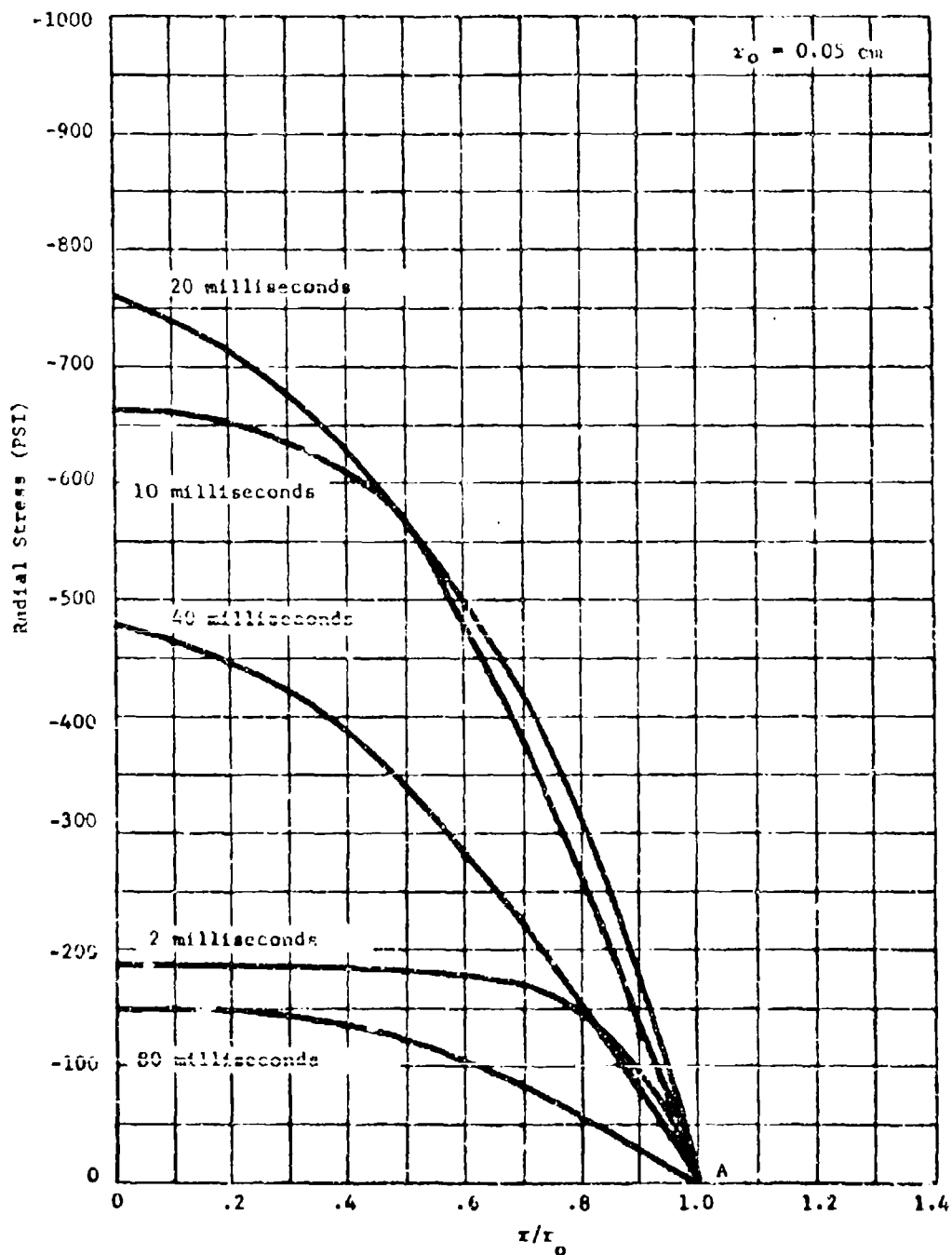


Figure 5-10. Radial Stress as a Function of Time Produced by Cooldown.
Maximum Rate Nucleate Boiling Heat Transfer.

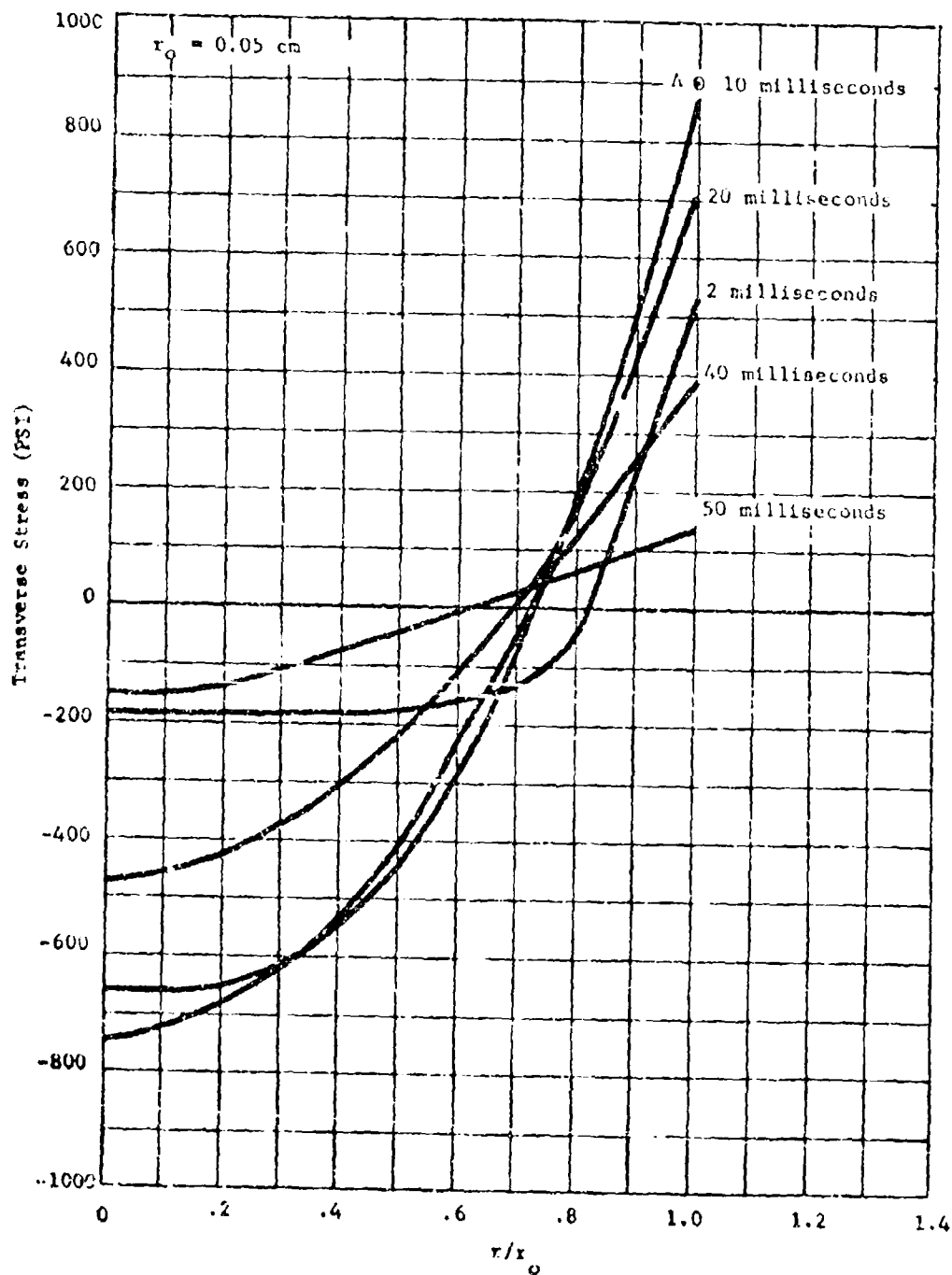


Figure 5-11. Transverse Stress as a Function of Time Produced by Cooldown.
Maximum Rate Nucleate Boiling Heat Transfer.

On heating, for $\nu_p = 0.3$ (see the failure section for a discussion of the Poisson's ratio ν), the maximum tensile stress is 380 psi which is hydrostatic $\sigma_r = \sigma_\theta$. Although this is a triaxial stress state, it is well below failure for the two dimensional equal-load ($S_1 = S_2$) biaxial limit, so the heating case does not appear to be a possible point of failure.

On cooldown, the maximal tensile stress occurs at the outer radius. The maximum tensile stress occurs at 10 milliseconds and is 885 psi. The stress state at this point is biaxial, with the stresses being equal in the two transverse directions and $\sigma_r = 0$. This is illustrated as Point "A" in figures 5-3, 5-4, 5-10, and 5-11. Therefore, between 25% and 50% failure would be expected for the virgin material. If used material were cooled down, since the mean failure stress is lower and the scatter is larger, between 75% and 95% failures would be predicted with this material. It should be reiterated that this is for the particular situation of 20-25 mesh, initial temperature of 1473°K (2191°F) and flow conditions such that the quenching liquid remained in the nucleate boiling regime, rather than film boiling.

These conclusions were drawn assuming $\nu_p = 0.3$. The tensile stresses which would be predicted decrease as ν_p decreases. If $\nu_p = 0.1$, then the maximum tensile stress on cooldown would decrease from 885 psi to 688 psi and fewer failures would be expected in either fresh or used materials. However, this latter value of Poisson's ratio appears much too low based on estimates made by Professor Hasselman (see Section 3.3), who predicts a value of 0.25 which is much closer to the original assumption of 0.3. The uncertainties in the predictions which arise from lack of accurate values for tensile failure stresses and Poisson's ratio, point up the need for experimental determinations of these important material properties.

In general, the results indicate that failure as a result of hot gas thermal shock during heating is unlikely, where failure from liquid quench thermal shock during cooldown is distinctly possible.

5.2.4 Pressure Profiles Developed Inside a Catalyst Particle by External Pressurization or Depressurization

If the boundary of a porous, permeable catalyst particle is suddenly exposed to a high pressure gas, a series of transient pressure profiles are developed in the particle, until pressure equilibration is finally obtained. If a catalyst particle has fully pressure-equilibrated at a high pressure, and suddenly has the boundary pressure reduced to a low value, the same sort of process occurs, with the flows being in the reverse direction. The processes of mass flow of gas through the permeable material, and accumulation of mass in the porosity volume, is quite analogous to the transient response to external heating or cooling. To determine the relevant time scale for the pressurization or depressurization process, a dimensionless parameter similar to the Fourier number may be developed.

The accumulation of gas mass in an element of porous solid is:

$$\Delta M = \frac{A L \phi M_w \Delta P}{R T} \quad (5.2-21)$$

where ϕ is porosity

M_w is molecular weight of the gas

ΔP is change of pressure

R is gas constant

T is temperature

The mass transport rate by D'Arcy flow is

$$\dot{M} = \frac{A K_m M_w P \Delta P}{\mu L R T} \quad (5.2-22)$$

where K_m is permeability in cm^2

μ is viscosity of the fluid

Dividing one expression by the other gives a dimensionless group analogous to the Fourier Number:

$$N_m = \frac{K_m P t}{\phi \mu L^2} \quad (5.2-23)$$

To find the appropriate time scale for particle pressurization or depressurization, it is only necessary to evaluate t in the above expression. Since the most damaging temperature distributions were obtained at a Fo of about 0.1, it is reasonable to evaluate the expression for pressure at the same value.

$$t = \frac{\phi \mu L^2 N_m}{K_m P}$$

$$\phi = .26$$

$$\mu = 6.66 \times 10^{-4} \text{ poise}$$

$$L = .05 \text{ cm}$$

$$K_m = .1 \text{ Darcy} = 9.869 \times 10^{-10} \text{ cm}^2$$

$$P = 100 \text{ psia} = 6.8947 \times 10^6 \text{ dyne/cm}^2$$

$$t = \frac{.26 \times 6.66 \times 10^{-4} \times .05^2 \times .1}{9.869 \times 10^{-10} \times 6.8947 \times 10^6} = 6.36 \times 10^{-6} \text{ second}$$

Hence, the pressure equilibration process is very rapid compared to the thermal equilibration process. The time scale for the depressurization of a thrust chamber at the termination of a pulse is on the order of 1 to 100 milliseconds. This is so much slower a process than the time required for depressurization of a pellet that we must conclude that no internal pressure stresses will occur during a normal cutoff. Very rapid pressurization of a pellet could take place, by local detonations or shock waves in the chamber. Since the catalyst is relatively strong in compression, a steep fronted wave of over a thousand psi would be required to cause any damage by pressure-generated stresses in the individual particles. Explosions of this amplitude would produce much more destructive effects by producing compaction pressures within the bed, so the effects of externally impressed pressure upon the individual particle may be identified as non-destructive. The worst-case pressure profiles and internal stress levels which would be generated by 1000 psi pressurization or depressurization episodes are illustrated in Figures 5-12 and 5-13.

5.2.5 Particle Stresses Resulting from Internal Pressure During Pressurization or Depressurization in the Absence of Liquid

The stresses resulting from internal pressure may be calculated in a manner quite similar to those for the temperature gradient. The total stress per unit area, e.g., τ_r is the sum of the average stress in the solid material, e.g., σ_r plus the average stress, $-fp$, caused by the pore pressure, (Reference 104) i.e.,

$$\tau_r = \sigma_r - fp \quad (5.2-24)$$

where p = pressure in the pore (psi)
 f = void fraction

Note that pressure is considered positive in compression and stress is considered positive in tension. The average stress in the solid material (per unit area of porous material) is what controls failure. Using equation (24), one finds that for an arbitrary point symmetric pressure profile $p(r)$ in a sphere of radius r_0 where the external pressure on the outer surface is equal to $p(r_0)$, the radial and tangential stresses are:

$$\sigma_r(r) = \frac{2(1-2\nu)}{1-\nu} f \left[\frac{1}{r_0^3} \int_0^{r_0} p(r) r^2 dr - \frac{1}{r^3} \int_0^r p(r) r^2 dr \right] + fp(r) - p(r_0) \quad (5.2-25)$$

and

$$\sigma_t(r) = \left(\frac{1-2\nu}{1-\nu} \right) f \left[\frac{2}{r_0^3} \int_0^{r_0} p(r) r^2 dr + \frac{1}{r^3} \int_0^r p(r) r^2 dr \right] + \left(\frac{\nu}{1-\nu} \right) fp(r) - p(r_0) \quad (5.2-26)$$

For the purposes of equations 25 and 26 the pressure, $p(r)$, is the absolute pressure.

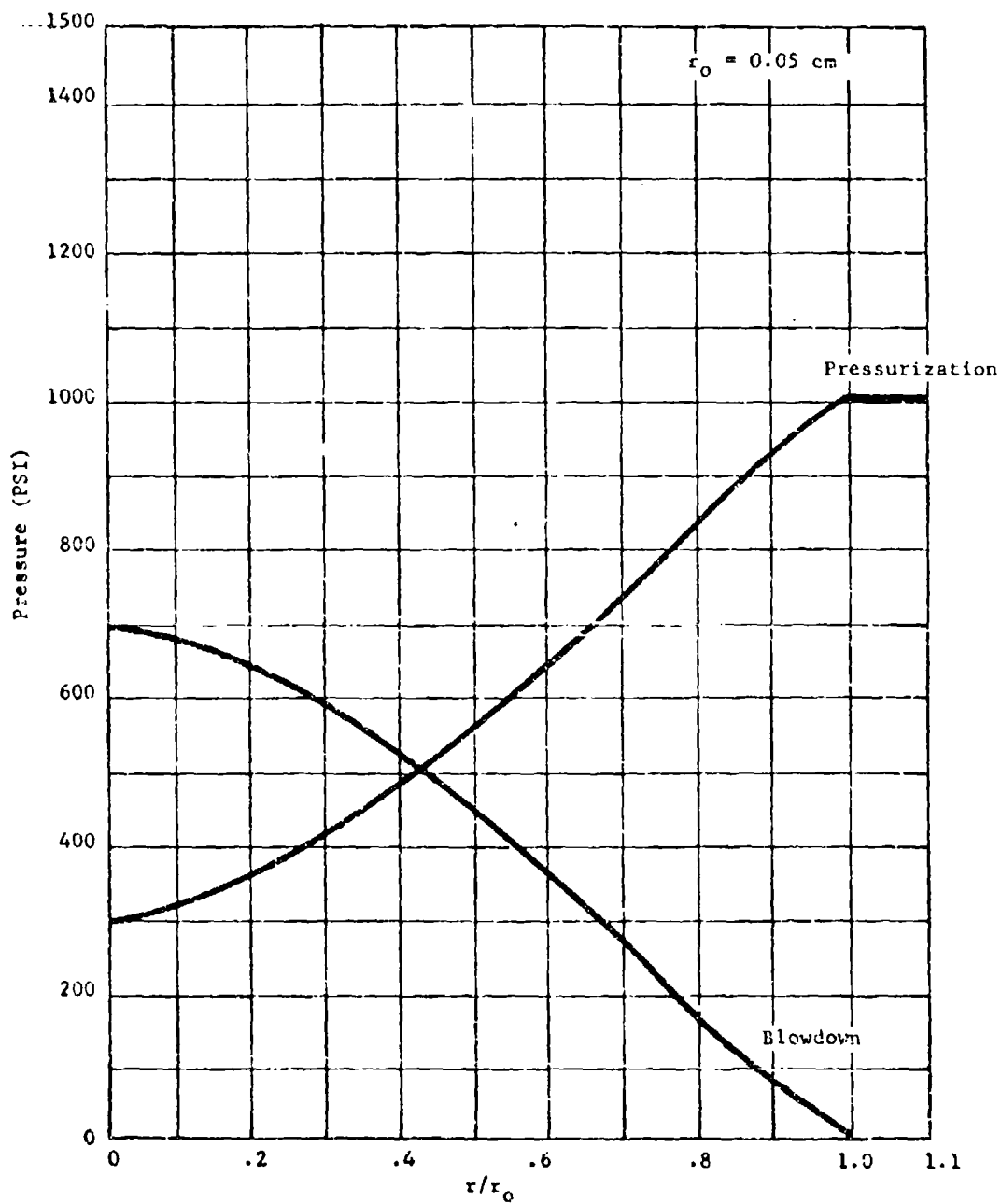


Figure 5-12. Worst-Case Pressure Profiles Due to Pressurization and Blowdown.

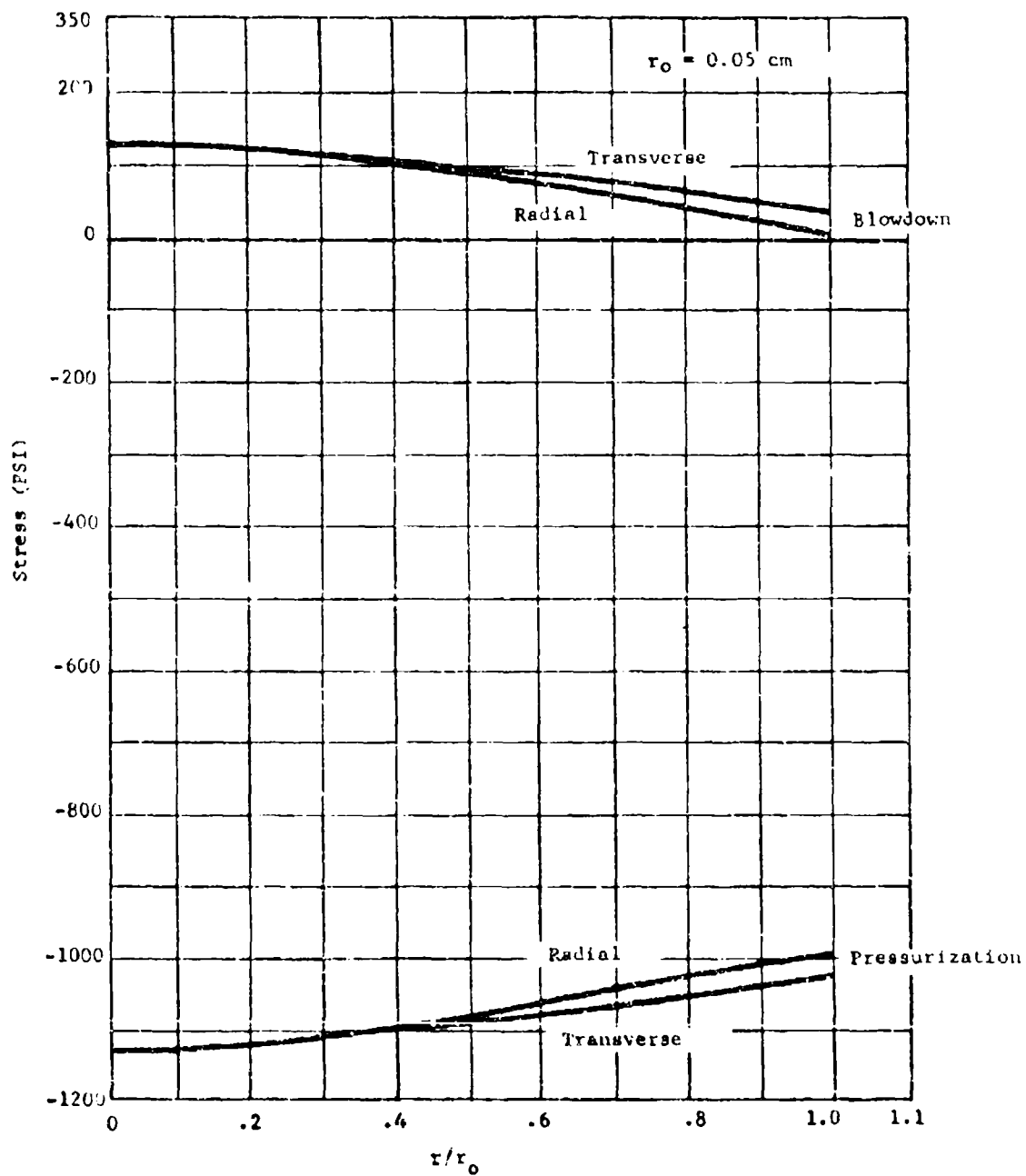


Figure 5-13. Stresses Produced by the Pressurization and Blowdown in Shell 405 Catalyst.

The effect of the internal pressure profiles on the stress in the substrate material can be studied by looking at the solution to two pressure cases, one which represents pressurization to 1000 psi and the other blowdown to 0 psi, and as shown in Figure 5-12. The stress distributions produced by these pressure profiles are shown in Figure 5-13. On pressurization to 1000 psi, the stresses are compressive in the body, and almost hydrostatic. On blowdown, the stresses are tensile, but are very low, even for this steep profile.

Because the stress-state in the body during pressurization is almost hydrostatic compression no material failure is expected. The stress state during blowdown is almost hydrostatic tension. The stress levels in the matrix are much lower than would be needed to produce failure, using the biaxial failure envelope given in Figure 5-3. Therefore, if these are the worst case pressure profiles, then the internal pressure stress should not produce material failure.

The solutions to equations (14), (15), (25), and (26) have been combined in a small computer program which solves both the thermal and internal pressure problems. The solution for the combined problem is obtained by superposition of the solutions. A pair of simultaneous pressure and temperature profiles are shown in Figure 5-14 and the corresponding combined stresses in Figure 5-15. These are typical profiles and are just to illustrate the principle of superposition. The resultant stress distributions shown in Figure 5-15 show the related magnitude of the thermal and internal pressure solutions. These solutions show that for our material and the pressure and temperature profiles of interest, the worst case thermally generated stresses are greater than those generated by the worst case internal pressure distribution due to pressurization and blowdown.

In general, it is concluded that the pore pressure gradients present in the catalyst particle during either rapid gas pressurization or depressurization in the absence of liquid will not cause particle failure.

5.2.6 Particle Stresses From Bed Compression

Whenever the bed of catalyst pellets is made to bear a compressive load, local stresses are produced at the tiny areas where the pellets actually come into contact with each other. It is the local stresses produced in the pellets at these points of contact which can cause local failure and the loss of material associated with bed compression stress. There are four relationships which must be determined to define the effects of compression:

1. What is the relationship between bed compression pressure and the normal force developed between adjoining particles (required for the analysis of flow-induced pressure loadings acting on the bed, and also for differential thermal expansion).

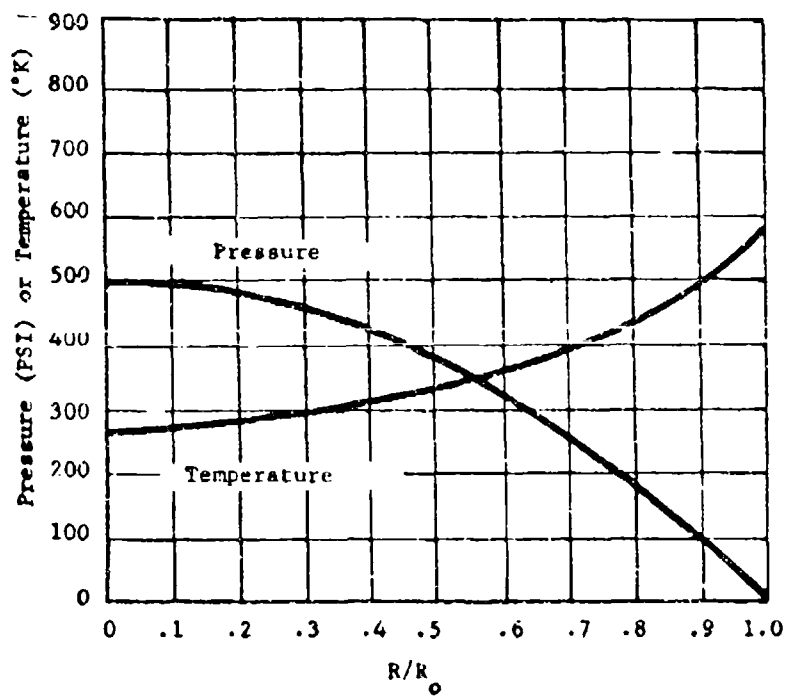


Figure 5-14. Pressure and Temperature Profiles to Determine the Radial and Transverse Stress Distributions.

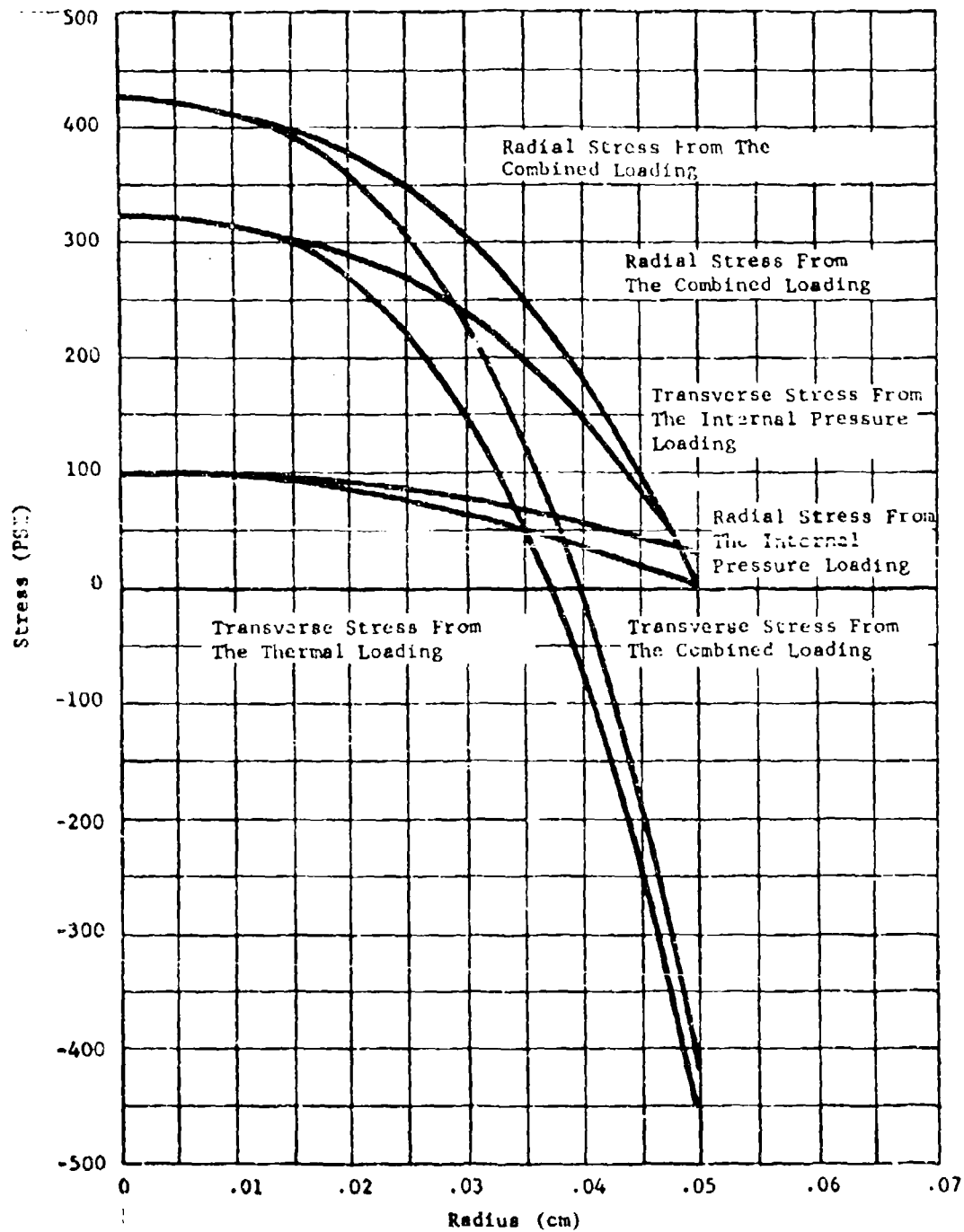


Figure 5-15. Radial and Transverse Stresses as a Function of Radius For Simultaneous Thermal and Internal Pressure Loading.

2. What is the relationship between bed volume change and the resulting bed compaction pressure (required for the problem of differential thermal expansion)?
3. What are the distributions of stresses produced in a particle by a given level of normal force applied by another identical particle.
4. What is the volume of material which will fail as a result of the stress distributions produced in the particle, and what happens to the smaller fractured particles i.e. are they blown out of the catalyst bed or trapped in bed interstices.

5.2.6.1 Particle-to-Particle Forces Resulting from Bed Compression

We will assume that the bed is composed of identical spheres arranged in a face-centered cubic array, (theoretical closest packing) as illustrated in Figure 5-16. It may be seen that Sphere E is in contact with twelve other adjoining spheres, and that all the bed compression forces acting upon Sphere E must be supported by these twelve points of contact. Let us assume that the spheres are frictionless at the points of contact, so that all of the points of contact produce only forces normal to the surfaces. From considerations of symmetry, the forces acting on the x, y, and z faces of the unit cube will be equal, i.e., the bed compression will act like a hydrostatic pressure. The force acting on the z-normal face will be equal to the bed compression stress multiplied by the area of the z-normal face of the unit cube. The length of the diagonal across this face includes the diameter of Sphere E and the radii of Spheres B and D, hence the length of the diagonal is $4R$ where R is the radius of the spheres. The length of the side of the unit cube, then, must be $2\sqrt{2}R$, and the area of the face must be $8R^2$. If the bed compression stress is P , then the force exerted on the z-normal face of the unit cube is $8R^2P$. This force in the z direction will be shared between the upper cut portions of Spheres E, A, B, C, and D, with Sphere E supplying one half of the total projected area in the plane. The force borne by Sphere E will be one half the total or $4R^2P$.

Since we have hypothesized frictionless contacts, with only normal forces, none of the z-directed force acting upon Sphere E can be balanced by its contacts with Spheres A, B, C, or D, hence, all of the support for Sphere E in the z direction must come from its contacts with Spheres F, G, and the other two equivalent hidden spheres. Each point of contact must contribute one quarter of the total z-directed force or R^2P . It may be seen that the forces acting between Sphere E and the spheres below it, are elevated 45° from the x-y plane, and hence each particle-to-particle force F is R^2P divided by the cosine of 45° , hence:

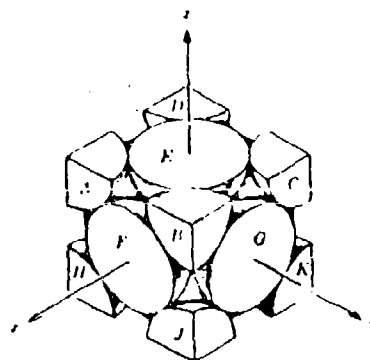


Figure 5-16. Unit Cube from a Face-Centered Cubic Array of Identical Spheres.

$$F = \sqrt{2} R^2 P \quad (5.2-27)$$

where F is the force between the particles
 R is the radius of the spheres
 P is the pressure applied to the bed

This derivation closely follows Reference 105. The relationship given in Equation 5.2-27 was also shown to be valid for hexagonal-close packing, (106). In a later section a method for determining the applicability of Equation (5.2-27) to our problem will be presented.

5.2.6.2 Stress Produced in the Particle from Point-to-Point Contact

The stresses from particle-to-particle contact, due to bed compression, may be calculated from Hertz contact theory. The Hertz contact analysis defines the stress distribution in a semi-infinite body due to the pressure distribution produced by a spherical indenter. The solution can be extended to the contact between two spheres if the radius of contact, a , is small compared to the radius of the body, R_0 , as shown in Figure 5-17. The solution is shown in Reference 101. If the approximation $R_0 \gg a$ is large is not valid, then the solution can only be obtained by the use of complex computer codes.

The solution to the contact problem as presented in Reference 101, assumed the displacements of points within the contact area, a , Figure 5-17, that were required to bring the points, on the surface of each sphere at $R = a$, into contact. Hertz assumed the stress distribution within the contact area was hemispherical, with the maximum occurring at the center of the contact area. The displacements predicted by the assumed stress distribution agree with those calculated to bring the points on the surface of the spheres in contact. Knowing the stress distribution and the contact force, F , the maximum contact stress was shown in Reference 101 to be:

$$q_0 = \frac{3}{2} \frac{F}{\pi a^2} \quad (5.2-28)$$

with a radius of contact of

$$a = \sqrt[3]{\frac{3}{4} \frac{(1-\nu^2)}{E} F R_0} \quad (5.2-29)$$

where ν is Poisson's ratio
 E is Young's Modulus

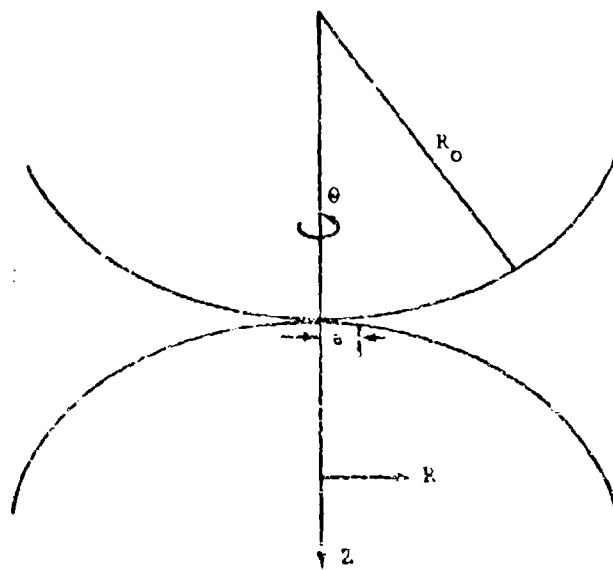


Figure 5-17. Schematic of the Contact Problem.

To relate the contact stresses to the bed pressures a relationship such as Equation (5.2-27) is required. For the remainder of the analysis of the contact problem, the bed will be assumed to be either a face-centered cubic or a hexagonal close packed sphere aggregate. Therefore, the contact stress and radius of contact can be related directly to the bed pressure by using Equations (5.2-27), (5.2-28) and (5.2-29).

For our case, using the Poisson's ratio of the porous sphere, ν_p , as described in the failure section, and solving Equations (5.2-28) and (5.2-29) and using F from Equation (5.2-27) yields.

$$q_0 = 0.6492 \sqrt[3]{\frac{E^2 P}{(1-\nu_p^2)^2}} \quad (5.2-30)$$

and

$$a = 1.0198R \sqrt[3]{\frac{P}{E} (1-\nu_p^2)} \quad (5.2-31)$$

With the values of q_0 and a , the resultant three-dimensional stress distributions in a semi-infinite flat body produced by a spherical indenter can be calculated by using the relationships developed by Love, Reference 107. Love showed the stresses are

$$\sigma_R = q_0 \left\{ \frac{(1-2\nu_p)a^2}{3R^2} \left[1 - \left(\frac{z}{\psi}\right)^3 \right] + (1+\nu_p) \frac{z}{a} \tan^{-1} \left(\frac{a}{\psi}\right) \right. \quad (5.2-32)$$

$$\left. + (1-\nu_p) \frac{z\sqrt{4}}{a^2 + \psi} - 2 \frac{z}{\sqrt{\psi}} + \frac{a^2 z^3}{(\psi^2 + a^2 z^2)\sqrt{\psi}} \right\} \quad (5.2-33)$$

$$\sigma_\theta = q_0 \left\{ - \frac{(1-2\nu_p)a^2}{3R^2} \left[1 - \left(\frac{z}{\psi}\right)^3 \right] + (1+\nu_p) \frac{z}{a} \tan^{-1} \left(\frac{a}{\psi}\right) \right. \\ \left. - (1-\nu_p) \frac{z\sqrt{\psi}}{a^2 + \psi} - 2\nu_p \frac{z}{\sqrt{\psi}} \right\}$$

$$\sigma_z = p_0 \frac{a^2 z^3}{(\psi^2 + a^2 z^2) \sqrt{\psi}} \quad (5.2-34)$$

$$\tau_{rz} = p_0 \frac{a^2 R z^2 \sqrt{\psi}}{(\psi^2 + a^2 z^2)(R^2 + \psi^2)} \quad (5.2-35)$$

$$\tau_{\theta} = \tau_{\theta} = 0$$

where

$$\psi = \frac{1}{2} \left\{ R^2 + z^2 - a^2 + \sqrt{(R^2 + z^2 - a^2)^2 + 4a^2 z^2} \right\} \quad (5.2-36)$$

The q_0 used in this analysis is that from two spheres in point-to-point contact, given Equation 20.

The amplitude of the stresses presented in Equations (5.2-32 to (5.2-37), as discussed in Reference 101, decrease very rapidly as R/a increase from 1.0, where R is the distance from the center of contact as shown in Figure 5-6. At the surface, for $R/a > 3$, the $\sigma_r/q_0 < 0.02$. Therefore, if R/a is large, the effect of the curvature of the bodies can be neglected. In our case, for 10 psi in the bed, $R/a > 31$. Therefore, the use of the contact solution and the stress distributions in a flat semi-infinite half space should produce very good results for the stresses produced by the point-to-point contact of two spheres of Shell 405 catalyst.

The discussion of the results of the contact solution in Reference 101 show the maximum compressive stress, q_0 , occurs in the Z direction, see Figure 5-17 and at the center of the contact area $R = 0$, $Z = 0$ and is given by Equation 5.2-36. The stresses in the other two orthogonal directions in the $R=0$ plane, at the same location are also compressive and related to the maximum stress, Reference 101 by

$$\sigma_r = \sigma_{\theta} = \frac{1 + 2 \nu_p}{2} q_0 \quad (5.2-38)$$

The contact load goes to zero at the edge of the contact area, $R = a$. This is the location of the maximum tensile stress

$$\sigma_r = \frac{1 - 2 \nu_p}{3} q_0 \quad (5.2-39)$$

At the same location, $Z = 0$, $R = a$, the σ_θ stress is equal to $-\sigma_r$ and $\sigma_z = 0$. This is equivalent to a state of pure shear in the $r-\theta$ plane at that location. The effect of Poisson's ratio and the location of possible failures will be discussed later.

A computer program developed under another program, contract No. DNA001-72-C-0024, was modified to calculate the total stresses due to contact forces, thermal gradients and internal pressures. The solutions discussed below were generated by this program.

The effect of the Poisson's ratio, ν_p , of the porous material on the maximum contact stress, from Equation (5.2-30), as shown in Figure 5-18 is small. Figure 5-18 does show the maximum contact stress, q_0 , increases very rapidly for very low bed stresses.

At the center of the contact area, $R=Z=0$, the effect of ν_p on the other two orthogonal stresses, σ_r and σ_θ , in the $r-\theta$ plane, given by Equation (5.2-30), is shown in Figure 5-19. These orthogonal stresses are also compressive at this point and can vary from $q_0/2$ for $\nu_p = 0$ to q_0 for $\nu_p = 0.5$. Therefore, the center of the contact area is in a compressive state. The failure model, developed in this Section, for a two dimensional stress state indicates the failure, probability maximizes at the center of contact, and at the edge of the contact area. The effect of ν_p on the maximum tensile stress, σ_r from Equation (5.2-39) is shown in Figure 5-20. Changing the value of ν_p from 0.3 to 0.1 can double the tensile stress. The other stress in the $r-\theta$ plane, σ_θ , is compressive with a magnitude equal to σ_r . This is a state of pure shear at this location.

The stress distributions for σ_z , σ_r , and σ_θ along the contact surface, $Z=0$, as a function of R , where R and Z are defined in Figure 5-17, are shown in Figure 5-21. These stress distributions were calculated using the computer program mentioned earlier, for 10 psi bed pressure, $\nu_p = 0.3$ and $E = 300,000$ psi. At $R=0$, the center of contact, the stresses are all compressive. The σ_θ and σ_z stresses remain compressive throughout the contact area, $R/a \leq 1$. The σ_z stress becomes zero on the surface outside the contact area, $R/a > 1$, as would be expected as no surface loads are being applied. The σ_θ stress remains compressive for all R/a . The σ_r stress starts as a compressive stress and becomes tensile only near the edge of the contact area. The exact location is dependent on the material properties. For $R/a > 1$, outside the contact area, at $Z=0$, $\sigma_r = -\sigma_\theta$ decrease very rapidly, as shown in Figure 5-21, as R/a increases from 1.0.

For any given level of bed compaction pressure, the radial distribution of surface stress in the vicinity of the particle-to-particle contact may be obtained by referring to 5-18 to find q_0 and 4-21 to find σ_r/q_0 and σ_θ/q_0 versus radius (i.e. R/a). The values for σ_r and σ_θ which result may be plotted over the biaxial failure surface (illustrated previously as figures 5-3 and 5-4) to indicate the probability of failure at various locations within or adjacent to the area where the particles are in contact. This has been done in figure 5-22. The points marked A, B, C, D, E, F and G represent the values for σ_r and σ_θ at values for R/a of 0.0, 0.25, 0.50, 0.75, 1.0,

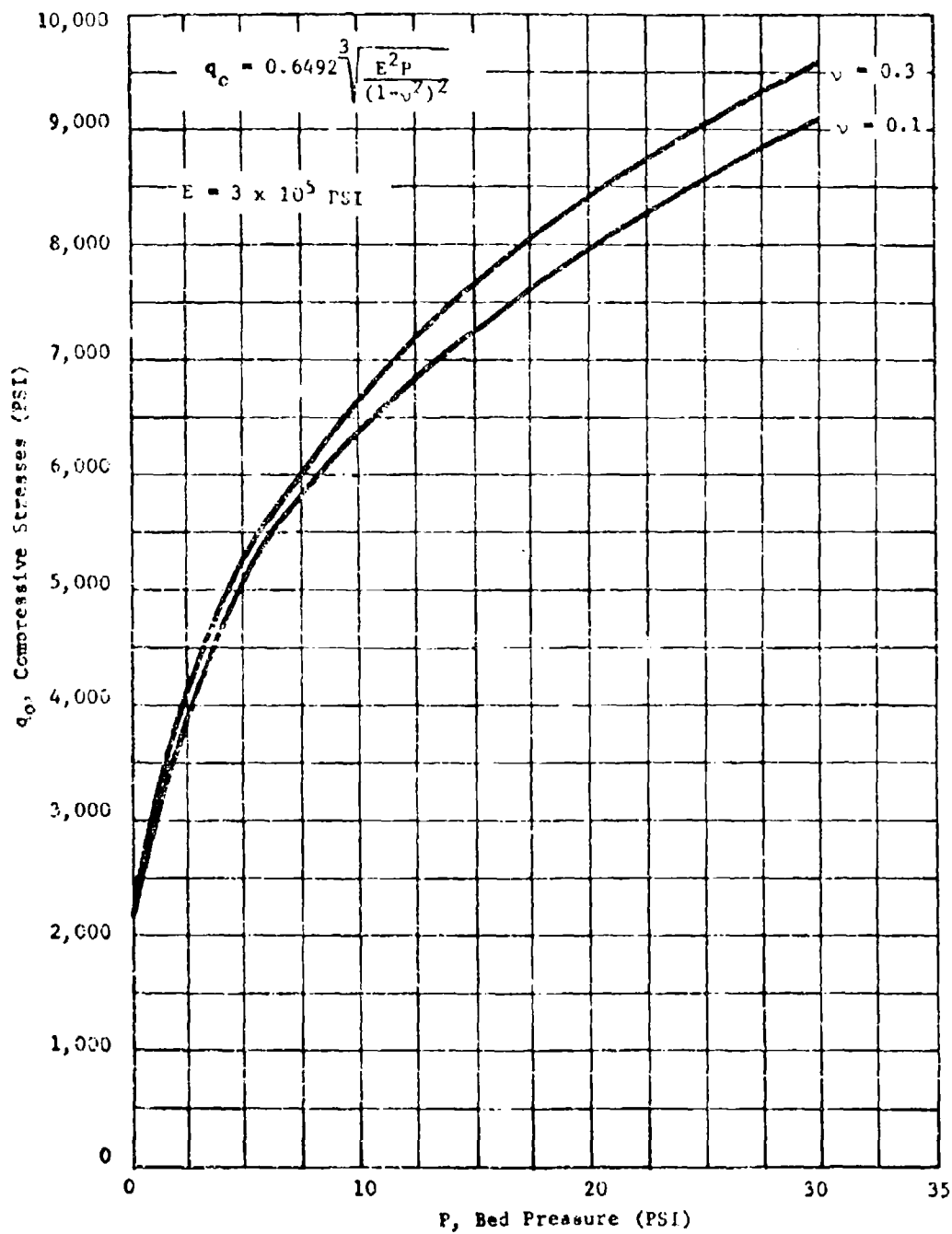


Figure 5-18. Maximum Contact Stress as a Function of the Mean Bed Pressure at the Center of the Contact Area.

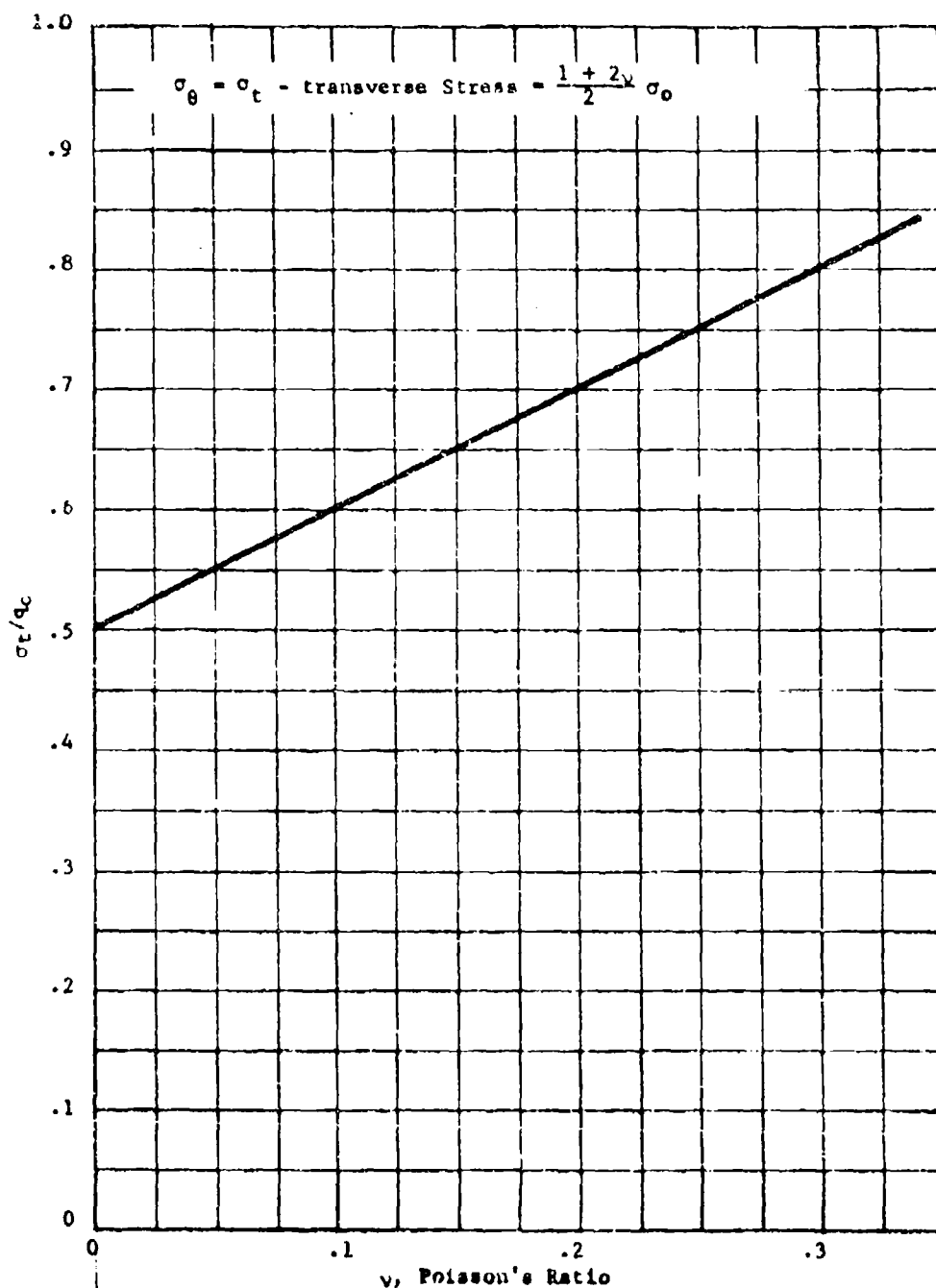


Figure 5-19. Effect of Poisson's Ratio on the Transverse Stresses at The Center of the Contact Area.

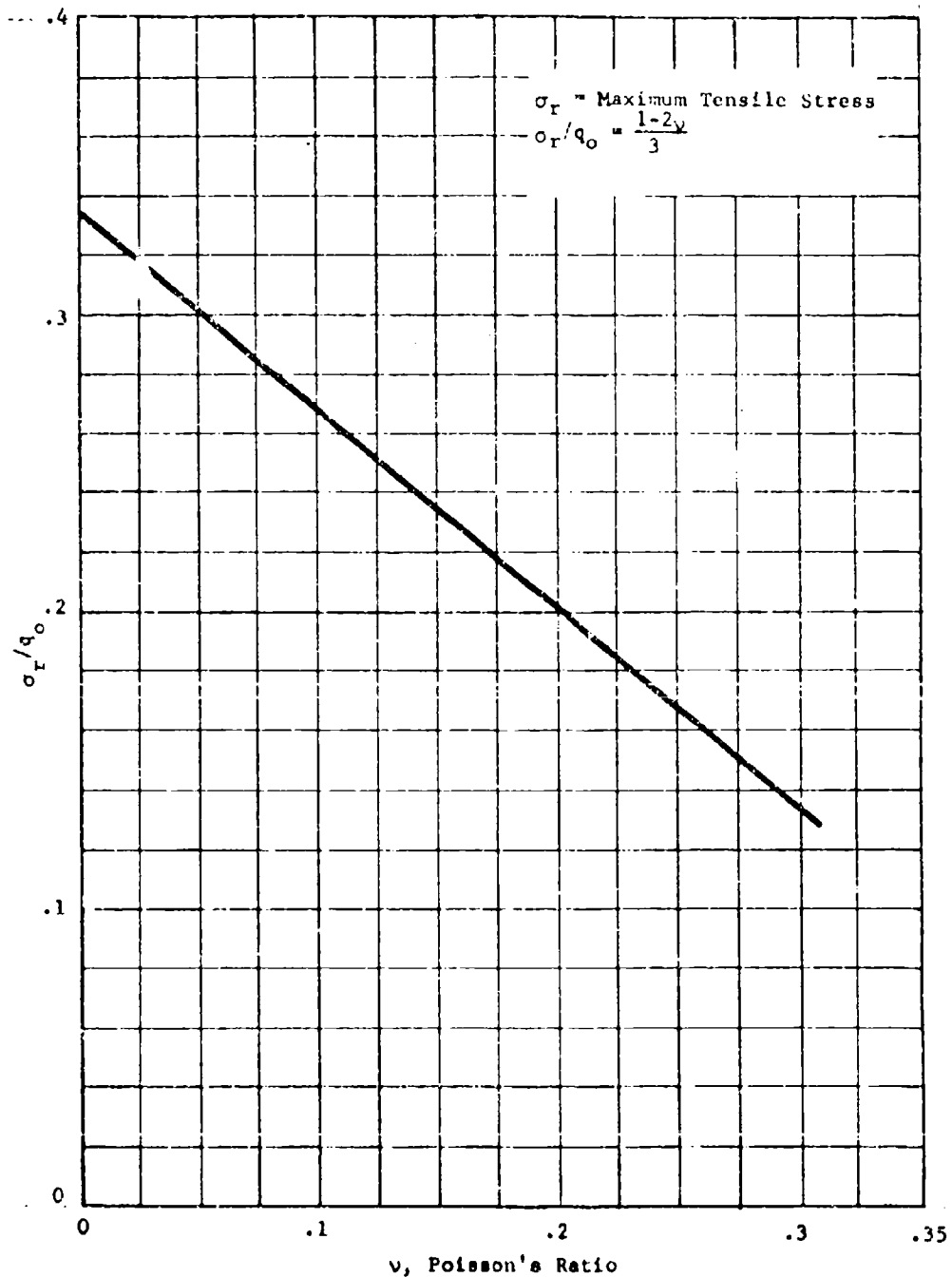


Figure 5-20. Effect of Poisson's Ratio on the Maximum Tensile Stress, at the Edge of the Contact Area.

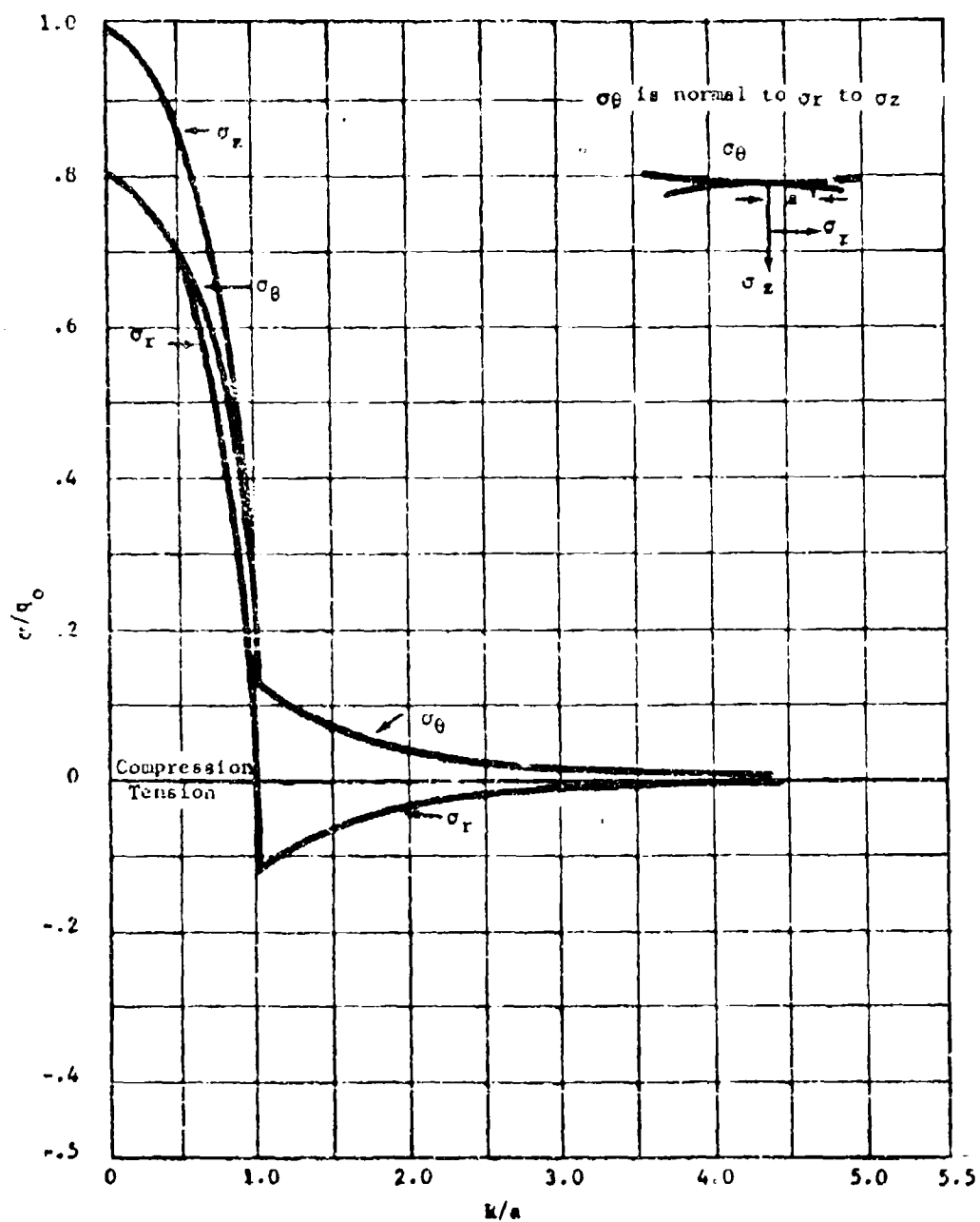


Figure 5-21. Stress Distribution on the Surface of Two Spheres of Fresh Shell 405 Catalyst with a Bed Pressure of 10 psi for $\nu_p = 0.3$.

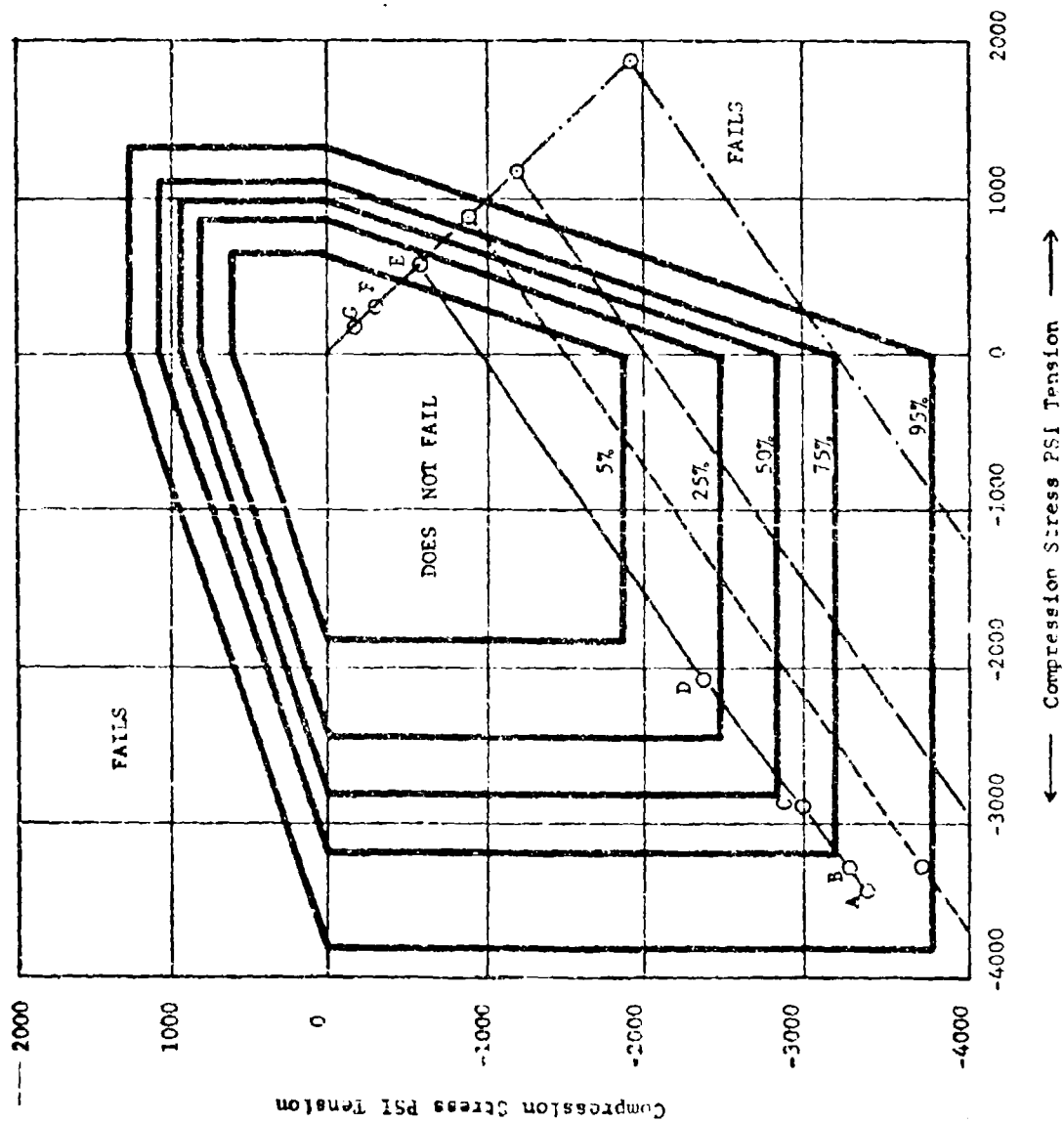


Figure 5-22. Failure Surface - Fresh Shell 405.

1.5, and 2.0. These points and the solid line correspond to a bed compaction pressure of 2.5 psi, and a poisson's ratio for the particle of 0.3. The line of short dashes is the same except the bed compaction pressure is 10.0 psi. The line of long dashes corresponds to a bed pressure of 25.0 psi. The line of long and short dashes corresponds to 100 psi.

It is apparent that as force is applied to the particles from bed compaction pressure, local failure appears first at the center of the area of contact, and spreads out as the bed pressure is increased. As the bed pressure is further increased, a second zone of failure begins independently at the outer edge of the contact area, and moves inward to meet the spreading central failure zone.

Figure 5-23 illustrates the effects of variation in Poisson's ratio for the particle. The biaxial stress loci all correspond to 10 psi bed compaction pressure. The solid line is for a Poisson's ratio of 0.3, the short dashes represent a Poisson's ratio of 0.2, and the long dashes correspond to a Poisson's ratio of 0.1.

With the two-dimensional failure model given in Figure 5-22 the mean bed pressure required to produce failure as a function of Poisson's ratio, v_p is shown in Figure 5-24. The most striking part of Figure 5-24 is the very low bed pressure, usually less than 5 psi, required for incipient material failure. The bed pressures required to cause failure increase rapidly as Poisson's ratio increases. The dramatic change in the bed pressure required to produce failure as a function of the Poisson's ratio of the particle show why Poisson's ratio must be determined very accurately.

The static room temperature bed failure experiment (Section 4.2.1) confirms these findings. The bed began to lose measurable mass at low bed pressure levels, less than 25 psi. These low failure levels indicate compaction of the bed by almost any stress level will produce measurable mass loss.

The effect of all this analysis can be shown by looking at the worst case bed compression from a single operational cycle. The worst case compressive volume change was shown to be 3 percent during the cooldown of the motor, Section 5.4. A bed modulus of 25,000 psi has been estimated (Section 3.3), therefore, mean bed pressure for 3 percent compressive volume change would be 750 psi. From the earlier analysis, this very high bed pressure would produce large amounts of failed material.

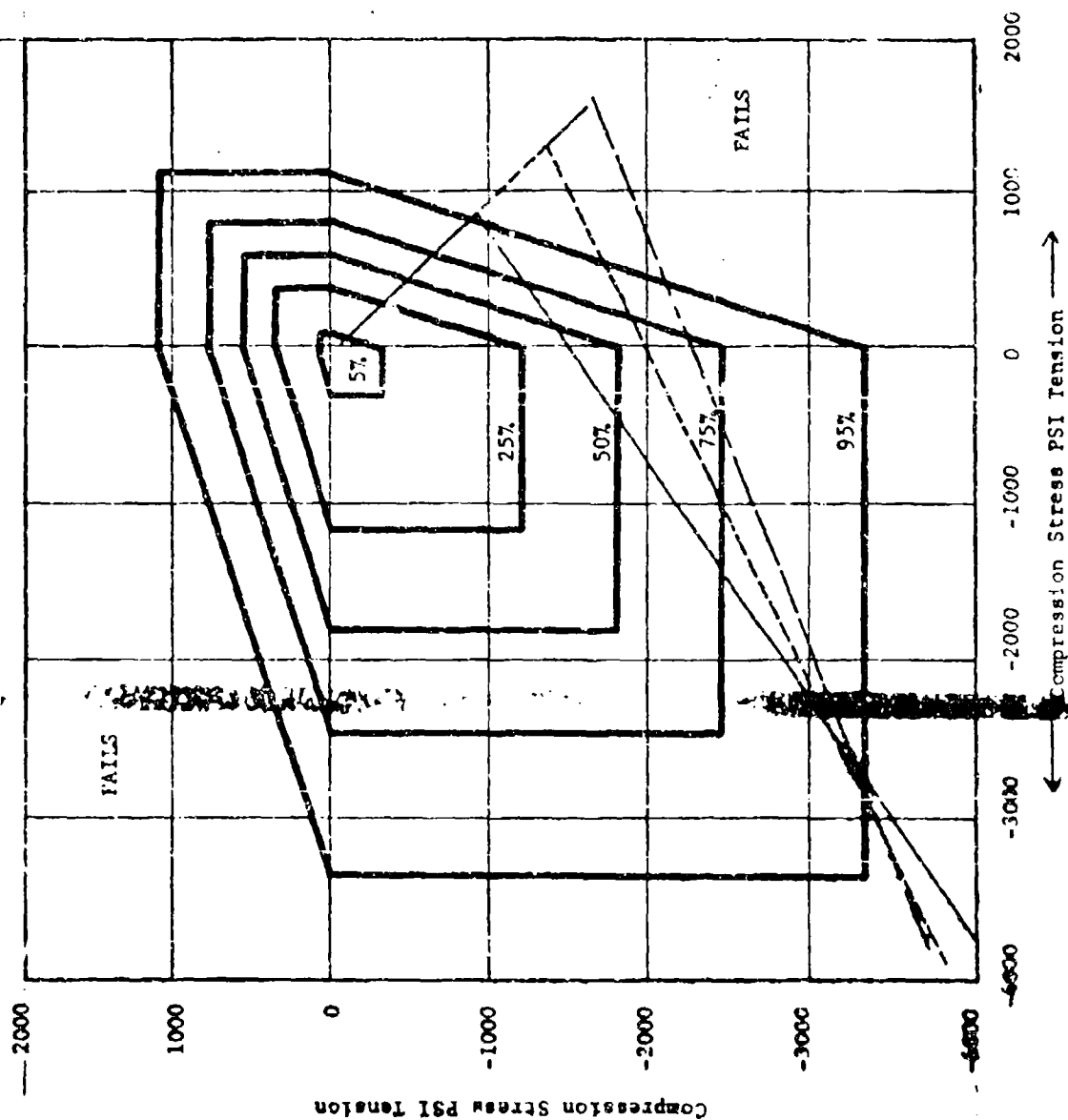


Figure S-23. Failure Surface - Used Shear 405.

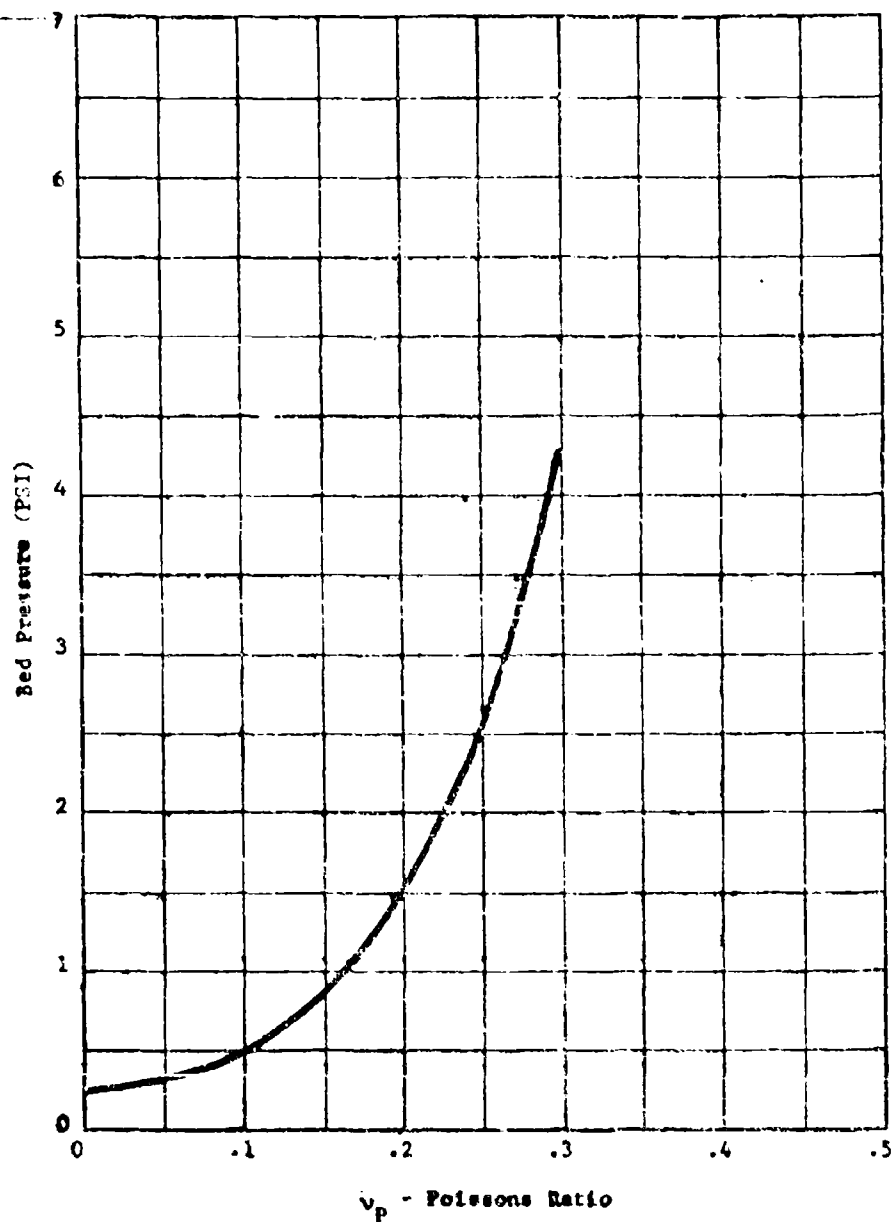


Figure 5-24. Bed Pressure Required to Produce Catalyst Failure as a Function of Poisson's Ratio.

Considering the predicted stresses produced by the thermal loading, the internal pressure loading and the particle-to-particle contact loading, the contact problem appears to be the most damaging. Thus, the calculations indicate, using reasonable assumptions regarding catalyst properties such as Poisson ratio, that failure resulting from static pressure forces causing excessive particle to particle contact loading in all probability is a significant mechanisms in catalyst breakup. The results suggest that longer engine life could be obtained if the contact area between particles were increased, which will require a redesign of the shape of the catalyst, or by techniques to isolate the particles from each other.

5.2.6.3 Relationship Between Bed Volume and Bed Compaction Pressure

In this section the relationship between the change in bed volume as a function of bed pressure for a sphere pack is presented. This relationship shows the relation between the pressure and volume change in nonlinear. The relationship also gives a simple method of checking the accuracy of the sphere pack assumptions used to calculate point-to-point contact forces from bed compaction pressure.

The relationship for the change in the bulk volume of a pack of identical, isotropic elastic spheres under an external pressure P was solved by Brandt, Reference 111. The solution was generated by using Hertz contact theory. The Hertz theory, as presented in Reference 101, shows the change in radius of one of the spherical particles at the point of contact decreases by the amount

$$\Delta R = \left(\frac{3 (1-\nu^2) F}{4 E R^{1/2}} \right)^{2/3} \quad (5.2-40)$$

where F = the contact force (lbs)
 ν = Poisson's ratios of the spheres
 R = radius of the spheres (in.)
 E = Young's modulus (lbs/in²)

Since the displacement is not linear with load, the volume change is also not expected to be linear with load. Brandt, Reference 111, using Hertz contact theory and a sophisticated energy technique showed for an aggregate of equal sized particles, in random packing, the relationship between the mean pressure in the bed and the bed volume change is

$$\frac{\Delta v}{v_0} = 3 \left[\frac{1.75 (1-\nu_p)^2}{E} \right]^{2/3} P^{2/3} \quad (5.2-41)$$

where P = pressure in the bed (psi)
 Δv = the volume change of the bed (in)
 v_0 = the initial volume of the bed (in)
 E = Young's modulus (psi)
 ν_p = Poisson's ratio of the porous sphere

This relationship was generalized in Reference 111 for a fluid filled bed, but the relationships are quite complicated and are not presented. Equation 5.2-41 shows that while the particles within the sphere pack remain elastic the pack does not follow a linear load volume relationship. If the change in volume ($\Delta v/v$) is plotted versus $p^{2/3}$ (the bed pressure to the 2/3 power) then a linear relationship is expected. Therefore, from Equation 5.2-41, nonlinear bed pressure volume relationship, even for elastic materials, is expected.

The accuracy of Equation 5.2-41 was tested (Reference 112) for low modulus (soft spheres ($E/(1-\nu)^2 = 0.54 \times 10^4$ psi) and high modulus (hard) spheres ($E/(1-\nu)^2 = 33 \times 10^6$ psi). Good correlation was obtained for the soft spheres while poor correlation was obtained for the hard spheres. This can be attributed to the random nonuniformities in the radius of the sphere which had a better chance to be evened out with the soft spheres than with the hard sphere at low pressures (Reference 106).

The non-uniform radius and size problem was considered in Reference 113. The model developed, also using Hertz contact theory, for spheres not in perfect contact as was assumed earlier, allows for an increasing number of contacts between the spheres as the pressure increases. The pressure-volume relationship in Reference 16 is

$$\frac{\Delta v}{v} = \begin{cases} a p^{2/3} & p \leq p_i \\ b p^{2/3} & p > p_i \end{cases} \quad (5.2-42)$$

where a , b are functions of the material properties of the spheres.

p_i is the bed pressure required to close all the gaps due to the initial nonuniformities of the spheres.

Good qualitative correlation with Ottawa sand was achieved with Equation 42. To determine if our material follows the 2/3 law of either Equation 5.2-41 or 5.2-42, more experimental compression tests should be done on particle beds of Shell 405. If significant deviation is found from Equation 5.2-41, the contact force given in Equation 5.2-23 should be modified. It was suggested in Reference 113 that the sphere radius be changed to an effective radius of curvature at the contact point which is determined experimentally.

5.2.7 Mass Loss Resulting From Bed Compression

In Section 5.2.1 a simple biaxial failure model is developed for Shell 405 catalyst. Section 5.2.6 develops methods for calculating the contact forces between catalyst particles subjected to bed compaction stresses, and the local biaxial stresses at and under the surface in the areas of contact. These analyses were sufficient to predict that catalyst failure would begin to occur at very low values for bed compaction pressure, and these predictions were qualitatively in agreement with the experimental bed crushing tests.

In order to make possible quantitative comparisons of theory and experiment in this area, and in order to make quantitative predictions of operational catalyst bed loss due to local particle crushing, a method of analysis and a computer program were required to calculate the mass loss associated with bed compaction. The computer program developed for this purpose is an extension of the one previously described in Section 5.2.6.1. It was originally developed under another program, Contract No. DNA 001-72-C-0024 to calculate stresses due to contact forces. It was first modified under the current contract to calculate stresses due to thermal gradients and internal pressure in catalyst particles, as described in Section 5.2.3 and 5.2.5, and now it has been further modified to calculate the mass of catalyst material which will fail under bed compaction stresses.

The particle-to-particle force resulting from bed compaction has been given in equations 5.2-27 through 5.2-31. The stresses in the body of material adjacent to the contact (approximated as a semi-infinite flat body) have been given in equations 5.2-32 through 5.2-36. To go from this stress distribution to the estimation of failed volume, it was necessary to combine the stress calculations with a failure criterion well suited to computer calculation, and with an algorithm for summing up the volume which falls within the failure boundary.

5.2.7.1 Failure Theories

A failure theory is generally defined as an equation relating the interaction of applied stresses at which failure occurs, to the properties of the material, such as strength and stiffness. A review of the literature revealed a number of possible failure criteria. Many failure criteria are not applicable to brittle materials such as Shell 405, since they do not make a distinction between tensile and compressive properties. A characteristic of brittle materials is that the compressive strength is generally considerably greater than the tensile strength; therefore, an essential requirement of a failure criterion for application to Shell 405 is the ability to distinguish between the tensile and compressive strengths of the material. Three theories which are discussed below were considered applicable to the material considered in this program. These theories are given in the following sections in their general form for orthotropic materials.

5.2.7.2 Maximum Tension Stress Criterion

The simplest failure criterion which is applicable to many brittle materials is the maximum tension stress criterion. This criterion assumes that failure occurs when the maximum tensile stress equals the allowable uniaxial tensile strength of the material. Since the compressive strength of brittle materials is generally considerably greater than the tensile strength, the maximum tensile stress criterion should generally apply to the failure of brittle materials. A special case of this approach, modified to consider the effects of catalyst porosity, has already been discussed in Section 5.2.1. This criterion has been found adequate to fit experimental data for a number of materials. The rationale is simple, and it is easy to use in hand calculations. The failure surface for biaxial stress in a porous material failing in microscopic tension is easily constructed graphically, as shown in Figures 5-3 and 5-4. The criterion, however, is limited in generality, and is not easy to represent analytically, especially for multiaxial stress.

5.2.7.3 Distortion Energy Approach

Based on the distortion energy approach by Hill (Reference 135) for orthotropic materials, Hoffman (Reference 136) proposed the following equation as a failure condition for an orthotropic material.

$$C_1 (\sigma_2 - \sigma_3)^2 + C_2 (\sigma_3 - \sigma_1)^2 + C_3 (\sigma_1 - \sigma_2)^2 \quad (5.2-43)$$

$$+ D_1 \sigma_1^2 + D_2 \sigma_2^2 + D_3 \sigma_3^2 + E_1 \tau_{23}^2 + E_2 \tau_{31}^2 + E_3 \tau_{12}^2 = 1$$

The condition for failure is thus defined in terms of the applied stresses σ_i and τ_{ij} ($k, j = 1, 2, 3$ as shown in Figure 5-25) and nine coefficients C_i, D_i, E_i ($i = 1, 2, 3$) that are defined below in terms of three uniaxial tensile strengths, F_{ti} ; three uniaxial compressive strengths, F_{ci} ; and three shearing strengths, F_{sij} ($i, j = 1, 2, 3$).

$$C_1 = \frac{1}{2} \left[\frac{1}{F_{tj} F_{cj}} + \frac{1}{F_{tk} F_{ck}} - \frac{1}{F_{ti} F_{ci}} \right]$$

$$D_i = \frac{1}{F_{ti}} - \frac{1}{F_{ci}} \quad (5.2-44)$$

$$E_i = \frac{1}{(F_{sijk})^2}$$

where

$$(i, j, k) = (1, 2, 3) \text{ or } (2, 3, 1) \text{ or } (3, 1, 2)$$

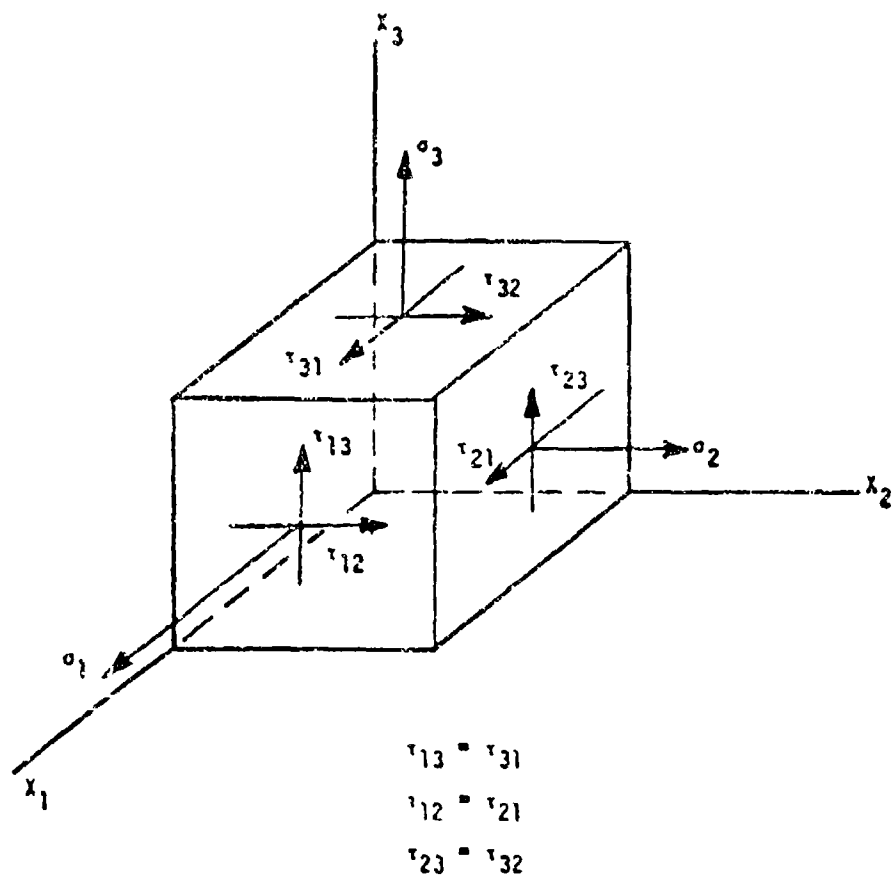


Figure 5-25. Stress Components Acting on Material Element

For the special case of isotropic materials the coefficients in Equation (5.2-43) reduce to

$$\begin{aligned} C_1 &= C_2 = C_3 = \frac{1}{2F_t F_c} \\ D_1 &= D_2 = D_3 = \frac{1}{F_t} - \frac{1}{F_c} \\ E_1 &= E_2 = E_3 = \frac{1}{(F_c)^2} \end{aligned} \quad (5.2-45)$$

where

$$\begin{aligned} F_t &= F_{t1} = F_{t2} = F_{t3} \\ F_c &= F_{c1} = F_{c2} = F_{c3} \\ F_s &= F_{s12} = F_{s23} = F_{s31} \end{aligned}$$

Equation (5.2-43) can be expressed in terms of principal stresses for an isotropic material as follows:

$$\begin{aligned} &[\sigma_1^2 + \sigma_2^2 + \sigma_3^2 - (\sigma_1\sigma_2 + \sigma_2\sigma_3 + \sigma_1\sigma_3)]/F_t F_c \\ &+ (\sigma_1 + \sigma_2 + \sigma_3) \left(\frac{1}{F_t} - \frac{1}{F_c} \right) = 1 \end{aligned} \quad (5.2-46)$$

For a material with equal tensile and compressive strengths, Equations 5.2-43 and 45 reduce to the widely used distortion energy theory as given by Equation (5.2-46).

$$\sigma_1^2 + \sigma_2^2 + \sigma_3^2 - (\sigma_1\sigma_2 + \sigma_2\sigma_3 + \sigma_1\sigma_3) = \sigma^2 \quad (5.2-47)$$

5.2.7.4 Strength Tensor Approach

In recent years the concept of a strength tensor, analogous to the tensor of elastic constants, has been introduced (References 137 to 140) in order to determine the strength of anisotropic materials as a function of the orientation of the stress state. The most recent of these publications (Reference 140) is the most general, and includes the nine strength values of the theory given by Equation (5.2-43); but, in addition, includes six biaxial strength values.

$$\begin{aligned}
 & a_1 \tau_{12}^2 + a_2 \tau_{23}^2 + a_3 \tau_{31}^2 + b_1 \sigma_1^2 + b_2 \sigma_2^2 + b_3 \sigma_3^2 + c_1 \sigma_1 \sigma_2 \\
 & + c_2 \sigma_2 \sigma_3 + c_3 \sigma_3 \sigma_1 = 1 + d_1 \sigma_1 + d_2 \sigma_2 + d_3 \sigma_3 \\
 & + (e_1 \sigma_1 + e_2 \sigma_2 + e_3 \sigma_3) (\sigma_1 \sigma_2 + \sigma_2 \sigma_3 + \sigma_3 \sigma_1 - \tau_{12}^2 - \tau_{23}^2 - \tau_{31}^2) \\
 & + f (\sigma_1 \sigma_2 \sigma_3 + 2 \tau_{12} \tau_{23} \tau_{31} - \sigma_1 \tau_{23}^2 - \sigma_2 \tau_{31}^2 - \sigma_3 \tau_{12}^2)
 \end{aligned} \tag{5.2-48}$$

The 16 coefficients a_i , b_i , c_i , d_i , e_i , f ($i = 1, 2, 3$) are defined below in terms of three uniaxial tensile strengths, F_{ti} ; three uniaxial compressive strengths, F_{ci} ; three shearing strengths, F_{sij} ; three biaxial tensile strengths, h_i , for a 1:1 stress state; and three biaxial compressive strengths, s_i , for a -1:1 stress state.

$$\begin{aligned}
 a_i &= \frac{1}{(F_{sij})^2} \\
 b_i &= \frac{1}{F_{ci} F_{ti}} \\
 c_i &= -(b_i + b_j) + \frac{1}{s_i h_i} \left[\frac{h_i^3 + s_i^3}{s_i h_i (s_i + h_i)} + (d_i + d_j) (s_i - h_i) \right] \\
 d_i &= \frac{-(F_{ci} \dots F_{ti})}{F_{ci} F_{ti}}
 \end{aligned} \tag{5.2-49}$$

$$e_i = \frac{1}{2}(B_i - B_j + B_k)$$

$$f = -3(e_1 + e_2 + e_3)$$

where

$$B_i = \frac{1}{h_i} (b_i + b_j + c_i) - \frac{1}{h_i^3} - \frac{1}{h_i^2} (d_i + d_j)$$

and

$$(i, j, k) = (1, 2, 3) \text{ or } (2, 3, 1) \text{ or } (3, 1, 2)$$

Isotropic materials permit the use of principal stress coordinates, and since the coefficients are direction-independent, Equation (5.2-48) can be simplified to

$$\begin{aligned} b(\sigma_1^2 + \sigma_2^2 + \sigma_3^2) + c(\sigma_1\sigma_2 + \sigma_2\sigma_3 + \sigma_3\sigma_1) &= 1 + d(\sigma_1 + \sigma_2 + \sigma_3) \\ + e(\sigma_1 + \sigma_2 + \sigma_3)(\sigma_1\sigma_2 + \sigma_2\sigma_3 + \sigma_3\sigma_1) + f\sigma_1\sigma_2\sigma_3 \end{aligned} \quad (5.2-50)$$

Equations (5.2-48 and (5.2-50) also reduce to the familiar distortion energy theory (Equation 5.2-47) for isotropic materials for which the uniaxial tension, biaxial tension, uniaxial compression and biaxial compression strengths are all equal ($F_t = R_c = h = s$).

5.2.7.5 Comparison of Failure Theories With Experimental Data

Figure 5-26 shows typical failure envelopes for the theories described in the previous sections (Equations 5.2-43 and 5.2-48) in terms of principal stresses for cast iron subjected to a state of biaxial stress. The strength parameters (F_t , F_c , h , s) are all normalized with respect to the uniaxial tensile strength (F_t). The failure envelopes predicted by theory are compared to experimental data from Reference 141. The theoretical results show fair agreement with the experimental data for the selected values of strength (F_t , F_c , h , s) used in the theoretical calculations. The theoretical curves can be varied by changing any of the strength values used in the theoretical calculations. For example, Figure 5-26 shows the effects on the failure envelope predicted by Priddy's theory (Equation 5.2-48) when the value of h (1:1 tensile stress state)

is varied from 0.707 to 0.800 and the value s (-1:-1 compressive stress state) is varied from 3.25 to 3.75. This shifts the tension-tension stress quadrant of the curve higher and lowers the compression-compression stress quadrant which gives better correlation between theory and experiment. The Priddy criterion for failure was used in our computer program because of its generality and convenient analytical form, because it agrees with data as well as the failure model of Section 5.2.1, and because it had already been coded, checked-out, and documented (Reference 142).

5.2.7.6 Results of Sample Calculations

Figures 5-27 to 5-31 illustrate the crater shapes calculated to be produced by local material failure adjacent to points of contact of 25 mesh spherical particles of fresh Shell 405. The particles were loaded with bed compaction pressures of 25 psi, 50 psi, 100 psi, 200 psi and 300 psi. The vertical axis in the figures is the axis of symmetry of the axisymmetric crater, and the horizontal axis is the original surface of the particle. The horizontal and vertical scales of the computer graphics are chosen to make the graphic fill the frame, so the scales and aspect ratios are not directly comparable from frame to frame. Since the generator of the figure of revolution is approximated by a series of linked straight-line segments, the volume of the crater may be approximated as the sum of the volumes of the stacked conical frustums. The total volume of crushed material per catalyst particle is twelve times the volume of each crater, since there are twelve symmetric points of contact per spherical particle. This volume may be compared with the volume of the original sphere to give the fraction of the sphere which is destroyed by the bed pressurization. Figure 5-32 illustrates the percent of the total particle volume (or mass) which is lost by bed pressurization to the five values illustrated in Figures 5-27-5-31. The experimental values obtained for crushed material which will pass through a 30 mesh screen are taken from Section 4.2.1 and replotted to compare the calculated results with experiment. It appears that the agreement is quite acceptable.

5.3 Internal Particle Model

When liquid hydrazine contacts a cold pellet of Shell 405 catalyst, a series of processes occur: imbibition of the liquid due to surface tension forces, decomposition of hydrazine to evolve heat and decomposition products, transport of heat, liquid and gases due to temperature and pressure gradient, and change of phase or change of physical properties associated with the increase in temperature and pressure. If sufficiently high temperatures and pressures are developed internally, they may be destructive to the catalyst pellet. To evaluate these processes in a quantitative way, a mathematical model of the internal particle processes had to be developed, capable of calculating the sequence of pressure and temperature profiles which are generated in the particle. These temperature and pressure profiles, once computed, may be transformed to radial and tangential stress profiles using the methods described in an earlier section of this report. Because of the complexity of the flow, state, and reaction rate processes, it is necessary to perform the calculations by a finite-difference approach, using digital computer numerical integration to obtain solutions.

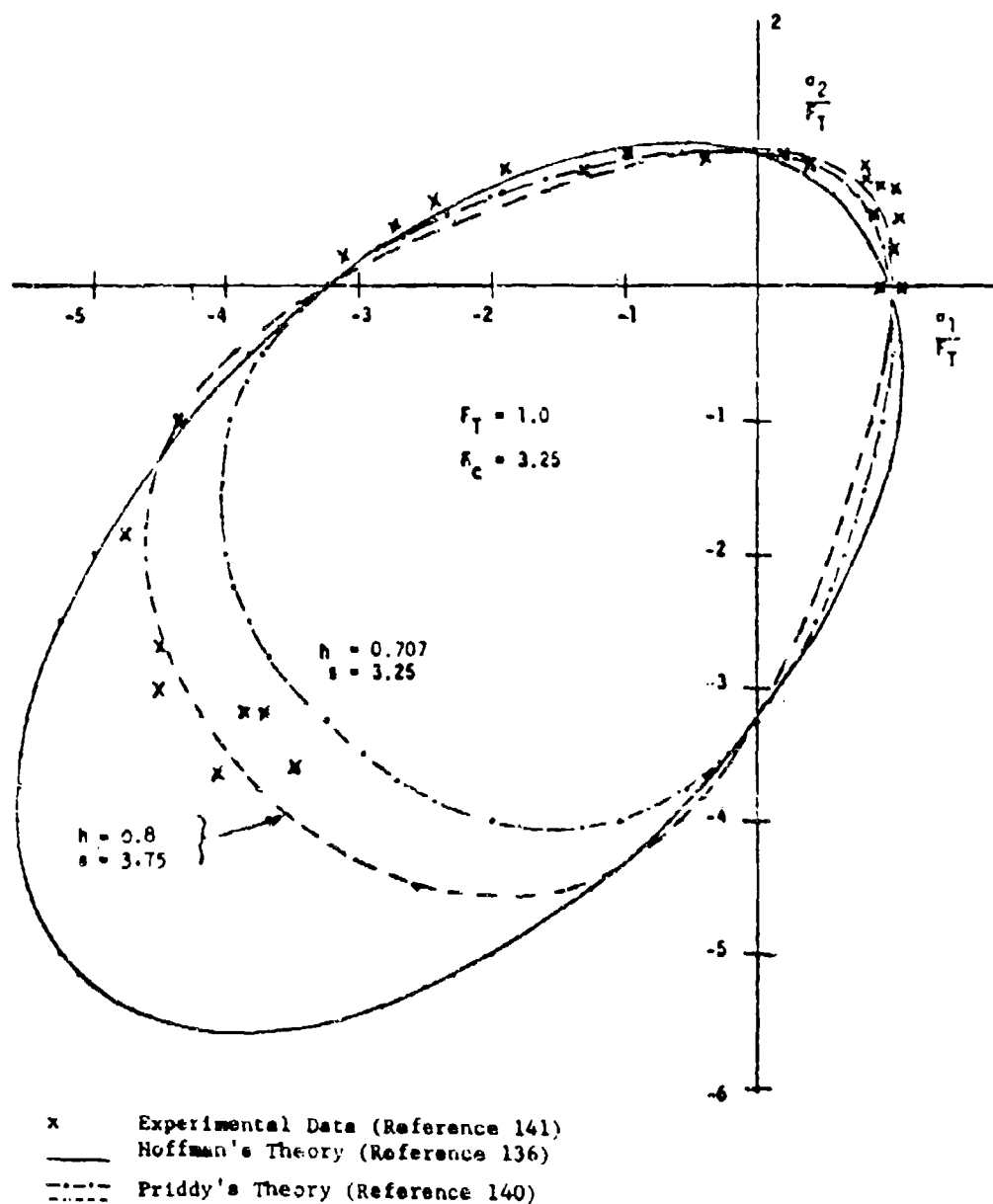


Figure 5-26. Comparison of Failure Theories With Experimental Data for Cast Iron.

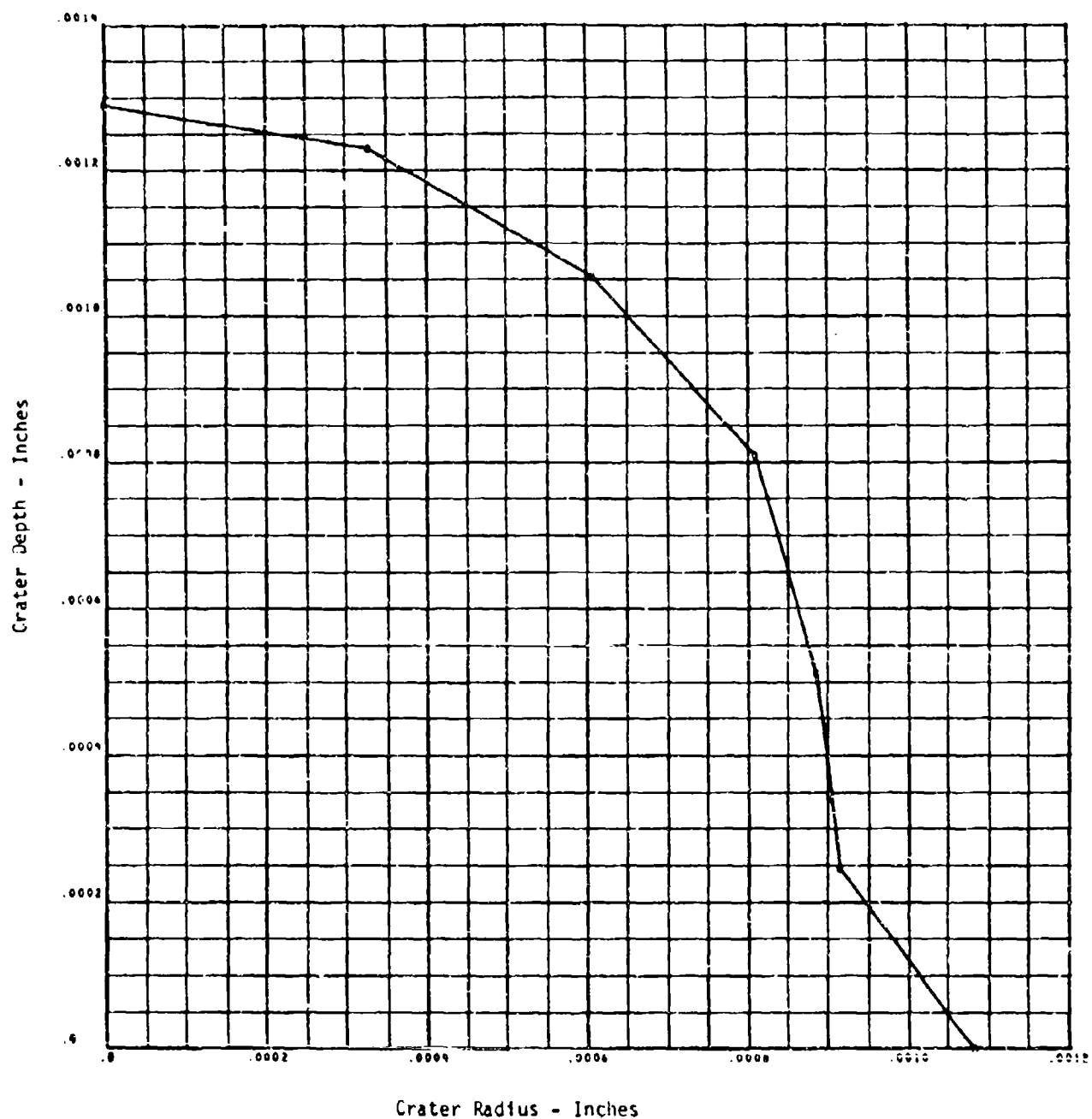


Figure 5-27. Crater Shape - 25 psi Bed Pressure

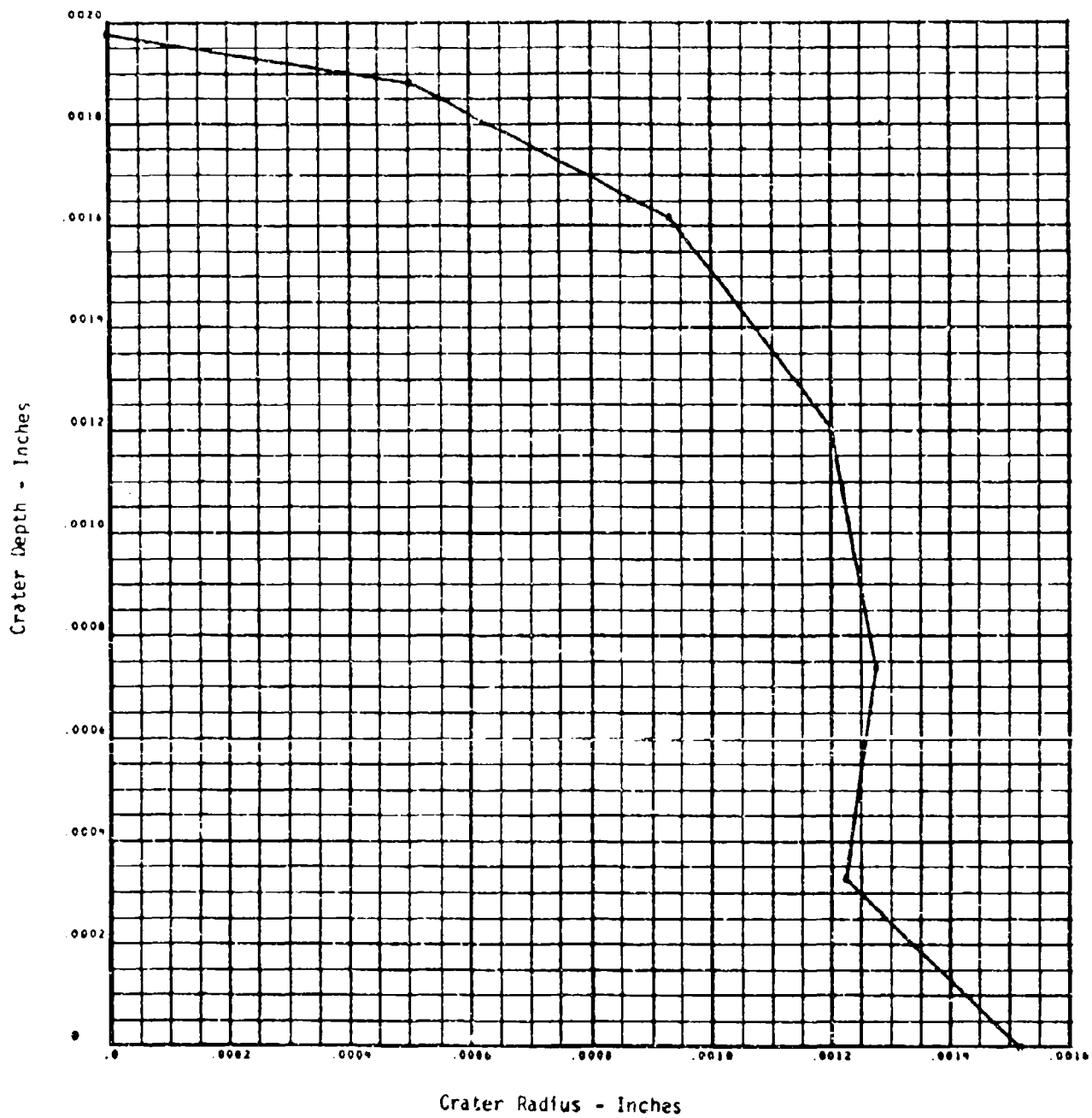


Figure 5-28. Crater Shape - 50 psf Bed Pressure

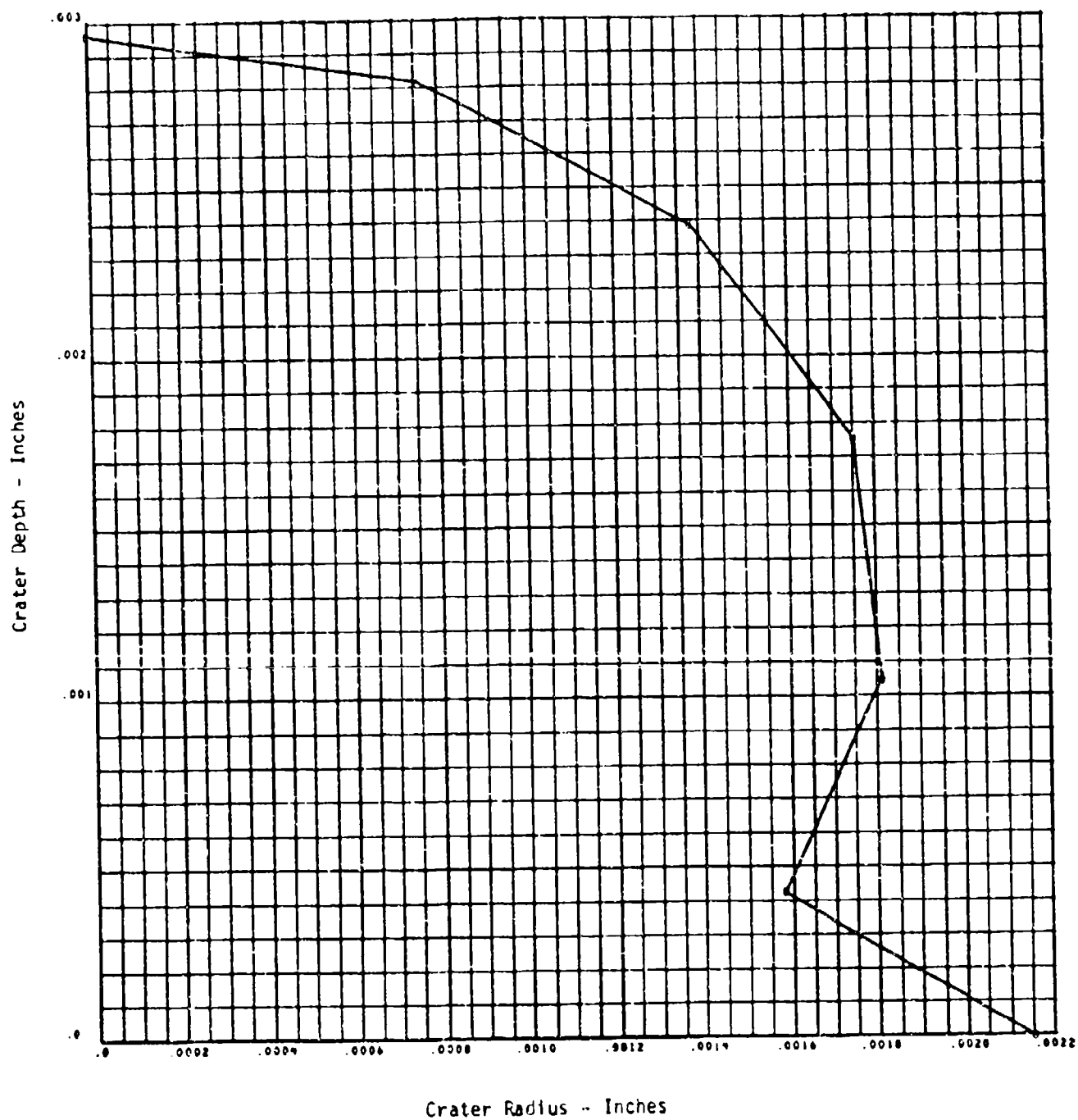


Figure 5-29. Crater Shape - 100 psi Bed Pressure

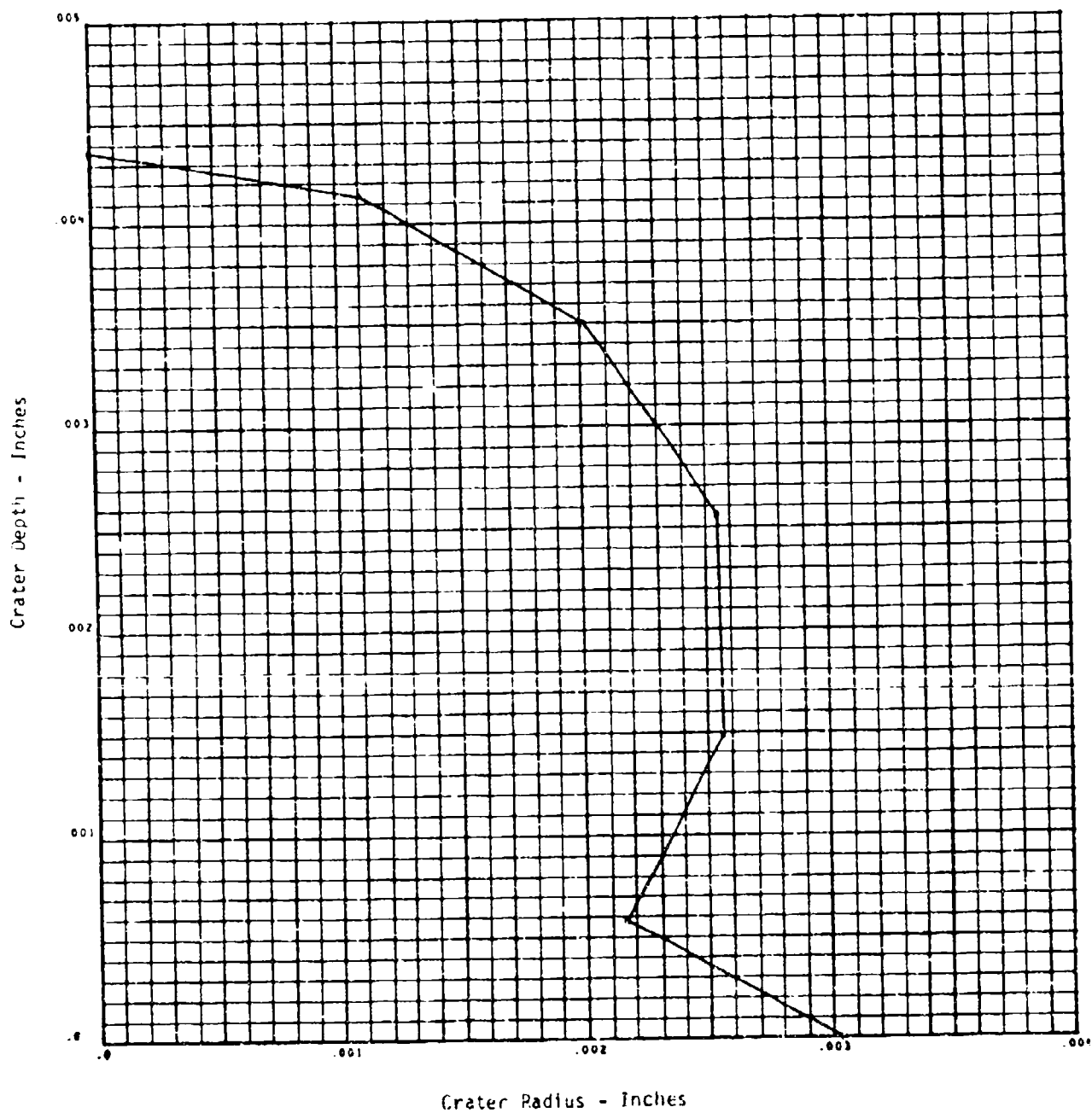


Figure 5-30. Crater Shape - 200 psi Bed Pressure

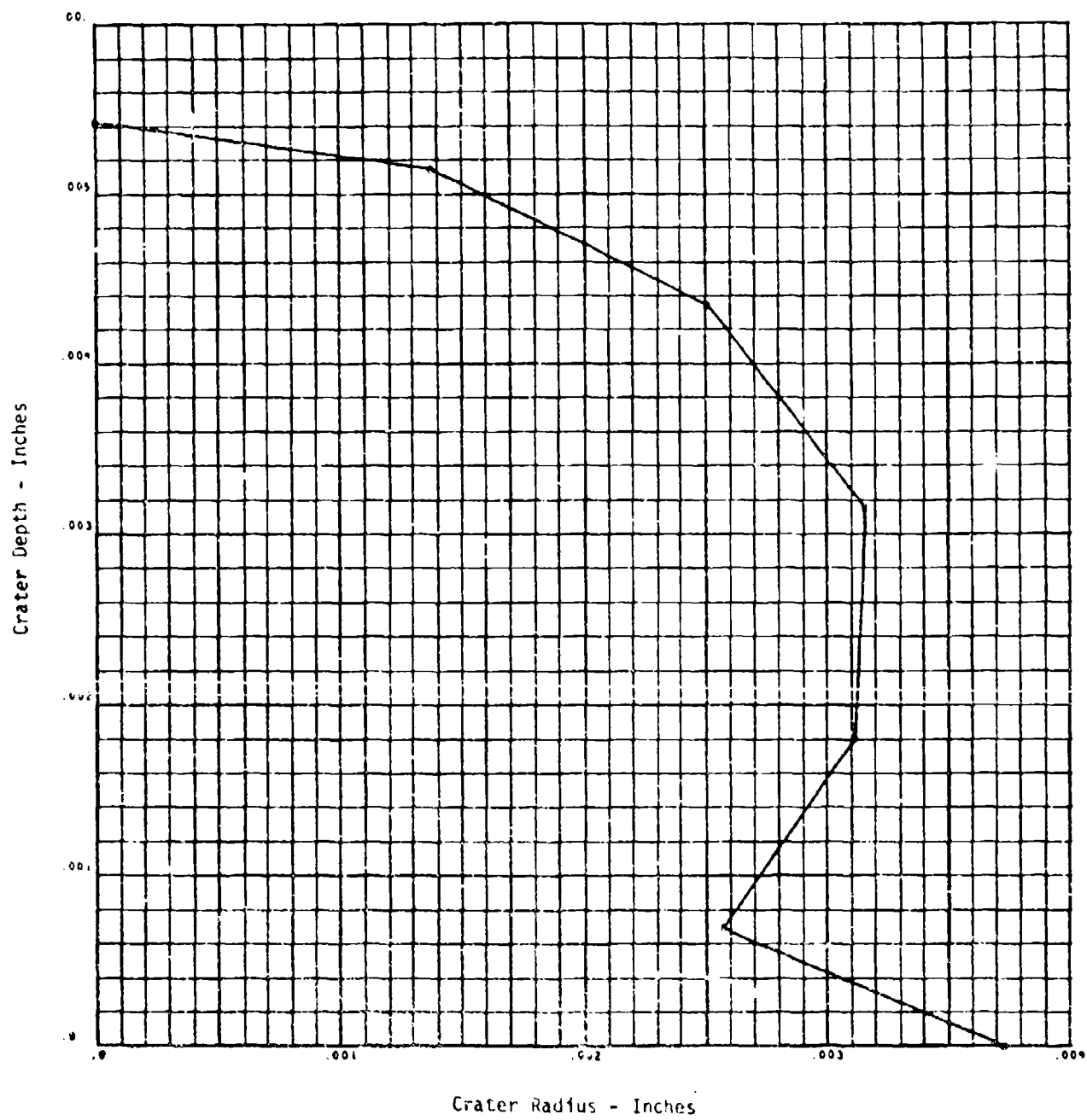


Figure 5-31. Crater Shape - 300 psi Bed Pressure

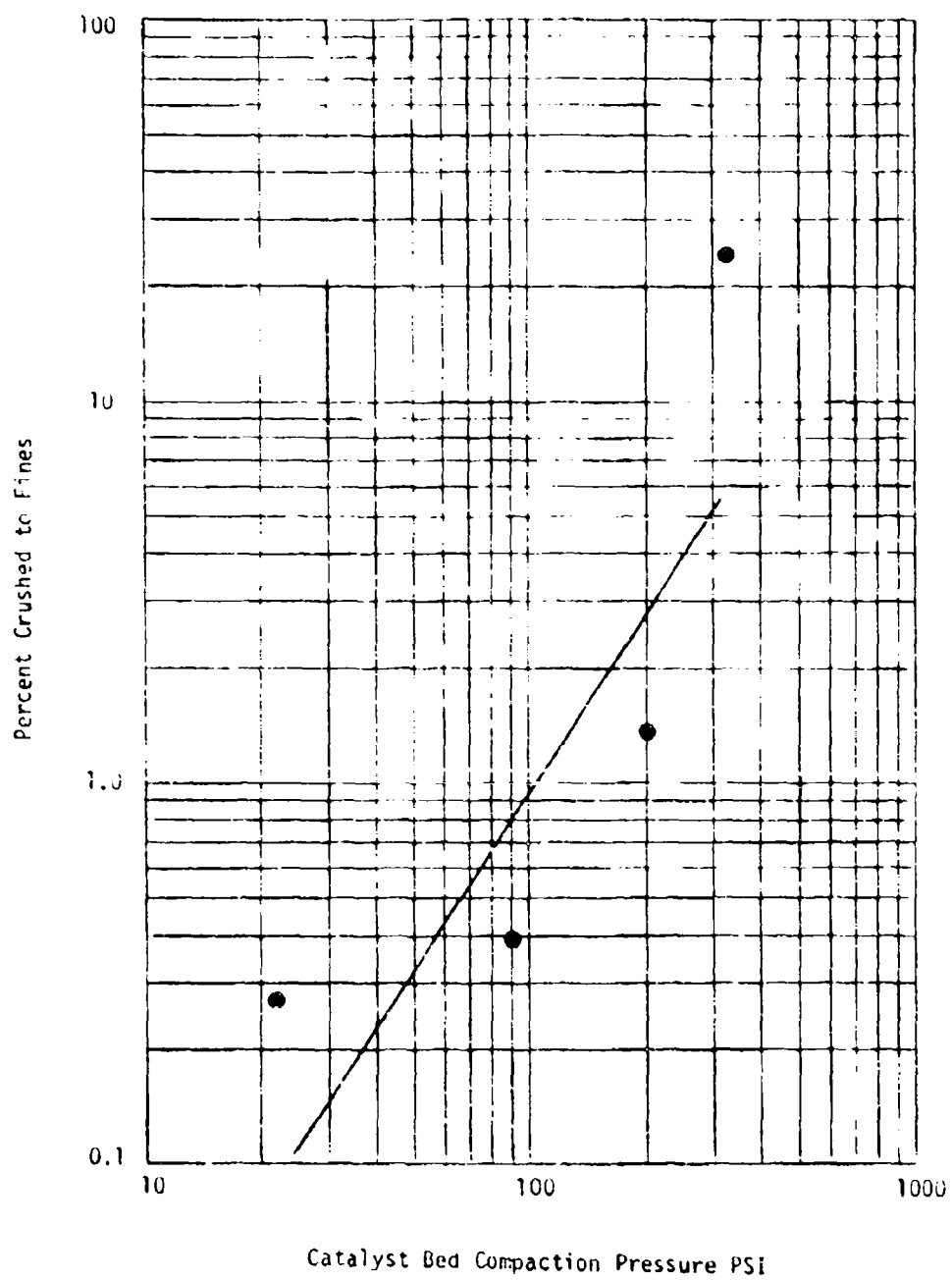


Figure 5-32. Catalyst Bed Damage vs. Bed Pressure

5.3.1 Flow Through A Porous Media

When a pressure gradient causes a single fluid phase to flow through a porous medium completely saturated with the fluid, under conditions where viscous, continuum flow is obtained, the flow rate is defined by D'arcy's Law

$$Q = \frac{K_m A}{\mu} \frac{dp}{dL} \quad (5.3-1)$$

or

$$\dot{M} = \frac{K_m A \rho}{\mu} \frac{dp}{dL} \quad (5.3-2)$$

where Q is volumetric flow rate

A is the cross-sectional area of the porous body

μ is the viscosity of the fluid

$\frac{dp}{dL}$ is the pressure gradient through the medium

K_m is the permeability, a property of the porous medium

ρ is the density of the fluid

When a catalyst particle is exposed to a reactive gas at its outer boundary in a system where appreciable pressure gradients do not exist, as is the case in many commercial chemical reactors, then the transport of reactant species into the catalyst pore volume takes place principally by molecular diffusion, driven by concentration gradient. Analyses of commercial catalyst pellet behavior has traditionally been based upon molecular diffusion as the principal (or only) transport mechanism. In contrast, when a Shell 405 pellet is wetted by liquid hydrazine, and then permitted to react, there are large pressure gradients developed, first by the capillary imbibition pressure of the liquid, and later by the high pressure gases generated by the decomposition of hydrazine which has flowed to the interior of the particle. D'Arcy flow and molecular diffusion may be compared to determine their relative importance in determining mass transport in a particle of Shell 405 catalyst. Molecular diffusion follows Fick's law:

$$\dot{M} = DA \frac{d\rho}{dL} = \frac{DA M_w}{RT} \frac{dp}{dL} \quad (5.3-3)$$

where D is the diffusion coefficient

A is the cross-sectional area

ρ is density of the diffusing component

L is distance

M_w is molecular weight

R is gas constant

T is temperature

When the flow rate associated with D'Arcy's Law is divided by the rate of molecular diffusion:

$$\frac{\dot{M}_{\text{flow}}}{\dot{M}_{\text{diff}}} = \frac{K_m P}{D\mu} \quad (5.3-4)$$

The values for the properties during the pressure buildup in a particle assumed were:

$$\begin{aligned}
 K_m &= .1 \text{ Darcy} = 9.869 \times 10^{-10} \text{ cm}^2 \\
 p &= 1000 \text{ psi} = 6.895 \times 10^7 \text{ dyne/cm}^2 \\
 D &= .482 \text{ cm}^2/\text{sec} \\
 \mu &= .00119 \text{ poise} \\
 \frac{M_{\text{flow}}}{M_{\text{diff}}} &= \frac{9.869 \times 10^{-10} \times 6.895 \times 10^7}{.482 \times .000119} = 1186
 \end{aligned}$$

The D'Arcy flow process is three orders of decimal magnitude greater than molecular diffusion, hence we felt justified in ignoring molecular diffusion in our model, and retaining only D'Arcy flow. Subsequent work described in Section 5.3.6.2 indicates that the permeability of the Shell 405 catalyst is much less than the 0.1 D'Arcy assumed in the above calculation which will change the calculated relative importance of molecular diffusion to D'Arcy flow.

The D'Arcy flow process is three orders of decimal magnitude greater than molecular diffusion, hence we feel justified in ignoring molecular diffusion in our model, and retaining only D'Arcy flow.

When two fluid phases are present simultaneously in a porous medium, then the presence of phase A reduces the permeability of the medium for the flow of phase B and vice-versa. The permeability for the flow of each phase is a fraction of the single-phase permeability, and this fraction is called the relative permeability. The relative permeability is a function of the saturation of the two phases, where saturation is defined as the volume fraction of the total pore volume occupied by the phase. Figure 5-33 shows the experimental relative permeability of the alumina to n-decane in the presence of air (Reference 117). By definition, the relative permeability to the flow of the liquid is 100 percent when the liquid saturation is 100 percent; however, the relative permeability falls to zero when the liquid saturation is still 30 percent. This indicates that if a wetting liquid penetrates into the interior of a porous particle, it cannot subsequently be entirely removed by a flow process, such as expulsion by the flow of gas past it, but rather can only be removed by evaporation or chemical reaction in situ. Figure 5-34 shows that when two phases are present in a porous medium, each interferes with the flow of the other, but that the effect is not necessarily symmetric between the wetting phase and the nonwetting phase (Reference 118). The sum of the two relative permeabilities at most saturations is usually well under 100 percent.

5.3.2 Klinkenberg Effect, Non-Continuum Flow of Gases

When the pore sizes in a porous medium become so small as to be comparable to the mean free path of the molecules of the fluid, then non-continuum flow effects become important. For flow through pipes or other man-made hardware of a simple known shape and size, the Knudsen number can readily be calculated. When the shapes and pore size distributions are no better known than is the case for a sample of porous medium, however, an experimental approach is necessary to define the effects of non-continuum flow. Figure 5-35 shows the variation in experimentally observed permeability when several gases having different molecular properties are flowed through a fine-grained porous medium at various pressures (Reference 110). The increase in observed permeability as the pressure decreases is the result of non-continuum flow becoming important in an increasing fraction of the pores in the total ensemble of pore sizes in the medium. The experimentally determined non-continuum flow effect can be described by the relationship

$$K_g = K_c \left(1 + \frac{b}{p}\right) \quad (5.3-5)$$

where K_g is the gas permeability with non-continuum effects
 K_c is gas permeability under continuum conditions
 p is the gas pressure
 b is a coefficient for a given gas and medium

The constant b in the above equation depends on the mean free path of the gas and the size of the openings in the porous medium. Since permeability also varies with the pore size, it would be expected that the Klinkenberg factor, b , could be correlated with the permeability. Figure 5-36 shows such a correlation (Reference 120).

In our model of the processes occurring in the pellet, the flow of liquid hydrazine and of hydrazine vapor or product gases considers the time-varying distribution of saturation within the pellet and considers the resultant local relative permeability for liquid and gas, and the extent of non-continuous flow in the gas phase through the Klinkenberg correction.

5.3.3 Imbibition Pressure

When a non-wetting fluid, such as mercury, is injected into a porous medium, displacing a wetting fluid phase, a considerable pressure may be required to introduce the non-wetting fluid, the pressure varying as a function of the saturation of the porous medium. Conversely, a wetting fluid phase will be preferentially drawn into a sample of porous medium, spontaneously generating a pressure which expels any non-wetting phase which may be present. These pressures can be measured to define the imbibition characteristics of the porous medium. Figure 5-37 shows raw experimental data obtained when a particular sandstone samples was injected with mercury, and when the same sample spontaneously imbibed water to displace hydrocarbon. The shape of the curves is the same for the two different fluids, with only the scale factor differing to correspond to the different values for the interfacial tension and contact angle, i.e., $\sigma \cos \theta$. (Ref. 121) H. C. Leverett proposed the J-function to correlate imbibition pressure data (Reference 122):

$$J(s) = \frac{P_c}{\sigma \cos \theta} \left(\frac{K}{\phi}\right)^{1/2} \quad (5.3-6)$$

where: P_c is imbibition pressure
 σ is interfacial tension
 θ is contact angle
 K is permeability of the medium
 ϕ is porosity of the medium.

It is instructive to compare this equation, rearranged:

$$P_c = \frac{\sigma \cos \theta}{1/2} J(s) \left(\frac{K}{\phi}\right) \quad (5.3-7)$$

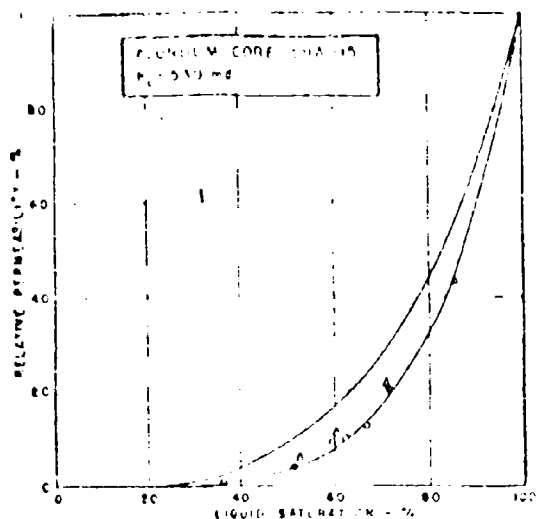


Figure 5-33

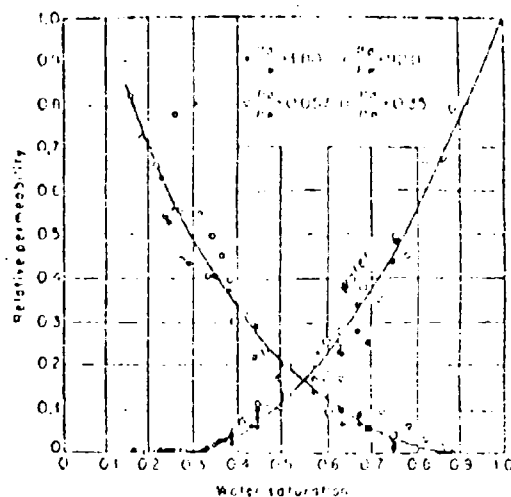
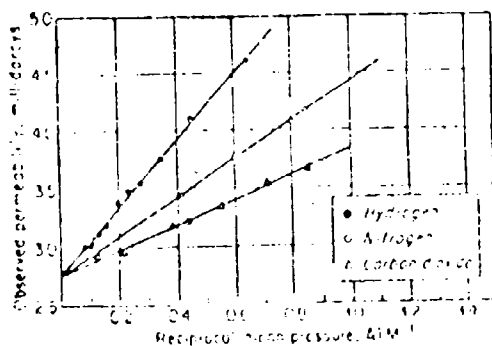
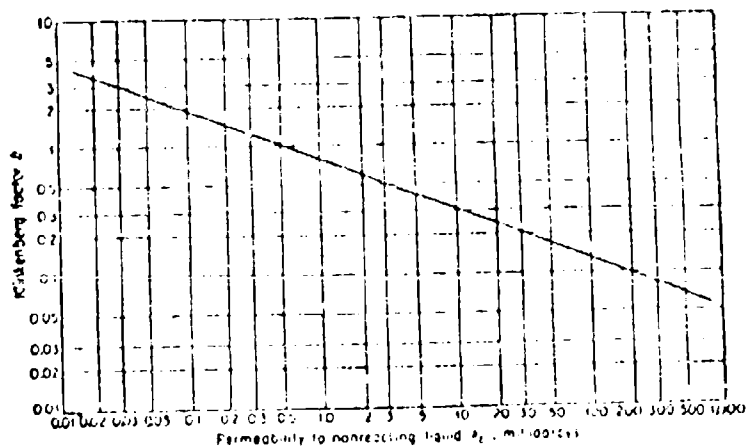


Figure 5-34



Permeability of core sample *L* to hydrogen, nitrogen, and carbon dioxide at different pressures. Permeability to isobutane, 2.65 millidarcys. (From Klinkenberg.)

Figure 5-35



Correlation of Klinkenberg factor *h* with permeability. (From American Petroleum Institute.)

Figure 5-36

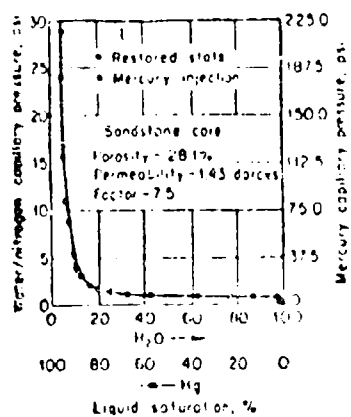


Figure 5-37

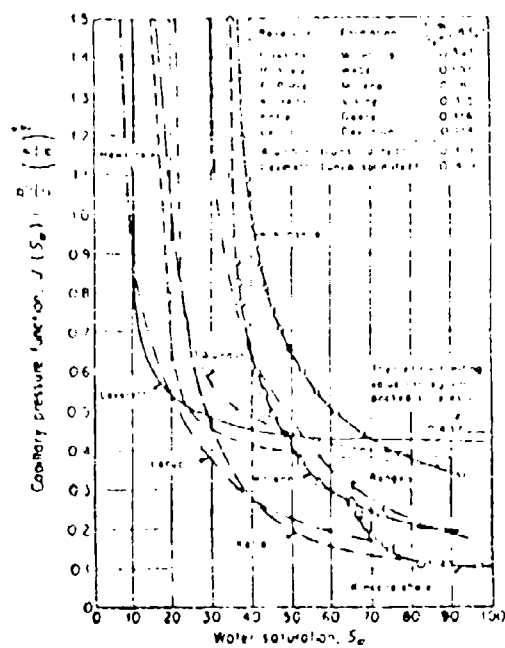


Figure 5-38

With the equation for the pressure difference across a meniscus in a capillary:

$$P_c = \frac{\sigma \cos \theta}{r} \quad (5.3-8)$$

The $\left(\frac{K}{\phi}\right)^{1/2}$ term is approximately proportional to the mean value of pore radius, and the undimensional function $J(s)$ describes the effect of pore diameter distribution, relative to the mean, over the entire pore volume. Figure 5-38 illustrates J-functions for a wide variety of different materials, including a porous alumina (Reference 123). The J-function for the alumina used in our model is taken from the experimental measurements of pore size distribution versus cumulative pore volume in Shell 405 done at U.A.R.L. (Reference 124). (Figure 5-39). This can be converted to a curve of capillary imbibition pressure versus saturation, or J-function versus saturation by using Equations 8 and 6 (Figure 5-40). The capillary pressure curve presumes room-temperature liquid hydrazine, having a surface tension of 65.7 dyne/cm and a zero wetting angle. The J-function curve presumes a permeability of 100 millidarcy and a porosity of .25. The imbibition pressures used in our model vary with time and location in the pellet according to the local values for saturation and temperature-dependent interfacial tension.

5.3.4 Thermal Effects

The MDAC internal particle model calculates the convection of heat due to flow of both liquid and gas, the conduction of heat through the particle, and the effects of local heat evolution or absorption due to decomposition reactions and hydrazine phase change. If the catalyst pellet were in the environment typical of most commercial gas-phase catalytic reactor, then pressure gradients would be small, D'Arcy flow of fluid through the particle would be small, and heat convection could be ignored. For a particle of Shell 405 catalyst exposed to liquid hydrazine, however, these assumptions are not valid, as can be shown:

Conduction of Heat:

$$\dot{Q} = K_t \frac{A \Delta T}{L} \quad (5.3-9)$$

Convection of heat:

$$\dot{H} = \frac{K_m \rho A^C \Delta T \Delta P}{\mu \Delta L} \quad (5.3-10)$$

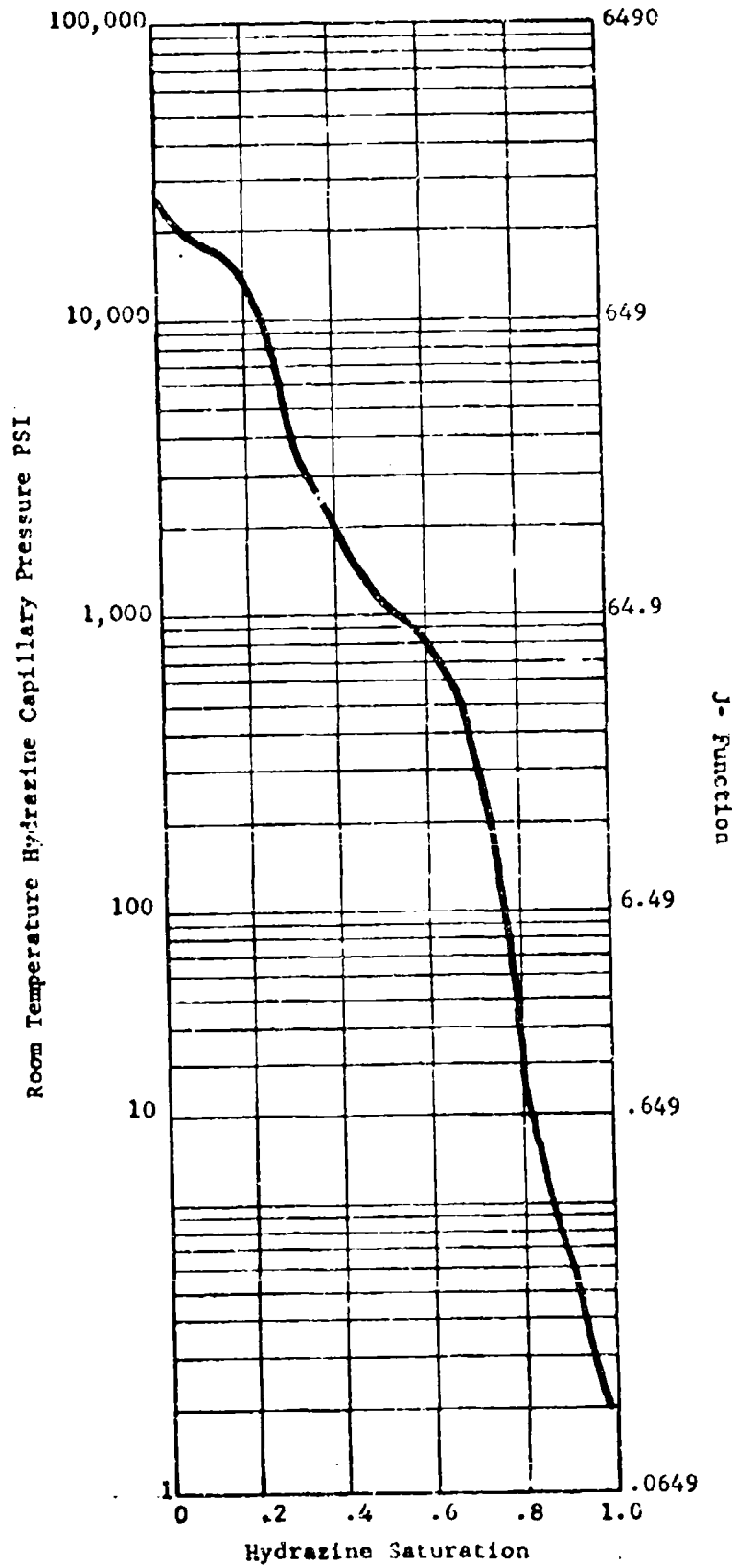
Take the ratio of convection to conduction:

$$\frac{\dot{H}}{\dot{Q}} = \frac{K_m \rho C_p T \Delta P}{K_t \mu \Delta T} \quad (5.3-11)$$

Use reasonable values for properties:

$$\begin{aligned} K_m &= .1 \text{ Darcy} = 9.869 \times 10^{-10} \text{ cm}^2 \\ \rho_{\text{gas}} &= .0122 \text{ gram/cm}^3 \\ C_{p_{\text{gas}}} &= .679 \text{ cal/gram } ^\circ\text{K} \\ T &= 728.8 \text{ } ^\circ\text{K} \\ \Delta P &= 1000 \text{ psi} = 6.8947 \times 10^7 \text{ dyne/cm}^2 \end{aligned}$$

Figure 5-40



$$K_t = .01 \text{ cal/sec cm } ^\circ\text{K}$$

$$\mu = .005 \text{ poise}$$

$$\Delta T = 728.8 \text{ } ^\circ\text{K}$$

Evaluate the ratio of convective to conductive heat transport

$$\frac{g}{Q} = \frac{9.869 \times 10^{-10} \times .0122 \times .679 \times 728.8 \times 6.8947 \times 10^7}{.01 \times .005 \times 728.8} = 11.$$

Convective heat transfer was seen to be an order of magnitude more important than conduction under the particular conditions chosen for this comparison. Obviously, either process can be important, under the appropriate conditions, and the importance at any particular time and location will depend upon the particular values in the catalyst pellet being analyzed. Also, subsequent work (Section 5.2.6.2) indicated the actual catalyst permeability was much less than the 0.1 D'Arcy assumed above.

In the solution of the internal particle processes, the viscosity of the liquid and gas, the interfacial tension, the vapor pressure, the specific enthalpies, etc., are calculated as functions of local time-varying temperature using correlations developed for the NDAC TCC computer program (Reference 125). Both the homogeneous gas phase decomposition rate of hydrazine and the heterogeneous, surface catalyzed decomposition are calculated using global Arrhenius equations, taken from the work done at U.A.R.L. For the sake of simplicity, the decomposition is assumed to be one-step:



5.3.5 Finite Difference Model

The interior of the pellet is represented by a linear sequence of nodal points and internodal paths extending from the external environment (boundary conditions) to the center of the sphere, as in Figure 5-41.

The internodal paths transmit gas (product gas plus hydrazine vapor), liquid hydrazine, heat and enthalpy. The nodal points accumulate gas, liquid and enthalpy and effectuate phase change and chemical reaction. The nodes possess extensive and intrinsic state properties: hydrazine mass, product gas mass, enthalpy, temperature, pressure and saturation.

The types of behavior associated with nodal points and internodal paths is illustrated conceptually in Figure 5-42. Thermal equilibrium between liquid, solid, and gas phases is presumed at each nodal point. Phase equilibrium between hydrazine liquid and vapor is also presumed. The fluid temperatures and vapor concentrations flowing from a nodal point are those of the nodal point. Viscosities and densities used in internodal flow calculations are arithmetic means of the adjoining nodes. Relative permeabilities are those characteristic of the saturation in the upstream nodal point.

The approximate forms of the more important governing equations are listed below.

Each node has state properties associated with it.

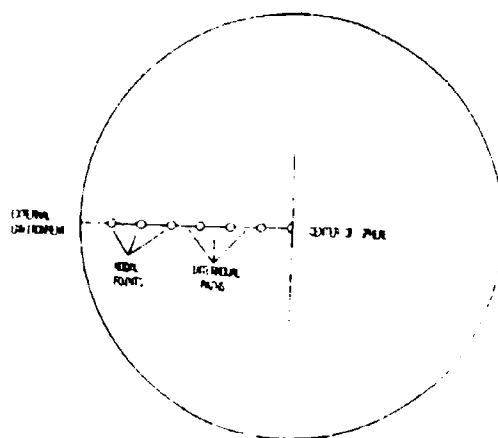


Figure 5-41

Catalyst Pellet Model

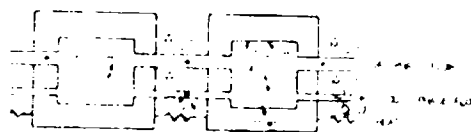


Figure 5-42

Conceptual Model of Nodal Behavior

$$\text{Nodal enthalpy} = H_n = H_{\text{Substrate}} + H_{\text{Liquid}} + H_{\text{gas}} \quad (5.3-13)$$

$$H_{\text{Substrate}} = \rho_s V(1-\phi) h_s(T)$$

$$\rho_s = \text{density of solid phase} \quad (5.3-14)$$

V = nodal volume = volume of spherical shell

ϕ = porosity = pore volume/nodal volume

$h_s(T)$ = specific enthalpy of solid phase at temperature T

$$N_{\text{Liquid}} = \rho V \phi S h(t) \quad (5.3-15)$$

S = liquid saturation = liquid volume/pore volume

$h(T)$ = specific enthalpy of liquid phase at temperature T

$$H_{\text{gas}} = \rho_g V \phi(1-S) h_g(T) \quad (5.3-16)$$

$h_g(T)$ = specific enthalpy of gas phase at temperature T

Nodal temperature is the value of T , found iteratively, which satisfies the above enthalpy relation when nodal enthalpy is known. The enthalpy versus temperature iteration is done while maintaining phase equilibrium between the liquid and vapor phase of hydrazine.

$$\text{Nodal pressure} = P_n = P_{\text{gas}} + P_{\text{vapor}} \quad (5.3-17)$$

$$P_{\text{gas}} = \frac{N_g R T_n}{M_{wg} V \phi} (1-S) \quad (5.3-18)$$

N_g is mass of gas in the node

R is the gas constant

M_{wg} is Mean Molecular Weight of the gas

$$P_{\text{vapor}} = f(T_n) \quad (5.3-19)$$

$f(T_n)$ is the vapor pressure of hydrazine

Generating a New Value for Nodal Enthalpy in Node 2 of Conceptual Illustration

$$H_n(t+\Delta t) = H_n(t) + \text{inflowd enthalpy} - \text{outflowd enthalpy} + \text{enthalpy of reaction} \\ + \text{inflowd heat} - \text{outflowd heat} \quad (5.3-20)$$

$$\text{Inflowd enthalpy} = \dot{M}_g(1) \cdot h_g(1) \cdot \Delta t + \dot{M}_L(1) \cdot h_L(1) \cdot \Delta t \quad (5.3-21)$$

$$\text{Outflowd enthalpy} = \dot{M}_g(2) \cdot h_g(2) \cdot \Delta t + \dot{M}_L(2) \cdot h_L(2) \cdot \Delta t \quad (5.3-22)$$

$$\text{Enthalpy of reaction} = \dot{M}_R(2) \cdot h_R \cdot \Delta t \quad (5.3-23)$$

$\dot{M}_T(2)$ is reaction rate of hydrazine in Node 2

h_T is specific heat release of hydrazine decomposition reaction

Δt is the time interval: used for numerical integration

$$\text{Inflow heat} = K_T (A(1)/L(1)) \cdot (T(1)-T(2)) \cdot \Delta t \quad (5.3-24)$$

$$\text{Outflow heat} = K_T (A(2)/L(2)) \cdot (T(2)-T(3)) \cdot \Delta t \quad (5.3-25)$$

Gas Phase Flow Rate into Node 2 of Conceptual Illustration

$$\dot{M}_g(1) = \rho_g \cdot g = \frac{K_a K_r K_k A (P_1 - P_2)}{\mu_g L} \quad (5.3-26)$$

K_a = permeability of the substrate

K_r = relative permeability for gas (empirical function of saturation)

$$K_k = \text{Klinkenberg rarefaction correction} = (1 + \frac{b}{P}) \quad (5.3-27)$$

b is the Klinkenberg constant for the substrate

A = cross-sectional path area

ρ_g = mean density of gas phase materials in Nodes 1 and 2

μ_g = mean viscosity of gases in Nodes 1 and 2 (empirical function of temperature)

L = path length

Generating a New Value for Nodal Gas Mass

$$M_g(t+\Delta t) = N_{g(t)} + \text{inflow gas} - \text{outflow gas} + \text{gas formed by reaction} \quad (5.3-28)$$

$$\text{inflow gas} = \dot{M}_g(1) \cdot \frac{N_g(1)}{N_g(1) + N_v(1)} \cdot \Delta t \quad (5.3-29)$$

N_g is mass of product gases

N_v is mass of hydrazine vapor

$$\text{outflow gas} = \dot{M}_g(2) \cdot \frac{N_g(1)}{N_g(1) + N_v(1)} \cdot \Delta t \quad (5.3-30)$$

$$\text{gas from reaction} = \dot{M}_T(2) \cdot \Delta t \quad (5.3-31)$$

Liquid Phase Flow Rate into Mode 2 of Conceptual Illustration

$$\dot{M}_l(1) = \rho_l q_l = \frac{K_a K_{re} A (P_1 - P_2) - (I_1 - I_2) \rho_l}{\mu L} \quad (5.3-32)$$

K_r = relative permeability for liquid (empirical function of saturation) evaluated for saturation of Mode 1

$$I_1 = \text{imbibition pressure} = \frac{\sigma_1 \cos \theta}{\left(\frac{K}{\phi}\right)^{1/2}} J(S_1) \quad (5.3-33)$$

$J(S_1)$ = J-function evaluated at saturation of Mode 1

σ_1 = interfacial tension at the temperature of Mode 1

Generating a New Value for Total Hydrazine in Mode 2

$$M_{H(t+\Delta t)} = M_{H(t)} + \text{inflowd hydrazine} - \text{outflowd hydrazine} - \text{hydrazine reacted} \quad (5.3-34)$$

$$\text{Inflowd hydrazine} = M_l(1) \cdot \Delta t + M_g(1) \cdot \frac{M_v(1)}{M_g(1) + M_v(1)} \cdot \Delta t \quad (5.3-35)$$

$$\text{Outflowd hydrazine} = M_l(2) \cdot \Delta t + M_g(2) \cdot \frac{M_v(2)}{M_g(2) + M_v(2)} \cdot \Delta t \quad (5.3-36)$$

$$\text{Hydrazine reacted} = M_r(2) \cdot \Delta t$$

Generating a New Value for Liquid Mass, Vapor Mass, Saturation

New values are found for liquid and vapor hydrazine by iteratively determining nodal temperature to agree with nodal enthalpy while maintaining hydrazine phase equilibrium.

$$M_v = \frac{P_{\text{vapor}} M_w V \phi (1-S)}{RT} \quad (5.3-37)$$

$$M_l = M_H - M_v \quad (5.3-38)$$

$$V_l = M_l / \rho_l \quad \text{where } V \text{ is liquid volume, } \rho_l \text{ is liquid density (empirical function of temperature)} \quad (5.3-39)$$

$$S = V_l / V \quad \text{where } S \text{ is liquid saturation} \quad (5.3-40)$$

Obviously an iterative approach is required to obtain S together with T and P from enthalpy, and known phase behavior.

The hydrazine vapor concentration is

$$\rho_v = \frac{P_{\text{vapor}} M_w}{RT} \quad (5.3-41)$$

Estimating The Chemical Reaction Rate

$$M_r = M_{r_{\text{heterogeneous}}} + M_{r_{\text{homogeneous}}} \quad (5.3-42)$$

$$M_{r_{\text{het}}} = V_n \phi(1-S) \rho_v * 10^{10} e^{-\frac{2758}{RT}} \quad (5.3-43)$$

V_n = nodal volume

ρ_v = hydrazine vapor concentration

$$M_{r_{\text{hom}}} = V_n \phi(1-S) \rho_v * 2.14 \times 10^{10} e^{-\frac{36,400}{RT}} \quad (5.3-44)$$

Initial Conditions

The interior of the particle may be set to a uniform initial value for temperature, pressure, and liquid hydrazine saturation.

Boundary Conditions

In addition to the internal behavior of the catalyst, it is necessary to impose conditions at the boundary. The boundary temperature and pressure may be specified in an arbitrary time-dependent way by designating eleven equally timed values, for temperature and pressure, with linear interpolation with time between specified points. A time may be specified, for the boundary to "dry up." The boundary will be wetted with liquid hydrazine before this time, and will contact only dry product gas after this time.

5.3.6 Results from the Operation of the Internal Particle Model

5.3.6.1 Initial Results Using an Estimated Permeability Constant

The Internal Particle Model was initially operated using an estimated permeability constant of 100 millidarcy. A sample case was calculated based upon a particle of 25 mesh Shell 405 within initial pressure of .001 psi and the initial temperature of 300°K. At time zero the boundary condition was changed to liquid hydrazine at 300°K and 1 psia. Results are shown in Figure 5-43.

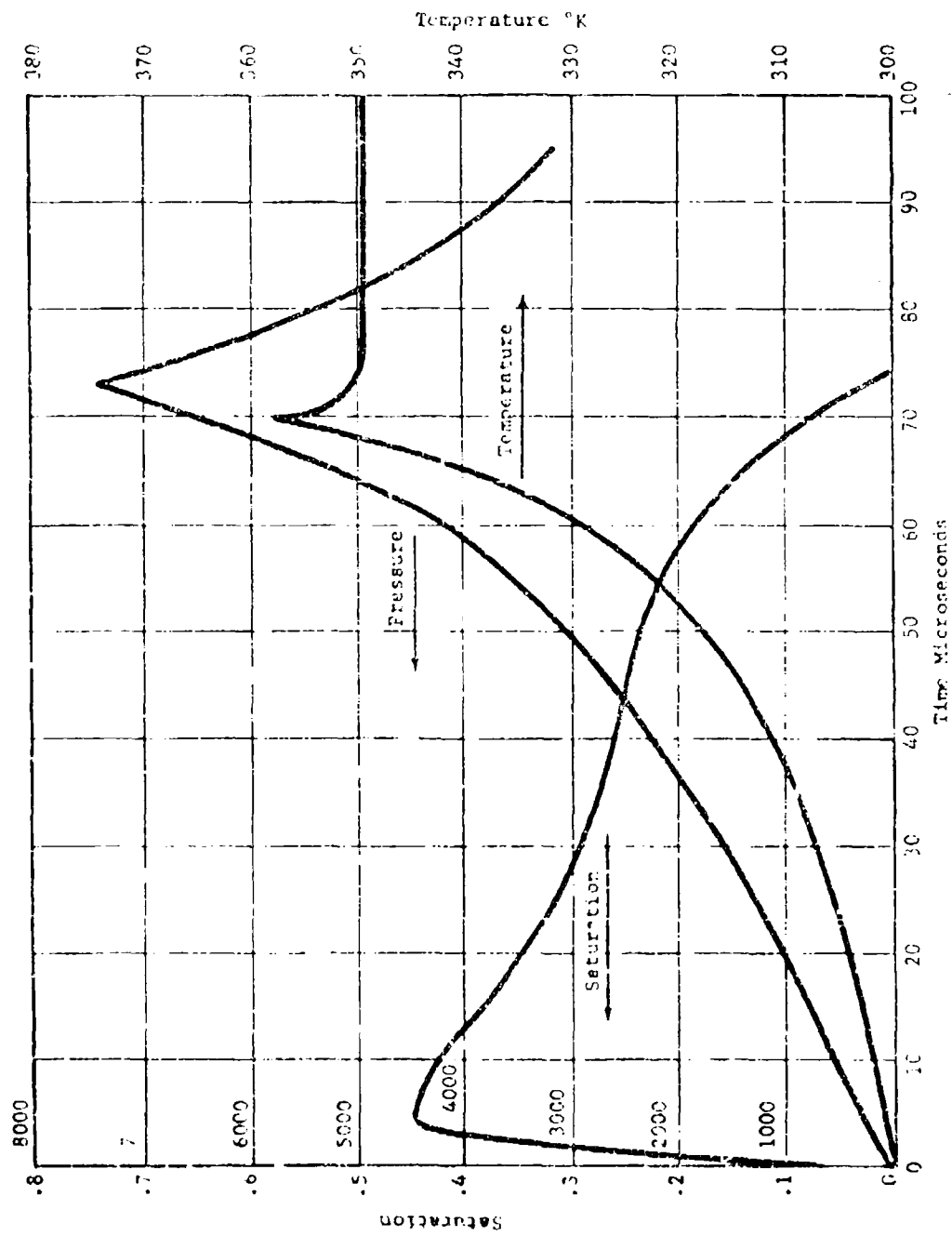


Figure 5-43. Partial Internal Particle Model
Assumed Permeability Value
00 Millidarcy.

The liquid imbibition proceeds very rapidly, concurrent with pressure build-up in the particle. On the order of .2 microseconds after start, the first gas commences to flow out of the particle. The internal gas pressure at this time is about 12 psia. The liquid hydrazine continues to flow inward very rapidly countercurrent to the outward flow of gas. At a time 4.0 microseconds after start, the liquid influx at the boundary is first cut off. At this time the internal gas pressure of 270 psia is finally able to overcome the liquid imbibition pressure, which is now much reduced from its earlier values, because of the high liquid saturation of the outermost portions of the particle (65 percent liquid saturation). The flow of liquid hydrazine at the outer boundary of the pellet reverses as the internal gas pressure continues to rise. At 12.19 microseconds after start the maximum outward flow rate of liquid hydrazine is attained. The "thermal explosion" is culminated at 70 microseconds after start, as the last of the liquid hydrazine in the pellet is consumed. The peak pressure is 7390 psia. Following the pressure peak, the passive blowdown of the particle begins, and by 95 microseconds after start, the pressure has declined to 3171 psia.

Consideration of the results of the initial calculation indicated that the time frame in which the processes took place (i.e. less than 100 microseconds or 0.1 milliseconds) appeared to be too short to be realistic and suggested a need for an experimental measurement of catalyst permeability.

5.3.6.2 Measurement of Permeability Constant by Imbibition

In the analytical work performed on single particle imbibition prior to the publication of the interim report, the permeability of Shell-405 substrate was estimated to be 100 millidarcy. This estimated value was obtained from U.T.R.L. mercury injection data by applying the method of Purcell and Burdine (144). This method integrates the flow conductance of the capillary (143) pore passages in the catalyst over the entire volume of various-sized pores which are present in a unit volume of material. Since the imbibition pressure of a pore is inversely proportional to the pore diameter, while the pore volume is proportional to diameter squared and flow conductance is proportional to the diameter taken to the fourth power, the integration takes the form:

$$K_m = 10.24(\sigma \cos \theta)^2 \phi \lambda \int_{s=0}^{s=1} \frac{ds}{p^2 c} \quad (5.3-45)$$

where K_m is permeability, millidarcys

ϕ is fractional porosity

s is saturation

p_c is capillary pressure, psi

σ is interfacial tension, dynes/cm.
(480 dynes/cm for mercury)

θ is contact angle (approximately 140°
for mercury against alumina)

λ is an empirical "lithology factor"
and has a value of .216

When this integral is evaluated numerically, using the U.T.R.L. data, a permeability of 106. millidarcy is obtained for Shell 405.

We recognized that there was a possibility of considerable error in this value, as well as the hydrazine imbibition pressure values, because of the unknown contact angle of mercury against Shell 405. Mercury is non-wetting with respect to alumina, with a contact angle on the order of 140° to 180° . Iridium impregnated alumina, however, would be expected to have a lower contact angle. If this was so, the "larger" pore sizes in Shell-405 could be smaller than they had been assumed to be, and the permeability would be considerably lower than had been assumed. Since permeability is a variable of prime importance to our calculations, it was necessary to make a direct determination.

The most desirable way to measure the required transport properties of Shell 405 substrate would be to determine the single-phase permeability of a geometrically precise prepared core, by measuring the volumetric flow rate of the test fluid at a fixed pressure drop. The relative permeability is best measured directly by simultaneously flowing two immiscible fluids through the core, using either the steady-state method of Hassler (145) or the transient method of Bossler and Johnson (146). The capillary imbibition pressure may be measured directly by the method of Welge (147) wherein the pressure developed by an expelled non-wetting phase is measured as the porous sample is allowed to saturate with the wetting phase, which is admitted through a semi-permeable membrane.

These functional relationships may then be mathematically manipulated using the analytic method of Buckley and Leverett (148) or the numerical method of Fayers and Sheldon (149) to obtain the desired value, which is the rate of advance of a water saturation front into the catalyst substrate by capillary imbibition pressure. It was readily apparent that these techniques would not be feasible with the time and facilities available, and hence a much simpler direct imbibition rate experiment was performed instead.

The principle of an imbibition experiment is most apparent when explained in terms of flow through a single capillary or a parallel bundle of identical capillaries, rather than in terms of flow through a natural porous medium, and hence the derivation will be given in these terms:

According to Poiseuille's Law for laminar flow through a circular tube of constant radius:

$$Q = \frac{\pi r^4 \Delta p}{8 \mu L} \quad (5.3-46)$$

where: Q is volumetric flow rate

r is radius of the capillary

Δp is the pressure drop across the tube

μ is the viscosity of the flowing fluid

L is the length of the tube

If the fluid is being drawn into the circular tube by capillary action, the pressure difference across the meniscus is given by the Laplace-Plateau equation:

$$\Delta p = \frac{\sigma \cos \theta}{r} \quad (5.3-47)$$

where: Δp is pressure

σ is surface tension

θ is contact angle

r is radius of the capillary

Combining 46 and 47:

$$Q = \frac{\pi \sigma \cos \theta r^3}{8 \mu L} \quad (5.3-48)$$

If the capillary is being progressively filled from one end, the filled volume is proportional to the length filled:

$$V = \pi r^2 L \quad (5.3-49)$$

Hence, the volume rate of filling is related to the rate of advance of the meniscus:

$$Q = \frac{dV}{dt} = \pi r^2 \frac{dL}{dt} \quad (5.3-50)$$

Combining 48 and 50, and assuming that the viscosity of the displaced non-wetting fluid is small compared to the viscosity of the wetting fluid:

$$\pi r^2 \frac{dL}{dt} = \frac{\pi \sigma \cos \theta r^3}{8\mu L} \quad (5.3-51)$$

This can easily be separated and integrated:

$$\frac{\sigma \cos \theta r}{8\mu} \int_{t=0}^{t=T} dt = \int_{L=0}^{L=L} L dL \quad (5.3-52)$$

Leads to:

$$\frac{\sigma \cos \theta r}{8\mu} T = 1/2 L^2 \quad (5.3-53)$$

or

$$L = \sqrt{\frac{\sigma \cos \theta r}{4\mu} T} \quad (5.3-54)$$

According to Equation 10, when a dry capillary (or bundle of identical capillaries) open at both ends, is immersed at one end in a wetting liquid, it will imbibe the wetting liquid at such a rate that the wetted length is proportional to the square root of time, and the value for the constant of proportionality can be used to deduce the pore radius, so long as the surface tension, contact angle, and viscosity of the wetting fluid are known.

A piece of Shell-405 substrate was roughly carved into a cylinder approximately .5 cm in diameter and 1.5 cm long. Marks were inscribed along the length of the cylinder at .1 cm intervals. One end of the cylinder was barely immersed in water which had been colored with a drop of ink, to render the water saturation front more easily visible, and the time for the water-wetted front to reach the inscribed marks was timed with a stop-watch. The experiment was replicated three times. The data from one of the experiments is illustrated in Figure 5-44. It is obvious that the data points fall along a line having the theoretical slope. The capillary radius may be calculated from the measured coefficient:

$$.08485 = \sqrt{\frac{\sigma \cos \theta r}{4\mu}} \quad (5.3-55)$$

or

$$r = \frac{4\mu .08485^2}{\sigma \cos \theta} \quad (5.3-56)$$

if

$$\mu = .01 \text{ poise}$$

$$\sigma = 70 \text{ dyne/cm}$$

$$\theta = 0.0$$

Then:

$$r = 4.09 \times 10^{-6} \text{ cm} = .0409 \mu = 409 \text{ \AA}$$

The corresponding value for permeability may be estimated by continuing to regard the Shell-405 substrate as a parallel capillary tube bundle.

The permeability of a tube-bundle is found by combining Darcy's law:

$$Q = \frac{K A \Delta p}{L \mu} \quad (5.3-57)$$

With Poiseuille's Law for N identical tubes:

$$Q = \frac{\pi r^4 \Delta p N}{8\mu L} \quad (5.3-58)$$

and the definition of porosity for a tube bundle:

$$\phi = \frac{N\pi r^2}{A} \quad (5.3-59)$$

These lead to:

$$K = \frac{r^2 \phi}{8} \quad (5.3-60)$$

Where permeability and radius are both expressed in cm^2 .

If $r = 4.09 \times 10^{-6} \text{ cm}$

$$\phi = .25$$

Then $K = 5.23 \times 10^{-13} \text{ cm}^2$

or $K = 0.053 \text{ Millidarcy}$

Despite the imprecision of the parallel tube bundle approximation, the actual permeability would be expected to fall within an order of magnitude of this value. This value for permeability is lower than the previous assumed value by a factor of 2000. Hence using the new value should greatly enhance the accuracy of the calculations in which it is a variable of major importance. It is gratifying that when this new value for permeability is used to calculate J-function values for Shell-405 from the U.T.R.L. Mercury imbibition data, that values are now obtained (Figure 5-45) having the proper order of magnitude, rather than the unrealistically high values previously reported.

5.3.6.3 Internal Particle Process Model Variation Study Using the Measured Permeability Constant

The processes following imbibition of hydrazine by a cold pellet of Shell-405 have been recalculated using the new measured value for permeability. A modest variation study has also been performed, in which the particle permeability, initial temperature, particle mesh size, and initial liquid saturation of the particle were arbitrarily varied (Table 5-3).

The most significant differences which arose from using the new value for particle permeability were in lowering the maximum value of the gas pressure calculated to be attained inside the particle, and in increasing the time scale required for the pressure to be attained. The maximum internal gas pressure is now calculated to fall within the range 750 to 5900 psi, and the response time is on the order of 5 or 10 milliseconds, depending on conditions. This range of pressures produces calculated internal particle triaxial stresses ranging from 190 psi to 1225 psi, and calculated particle

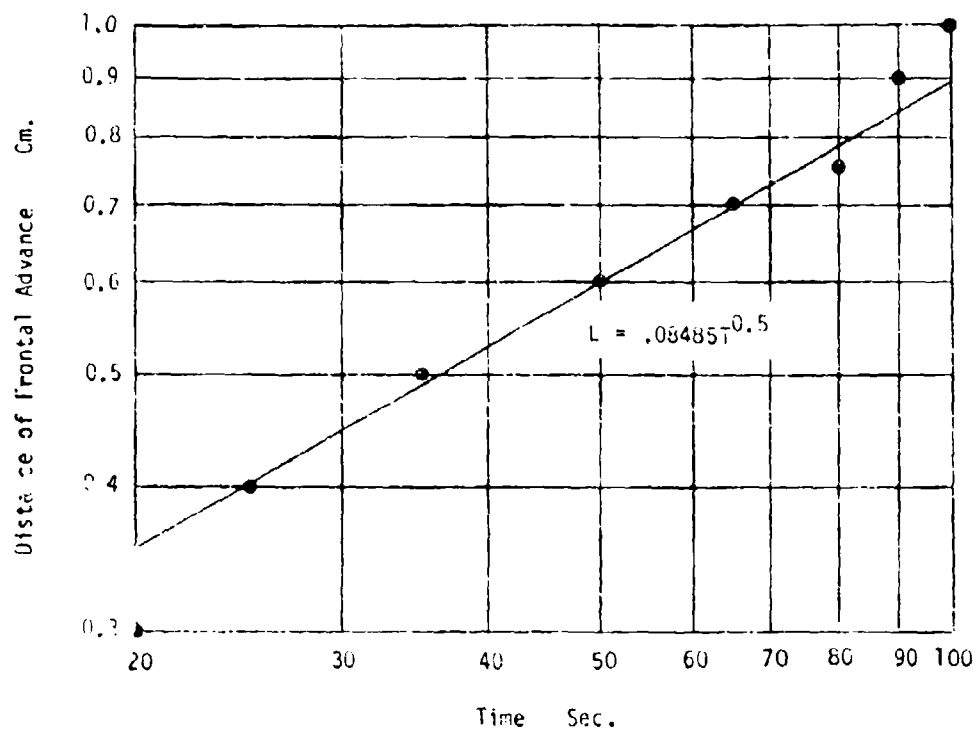


Figure 5-44. Frontal Advance Rate of Water into Shell 405 Substrate.

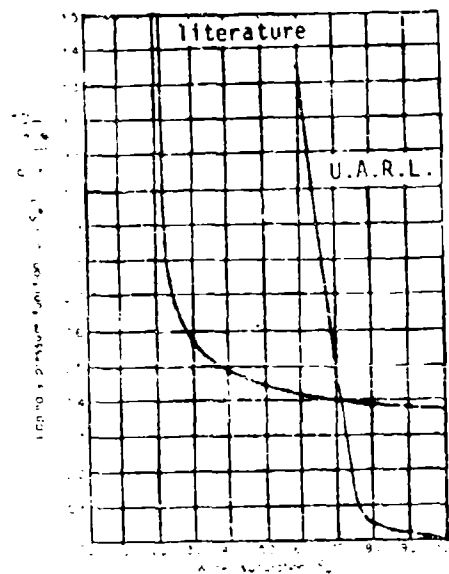


Figure 5-45. Capillary J-Function For an Alumina and Shell 405 Substrate

failure probabilities ranging from less than 5 percent to approximately 95 percent, depending on the particular conditions. This envelope of failure probabilities and response times appears to be of the same order of magnitude as experimental evidence which has been gathered by other workers (150).

5.3.6.3.1 Effect of Variation in Particle Permeability

According to our variation study, particles of higher permeability develop lower internal gas pressure, and particles of lower permeability develop higher internal gas pressure and stresses, Figure 5-46. This may be of practical importance, since our imbibition experiment indicated that there was considerable variation in permeability from particle to particle. It may be possible to modify the particles, or to select particles, on the basis of permeability, to resist failure from hydrazine imbibition.

5.3.6.3.2 Effect of Variation in Particle Size

When calculations were performed for particles of 25 mesh, 16 mesh, and 9 mesh sizes, the smaller particles were more highly stressed than the large particles during the early portions of the pressure-buildup transient, Figure 5-47. The lesser internal pressure of the larger sized particles at fixed times, appears to be a result of the longer relaxation time for larger particles, however the comparison of stresses at, say 10 milliseconds after start, may still be a quite valid comparison, since the hydrazine-wetted boundary condition of the particles exists for only a very limited time during the startup events of a cold engine, or even for a cold solitary wetted particle which may film-bind when its activity becomes high. The calculations, evaluated at a particular fixed time, such as 10 milliseconds, would rank the failure probability of different sized particles in agreement with the experiments conducted at U.T.R.L. (150).

5.3.6.3.3 Initial Temperature Effects

The initial temperature effects illustrated in Figure 5-48 are mostly reflections of the variation in the surface tension of hydrazine with temperature, which directly affects the imbibition pressure of the liquid hydrazine. Although temperature also affects the reaction rate of the hydrazine vapor, our Arrhenius type approximation of reaction rate indicates that the reaction rate is always fast compared to the transport of liquid hydrazine into the catalyst particle, i.e., with the reaction rate and transport property values currently used it is not possible to calculate the accumulation of appreciable amounts of liquid hydrazine in the catalyst particle, which could lead to explosive overshoots of pressure. Since such behavior (i.e., passive behavior of the catalyst particles long enough to imbibe appreciable liquid hydrazine) has been experimentally observed, we must conclude that our current Arrhenius type description of the hydrazine reaction rate is inadequate to describe all of the observed experimental

Table 5-2

Internal Particle Processes Variation Study

Initial Temperature °F	Particle Permeability Md.	Particle Size Mesh-Inches	Initial Liquid Saturation Percentage	Highest Internal Gas Pressure PSIA Time After Start		
				5 Millisec	10 Millisec	20 Millisec
80.	.01	25.	0.	2098.	2295.	2353.
*120.	.01	25.	0.	2046.	2138.	2172.
* 40.	.01	25.	0.	2000.	2400.	2535.
80.	*.10	25.	0.	746.	750.	
80.	*.001	25.	0.	2245.	3379.	4860.
80.	.01	*16.	0.	1579.	1994.	2262.
80.	.01	* 9.	0.	894.	1311.	1719.
80.	.01	25.	*10.%	3571.	3534.	3480.

* Indicates the parameter being varied from the values in the first line,
which are "standard" values.

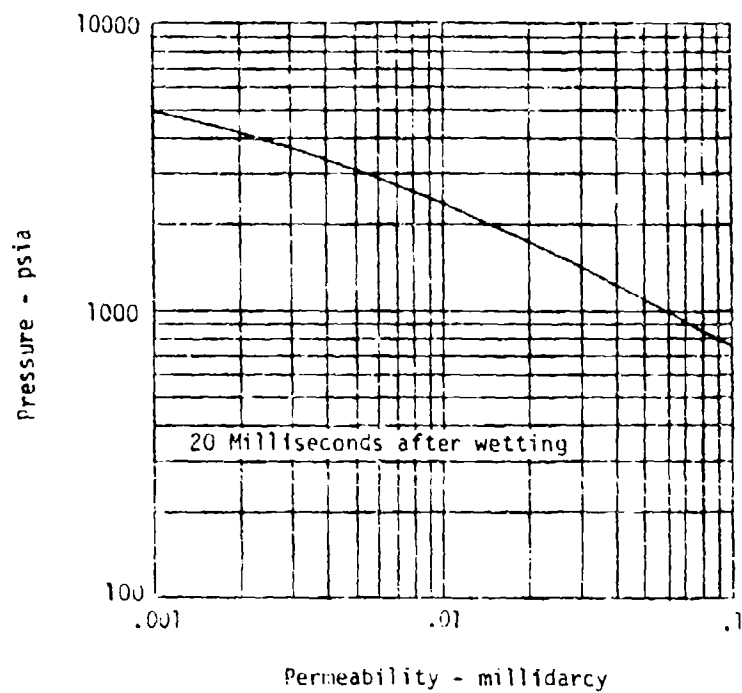


Figure 5-46. Internal Pressure vs. Particle Permeability

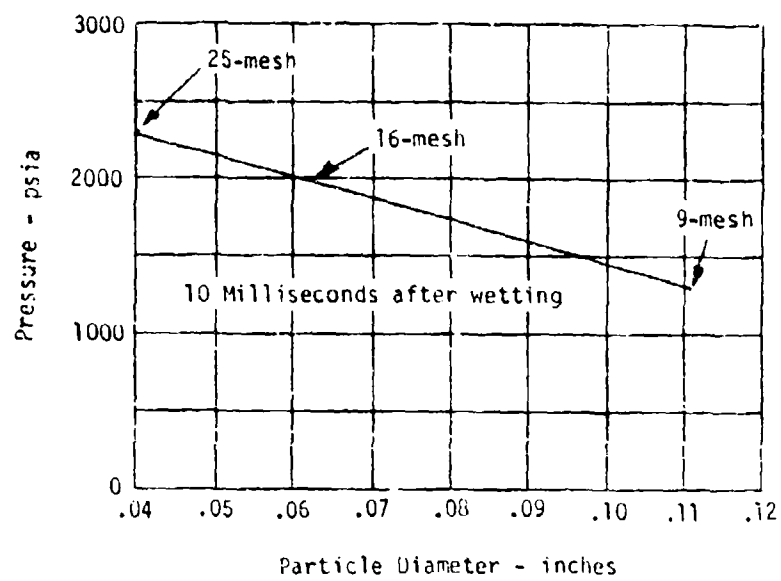


Figure 5-47. Internal Pressure vs. Particle Diameter

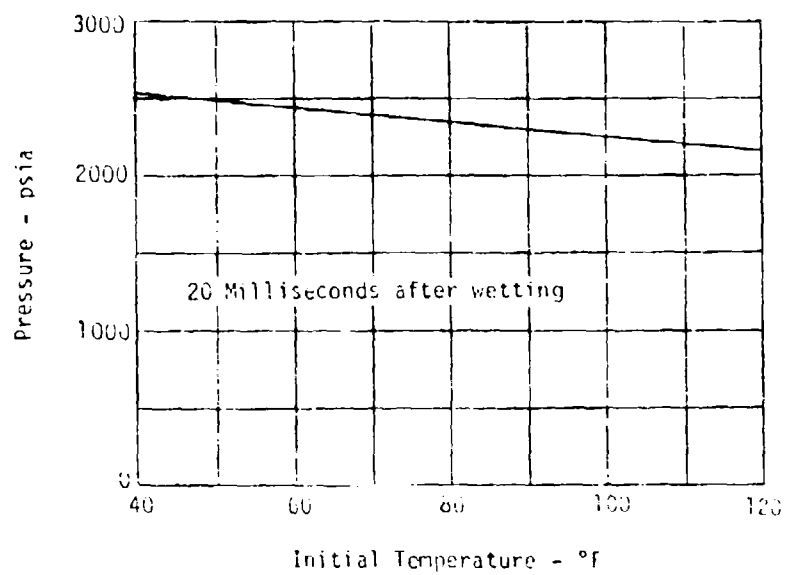


Figure 5-48. Internal Pressure vs. Initial Temperature

behavior. In order to approximately calculate the behavior of a passive catalyst particle, which imbibes liquid hydrazine, and then suddenly becomes chemically active, we have performed calculations in which the catalyst particle has an appreciable liquid saturation as an arbitrarily imposed initial condition.

5.3.6.3.4 Initial Saturation Effects

It has been experimentally determined that under certain conditions, which are not fully understood, a cold catalyst pellet can become passive to liquid hydrazine, and remain wetted by the liquid for an extended period of time without appreciable chemical reaction taking place (150). Our measurements of the frontal advance rate of liquid water into Shell 405 substrate lead to the expression

$$L = \sqrt{\frac{\sigma \cos \theta r}{4 \mu}} \sqrt{T} \quad (5.3-61)$$

where L is depth of penetration and T is time
 r is pore radius
 σ is surface tension
 θ is contact angle
 μ is viscosity

If the appropriate value for pore radius, and the properties of liquid hydrazine are used, then:

$$L = .0873 \sqrt{T} \quad (5.3-62)$$

which infers that liquid hydrazine would be expected to penetrate to the center of a passive 25-mesh catalyst particle in .328 seconds, while 16 mesh pellets should take .819 seconds, and 9 mesh pellets 2.608 seconds.

The liquid saturation behind such a frontal advance, would depend on the shape of the relative permeability curves, but would always be less than the liquid saturation which corresponds to a zero relative permeability for the gas phase, that is, liquid permeability would always be less than some limiting value, on the order of 90 percent.

The computer model calculation for a particle with 10 percent initial saturation, showed that the decomposition of the imbibed hydrazine took place very rapidly once the particle became non-passive if the normal reaction rate expression is used. The reaction rate of the imbibed hydrazine was so much faster than the outflow of the product gases that the peak pressure attained may be accurately estimated by assuming that all imbibed hydrazine is converted to product gases before any escapes. The conclusion from such an approximation is shown in Figure 5-49. This curve implies that if a passive catalyst pellet, appreciably saturated with liquid hydrazine were to suddenly become fully reactive, that there would be essentially no intact particles surviving such a transition if the initial hydrazine saturation was higher than approximately 10 or 12 percent. Since catalyst pellets, which are almost certainly more highly saturated than this do survive the transition from passive to active, it is strongly implied that the catalyst reactivity is considerably less than the normal value immediately after such a transition takes place.

5.4 Differential Thermal Expansion

One of the mechanisms that may cause or contribute to catalyst breakup is differential thermal expansion. Differences between the thermal expansion rates for the catalyst bed and chamber walls can result in application of compressive forces to the bed and/or the creation of voids in the catalyst bed which, in turn, produces considerable particle abrasion, settling and channeling. The differential expansion is compounded by the simultaneous effect of chamber strain associated with the internal pressure forces. The differential expansion phenomenon normally occurs during the initial ambient start of a firing sequence and during cooldown after the last pulse.

This section presents the differential thermal and pressure expansion analysis of a monopropellant hydrazine catalyst thruster. An evaluation of the effects of various operating and design parameters on the thermal response of the catalyst bed and chamber wall and the resulting net expansion (or contraction) is also presented.

5.4.1 Method of Calculations

Kesten's (Reference 124) analysis of catalyzed hydrazine decomposition reactors was used to obtain the temperature distributions in the catalyst bed. Calculations of the temperature and reactant concentration distribution as functions of time and axial position in typical reaction chamber configurations

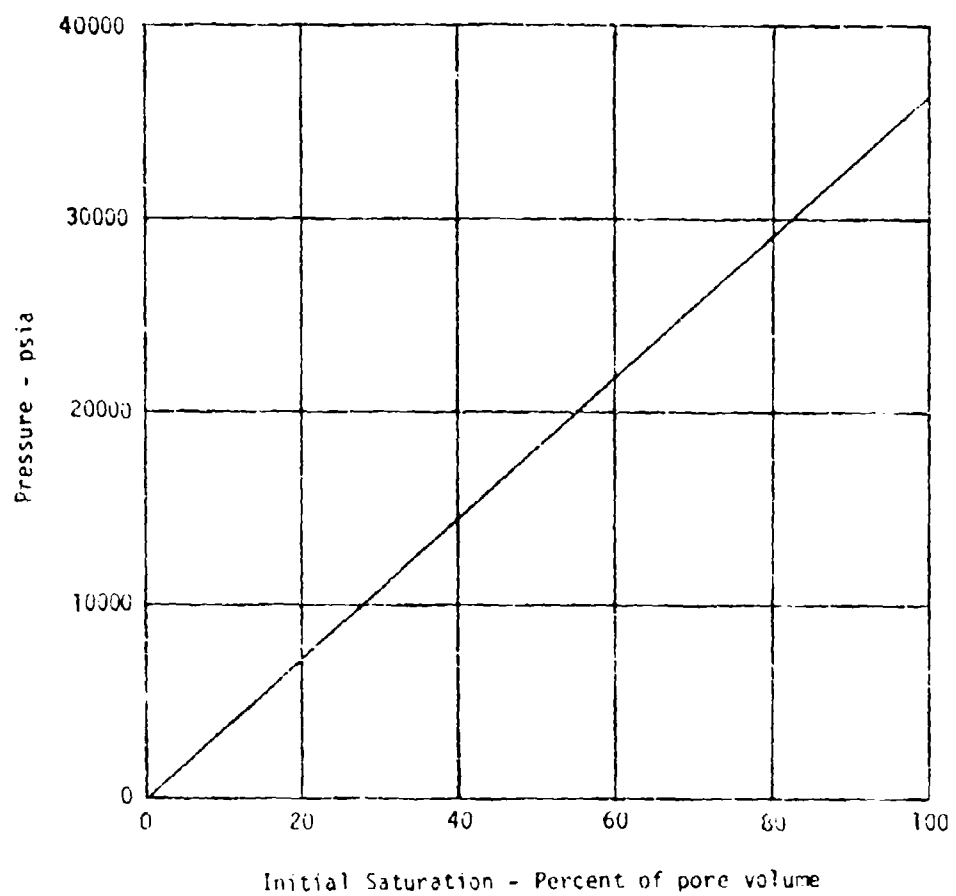


Figure 5-49. Internal Pressure vs. Initial Saturation

can be made with Kesten's steady state and transient computer programs. The steady state calculations are required to provide certain inputs to the transient program. Kesten's transient program was used to give a representation of the thermal transient in the catalyst bed and chamber wall. For computational purposes the catalyst bed is divided into nodal segments (usually around 50 segments) and temperature and pressure calculations are made for these segments as a function of time.

For this study, the transient computer program was modified to include the calculation of thermal expansion. Corresponding to the nodal particle temperatures at each selected time point, the linear deformation, δ_T , is calculated by the relation

$$\delta_T = \alpha L (\Delta T) \quad (5.4-1)$$

in which α is the coefficient of linear expansion, L is a length and ΔT is the temperature change. Calculating the dimensional change of each segment in this manner, the incremental volume change is obtained. The change in bed volume is summed from the inlet position to the end of the bed for every selected time increment.

Thermal expansion of the chamber wall is calculated from the wall temperatures predicted by Kesten's computer program. Kesten calculates the chamber wall temperature assuming Newtonian heating or cooling, i.e., internal resistance (L/KA) \ll surface resistance ($1/hA_1$) where K is the wall thermal conductivity, A is the conducting area, h is the surface conductance, and A_1 is the surface area. For the thin-wall, metallic chambers of typical flight reactors, this level of approximation is adequate for providing qualitative information on the effects of various design variables on the differential thermal expansion. With this assumption the temperature in the chamber wall is uniform and is calculated by the equation

$$M_W C_W \frac{dT_W}{dt} = \pi d_c \int_0^L h_W (T_i - T_W) dz \quad (5.4-2)$$

where

T_W = Wall temperature

T_i = Interstitial phase temperature

t = Time

M_W = Thermal mass of chamber wall

C_W = Specific heat of chamber wall

d_c = Diameter

h_W = Heat transfer coefficient between bulk fluid and wall

z = Axial distance

L = Length of reaction chamber

The equation is valid if the outer wall surface is insulated. Heat loss from the chamber wall to the surrounding atmosphere can be accounted for by adding a term to the right side of the above equation. Heat loss by natural convection and radiation to space were the only heat transfer modes considered and can be represented by the form $-h_a A_w (T_w - T_a)^{1.25}$ or $-\sigma \epsilon A_w (T_w^4 - T_a^4)$, respectively where h_a is the natural convection heat transfer coefficient, A_w is the chamber wall surface area, T_a is the ambient temperature, σ is the Boltzmann constant, and ϵ is the wall emissivity.

The time dependent free chamber volume is based on the wall thermal expansion and the simultaneous effect of chamber strain associated with the internal pressure forces. For a cylindrical chamber the pressure deformation is calculated by

$$\delta_P = \frac{PD^2}{2tE} \quad (5.4-3)$$

where P is the chamber pressure, D is the diameter, t is the wall thickness and E is Young's modulus.

5.4.2 Results of Calculations

Calculations were made for a monopropellant hydrazine reactor with the modified transient computer program to evaluate the effects of various system parameters on the differential expansion of the catalyst bed and chamber walls. Table 5-3 summarizes the base line operating and design characteristics which were used for the calculation. The catalyst bed is cylindrically shaped with two layers of Shell-405 catalyst. The overall bed length is 2 inches with the upper bed consisting of 25-30 mesh particles in the first 0.2 inch and 1/8 inch pellets for the remainder of the bed. The vacuum thrust is 5 lbf and the bed loading is 0.05 lb/in²-sec which results in a chamber diameter of 0.84 inches (nozzle area ratio of 2). Chamber wall material is Haynes Alloy 25 (L605) which is a common structural material for monopropellant applications. The structural thickness of the chamber wall is sized from hoop stress considerations unless the value calculated is less than the minimum handling thickness of 0.05 inches. The wall heat transfer mode assumed for the base line calculations is natural convection.

Figure 5-50 illustrates the cold (ambient) start temperature histories in the catalyst bed and chamber wall for the baseline conditions. The temperature response of the catalyst particles varies along the length of the bed with the response decreasing with distance from the inlet end. As expected the chamber wall temperature lags behind the catalyst particle temperatures. Corresponding to the temperature histories in the bed and chamber wall, the volume change is presented in Figure 5-51. Although the chamber wall temperature is always less than the catalyst bed on start-up, the volume increase in the chamber is greater than the volume increase in the catalyst bed after 0.7 seconds. This is the result of the wall coefficient of thermal expansion being four times that of the catalyst particle. Prior to 0.7 seconds the catalyst bed is compressed by differential thermal expansion between the bed and chamber wall. The chamber wall volume change shown in Figure 5-51 includes the volume increase due to internal pressure forces. The pressure induced volume change is significant only during the first 0.2 seconds of operation. After 5 seconds, the contribution of the pressure strain is only one percent of the total wall volume increase.

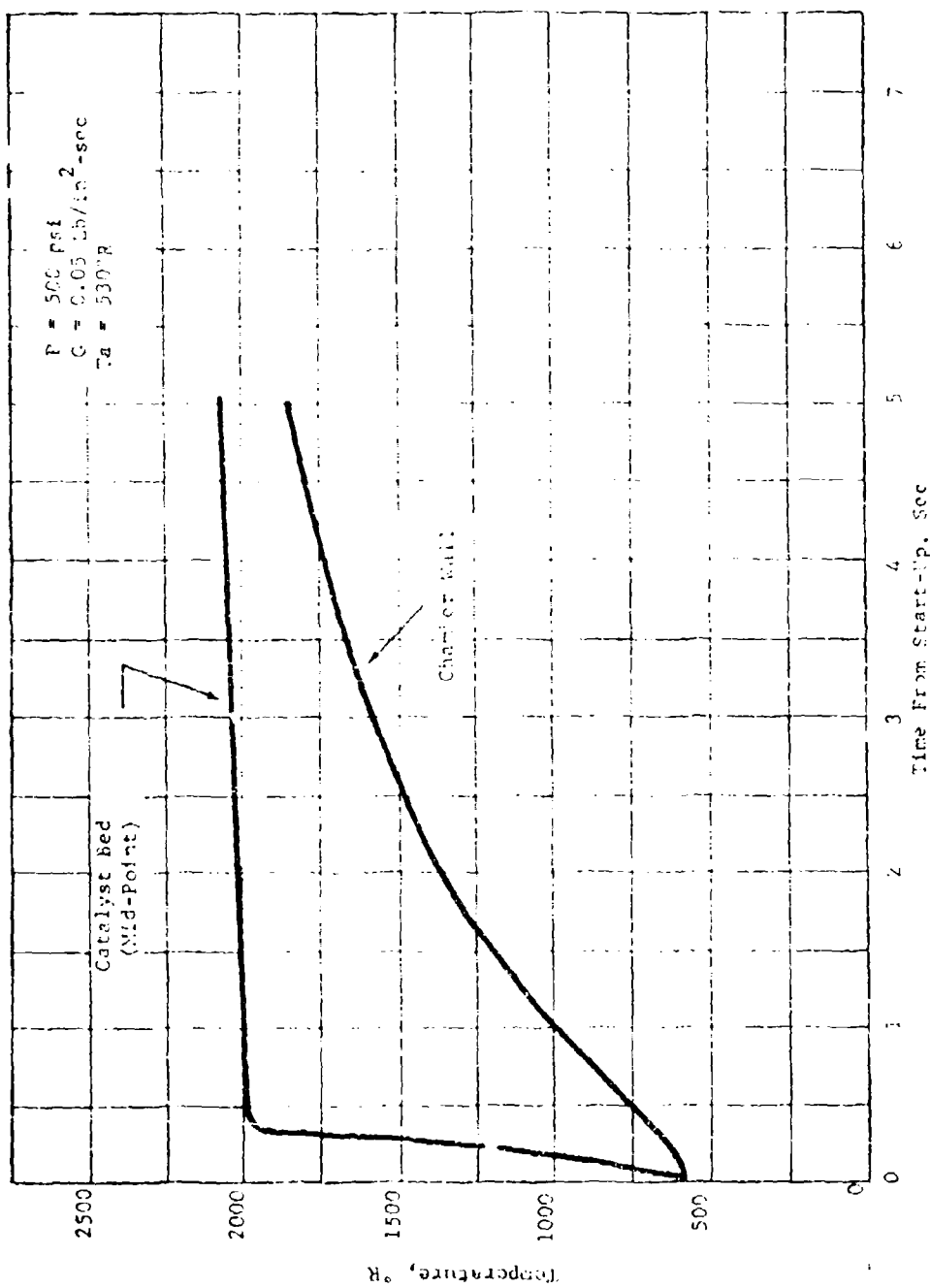


Figure 5-30. Start-Up Temperature Response.

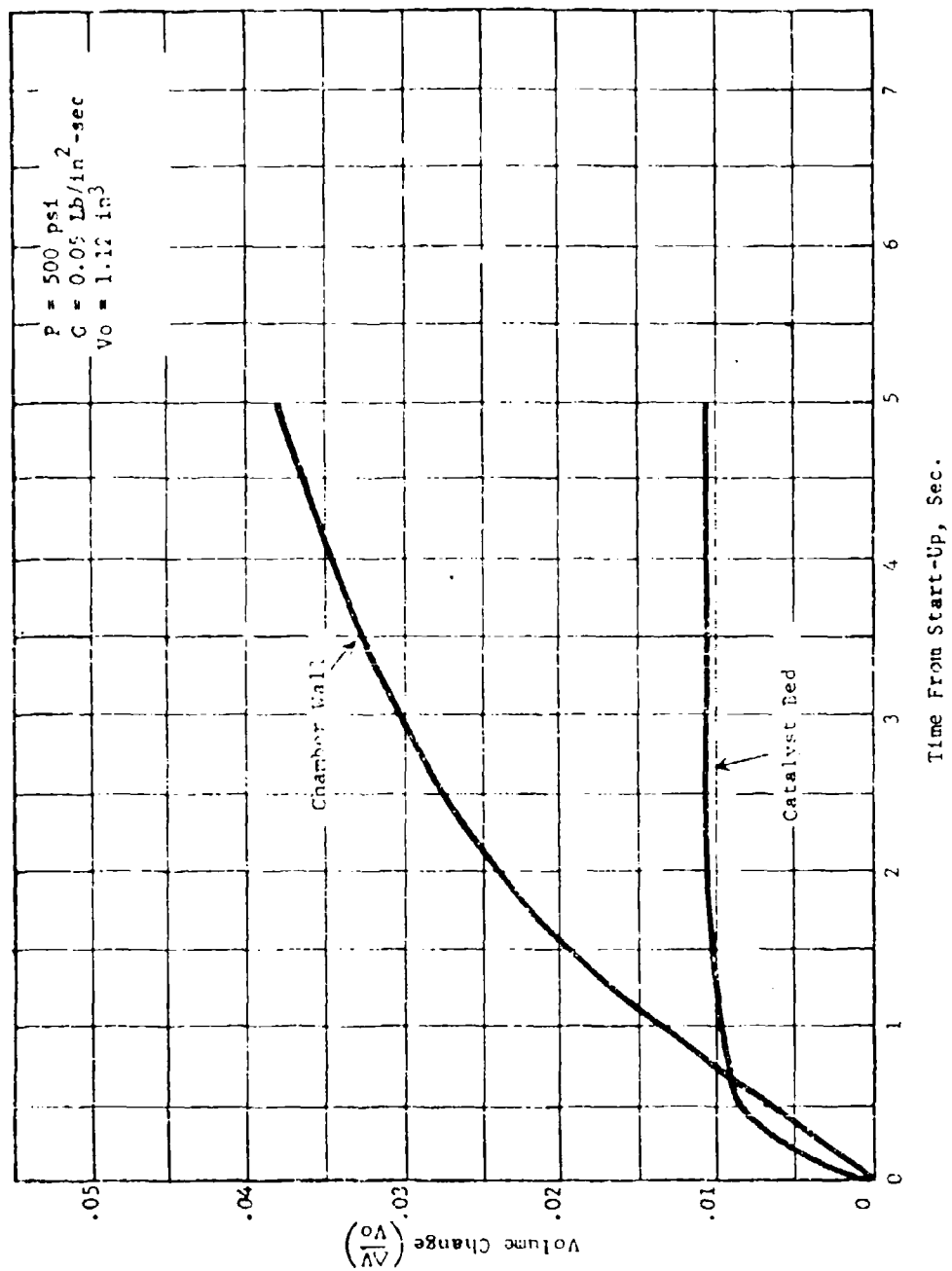


Figure 5-51. Catalyst Bed and Chamber Wall Expansion Histories.

The reactor temperatures at the end of the on pulse form the initial conditions for the cooldown period as shown in Figure 5-52. Translating the temperatures into volume changes produces the results shown in Figure 5-53. It can be seen that the dilation of the catalyst bed at the end of the on pulse is maintained throughout shutdown. This assumes that there is no repacking of the catalyst bed from pressure forces on the bed or by mechanical devices, such as springs. If the volume change shown in Figure 5-53 is re-calculated so that the change is relative to the volume at the end of the on pulse rather than the original volume, a net compression of the catalyst bed occurs during cooldown.

5.4.2.1 Effect of Bed Loading

The effect of varying the bed loading, with all other conditions taken as those of the base line, on the start-up differential expansion is illustrated in Figures 5-54 and 5-55. A compression of the catalyst bed occurs initially but changes to a dilation 0.7 sec after start-up. The magnitude of the peak compression and dilation increases with increasing bed loading. This trend is caused by the faster temperature response at increasing bed loading of (1) the catalyst bed initially, and (2) the chamber wall after the normal thermal lag. The loose bed condition at the end of the on pulse is maintained during cooldown for all values of bed loading investigated if the bed is not repacked. Allowing bed repacking a greater compression takes place at higher bed loading as illustrated in Figure 5-56. This effect of bed loading will diminish if the bed length is optimized for each bed loading value. The bed length is more nearly optimized in terms of gas temperature for the highest bed loading of $0.10 \text{ lb/in}^2\text{-sec}$. At lower bed loadings the ammonia dissociation increases with a subsequent lowering of the bed exit gas temperature. Reducing the bed length to maintain a constant ammonia dissociation will have the effect of narrowing the differential expansion differences near steady state conditions and on cooldown.

5.4.2.2 Effect of Chamber Inlet Pressure

Pressure effects on the start-up differential expansion is shown in Figure 5-57. The contribution of pressure induced strains is clearly illustrated in the figure. The sharp initial rise in the net volume change is produced by the buildup in chamber pressure. This phase is followed by bed compression as the catalyst bed begins to increase in temperature. As the wall begins to respond to the hydrazine decomposition environment, the wall thermal expansion becomes dominant. Pressure does not have a strong effect on the bed compression portion of the volume change cycle other than to vary the compression duration. Bed void volume increases as the pressure is increased. The increased wall heat transfer at higher pressures accounts for the greater bed void volume as steady state is approached.

An interesting result is obtained during cooldown if the volume change is taken relative to the beginning of the shutdown cycle. Figure 5-58 shows that the bed is compressed at higher pressures while a loose bed is obtained at the 200 psi pressure condition. For the relatively low bed loading ($G = 0.01 \text{ lb/in}^2\text{-sec}$) and pressure (200 psi) case, the chamber wall temperature is still increasing after shutdown occurs. Therefore, the chamber wall volume continues to increase for another 3 seconds after reactor shutdown.

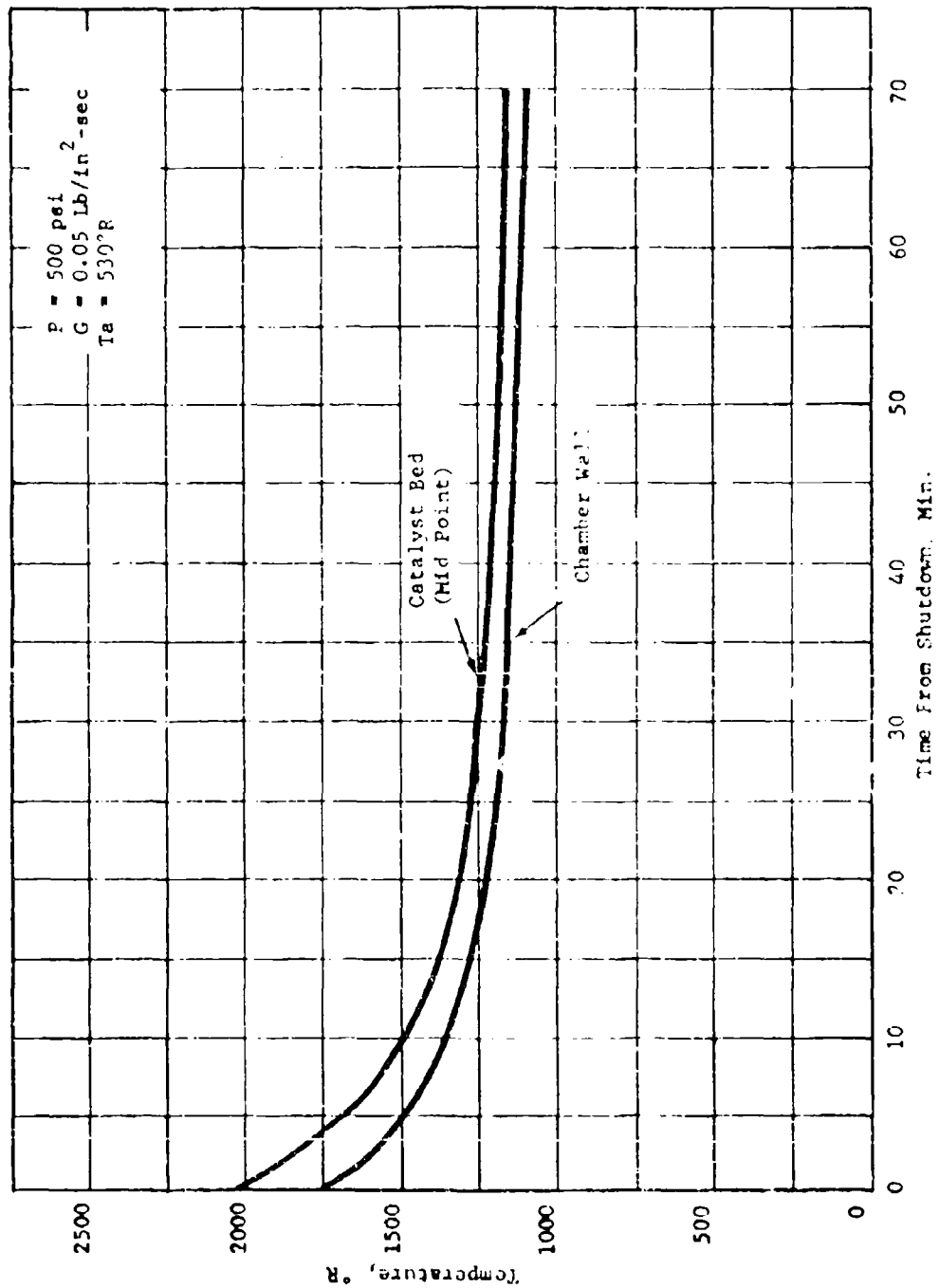


Figure 5-52. Cooldown Temperature Histories.

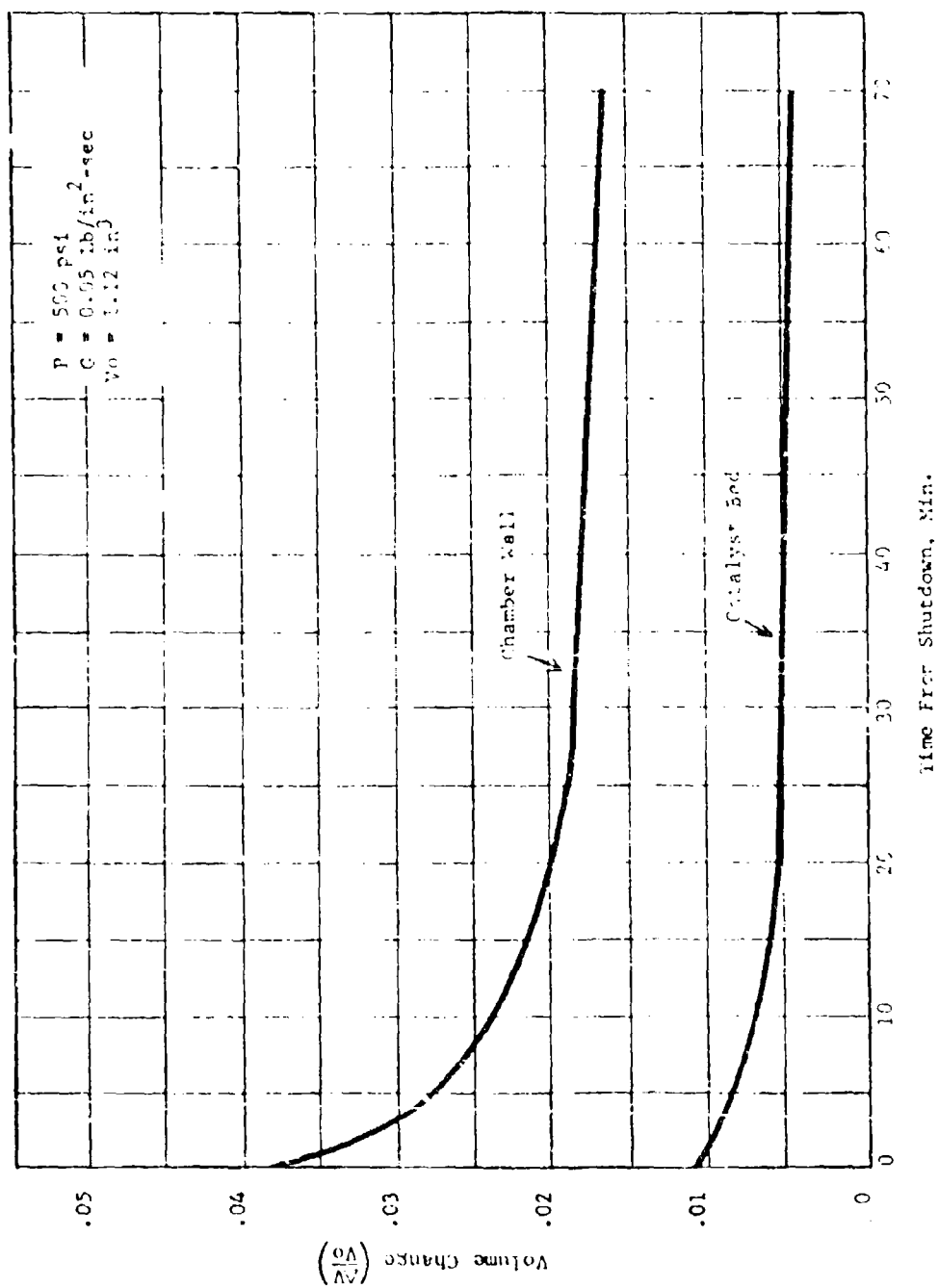


Figure 5-53. Catalyst Bed and Chamber Wall Contraction During Cooldown.

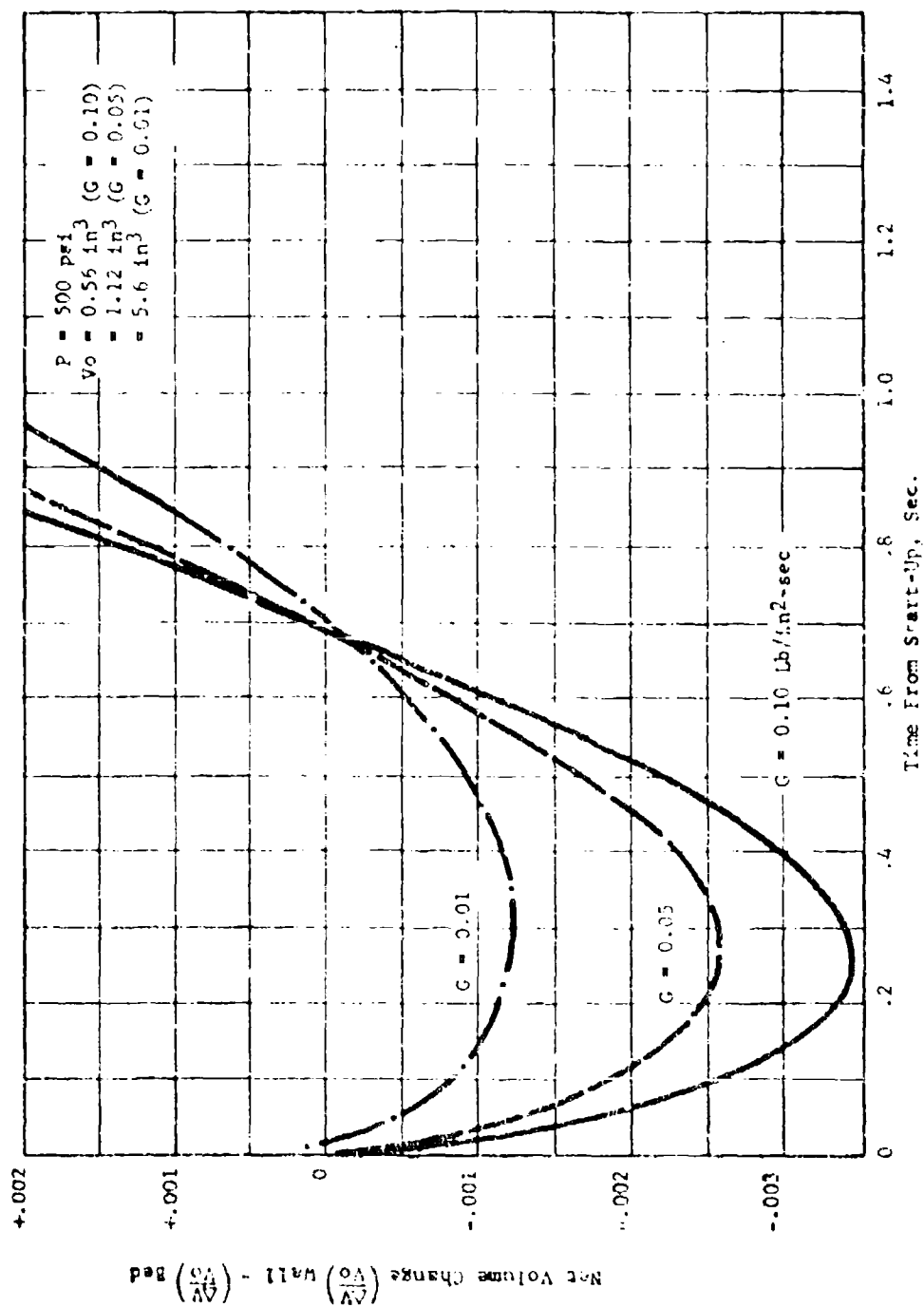


Figure 5-54. Effect of Bed Loading on Differential Expansion.

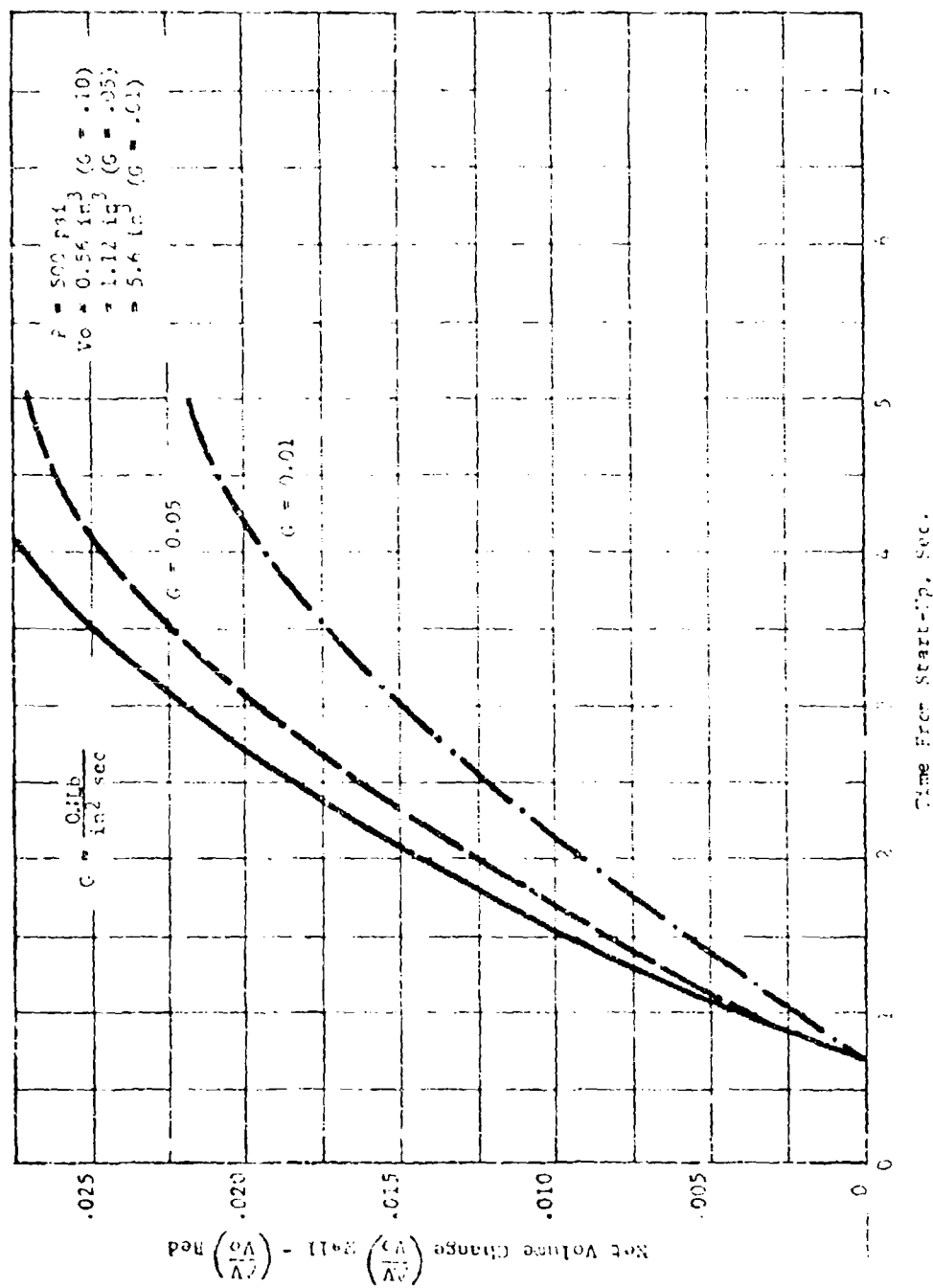


Figure 5-55. Effect of Pad Loading on Differential Expansion - Near Steady State

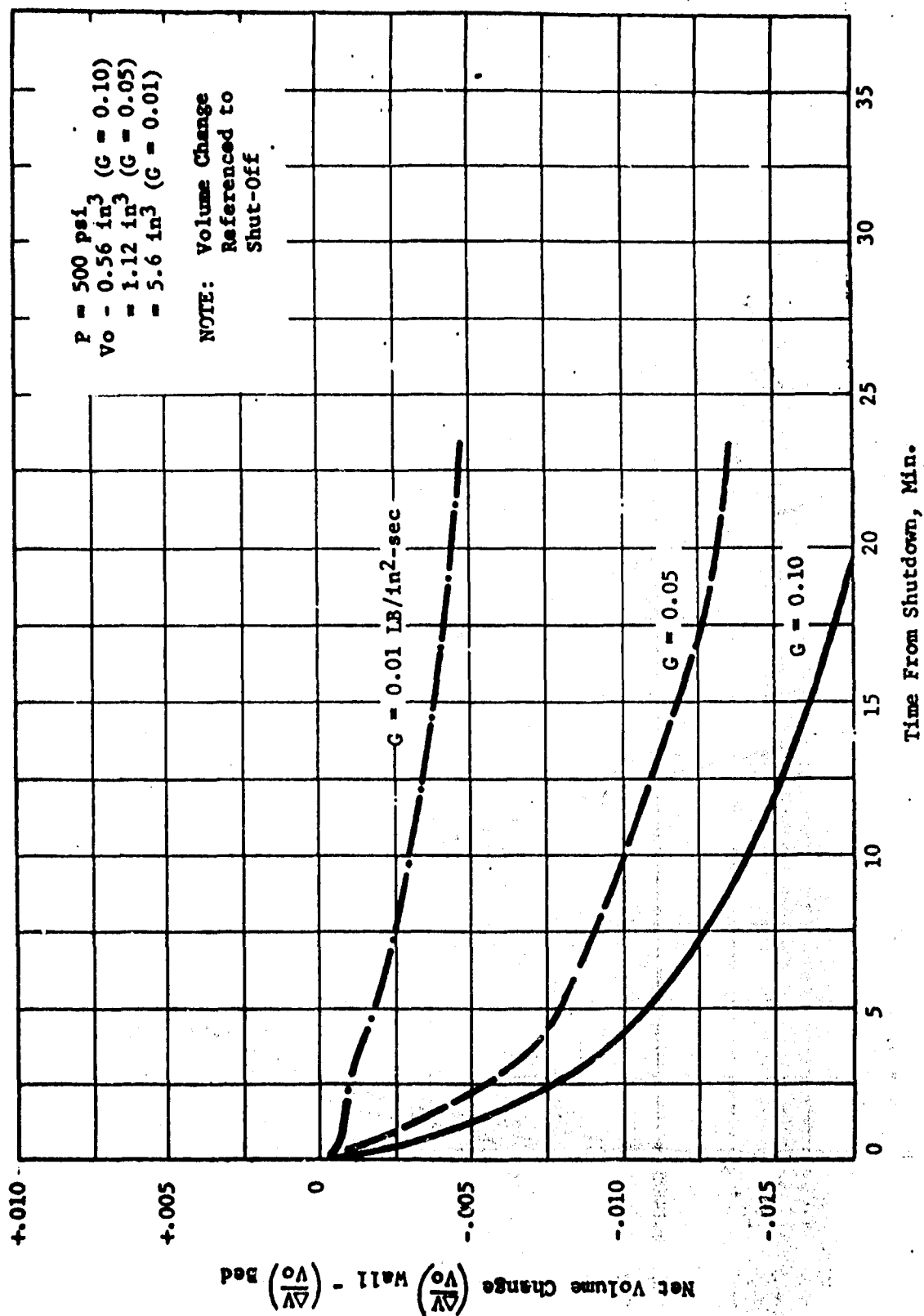


Figure 5-56. Effect of Bed Loading on Cooldown Differential Expansion.

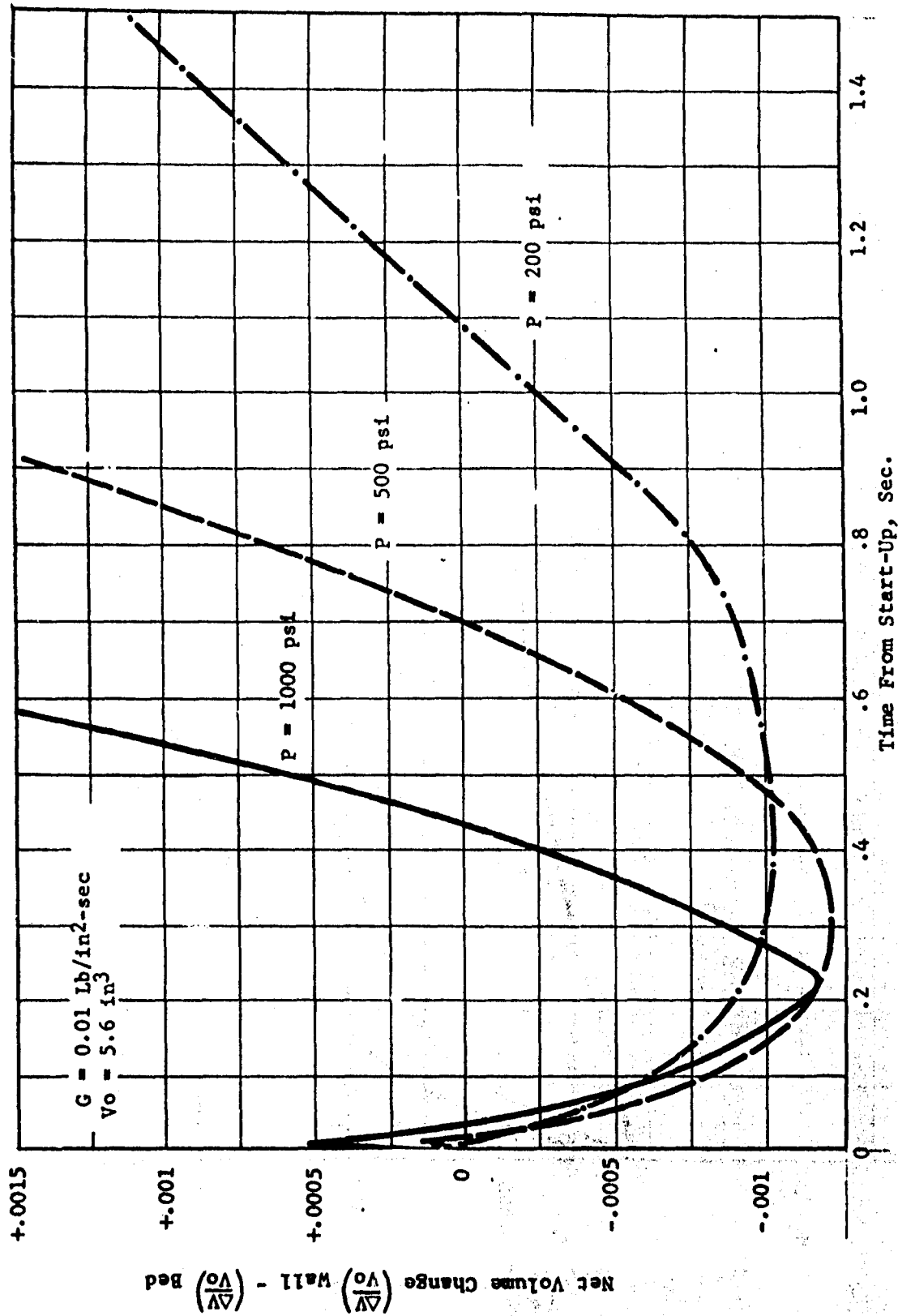


Figure 5-57. Effect of Pressure on Start-Up Differential Expansion.

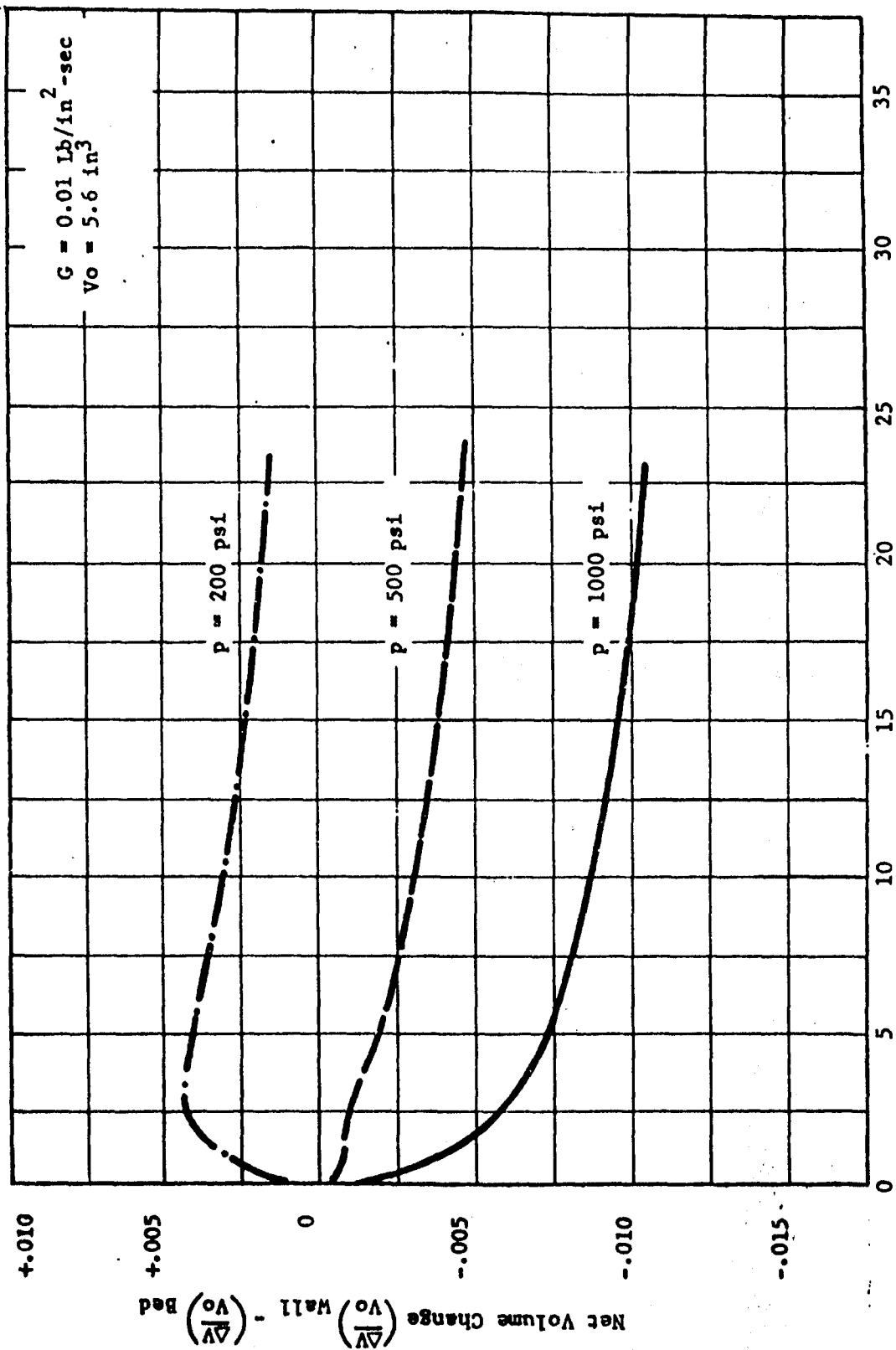


Figure 5-58. Effect of Pressure on Cooled Differential Expansion.

Table 5-3

Conditions Used in Differential Thermal Expansion Calculation

Catalyst Type	Shell-405
Catalyst Size	
Upper Bed	25-30 Mesh
Lower Bed	1/8 in Pellets
Catalyst Bed Total Length	2 In
Upper Bed Length	0.2 In
Vacuum Thrust	5 Lb _f
Pressure	500 PSI
Bed Loading	0.05 LB/In ² -Sec
Chamber Material	L605
Chamber Wall Thickness	0.050 In
Bed Diameter	0.844 In
Chamber Wall Cooling	Natural Convection

5.4.2.3 Effect of Thrust

As anticipated, the higher surface-to-volume ratio of the smaller reactors leads to greater heat losses from the chamber wall. As shown in Figure 5-59, the resulting lower wall temperatures produce a greater bed compression but a smaller bed void later on in the starting pulse. The differences in volume between the two illustrated thrust values is less than the effects of bed loading and pressure previously shown. Since the thrust variation was made at constant bed loading the results of the variation are also applicable to a change in bed diameter.

5.4.2.4 Effect of Case Material

Selection of a thrust chamber material for monopropellant applications is usually based on strength properties, resistance to nitriding and oxidation, and compatibility with hydrazine. Nickel or Cobalt base superalloys are usually chosen for the engine material and the coefficient of thermal expansion of these materials show little variation. As the chamber material coefficient of expansion approaches that of the catalyst particles, the steady state bed dilation would diminish. However, the transient bed compression condition would be increased in magnitude.

5.4.3 Effects of Differential Thermal Expansion/Contraction on the Catalyst

If we assume a bed compaction law of the form discussed in the section on particle stresses:

$$\frac{\Delta V}{V} = K P^{2/3} \quad (5.4-4)$$

where

V = Bed volume

P = Bed compaction pressure

The value for K may be obtained from the Exxon experimental measurement of 4 percent bed compression at a pressure of 1000 psi. When this is done, and the equation restated, pressure due to bed compression may be calculated:

$$P = 125,000 \left(\frac{\Delta V}{V} \right)^{1.5} \quad (5.4-5)$$

Figure 5-54 shows that the start transients in engines having bed loadings of .01, .05 and .10 lb/in² sec. will produce bed compressions ($\Delta V/V$) of .0012, .0026, and .0034 respectively. These compactions, using the above expression should correspond to bed pressures of 5.2 psi, 16.6 psi and 24.8 psi.

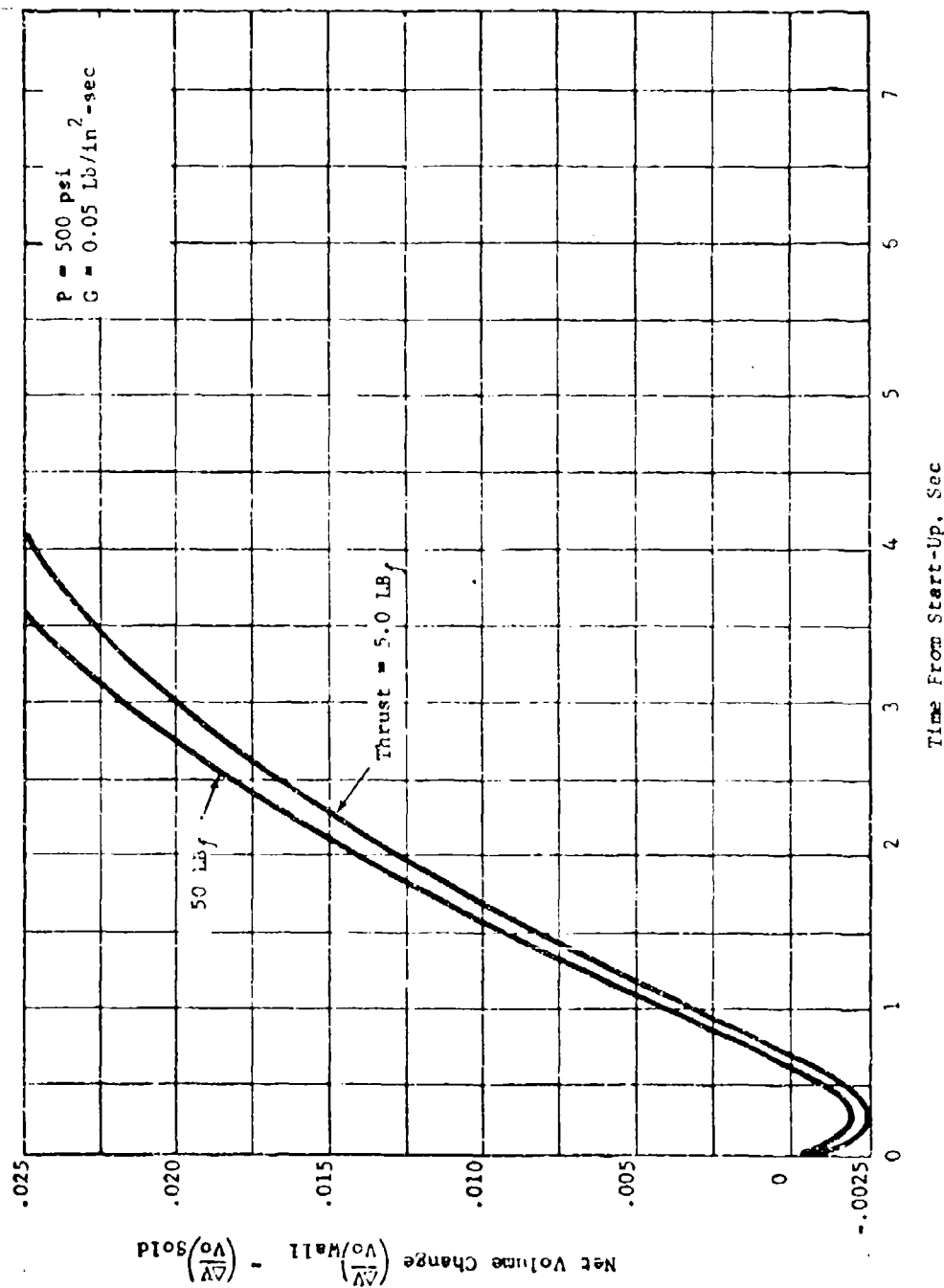


Figure 5-59. Effect of Thrust on Start-Up Differential Expansion.

The expression (taken from a previous section, equation (5.2-27) for the force acting on a pellet in a bed at a location of point-to-point contact is:

$$F = \sqrt{2} R^2 P \quad (5.4-6)$$

where

F is contact force at a point of contact

R is radius of the pellet

P is bed compaction pressure

Using the values

$$P = 24.8 \text{ psi}$$

$$R = .02 \text{ inch (25 mesh)}$$

$$F = 2 \cdot .02^2 \times 24.8 = .014 \text{ pounds.}$$

This is well under the .61 pounds of compressive force which is given in Table 4-10 as the average force required to completely crush a 20-30 mesh particle. Hence it may be concluded that the differential thermal expansion of a single cold start by itself will not be adequate to cause catastrophic destruction of the catalyst pack.

Referring to Figure 5-18 of the section on particle stresses, however, indicates that a bed compression stress of 25 psi produces a local peak stress of 9000 psi in the catalyst pellet at the center of the point of contact. Referring to Figure 5-22 of the same section shows that 25 psi of bed compression is sufficient to initiate failure in either used or new catalyst material, hence local failure and mass loss at points of contact should be expected from 25 psi of bed compression stress. This conclusion is experimentally confirmed by the bed crushing tests which indicated that approximately 0.4 percent of the bed mass should be lost from a 25 psi compression of the bed.

When the engine cools off from the maximum thermal dilation which occurs at steady-state, the bed may be subjected to compression stresses if it has repacked itself during this period of maximum dilation. According to Figure 5-56, engines having bed loadings of .01, .05 and .10 will give bed compressions of .004, .013, and .0175 in the first twenty minutes after cutoff. These correspond to bed pressures of 31.6 psi, 185 psi and 289 psi. The highest of these bed compression pressures is sufficient to crush 15 percent of the catalyst in the bed according to bed pressure crushing experimental results. The largest unknown in this process appears to be the flow behavior of the catalyst bed under pressure in the thruster environment e.g. will it repack during a dilation phase. Regarding this latter point, it should be noted that on occasion when a used thruster is opened, the catalyst bed is so tightly packed that it will not flow under the force of gravity alone.

In general, it can be seen that the pressure crushing forces which result from differential thermal expansion effects are potentially significant factors in catalyst breakup.

5.4.4 Differential Thermal Expansion Calculations Carried Out by AFRPL

Further calculations using the differential thermal expansion model were carried out by Lt. S. G. Wax, Air Force Rocket Propulsion Laboratory (AFRPL).

5.4.4.1 General Approach

As described in the Interim Report (100) and Section 5.4.1 of this report the NASA transient code for a monopropellant thruster was modified to calculate the differential thermal expansion (DTE) between the thruster wall and the catalyst bed. From the difference in volume changes (normalized to initial chamber volume, V_0) the net volume change, $\left(\frac{\Delta V}{V_0}\right)_N$ was calculated as:

$$\left(\frac{\Delta V}{V_0}\right)_N = \left(\frac{\Delta V}{V_0}\right)_{\text{wall}} - \left(\frac{\Delta V}{V_0}\right)_{\text{bed}}$$

When the net volume change is negative, the catalyst bed is under a compression pressure, P , where:

$$P = 125,000 - \left(\frac{\Delta V}{V_0}\right)_N \Big]^{1.5}$$

Once the bed compression is calculated, mass loss may be calculated using the results of the bed crushing tests for the appropriate mesh size catalyst. Figure 5-60 indicates the results of two separate series of measurements for 25-30 mesh catalyst. A fit to the curve, $\text{loss} = a\sqrt{P}$ appears to be reasonable and,

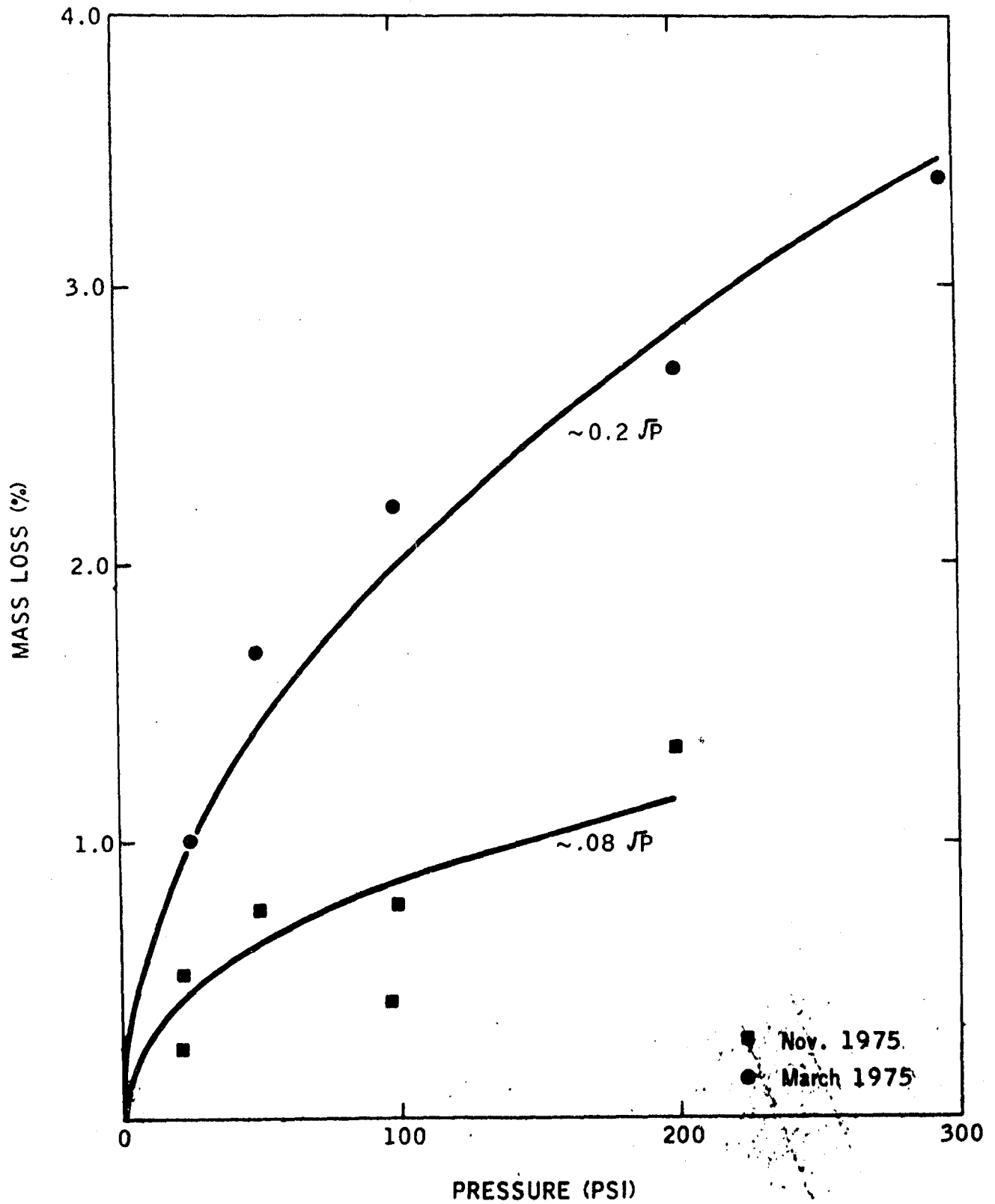
$$\text{mass loss (\%)} = .2 \sqrt{P}$$

$$\text{mass loss (5)} = .08 \sqrt{P}$$

may be used to represent the latest and earliest data points respectively. The difference between these may indicate a batch to batch variation in catalyst strength. At any rate, they provide a range of losses which one could reasonably expect to experience. This range will be used in the following examples. It is not, however, a universal mass loss, but rather a representation of mass loss increases with increased pressure.

Figure 5-60

Mass Loss Vs. Pressure - 25-30 Mesh



5.4.4.2 Continuous Operation Calculations

As described in the interim report, and Section 5.4.2 of this report parametric variations were made to a "standard" thruster by MDAC in order to assess the effects of chamber pressure, flowrate, and thrust level. Table 5-4 shows the characteristics used for that thruster. The model was run continuously and the net compression calculated as a function of time. In order to extend this parametric study, two additional thrusters were modeled; a Hamilton Standard, (HS) 0.1 lbf thruster and a 5.0 lbf thruster which was representative of the thruster used by Bell Aerospace (BAC) in their 5-lbf Long-Life Design Criteria program (151). A description of these engines may also be found in Table 5-4.

Figure 5-61 shows the start-up of a continuous run for the 0.1 lbf HS thruster, the 5.0 lbf BAC thruster and the 5 lbf "worst case" example presented by MDAC ($G = 0.10$ lb/in-sec, $P = 500$ psi). Maximum bed compressions were calculated as 174 psi (BAC) 44.2 psi (HS) and 28.7 psi (MDAC). For the 5.0 lbf BAC engine, one expects mass losses between 2.6 and 1.0%. This is in the range where mass losses begin to be important. Since, the 5.0 lbf thruster modeled here was designed to represent a simplified 5 lbf thruster, the mass losses would be considered typical of that thrust range. The worst case example used by MDAC has a predicted maximum loss of 1%, while for the 0.1 lbf a maximum loss of 1.3% is calculated. It is interesting to note that regardless of the thruster used maximum mass losses are between 1 and 2.6%; serious but not catastrophic.

5.4.4.3 Pulsed Mode Calculations

In terms of thruster life, it is not continuous, but rather pulsed operation which is the most severe condition. Thus, it is important to assess the DTE mechanism for pulsed operation. Figure 5-63 shows the wall and catalyst (center of bed) temperature for the 0.10 lbf thruster. Operation is 10 ms on and 10 seconds off. During the on time, the catalyst bed rapidly increases in temperature and cools during the off time. The thruster wall is heated by the catalyst bed and thus rises in temperature any time the bed is hotter than the wall. (The model cools the bed by convection and radiation during the off time, but this cooling is negligible when the bed is very much warmer than the wall). Thus, compression of the bed is expected during the on period with a relaxation during the off period. Figure 5-63, depicting the compression of this thruster, confirms this. For this duty cycle, the wall expands beyond the bed during the first off time and relieves the compression. But, when the thruster is turned on again, the bed is recompressed. The magnitude is less than the original compression (1.8 psi vs. 23.6 psi), and may be smaller still since the mass loss from the first compression would reduce that from the subsequent compression. Even so, the potential for cumulative losses due to duty cycle effects is clearly demonstrated. Figure 5-64 compares two other duty cycles for the 0.1 lbf engine. If one assumes that compaction can be repetitive then the effects of multiple pulses can be more deleterious than that of a single steady state firing. For the 0.1 lbf thruster,

Table 5-4

Thruster Characteristics

	McDonnell Douglas Astronautics (MDAC) (a)	Bell Aerospace Corp. (BAC)	Hamilton Standard (HS)
Thrust Size, Lbf	5 Lbf	5 Lbf	0.1 Lbf
Catalyst Bed Length (in)	2.0	1.16	0.42
Upper Bed Length (in)	.2	0.04	(single bed)
Catalyst Size			
Upper Bed	25-30 mesh	25-30 mesh	25-30 mesh
Lower Bed	1/8 in pellets	14-18 mesh	---
Pressure, PSI	500	100	81
Injector Type	Showerhead	Showerhead	Burried Injector
Bed Loading (lb/in ² -sec)	0.05	0.02	0.01 (b)
Bed Diameter (in)	0.844	1.17	0.26
Initial Bed Temp (°R)	530	530	850
Catalyst Bed Length/Bed Diameter (L/D)	2.37	0.99	1.62

(a) Case used in Section 5.4.2.

(b) 90% through Burried Injector.

Figure 5-61

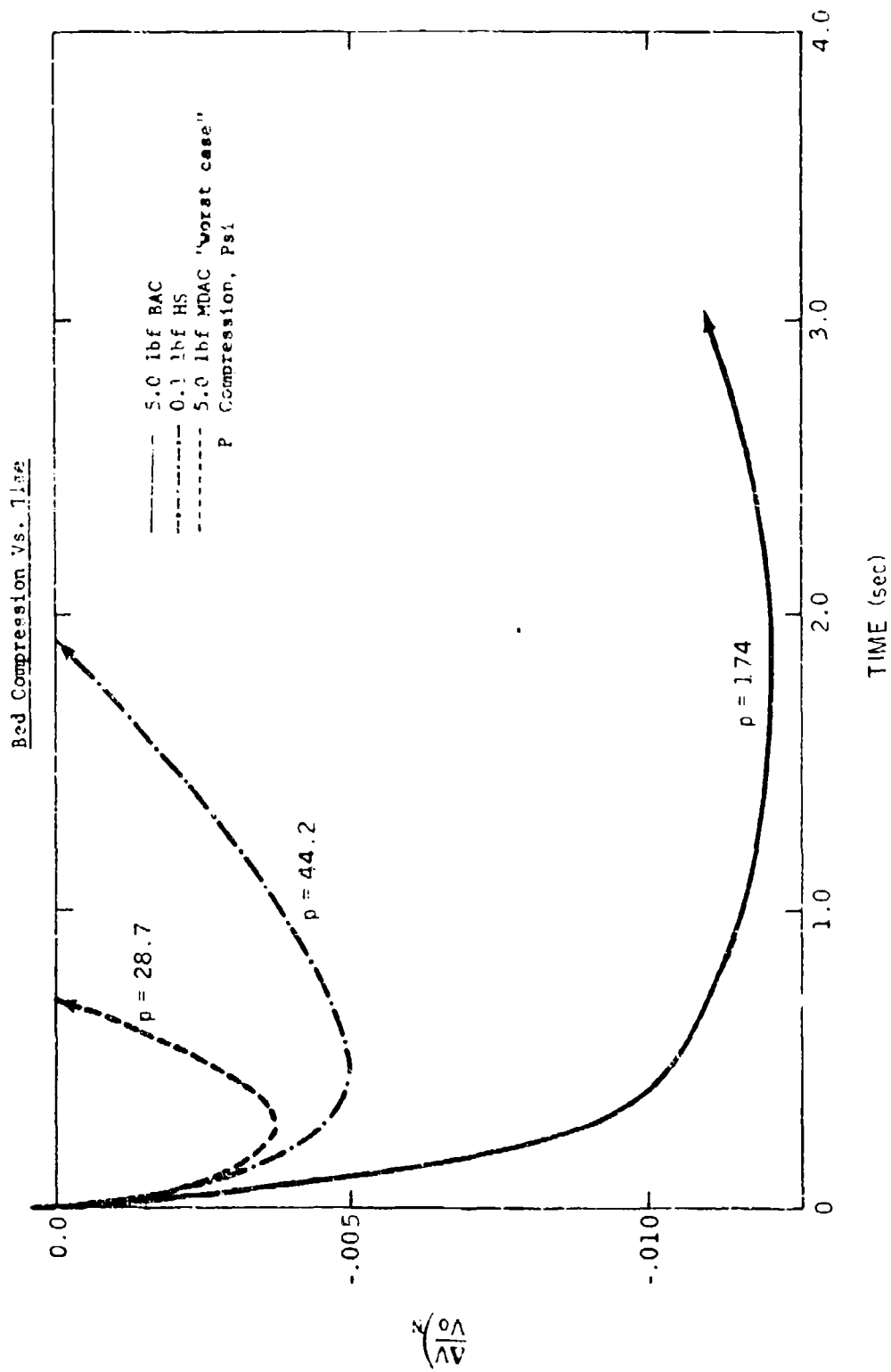


Figure 5-62

Temperature Vs. Time

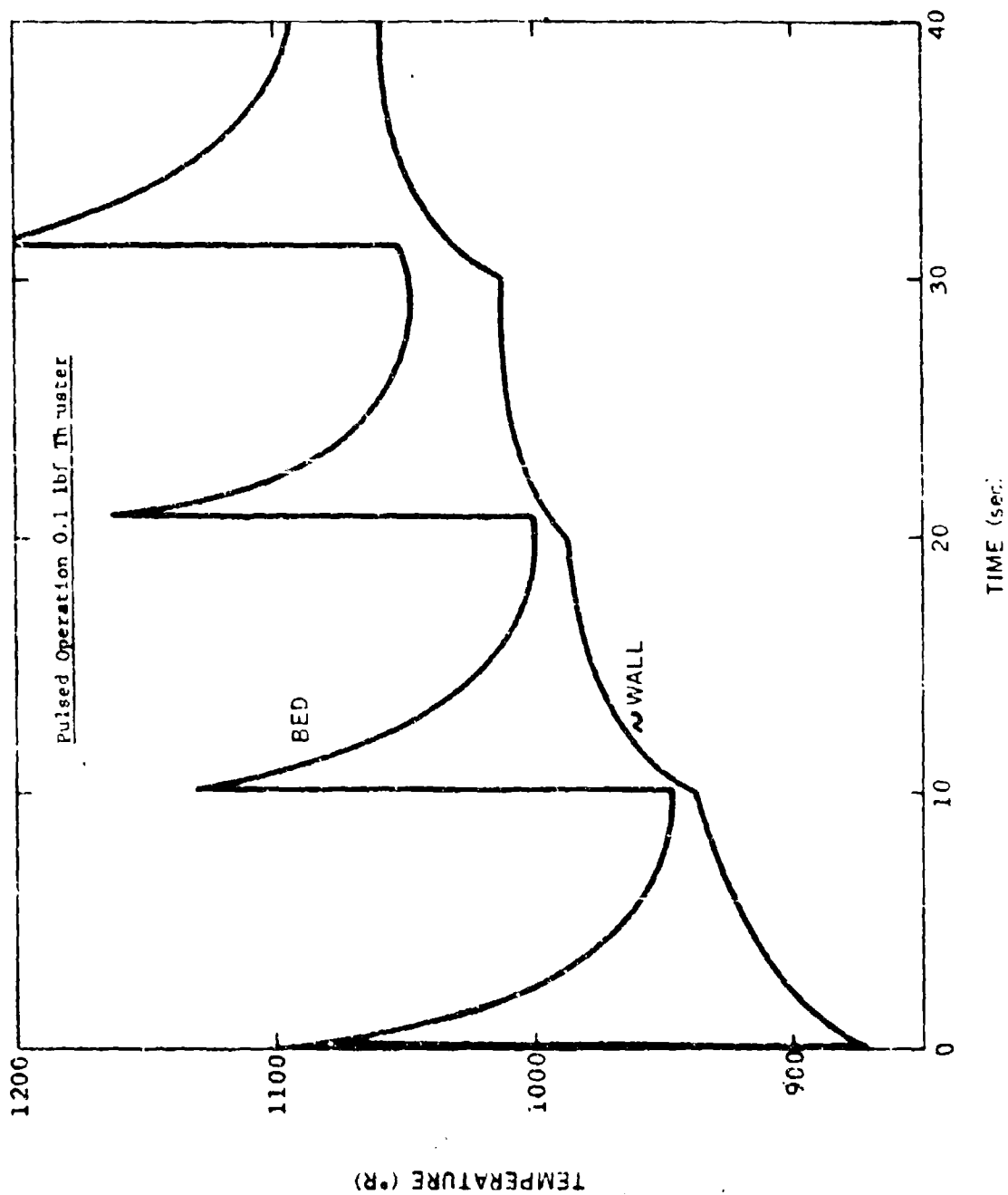


Figure 5-63
Bed Compression Vs. Time

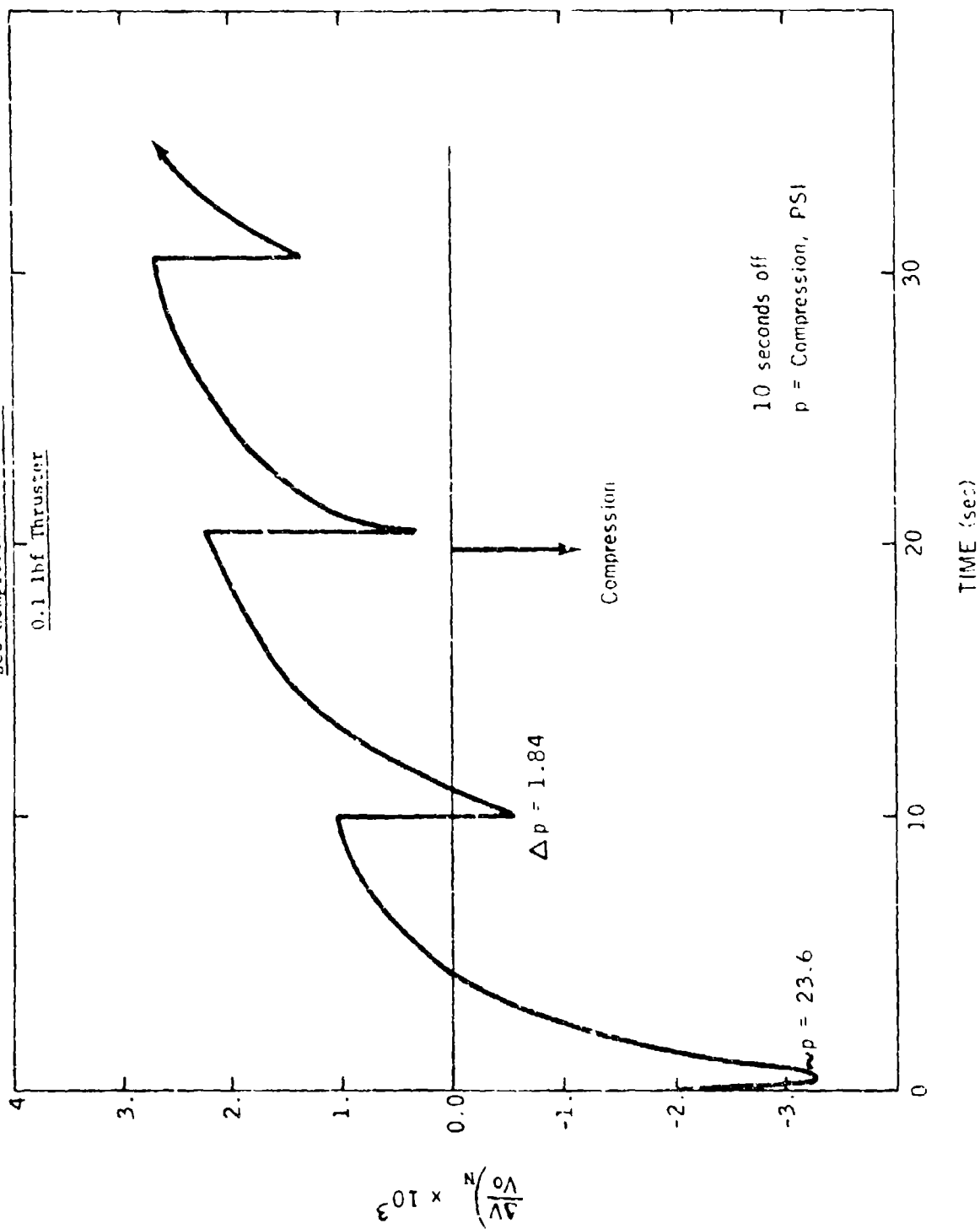
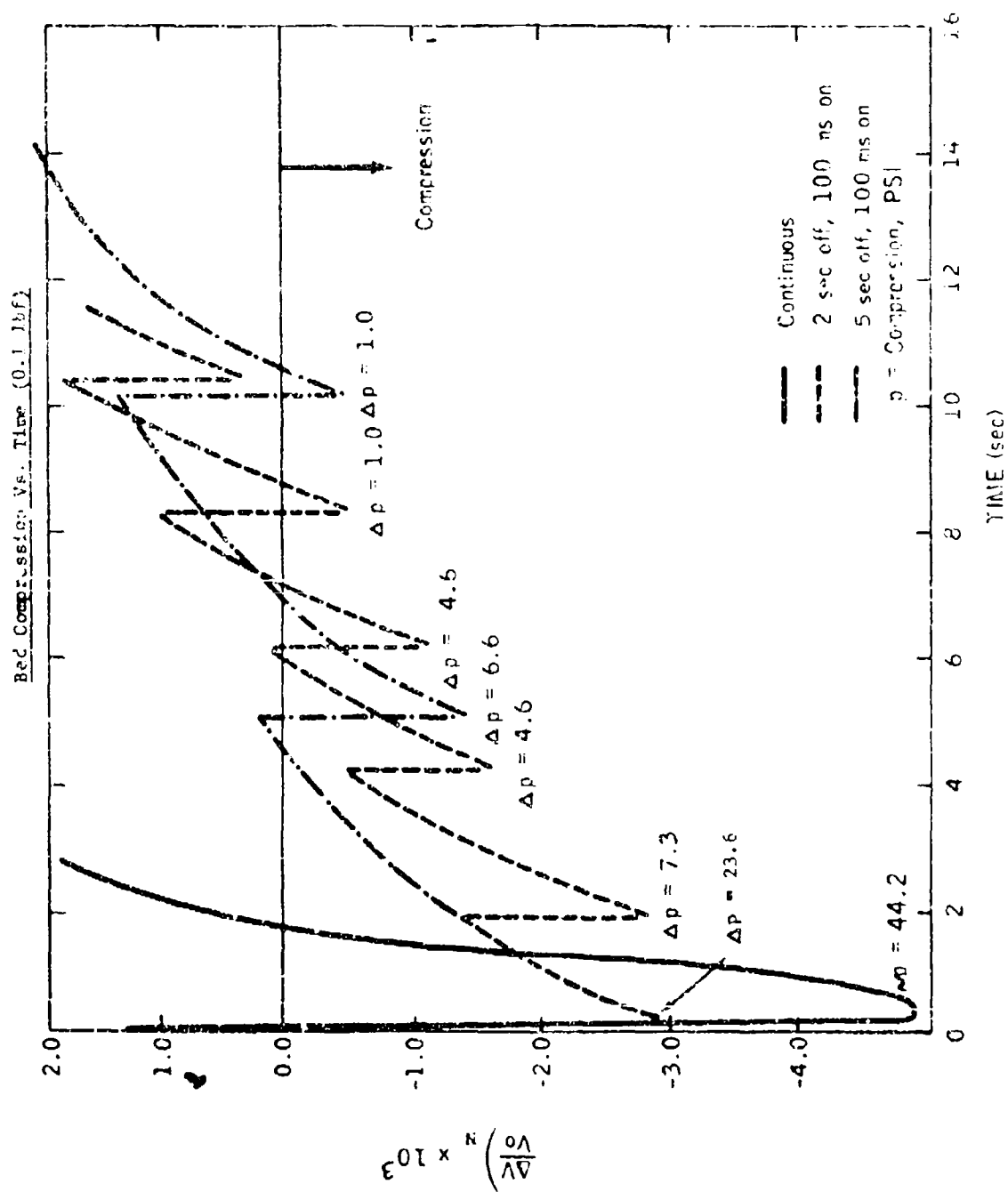


Figure 5-64



the 100 msec on, 2 seconds off duty cycle would crush approximately 2.55% of the bed, compared with 1.32% for the steady state. The 5 lbf engine behaves in a similar manner. As shown on Figure 5-65 three pulses (100 msec on, 10 seconds off) would be expected to crush a greater percentage of catalyst than the steady state. With an increased number of pulses, more catalyst would be lost. In actuality, the losses are not additive since they are percentages of the remainder. Furthermore, this repetitive crushing mechanism is only postulated as the initial crushing of the bed, may, in fact, relieve all crushing losses for any compression less than the original.

5.4.4.4 Conclusions

The thruster modeled here are representative of 0.1 lbf and 5.0 lbf thrusters. Thus, although the numerical results will differ somewhat from thruster to thruster, the range of results will be the same. No attempt was made to model a 300 lbf engine since their design is not amenable to the DTE computer code. Also, no work was done on cooling with repacking since this was handled in detail in the Interim (100) and Section 5.4.3 of this report.

Given an appropriate mass loss model, the DTE code is capable of predicting mass losses from a catalyst bed. The results indicate that the same degree of concern is discussed in the Interim Report is warranted. The DTE mechanism has the potential for crushing up to 2.6% of the catalyst bed on a continuous run and somewhat more in the pulsed mode. This mechanism most assuredly adds to the loss of catalyst in the 0.1 and 5.0 thrust range, especially over the first few pulses.

5.5 Fluid Erosion

The objective of this section is to determine the amount of wear caused by particulate contaminants carried in the propellant stream under various design and operating conditions. To do this a computer program was developed, capable of calculating the erosion wear of catalyst pellets under a variety of conditions. This computer program was then exercised with input parameters selected to represent specific design and/or operating conditions of interest, to determine the amount of damage to the bed with the various conditions.

5.5.1 Program Development

Nielsen and Gilchrist (Reference 129) have postulated that abrasion wear of a substrate by impinging particles occurs by a combination of two mechanisms: (1) cutting wear, in which the impinging particle digs into the surface, like a machine cutting tool; (2) deformation wear (work hardening due to repeated deformation, then cracking of the surface layers) which is due to impact alone. (The term "fatigue wear" will be used for deformation wear in this report.) Cutting wear is at a maximum at relatively low angles of attack (ca 30°) on the substrate, and falls to zero at angles near 90°; fatigue wear exhibits the opposite dependence on angle of attack, reaching a maximum of 90°. The wear in all cases is proportional to the kinetic energy of the impinging particles.

Nielsen and Gilchrist correlated published literature and their own experiments by the equation

$$W = \frac{MV^2 \cos^2 \alpha \sin \alpha}{2\alpha} - \frac{M(V \sin \alpha - K)^2}{2\epsilon} \quad (5.5-1)$$

Figure 5-65

Bed Compression Vs. Time (5.0 lbf BAC)

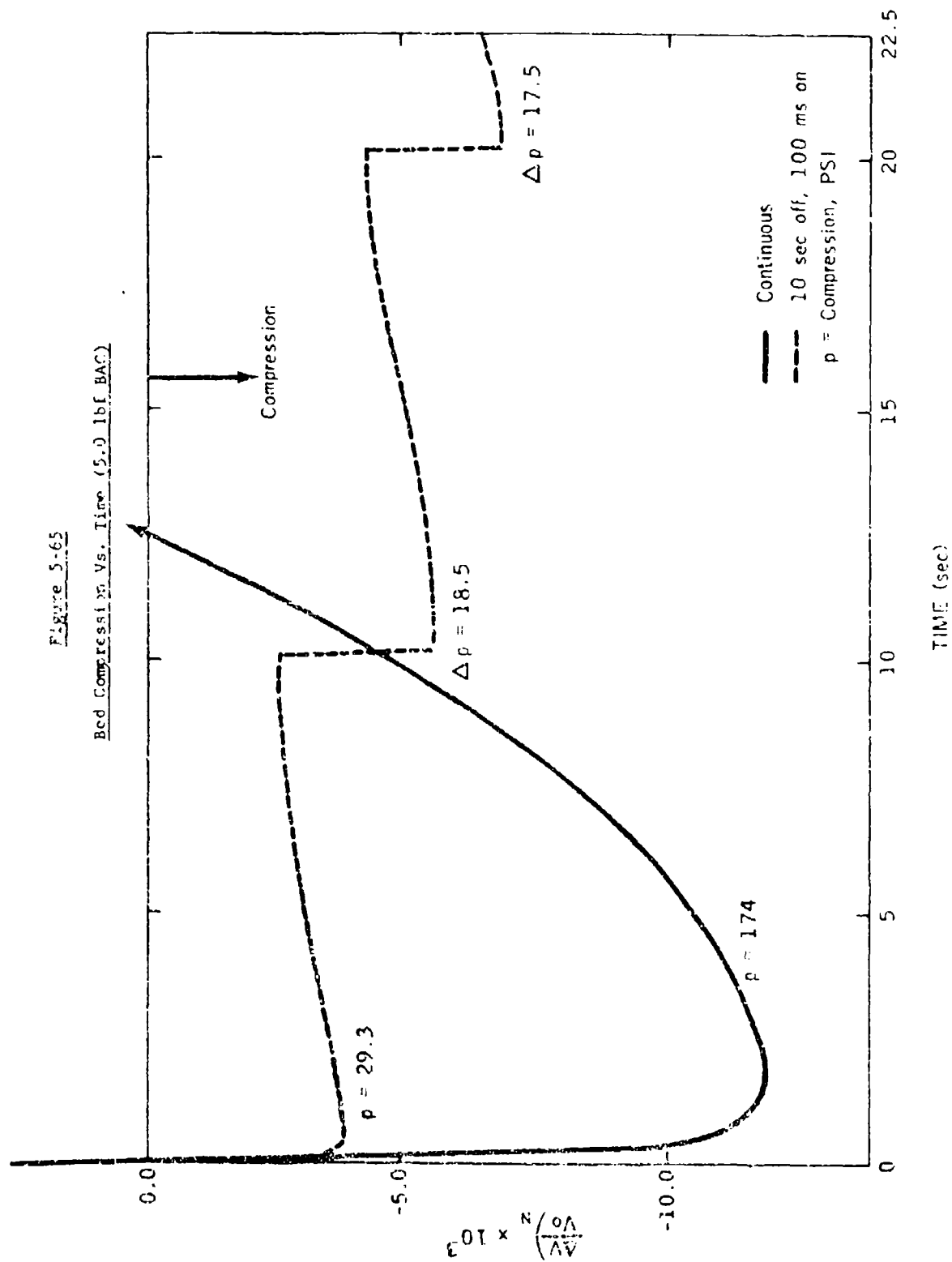
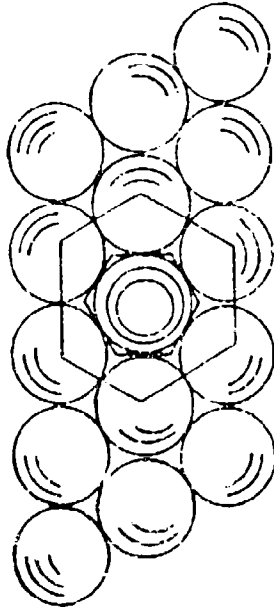


Figure 5-66

Pellet Configuration
Hexagonal Packing



in which W is the "erosion" [pounds (mass) of substrate removed] caused by impact of M pounds (mass) of particles at angle of attack α and average particle velocity V feet/second; K is a cut-off velocity, below which no fatigue wear occurs; n is a material-dependent constant; o and e , the wear rate constants, are the amount of kinetic energy which must be "absorbed" by the surface to release one unit mass of eroded material. The first term of the Nielsen-Gilchrist equation calculates cutting wear; the second term calculated fatigue.

5.5.1.1 Catalyst Bed Configuration Assumptions

The arrangement of catalyst pellets in a well-packed bed consists of a series of layers of pellets, each layer made up on an approximate hexagonal arrangement, with triangular interstice passages between the pellets. The passages are perpendicular to the plane of the layer. Figure 5.66 is a sketch of this structure, using spherical pellets for the example, and viewing the spheres cut through on their equators.

Pellets of one layer fit in the "cavities" formed between pellets in adjacent layers, as shown in Figure 5-67. In this position, the upper surface of each pellet in layer 2 is directly below and perpendicular to the passage between the pellets in layer 1. The optimum configuration of the layers places a second layer pellet behind 50% of the passages through layer 1; the remainder of the passages through layer 2 lie directly above similar passages through layer 1. The arrangement of "blocked" and "open" passages is symmetrical, as sketched in Figure 5-68.

5.5.1.2 Effect of Temperature on the Fatigue Wear Coefficient

The Nielsen-Gilchrist equation does not include consideration of the effects of temperature on the abrasion process, and little of the published work on change of abrasion with change of substrate temperature is applicable for the purposes of this program. It has become accepted that surface wear rates of most materials for many types of wear are inversely proportion to the surface hardness (References 130 and 131). If this relationship is accepted, then the change of wear rate with temperature will be related to the change of surface hardness with temperature.

5.5.1.3 Threshold Velocity for Fatigue Wear

The factor K in the Nielsen-Gilchrist equation is based on the assumption that fatigue wear ceases abruptly if the velocity of impingement falls below some lower limit equal to K (which is material dependent). Examination of published data demonstrated that there is no true cutoff, but rather a rapid decrease in damage below a threshold velocity. If the fatigue wear constant, e , (units are ft lbs/lb) is calculated as a function of velocity, it is found that e increases abruptly below a certain velocity, but does not become infinite (Figure 5-65). The slopes of the portion of the plots below the velocity limit were found to be parallel for glass, plastics (TFE and Acrylic), and the metals aluminum, copper and steel.

The velocity threshold at which the curve breaks ranges from 180 to 1000 ft/sec, and of course the plateau value for e depends on the substrate material.

Figure 5-67
Multi-Layer
Pellet Configuration

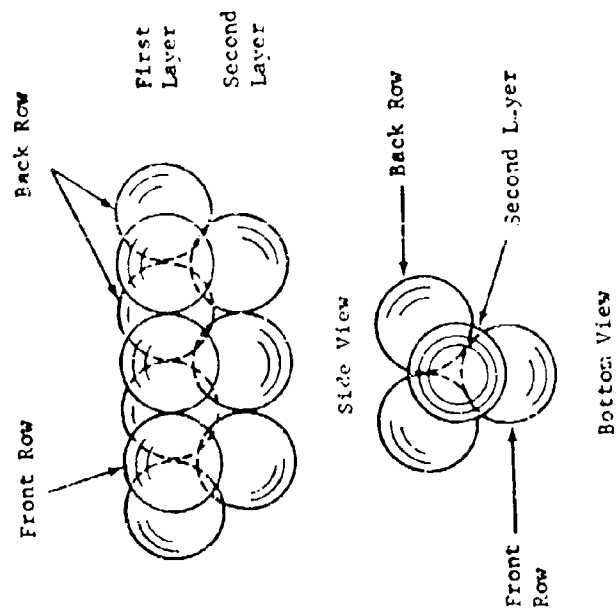
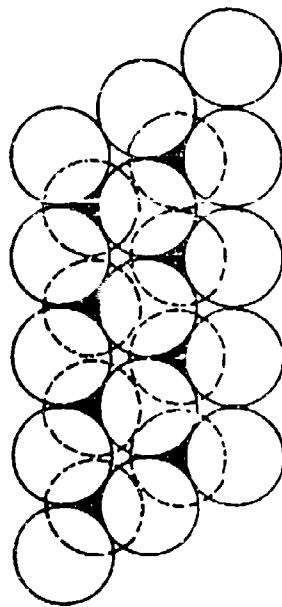


Figure 5-68

Impingement Focusing

▲ Blocked Passage △ Open Passage
Top View



Dashed Circles are Pellets in Second Layer.

5.5.2 Method of Calculation

The algorithm for calculation of particle impingement erosion was developed using the following assumptions.

Erosion (or abrasion wear) is presumed to be caused solely by condensed phase (liquid or solid) materials carried by a flow of gas or vapor. No wear is calculated for solid particles suspended in liquid hydrazine. Under the conditions which apply in a rocket engine catalyst pack, the cutting wear term of the Nielsen-Gilchrist equation is relatively unimportant, and is assumed equal to zero. Liquid droplets are presumed to arise from incomplete vaporization of the hydrazine. The Kesten steady state program supplies values for the amount of liquid at specified locations in the catalyst bed. The data from the Kesten program are interpolated for the required locations.

Solid particles are presumed to arise from three sources; contaminants in the hydrazine, particles generated in the bed by compression, rubbing, thermo-mechanical shock and pore pressure imbalance, which may be supplied as auxiliary input from the other processes considered in this study, and particles generated by particle impingement erosion at other locations upstream in the bed.

Droplets and particles are presumed to travel at the same velocity as the gas/vapor in which they are carried, i.e., newly generated particles are presumed to accelerate instantaneously to the stream velocity.

The fatigue wear term in the Nielsen-Gilchrist equation is used as the model for calculating wear, with the following modifications; the constant K is eliminated and the fatigue wear coefficient, ϵ , is treated as a function of velocity for impingement velocities less than K:

$$\epsilon_V = \epsilon_0 * \left(\frac{\text{Velocity}}{\text{Limit Velocity}} \right)^{-3.5625} \quad (5.5-2)$$

The value of ϵ is also regarded as a function of the substrate (pellet) temperature

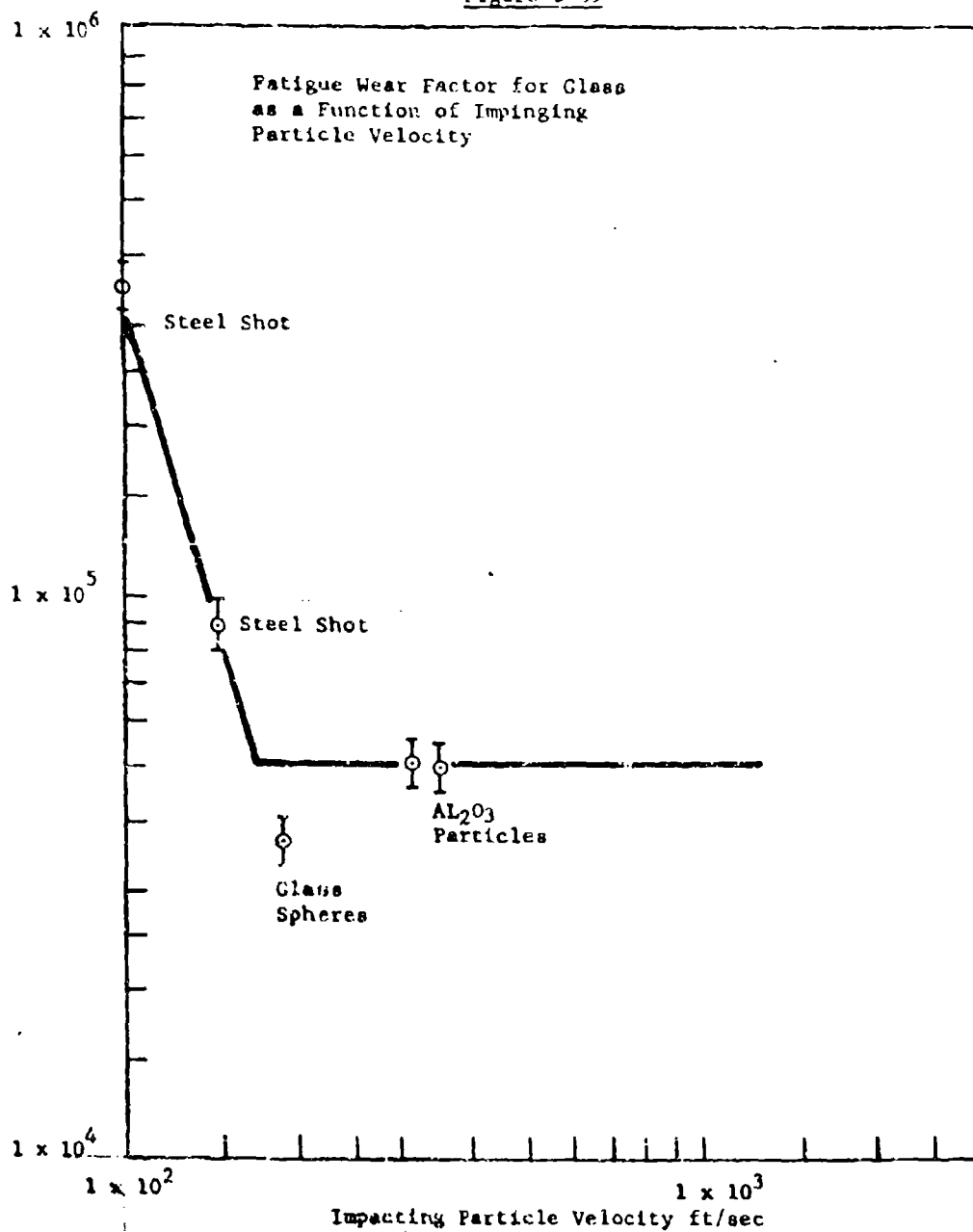
$$\epsilon_{T,V} = - 2.82 \times 10^{-4} (T-T_0) \epsilon_V \quad (5.5-3)$$

The variation in pellet temperatures with axial locations and operating times is used for the calculation of ϵ , and are taken from the output from the Kesten-U.T.R.L. transient computer program. The data are interpolated to obtain the time and location required.

The temperatures of the vapor and of the impinging particles are not presumed to affect the wear rate as calculated by this model. Impingement velocities are calculated as follows.

The unimpeded mass flow rate of the liquid hydrazine upstream of the catalyst bed is input to the program. The total cross section area of all the passages through a layer of pellets at the narrowest point (maximum cross section of the pellets) is calculated, assuming a circular cross section for the pellets and hexagonal packing. Because of conservation of mass, the same total mass of fluid must flow through the restricted area as through the unimpeded area ahead of the bed. Therefore, the velocity must be increased by a factor equal to the cross section without pellets divided by the minimum area through the pellet layer. The unimpeded velocity is calculated from the mass flow rate, then the

Figure 5-69



velocity through the layer is calculated by multiplying by the area ratio. The liquid impingement velocity at any layer is taken as the maximum velocity through the preceding layer. The volume of a unit mass of liquid hydrazine is expanded to the volume of gas/vapor at the local pressure, temperature and composition, assuming ideal gas law behavior and the exit composition of reaction products, and correcting for vapor quality. The gas velocity is then calculated by multiplying the liquid velocity by the relative volume increase.

A simple model of the catalyst bed is assumed. This is illustrated in Figure 5-70. The pellets are assumed to be spherical, with a radius which will result in the same volume per pellet as the average for the actual pellets. If the bed being modeled consists of only a single type of pellet, it is necessary to input the data on pellet characteristics twice, and to assume a fictitious division between the two sections. Eleven stations along the bed are selected for calculation of damage. Two of these are invariant; the first station is always the second layer of pellets in the forward section, and the fifth station is always the front layer of the aft section. The remaining stations are automatically selected to select four equally spaced locations in the forward bed and seven equally spaced locations in the aft bed.

The operating time is divided into 17 increments. The first four increments are equally spaced in the start-up transient, the last four increments are equally spaced in the tail-off transient, and the remaining nine increments are equally spaced in the steady state operating period. The tail-off is considered to be complete when the chamber pressure drops to atmospheric; it does not include the extended cooldown period when there is no flow. Any of these periods can be assigned a zero duration in the data input, in which case the time increments are assigned to another period.

Calculation Sequence

1. Read in data defining bed configuration, pellet specification, propellant specifications, operation parameters, and bed conditions during operation.
2. Establish calculation locations and time increments.
3. Calculate specific details of bed structure including layer spacing, interstice volume, passage area, number of pellet layers per section, etc.
4. Calculate the velocity of liquid hydrazine flow.
5. Calculate the time for a volume of hydrazine equal to pore volume of the bed to flow through the bed (wave duration).
6. For time increments 1 to 17 carry out the following calculations (7-22).
7. For calculation locations 1 to 11 carry out the following calculations (8-17).
8. Interpolate the time-location-temperature table to determine the substrate temperature.
9. Interpolate the propellant quality-location table to determine the propellant quality.
10. Interpolate the intra-bed particle generation-time-location table to find the generated particle concentration.
11. Calculate the mass of impinging particles and droplets.

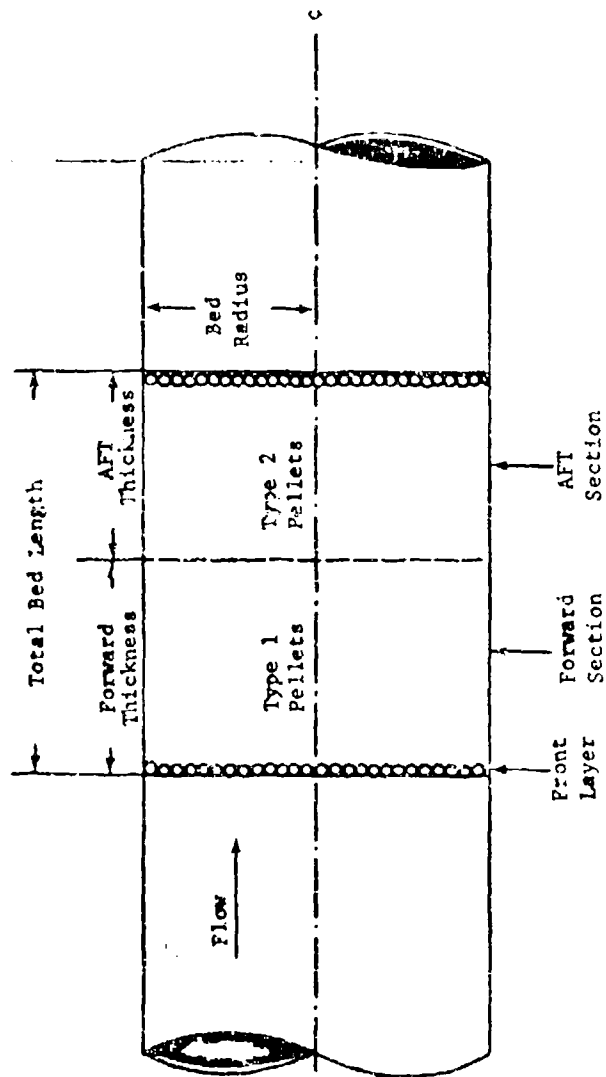


Figure 5-70. Catalyst Bed Model.

12. Calculate the impingement velocity.
13. Calculate the wear rate factor corrected for velocity and substrate temperature.
14. Calculate the wear during a time equal to the wave duration.
15. Calculate the wear rate.
16. Calculate the damage (amount of material removed).
17. Add the material removed to the mass of impinging particles and integrate the wear forward to the next station, layer by layer.
18. Average the wear rate between the last time increment and the current time increment, and calculate the damage over the time increment.
19. Calculate the average pellet dimensions in each bed section at the end of the time increment.
20. Recalculate the bed parameters: length, pellets per layer, layers per section.
21. Print notice of extreme wear (5% change).
22. Use new bed and pellet parameters as basic condition for calculations at the next time increment.
23. Calculate the total change.
24. List results; final condition of bed, total mass and volume change, wear at selected locations at each time increment.
25. Plot results.
26. Test for new case. Reset variables and read in new data if another case is to be run.

Input Data Values Used to Run the Computer Program

The program has been run using a single nominal engine and pulse, varying only the solid contaminant concentrations in the hydrazine supply. The basic data are the following.

1. Bed/pellet description:
 - Bed radius 0.10656 meter (4.195 inch)
 - Bed length 0.05596 meter (2.203 inch)
 - Forward Section length 0.00508 meter (.20 inch)
 - Aft Section length 0.0508 meter (2.0 inch)
 - Pellet Radius, Forward Section 0.00305 meter (.012 inch)
 - Pellet Radius, Aft Section 0.001951 meter (.079 inch)

2. Propellant properties:
Flow Rate 35.13 kg/sec-m² (.05 Pounds/Square inch-second)
Density 1008.3 kg/m³ (1.0083 gm/cc)
Chamber Pressure 3.446 x 10⁷ N/m² (4989 psi)
3. Times
Start-up 0.0115 sec
Steady State 5.0 sec
Tailoff 0.022 sec

The times were selected from the output of the Kesten Transient program which was executed with the same bed, pellet and propellant data to supply the time-location-pellet temperature table required as input by ABRADE. Propellant quality vs location was obtained from a run of the Kesten One-Dimensional Steady-State program.

Values for the important wear rate coefficients ϵ (energy/unit mass removed), VLL (velocity lower limit, the velocity below which ϵ is no longer constant), EXP (the slope of the $d\epsilon/dV$ curve), and TFACT, (the change in ϵ with temperature) for the catalyst pellets could not be found in the literature, and the values used for the calculations were estimated from analogous materials and related properties.

$$\begin{aligned}\epsilon &= 0.477904 \text{ JOULE/KG} \\ \text{EXP} &= - 3.5625 \\ \text{VLL} &= 25.5 \text{ M/SEC} \\ \text{TFACT} &= - 2.82 \times 10^{-4} \text{ JOULE/KG-DEG}\end{aligned}$$

When the program was operated with these data as input, and with clean hydrazine (no particles), a value of zero was calculated for total damage. Using the same basic data, but including particle contaminants in the hydrazine resulted in mass loss calculated for the pellets. For a particle mass fraction concentration of 1×10^{-4} the calculated damage during the 5-second pulse was 5×10^{-3} percent.

5.5.3 Results

The ABRADE program to calculate abrasion wear by particles carried in the gas phase has been coded and executed. Calculations by the program are in accord with experience in that there is negligible erosion damage from operation of the bed even with a cold start. Particulate material carried in the gas stream is needed for appreciable wear. The numerical values obtained appear to be reasonable. The results calculated are compromised by the necessity to estimate the most important of the physical properties. It would be desirable to determine actual values for ϵ for pellets at several flow rates and substrate temperatures, to provide real values for the coefficients used in ABRADE.

5.5.3.1 Parametric Variation Study

An evaluation was conducted to determine the effects of several parameters on the wear of catalyst pellets, by calculation of the wear at several levels of the parameters. The parameters studied in this fashion include:

1. Solid contaminant concentration in propellant.
2. Propellant quality (vapor/liquid) distribution.
3. Propellant flow rate.
4. Chamber pressure.
5. Bed L/d ratio at constant volume.

The various parameters affected the wear to different degrees. The results for each analysis are discussed below. In all cases, the parameters under study were held constant. The values described above for the standard test case were used.

Contaminant Concentration

A set of eight runs were conducted in which the concentration of solid particulate contaminant in the incoming liquid propellant was varied over the range 0 to 0.1 kg/m^3 (mass fraction range 0 to 1×10^{-4}). Two additional runs were conducted at the highest concentration with 5 pulses and 10 pulses. The wear was found to vary linearly with particle concentration, and it became significant (1×10^{-4} percent in a single 5 second pulse) at about 0.5 PPM. The results are plotted in Figure 5-71. The wear for multiple pulses at the higher concentrations of particles was not linear with the number of pulses, due to progressive degradation of the bed. There was a multiplication factor of 1.06/pulse for 5 pulses and 1.08/pulse for 10 pulses.

Liquid Droplet Concentration

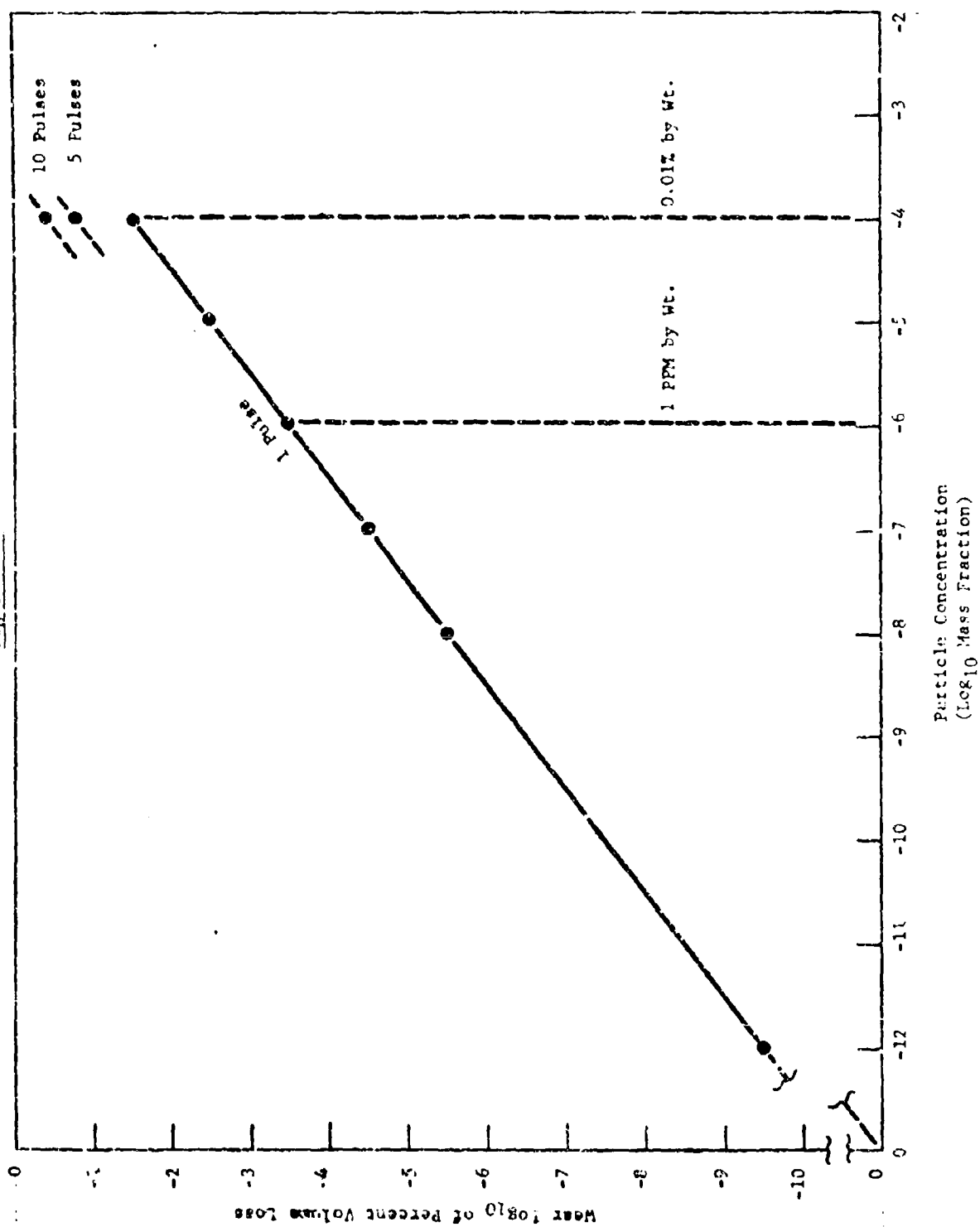
A set of four runs were conducted in which the fraction of injected hydrazine moving as droplets at various locations was varied. The liquid droplet particle concentrations were:

1. 50 percent liquid at 1.1747×10^{-4} meters (.00462 inch), 0 percent liquid at 1.1790×10^{-4} meters (.00464 inches).
2. 50 percent liquid at 4.5×10^{-4} meters (.00984 inch), 0 percent liquid at 4.3×10^{-4} meters (.01693 inch).
3. 50 percent liquid at 6.2×10^{-4} meters (.02441 inch), 0 percent liquid at 1.2×10^{-3} meters (.04724 inch).

Only in the last case did the calculations indicate any wear, and in that case the wear was 0.23 percent in one 5 sec pulse, which is quite significant.

An implicit assumption in this calculation is that any liquid present is carried as droplets in the gas/vapor, and condensed state flow along surfaces is not considered.

Figure 5-71



Propellant Flow Rate

A set of 3 runs was conducted to study the effect of propellant flow rate on wear of catalyst pellets. The conditions selected included a particulate concentration of 0.1 percent by weight, and flow rates 14 percent below and above the nominal rate of 34 Kg/sec M² (.05 pounds/sec in²). Since a constant chamber pressure was assumed, the increased propellant flow rate is interpreted as an increased gas velocity.

The results are plotted in Figure 5-72. The flow rate has a significant effect of wear rate. When the rate increases by 33 percent (from 33 to 40 Kg/sec-m², .0426 to .0568 pounds/sec-in²), the wear rate is increased by 2 orders of magnitude.

This effect is not only important in its own right, but also must be considered in the basic wear process by contaminant particles. The program currently accelerates newly generated particles to full gas stream velocity instantaneously. This cannot be strictly correct--the actual velocity of a particle is determined by the diameter of the particle, the velocity of the gas, the relative density of the particle and the gas, and the length of time to which the particle is exposed to the acceleration drag of the gas. In the typical conditions in the catalyst bed, a particle 1 μ in diameter will reach gas velocity (10 m/sec) in about the diameter of a catalyst pellet, but a 10 μ particle will only be moving at about 1 m/sec after traveling the same distance.

In the calculations for particle wear with the propellant contaminated with 1×10^{-4} mass fraction of particles, during the period of maximum wear rate the concentration of abraded material was 2 to 3 orders of magnitude greater than the contaminant concentration. Without experimental data on wear-generated particle sizes, it is impossible to determine the exact effect of the neglected acceleration, but the wear rate could be reduced appreciably.

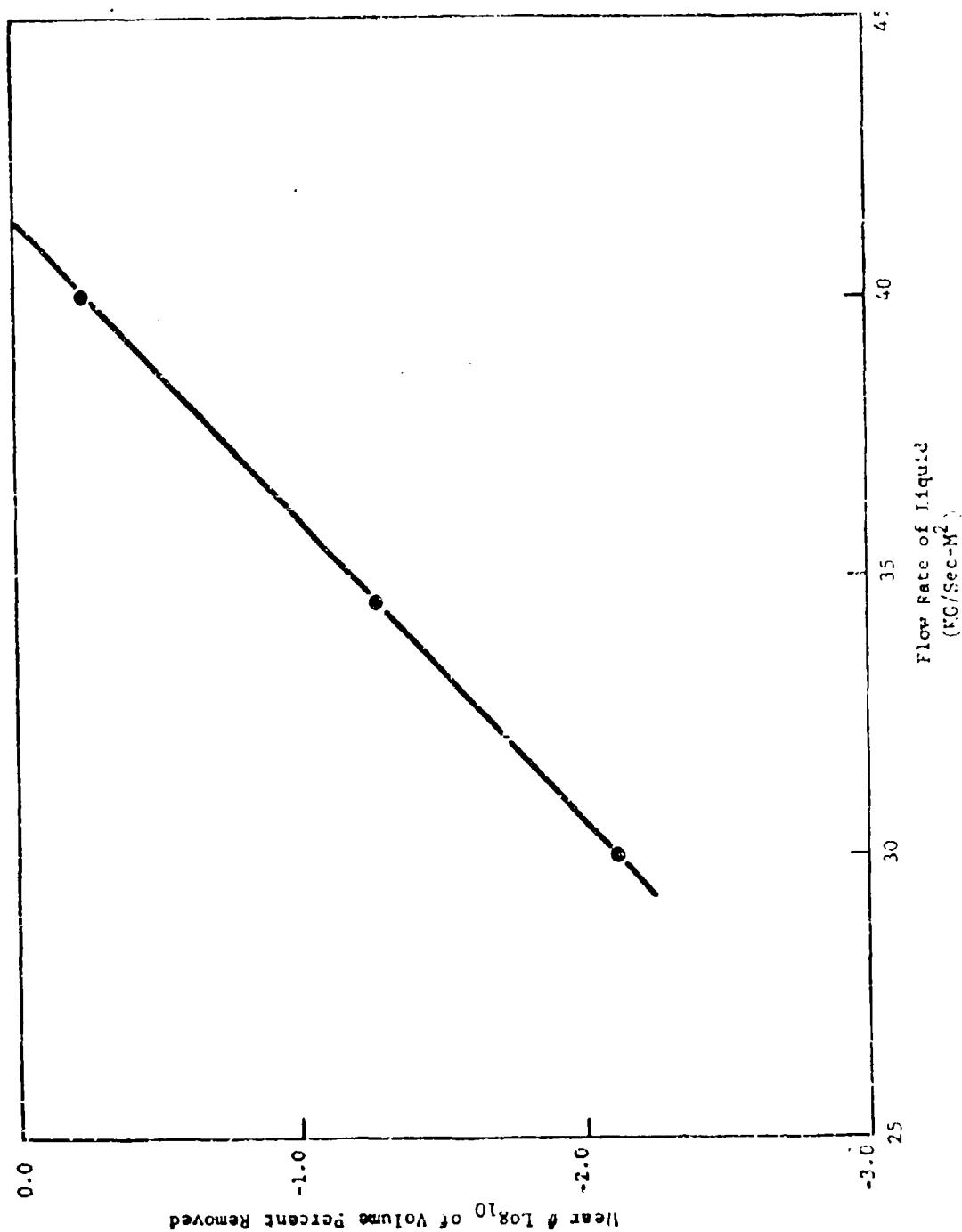
Chamber Pressure

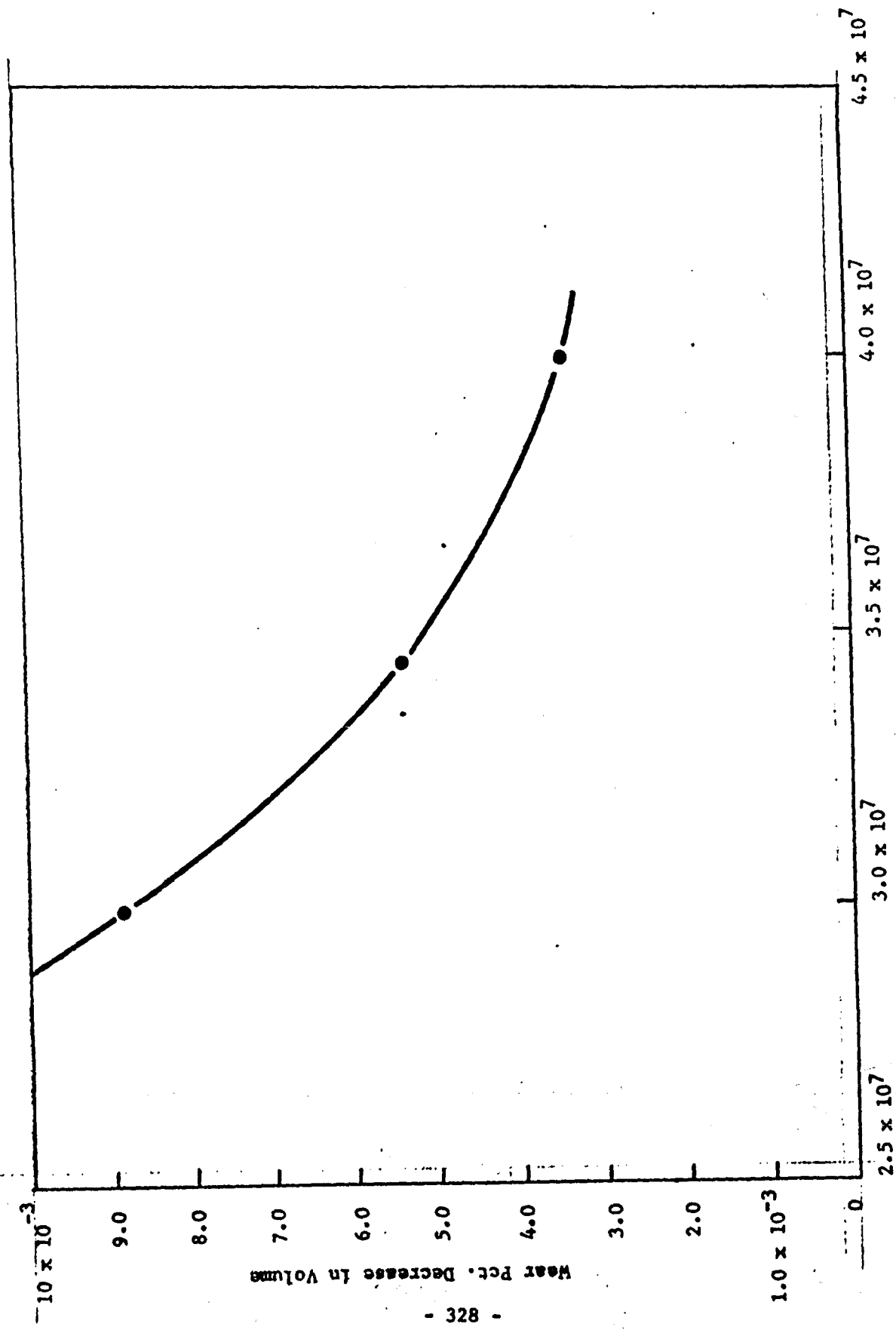
Three runs were conducted with all parameters except the chamber pressure held constant, and at 3 levels of chamber pressure, 3.0, 3.45 and 4.0×10^7 N/m² (4343., 4989. and 4791. psi). It was found that wear rate is inversely proportional to the square of the pressure, on a parabolic curve. The effect is significant, but not greatly so; an increase of 33 percent in the pressure from 3 to 4×10^7 N/m² caused the wear rate to decrease by about 50 percent. The results are shown in Figure 5-73. These results must also be interpreted as velocity effects, as the program assumes gas velocity to be inversely proportional to gas density.

Bed L/D at Constant Volume

Two runs were made in which the bed radius and length were varied in opposite directions while holding the volume constant. There was an insignificant decrease in wear as the L/D increased. Thus, the L/D ratio is not a significant factor affecting wear.

Figure 5-72





Chamber Pressure
(N/M²)

Figure 5-73. Erosion Versus Pressure

Bed Length		Bed Radius		L/D	Percent Volume Removed
(meter)	(inch)	(meter)	(inch)		
4.477×10^{-2}	(1.76)	0.12	(4.72)	0.187	6.7×10^{-3}
10.02×10^{-2}	(3.94)	0.08	(3.15)	0.0626	5.6×10^{-3}

5.5.3.2 Additional Calculations and Discussion

The fluid erosion program variation study reported in Section 5.5.3 served to indicate the trends in fluid erosion catalyst damage associated with particulate contaminant concentration in the fuel, the transport of hydrazine through the bed in the form of liquid droplets (a hypothetical process), propellant flow rate, chamber pressure, and bed length/diameter ratio.

Since the abrasion properties of Shell 405, the fuel contaminant particulates, Shell 405 particulates, and liquid hydrazine droplets were not known, the abrasive properties used in the computer calculations were those reported for steel shot, glass spheres, and corundum particles.

The chamber pressure used in the original variation study was 5000 psi, which is considerably higher than the chamber pressure used in most hydrazine propulsion systems, hence the variation study was repeated, using a chamber pressure of 500 psi.

The computer program calculates gas velocity from the continuity equation and ideal gas law:

$$V = \frac{M RT}{PM_w A_o}$$

and assumes the abrasive particles velocity-equilibrate with the gas, hence the particle impact velocities are calculated to increase as chamber pressure is decreased. As a result of the higher particle impact velocities calculated at a 500 psi chamber pressure, the erosion losses were calculated to be much higher than those earlier calculated for a 5000 psi chamber pressure. The calculated bed loss values were unrealistically high when compared with real engine firing experience, hence we must conclude that the fluid erosion program will not be capable of giving accurate absolute value figures for bed erosion until after the abrasion properties of Shell 405 and the particulates which are expected to impinge upon it have been experimentally determined.

5.6 Pressure Shock

5.6.1 Catalyst Bed Flow Numerical Model

The compressive force on a catalyst bed associated with a hard start comes from the flow impedance as the gas, explosively produced at the upstream end, attempts to pass through the bed to escape through the nozzle, Figure 5-74. Because of the obvious complexities associated with the non-linear flow relationship in the catalyst bed the sequence of pressure profiles through the bed must be obtained by numerical means. It would be desirable to be able to predict the upstream pressure-time history of an explosive hard start from first principles, however, since this is beyond the present state-of-the-art, our computer model starts with an experimental or hypothesized upstream chamber pressure history, as an imposed upstream boundary condition. The measured (or hypothesized) pressure history is approximated in our computer model by ten straight-line pressure-time segments, each covering one tenth of the total computer time interval. The flow through each axial element of the bed is first calculated based on the assumption of D'arcy Flow (i.e. completely viscous flow). Local Reynolds Number is then calculated, based on mean particle diameter. If the Reynolds Number is higher than 10 a drag coefficient is calculated, a new flow rate, new Reynolds Number, and finally a new drag coefficient. This iteration is continued until the flow rate converges to the correct value. The drag coefficient correlation comes from the work at Fancher, Lewis, and Barnes (Reference 132) and is illustrated in Figure 5-75. The 20-30 mesh Ottawa sand used to produce the curve labeled "unconsolidated sand" should be very close to 20-30 mesh Shell 405 in grain geometry, and have similar flow characteristics. The conductive and convective heat transport through the bed is calculated simultaneously with the mass flow, using standard explicit numerical techniques quite analogous to those used for the mass flow. The conditions at the downstream boundary of the bed are determined by evaluating the time-varying state in a downstream plenum which has gas and enthalpy flowing into it from the bed, gas efflux through a sonic throat and which can accumulate mass and enthalpy in accordance with the calculated influx and efflux rates to give its time-varying pressure and temperature.

The output from the program consists of a large number of pressure and temperature profiles corresponding to various times after the start of the calculations. The same information is machine plotted on a Stromberg-Carlson SC-4060 microfilm plotter.

5.6.2 Sample Calculation

The particular hypothetical motor for which the calculations were performed has a cylindrical catalyst bed 1 inch long and with 1 square inch of cross-sectional area. The catalyst load is all 25-30 mesh Shell 405. The downstream plenum has a volume of 0.2 cubic inches and the throat area is

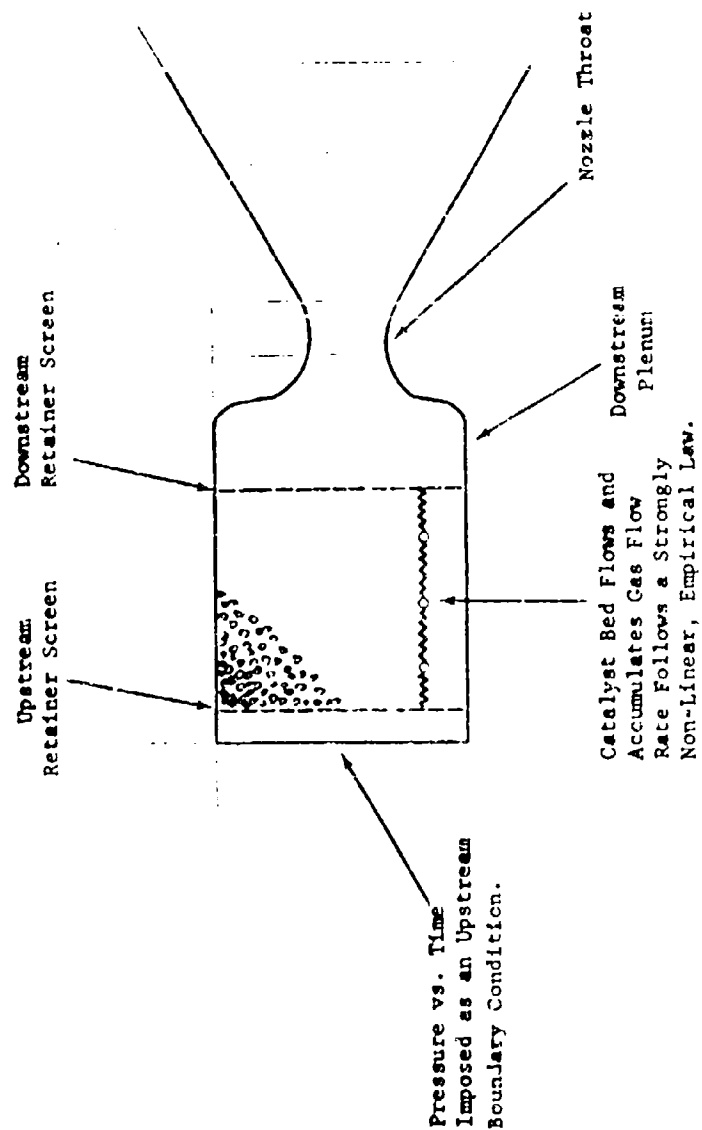


Figure 5-74. Conceptual Model of Hydrazine Rocket.

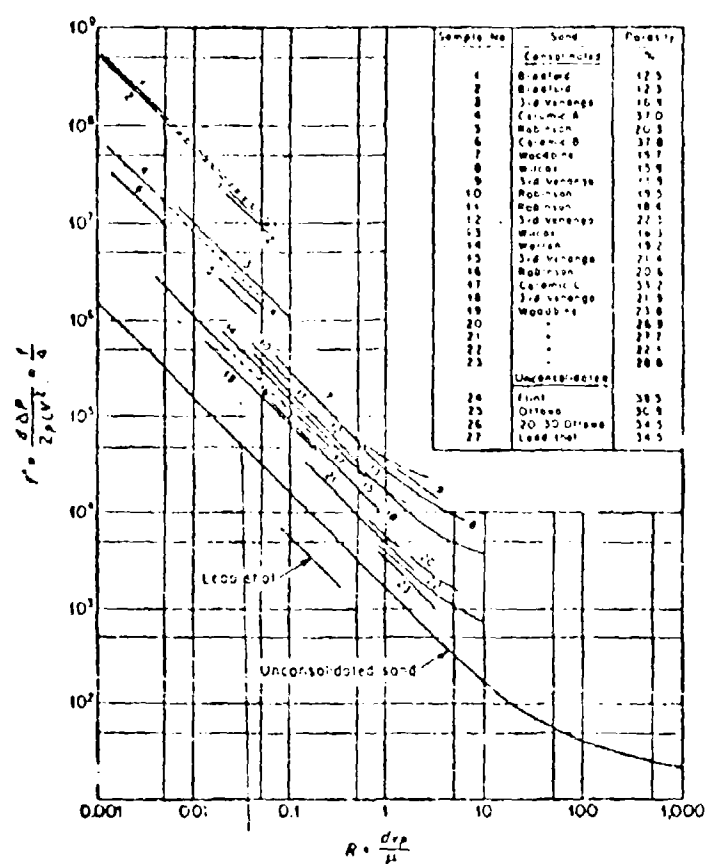
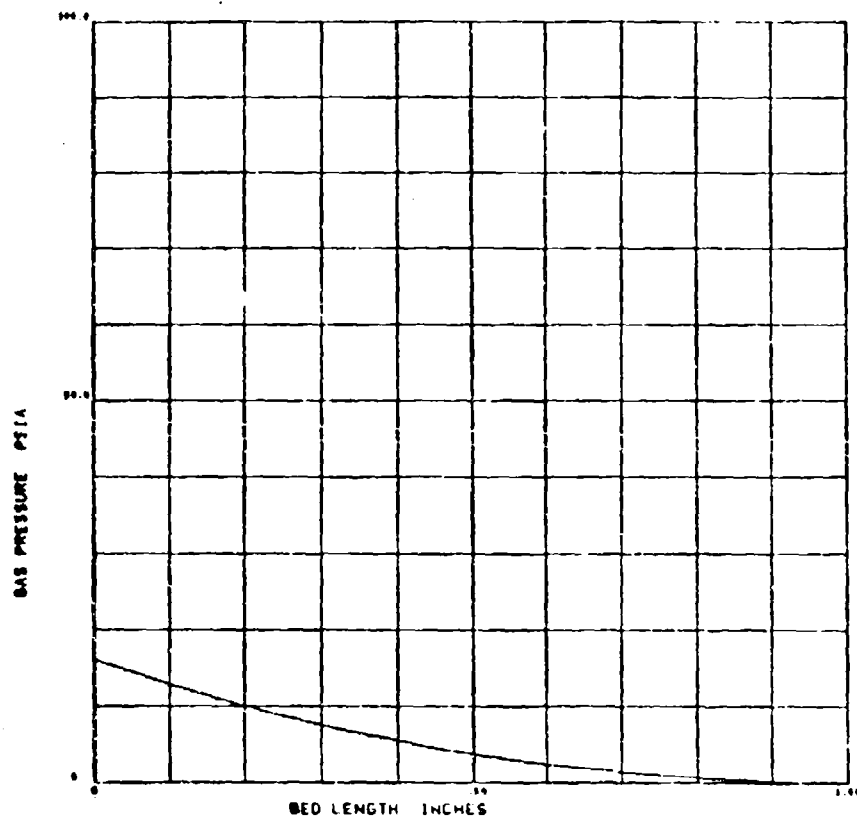
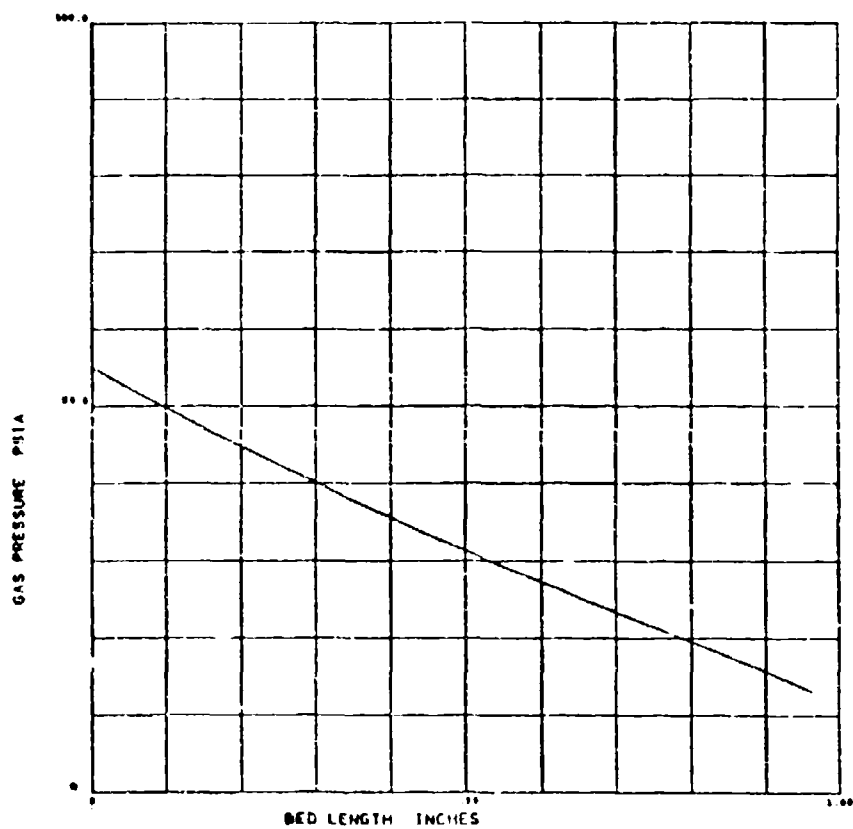


Figure 5-75. Correlation of friction factor with Reynolds number for flow of homogeneous fluids through porous media, where d is defined as the diameter of the average grain and l is the apparent velocity, i.e. volume rate of flow/total cross-sectional area (After Fancher, Lewis, and Barnes).



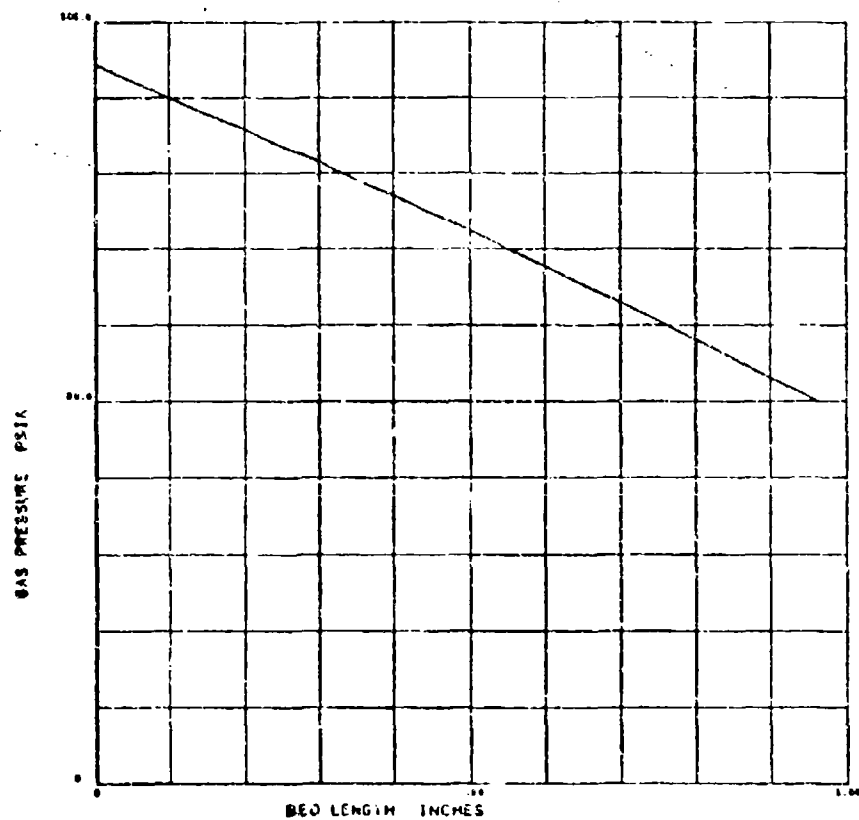
Pressure Profile 0.35 Millisecond After Start.

Figure 5-76



Pressure Profile 1.0 Millisecond After Start

Figure 5-77



Pressure Profile 2.0 Millisecond After Start

Figure 5-78

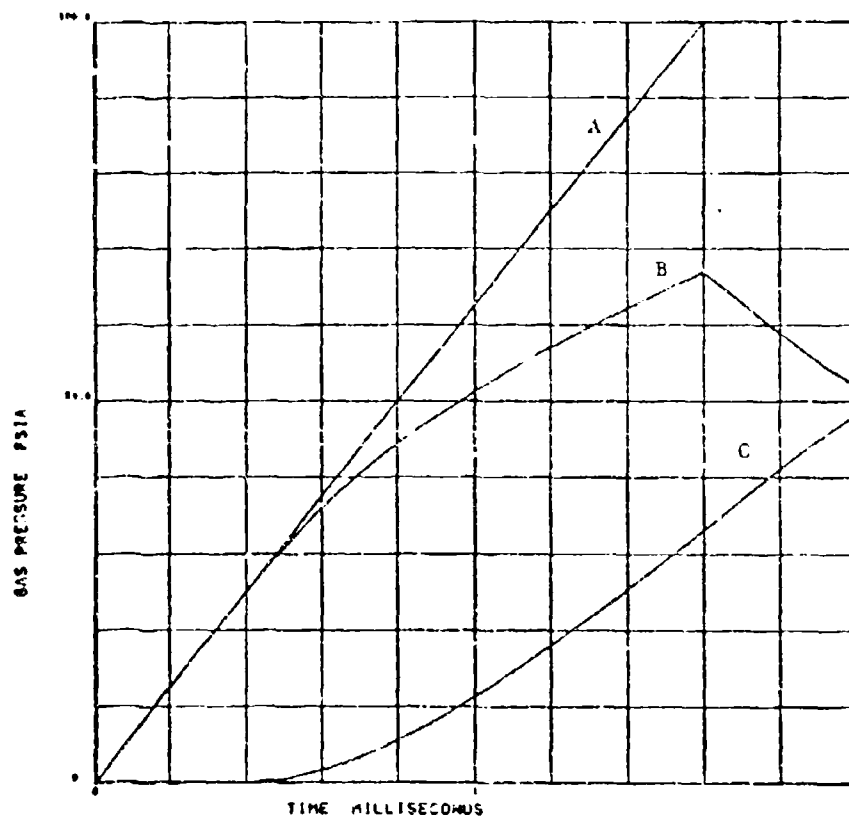


Figure 5-79

Figure 5-80

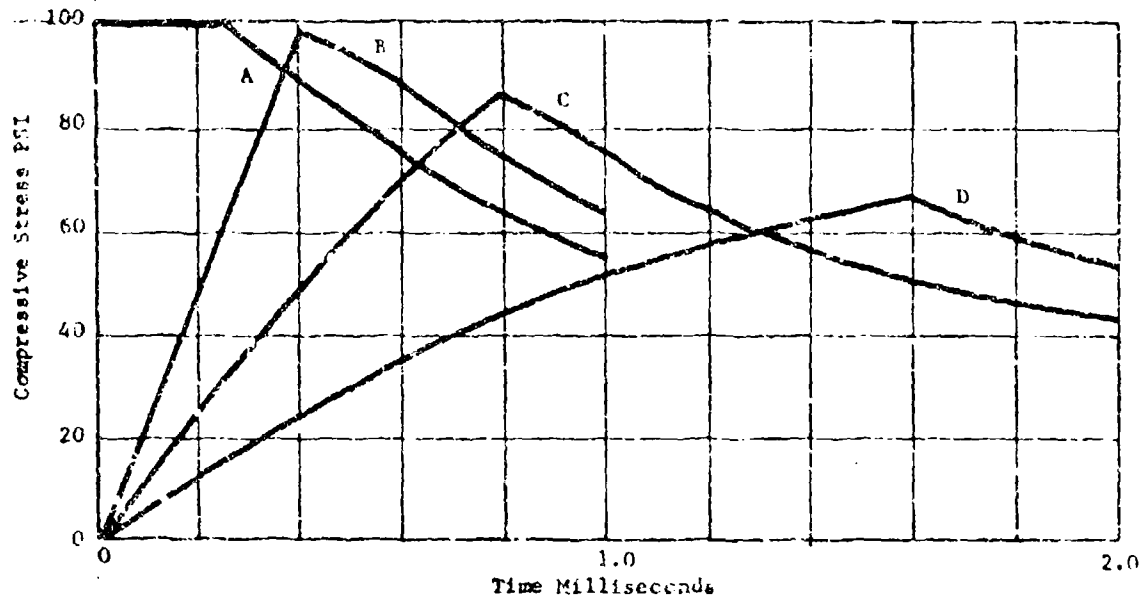
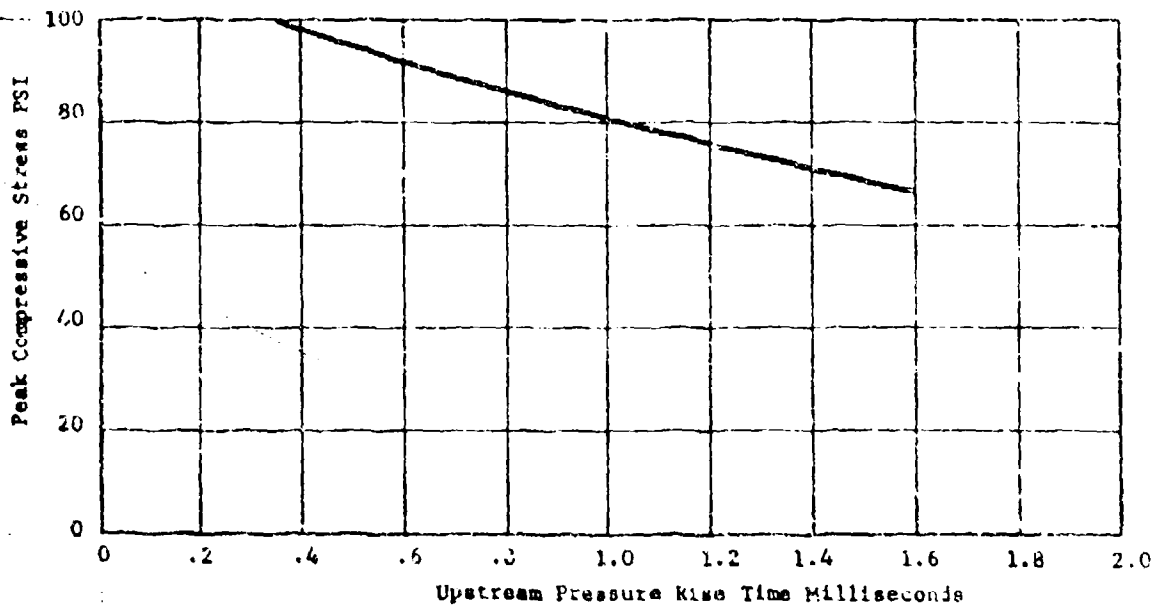


Figure 5-81



0.4 square inches, corresponding to a contraction area ratio of 25. The upstream gas pressure is applied in a linear ramp in which pressure is raised from an initial value of .001 psia to the final value of 100 psia in 1.6 millisecond. Curve A of Figure 5-79 shows the head-end pressure vs. time. Figure 5-76 illustrates the pressure profile through the bed at a time .35 millisecond after start. It is obtained by numerical calculation of the flow and accumulation of gas in the 25 nodal segments which are used to approximate the bed. Figure 5-77 shows the pressure profile 1.0 millisecond after start and Figure 5-78 shows it 2.0 milliseconds after start.

Curve C of Figure 5-79 shows the calculated pressure downstream of the bed. It is determined in the numerical calculations by simultaneously flowing material out of the downstream end of the bed, accumulating the flow leaving the bed in a small plenum and exhausting from the plenum through a sonic nozzle. Curve B of Figure 5-79 is the compressive and exhausting from the plenum through a sonic nozzle. Curve B of Figure 5-79 is the compressive stress on the catalyst bed from the difference between the upstream and downstream gas pressure forces, which force the bed against the downstream screen or bed restraint. B is the difference between A and C.

Figure 5-80 re-plots curve B of Figure 5-79 along with three other curves of compressive stress versus time for different rates of application of head-end pressure. The curves are for rise-times 0.0, 0.4, 0.8, and 1.6 milliseconds. It can be seen that when the rise times are increased, the peak compressive stress produced tends to decrease.

Figure 5-81 is the locus of peak values from Figure 5-80 and shows how the peak compressive stress produced in a bed decreases as the rise-time of the upstream pressure loading increases.

5.6.3 Mechanical Response of the Bed to Rapid Loading

If the compressive loading of the bed were rapid compared to the natural period of oscillation of the bed, then the peak compressive stress would be higher for a rapid transient loading than for a slow application of load. As a first cut, the bed may be approximated as a system having a single degree of freedom. In this case the natural period of oscillation of the bed would be:

$$\tau = 2\pi \sqrt{\frac{M}{K}} = 2\pi \sqrt{\frac{\rho L A}{E \frac{A}{L}}} = 2\pi \sqrt{\frac{\rho L^2}{E}} \quad (5.6-1)$$

where

M is mass of the bed
K is spring constant of the bed
 ρ is bulk density of the bed
L is length of the bed
A is cross-sectional area of the bed
E is the compressive modulus of the bed

The compressive modulus of the bed is the only property difficult to estimate. Compression (or compaction) of a granular material may be partly dependent upon the prior history of compaction, and may be irreversible instead of elastic. The stress-strain relationship of a bed of Shell-405 granules has been measured as a part of this study (Section 3.3). A volumetric compaction of 4% was measured at a compressive stress at 1000 psi. This corresponds to an average bed modulus of 25,000 psi over this range of pressure. This number was compared with literature values reported for a bed of flint shot of 28-35 mesh, which should behave similarly to a bed of Shell 405 at low pressures. At a net compressive stress of 100 psi a compressibility of $35 \times 10^{-6} \text{ psi}^{-1}$ has been reported, which translates to a compressive modulus of 28,571 psi. The values are obviously in good agreement.

Using the values:

$$\begin{aligned} \rho &= 1.60 \text{ gm/cm}^3 \\ L &= 2.54 \text{ cm} \\ E &= 1.723 \times 10^9 \text{ dynes/cm}^2 \text{ (25,000 psi)} \end{aligned}$$

$$\tau = 2\pi \sqrt{\frac{1.60 \times 2.54^2}{1.723 \times 10^9}} = 5.7 \times 10^{-4} \text{ sec} = 0.48 \text{ millisecond}$$

Hence, the compressive loading of this bed will be "impulsive" only if the time of load application is considerably shorter than 0.5 millisecond.

The literature was consulted to obtain typical pressure rise times in experimental "hard starts" of hydrazine combustors, Reference 124. An oscillograph trace was found for the start of a combustor preconditioned to 35°F at 9×10^{-5} torr. Although the start is delayed and "hard", the most rapid portion of the chamber pressure rise takes approximately 15 milliseconds to be completed. This is a very slow pressure rise in terms of either the time to pressurize the bed, or in terms of the natural period of oscillation of the bed, and would subject the bed only to the normal steady pressure drop associated with the flow of gas through the bed.

5.6.4 Other Conclusions From the Catalyst Bed Mass and Heat Transport Model

For a typical calculation the bed Reynolds number based on particle diameter is approximately 2000. Since the effects of Reynolds number rapidly become important above Reynolds numbers of 10, the flow through the bed is far above flow rates where it could be adequately represented as completely viscous Darcy flow. The value calculated by our model for steady-state pressure drop (35-40 psi/inch) appears to be of the correct order of magnitude to agree with reported experimental values.

Although the catalyst bed flow model simultaneously calculates the flow mass and Heat, the time scale for the thermal transient is much longer than for the pressure transient, so there is not much dynamic linking between the processes, i.e., the thermal profile through the bed is essentially stationary during the short period of time required for the pressure transient to be completed.

In general, although the transient effects per se in bed pressure buildup are not expected to be important in normal startup, the static effects must nevertheless be considered. The calculations for a typical catalyst which are represented in Figures 5-76 through 5-81 indicate that steady-flow pressure drops through a bed will be on the order of 40 psi. Since the pressure profile through the bed is approximately linear, this indicated that the downstream portions of the bed will be exposed to compaction pressures of 40 psi or more, with the compaction pressure decreasing almost linearly to zero at the upstream portion of the bed. Since both theory and experiment predicts local loss of material at bed compaction pressures considerably lower than this it must be concluded that steady-state pressure drops through the bed can be damaging. The physical weakness of the catalyst particles, combined with their high rigidity and spheroidal shape make them extremely intolerant of bed compression stresses. Corrective measures could be to either shield the catalyst particles from physical stress, or else to modify the shape of the catalyst particles so as to provide larger particle-to-particle bearing areas.

6. CRITICAL ASSESSMENT OF RESULTS AND CONCLUSIONS

Commercial catalytic reactors employing noble metal on alumina catalysts can experience catalyst breakup problems. The general philosophy involved in selecting design parameters for commercial fixed bed reactors is to eliminate the initial catalyst break-up, since the bed after the occurrence of extensive primary degradation generally will be experiencing a major problem requiring a shutdown and catalyst replacement (e.g., channeling of reactants, excessive pressure drop). Many commercial fixed catalyst beds are not mechanically restrained and thus are potentially subject to fluidization. Commercial experience with fixed bed reactors has indicated that inadvertent fluidization in part of the bed often leads to serious problems. Thus factors such as bed inlet design and maximum linear velocities are carefully controlled. Even in a downflow vapor phase reactor fluidization can occur in the inlet area since the vapor jet discharging from the inlet distributor upon striking the surface of the bed will tend to turn and develop a radial velocity component. If the magnitude of this radial gas flow is such that the drag and lift forces generated on the particle overcome gravitational forces then the particle will begin incipient entrainment. In a simple impinging jet designed inlet (located approximately one inlet diameter away from the bed), the maximum surface velocity would occur approximately one diameter away from the axis of the jet. Particles are moved away from the impinging jet in a direction parallel to the bed surface. As erosion proceeds, the particles in the vicinity of the jet are removed also, ultimately leaving a crater in the center of the reactor. The fixed catalyst bed in a hydrazine thruster is mechanically restrained. However, mechanisms or factors leading to void formations in a thruster can similarly expose such a bed to particle movement problems.

Information indicates that the pressure drop across an operating thruster typically ranges from 15 to 40 psi and involves catalyst bed depths of 0.5 to 1 inch. Thus, there is the possibility of static pressure drops of up to 80 psi/inch of bed, not including any effect of bed preloading. Such a pressure gradient is very severe when compared to commercial practice in vapor phase fixed bed reactors. As an example, commercial hydroformers used for the production of gasoline generally operate with a pressure drop of 5 to 10 psi per reactor and typically employ catalyst bed depths of 5 to 10 feet, which would be equivalent to static pressure drops ranging from .05 to 0.2 psi/inch of bed. Similarly, it has been estimated that the average gas velocity in a thruster is approximately 110 feet per second. This gas velocity is an order of magnitude greater than that normally experienced in hydroformers. Also design and operating procedures for commercial fixed bed catalytic units normally avoid rapid temperature or pressure transients. Even in catalytic beds used in the treatment of auto exhaust gases the transients experienced when the bed is cycled during the various driving modes are not as rapid as those experienced in a hydrazine thruster, for example, during a cold start. It can be seen that, in general, the environment to which Shell 405 catalyst is exposed in hydrazine thruster use is quite severe compared to the environment experienced by similar alumina based catalysts in use in the petroleum and chemical industries.

A number of potential mechanisms or factors involved in individual catalyst particle degradations have been screened either experimentally or analytically or by means of both techniques. The areas investigated and the interaction between the experimental and analytical studies was summarized in Table 2-1.

• Fluid Dynamic Erosion

A number of mechanisms in the fluid dynamic erosion area were investigated either experimentally or analytically. Sensitivity tests in the HSGET apparatus indicate that fresh Shell 405 granular catalysts do not experience any degradation at 1700°F even with exposure to gas velocities up to 250 feet per second. These data indicate that gas fluid dynamic erosion per se is not a mechanism contributing to catalyst degradation.

An analytical investigation was made of the effect of the presence of liquid droplets or solid particles in the flowing gas stream on erosion. The calculation indicated directionally that in the absence of particulates in the gas stream the erosion rates could be expected to be significant. On the other hand, the presence of particulates suggest wear rates which cannot be ignored. Current specifications for hydrazine used in catalytic thrusters limit solids to a maximum allowable level of 1 mg/liter, which is equivalent to 1 ppm by weight. In addition to particulates in the liquid hydrazine entering the thruster, particulates could be generated internally to much higher levels via a rapid decomposition of the catalyst bed as a result of another breakup mechanism. Since the particulate velocity exerts a major effect on the wear rate, a consideration in the latter case is how fast the solids accelerate up to the gas stream velocity. Since the calculations that were made assumed an instantaneous acceleration of catalyst breakup particles, they obviously represent a pessimistic or limiting case. The calculations show a need for (1) as low a particulate contaminant level in the fuel as possible, and (2) lower gas velocities to minimize potential particulate abrasion loss by limiting the ultimate velocity the particles can reach in the event another mechanism causes catalyst breakup. The magnitude of these abrasion effects are not clear at the present, however, as the results are totally dependent on analytical calculations which must be verified by experimental measurements

Results obtained with the PLPET experiments indicate that a pulsed liquid stream can cause a weight loss with fresh Shell 405 catalyst. This weight loss increases with increasing number of pulses and linear velocity and is higher for 8-12 mesh granules than for 1/8" cylinders. An Analysis of Variance of results from a full factorial statistically designed experiment indicate that the effect of these variables on weight loss is significant but that no interactions exist between the variables. The magnitude of this weight loss, however, will be small at lower liquid velocities. For example, when the linear velocity is held below 50 feet per second, the weight loss experienced by a fresh granular catalyst will be below 1 wt. %.

• Particle Movement

An experimental study was made to determine the minimum gas velocity at which particle movement will first occur and expose a voided catalyst bed to particle fluidization, and thus to particle-to-particle abrasion effects. Results from the particle fluidization experiments have shown that the incipient particle movement velocity varies with gas density and particle size as expected. A successful correlation of incipient particle movement velocity as a function of the square root of the ratio of particle diameter to gas density was made. Results indicate that for the range of granular catalyst sizes, gas densities, and gravitational fields expected for hydrazine thrusters, the incipient particle movement velocity will be much lower than an average gas velocity of 110 feet per second. Thus, in general, particle movement will be possible once sufficient void space is present in the catalyst bed. Since a Shell 405 catalyst exposed to a pressure load of 100 psi will compact less than 0.5%, actual breakup of catalyst particles will be required for substantial void volume formation.

The possibility of catalyst loss via particle to particle abrasion in a voided bed was investigated experimentally using several approaches. In a series of tests in a glass reactor at ambient conditions it was demonstrated that significant abrasion losses would occur in a bed that was forced to undergo rapid internal motion. Observations from this and other glass apparatus with different configurations indicated that simply exceeding the incipient particle movement velocity would not necessarily result in appreciable internal bed movement. Thus, exceeding the incipient particle movement velocity is a necessary but not sufficient cause for bed movement. Void volume abrasion tests carried out at conditions much closer to actual thruster conditions showed some abrasion effects but appeared to confirm the complexity of the problem as no noticeable trends were observed in the data. Thus, particle to particle abrasion losses in a voided bed undergoing rapid internal motion is a major secondary breakup mechanism and void volume formation is a major deleterious occurrence in overall bed breakup. However, the fluid dynamic conditions at gas velocities above the incipient movement velocity which determines if appreciable particle movement and abrasion losses will take place are obviously complex and have not been defined as of yet.

• Pressure Crushing

Experimental static pressure crushing studies were carried out with both individual particles and aggregate beds. Individual particle measurements were made with fresh and used Shell 405 catalyst and with the catalyst support both before and after the attrition step. The use of the attrition procedure improves the average crush strength of the larger mesh size granules but does not significantly improve the strength of the smaller material. The addition of the iridium metal to the support, in general, does not effect the crush strength. Even with the use of the attriting

procedure, the scatter in the individual crush strengths of both Shell 405 pellets and particles is quite large, which means that an appreciable fraction of aggregate of Shell 405 catalyst such as a bed will have particles with a crush strength significantly lower than the mean crush strength. For example, it is estimated that 10% of fresh Shell 405 particles have a crush strength which is lower than a value equivalent to 68% of the average value for that particle size. Tests with samples of various batches of fresh Shell 405 catalyst indicates that substantial differences exist in mean crush strength of the different batches.

Experimental pressure crushing studies were extended from tests with individual particles to tests involving the static pressure crushing of a small bed of granular catalyst. Data was obtained on all the standard mesh sizes of fresh Shell 405 i.e. 8 to 12, 14 to 18, 20 to 25, 25 to 30 and 20 to 30 mesh, and the product was characterized as to its size distribution by sieving through progressively smaller sieve openings down to a through 35 mesh size. As the bed pressure increased, the amount of breakage in the starting mesh material increased slowly at first, but finally increased sharply at higher pressures. This exponential increase in the weight of material through a given mesh size as pressure is increased is characteristic of the general experience with catalysts under pressure loading. With a fresh catalyst under a static bed pressure load of 100 psi the weight of material lost from the initial mesh size ranged from 2 to 6%. If bed "fines" are defined as the through 35 mesh fraction, at a 100 psi loading the weight of "fines" is generally less than 1% with a fresh catalyst. However, as discussed in a subsequent section, a test of a thruster aged catalyst showed much higher losses under bed pressure crushing than did fresh catalyst. Assuming that the particles are spherical in shape, the contact area between particles all of the same size will not depend on the absolute size of the particles. For an actual Shell 405 mesh size material, the contact area, however, will be a function of the distribution of particle sizes with the contact area increasing as the width of the distribution of particle sizes increases. As a rule of thumb, this effect becomes important when the ratio of the diameter of the largest particle to the smallest particle exceeds the $\sqrt{2}$. Since this is not the case with the standard starting mesh sizes employed with Shell 405, the various mesh sizes should have approximately equivalent contact areas. It does suggest, however, that the small mesh size fines generated as the bed breaks up will tend to increase the particle to particle contact area and thus help to stabilize the bed against pressure crushing forces. It also suggests that a mixture of small and large mesh size catalyst (e.g. 8 to 12 and 25 to 30 mesh) will be able to resist pressure crushing forces better than a single mesh size catalyst because of increased contact area, assuming, of course, that gas velocities are adjusted to produce an equal pressure drop in both cases.

Analytical studies were made to predict the particle stresses which result when a bed of catalyst particles is subjected to a compression load. These calculations show that particle to particle contact stresses resulting from external bed compression forces are quite severe, and indicate that some catalyst breakup should occur, even at very low bed pressures. Mass loss calculations which predicted the percent fines as a function of bed pressure loading agreed well with experimental results. Thus both experimental and analytical studies indicate that the ability of Shell 405 catalyst to resist pressure crushing from external forces in a thruster bed is an area for genuine concern.

An analytic study was made of the effect of the transients involved when a bed is pressure loaded, i.e. pressure shock effects. Results from this study indicate that a pressure loading occurring in load application times greater than 1/2 millisecond is slow, either in terms of the time to pressurize the bed or in terms of the natural period of oscillation of the bed, subjecting the bed only to the normal steady pressure drop associated with the flow of gas through the bed. Thus, the dynamics per se of a normal pressure shock would not appear to be a major mechanism for catalytic degradation, and the effect of a normal pressure transient can be analyzed in terms of the effect of an equivalent steady state load applied to the bed.

Experimental studies of "pop shock" dynamic pressure crushing were made using an actual catalyst bed exposed to hydrazine decomposition pressures waves at pressures up to 2400 psi and with a pressure rise time of 2 to 4 milliseconds. The results of these tests both have demonstrated for the first time the extremely deleterious nature of "pop shocks" and have quantified their effect in terms of both the intensity and the number of shocks. In accordance with analytical predictions the bed response time was faster than the pressure rise time and a pressure gradient as large as the peak pressure was never experienced by the bed. The bed pressure drop was correlated against the peak pressure and was generally less than 20% of the peak pressure.

Important findings from the work include:

- The threshold "level" for significant damage, with a single "pop shock" was in the 1700 to 2000 psi range.
- Damage, however, occurred from cumulative "pop shocks" at lower levels i.e. 1000 psi and the bed breakup was successfully correlated as a function of the number of "pop shocks" above the threshold level.

- For an equal number of "pops" above 1000 psi the 14 to 18 mesh catalyst experienced approximately twice the bed damage as did the 25 to 30 mesh catalyst.

These results clearly demonstrate a need for avoiding "pop shocks" in excess of 1000 psi and indicate an advantage for employing small mesh size catalyst in the downstream sections of a thruster where the maximum pressure crushing forces from a "pop shock" will be experienced. The experimental corroboration of the bed pressure wave response effects predicted by the analytical modeling studies also confirm the merits of the analytical work.

• Differential Thermal Expansion

An analytical study was made of the effect of the differential thermal expansion of the bed and thrust chamber hardware. During startups the bed heats up more rapidly than the wall. Because of this, the bed first undergoes compression but then changes to dilation as the effect of the much higher coefficient of thermal expansion of the metal wall relative to that of the catalyst bed is manifested. On cooldown two possibilities are possible. If the bed does not repack itself during the startup dilation phase, it remains in dilation during the cooldown period. If, on the other hand, the bed repacks itself after the startup dilation, it will experience compression during cooldown. The magnitude of the peak compression and dilation increases with bed loading. A bed loading of 0.1 lb per in²-sec produces a peak startup bed compression of 0.3 vol %, which translates into a bed pressure of 25 psi. If the bed repacks itself after the startup dilation, with a similar loading of 0.1 lb per in²-sec, the bed will experience a maximum compression of 1.75 vol % during cooldown, which translates into a 290 psi bed pressure. The calculations also point out that higher bed loadings increase the magnitude of the bed compression forces, both during initial startup and during cooldown with a repacked bed. Also, higher thruster pressures do not markedly effect the magnitude of the bed void volume during the startup dilation period.

Additional calculations were carried out by AFRPL on differential thermal expansion effects using two other thruster configurations and typical duty cycles in addition to steady state operation. These results confirmed the importance of differential thermal expansion as a significant catalyst breakup mechanism. The relative wide variation in the maximum pressure experienced by the different thrusters also suggests strongly that thruster design and configuration has a strong influence on the magnitude of differential thermal expansion effects.

• Thermal Effects

An analytical study was made of particle thermal shock. Thermal shock from externally heating a cold particle by hot combustion gases or from externally cooling a hot particle by impingement of cold liquid hydrazine were both analyzed in terms of the temperature profiles obtained, which were taken from dimensionless correlations of temperature ratio with Biot number and Fourier number. The stresses induced in the pellet were obtained from the temperature profiles. These calculations indicate that hot gas thermal shock is not a failure mechanism, but that liquid quench thermal shock could be a failure mechanism. Thus, the calculations suggest merit to the avoidance of cold liquid impingement upon hot catalyst material. The analytical results also predicted that (1) liquid impingement will not be damaging if the catalyst temperature is sufficiently high to induce film boiling and thus reduce liquid to particles heat transfer, (2) reducing the diameter of the particles will reduce the Biot number, and the stress level produced by cooldown.

The effect of hot gas thermal shock, thermal cycling and thermal fatigue were investigated experimentally using hot hydrazine decomposition gases and an actual catalyst bed. Catalyst beds were exposed to up to 200 cycles of hot gas thermal shock (300 to 1500°F) at bed pressure drops of 20 to 50 psi. Both 14-18 mesh and 25-30 mesh catalyst bed showed relatively little bed breakup (approximately 5% total fines). These experiments confirm analytical predictions that hot gas thermal shock would only result in the breakup of the weakest bed particles and thus is not a major mechanism for catalyst bed breakup. Exposure of catalyst beds to up to 1200 seconds of steady state hot gas flow (thermal aging) also resulted in relatively little bed breakup. Thus, hot gas thermal shock, thermal cycling and thermal aging per se are not major catalyst breakup mechanisms. Examination of the catalyst beds after the experimental tests indicated, however, that hot gas thermal cycling caused a major bed rearrangement resulting in a much tighter bed packing. Thus, hot gas thermal cycling may play an important role in the overall bed breakup process via its influence on bed repacking and void volume generation.

Experimental measurements were made of liquid quench thermal shock using liquid ammonia and actual catalyst beds. Samples of new, thruster exposed and thermally fatigued catalyst were tested. Both 14-18 and 25-30 mesh thruster exposed catalysts experienced significant bed breakup after exposure to 200 cycles of liquid quench thermal shock. Samples of both fresh and thermally fatigued 14 to 18 mesh catalyst also showed significant bed breakup. The data for the fresh 14-18 mesh catalyst indicated that bed breakup (% fines) could be correlated as a function of the number of liquid quench thermal shock cycles. In contrast, the fresh and thermally aged samples of 25-30 mesh catalyst showed relatively low levels of bed breakup. Thus, smaller catalyst particles showed better resistance to liquid quench thermal shock. This experimental result on the effect of catalyst particle size corroborates the analytical prediction that reducing the diameter of the catalyst particle will reduce the Biot number and thus reduce the stress level produced by liquid quench thermal shock. In general, the liquid quench thermal shock experimental results confirm the analytical prediction that this mechanism per se should be a significant catalyst breakup mechanism, as contrasted to hot gas thermal shock which should not be important.

- Internal Pore Pressure Gradients

The internal particle stresses produced in a particle by rapid gas pressurization or depressurization in the absence of liquid hydrazine were also analytically investigated by calculating the internal pore pressure profiles and the stress distribution resulting from these profiles. Particle depressurization is very fast relative to the rate of thruster chamber depressurization at cutoff so that no significant internal pressure stresses will occur during a normal cutoff. Internal pressurization is also a very fast process producing only compressive stresses in the particle. Pressure loadings of sufficient magnitude and speed to cause significant internal pore pressure generated stresses are much more likely to cause damage by simple bed composition pressure stresses. Thus, internal stress failure caused by internal particle pore pressure changes as a result of rapid pressurization or depressurization is not an important mechanism. The results also indicate that pressure equilibration is a very rapid process compared to thermal equilibration, and thus the processes would not be expected to be coupled.

An internal processes computer program was written to investigate the temperatures, pressures, and flow processes which occur when a catalyst particle is wetted with liquid hydrazine. Studies carried out by United Technologies Research Company (UTRC) under Contract FO4611-74-C-0031 have indicated that the internal pressure generated within a Shell 405 catalyst particle as a result of wetting with liquid hydrazine can cause a catalyst particle to undergo break-up. Our analytical modeling studies support this conclusion. Mass transport within the particles was modeled by D'Arcy flow driven by the pressure gradients resulting from first the capillary imbibitions pressure of the liquid hydrazine and later by the high pressure gases generated from the decomposition of the hydrazine rather than simply by molecular diffusion driven by concentration gradients. The D'Arcy flow approach has previously been used by workers in fields such as hydrology and petroleum reservoir engineering to treat the complex problem of flow through porous media which normally do not contain uniform, parallel pores. Heat transport within the particle was modeled considering both convection of heat resulting from flow of gas and liquid plus conduction of heat through the formation rather than just considering heat conduction alone. Results of initial operation of the internal particle processes model using an assumed permeability value suggested that this value was too large and a subsequent experimental determination confirmed this. With the measured permeability value our model predicts a response time in the order of 5 to 10 milliseconds at 80°F which is in excellent agreement with typical Shell 405 thruster ignition delay times for this temperature. In contrast, the U.T.R.L. developed model can only predict such a response time at this temperature by using unrealistically high values for Shell 405 catalyst pore sizes (i.e. 400 to 600 Å²); and when using realistic values for pore sizes (e.g. 20 to 100 Å²) predicts response time which are much too slow to match actual catalyst ignition delay times. Results of the internal particle processes model studies indicate the following.

- Contact with liquid hydrazine can result in damagingly high internal pressures being generated. Thus, an obvious engineering remedy for this problem would be to prevent the contact of liquid hydrazine by means such as raising the bed temperature or providing sufficient open volume between the injector and bed so as to insure hydrazine vaporization.
- A catalyst with larger pore sizes (i.e. increased permeability) experiences much lower internal pressures. Thus, altering the catalyst pore size distribution can mitigate the deleterious effect of contact with liquid hydrazine.
- At a fixed time period (e.g. 10 milliseconds) a larger particle size catalyst will experience lower internal pressures as a result of exposure to liquid hydrazine. This result corroborates U.T.R.L. data showing increasing particle breakage in liquid immersion tests as the catalyst particle size was reduced (150, Report No. 13). It also suggests an advantage to using a larger mesh size catalyst in thruster areas which may experience liquid hydrazine.
- Calculations indicate that at the conditions investigated an active catalyst will not accumulate appreciable quantities of liquid hydrazine because the hydrazine is consumed faster than the liquid can penetrate into the inner core of the pellet. Thus, an active catalyst essentially will not wet, whereas an inactive catalyst can experience wetting. If the lack of catalyst activity is temporary (i.e. temporary poison) and the catalyst suddenly becomes active after it has been wet with hydrazine the catalyst will not be able to relieve itself of the product gases fast enough to escape destruction. This catastrophic effect of a "temporarily poisoned" catalyst being exposed to liquid hydrazine may be important when a thruster is first fired since the active irridium metal will be covered by an oxide layer if the catalyst has been handled in air, and this oxide layer will be removed via reaction with the hydrazine thereby "activating" the catalyst. Other "temporary poisons" such as carbonaceous surface residues resulting from hydrocarbon contaminants such as aniline in the feed will be more difficult to remove than a surface oxide layer and thus should not expose the catalyst to the danger of rapid reactivation after it has been wetted with liquid.

• Effect of Use on Fresh Catalyst Physical Properties

The effect on the physical properties of fresh Shell 405 of thruster exposure was investigated by testing samples of catalysts exposed to both actual thruster use and samples exposed to controlled environments typical of those experienced during thruster use. Particle crush strength tests on nine samples of thruster exposed catalysts indicated that in four of the samples a significant loss of mean crush strength was observed and in two of these four samples a significant increase in the scatter of the individual particles crush strength also was observed. The effect of such changes, of course, is a marked increase in the number of very weak particles present in an aggregate such as a bed. This was confirmed

in a bed pressure crushing test of a used thruster exposed sample which exhibited a larger percent of material leaving the original mesh size for a given bed pressure. Tests on the ability to resist pulsed liquid stream erosion were performed on three samples of thruster exposed catalysts. All three samples showed evidence of a loss of resistance to pulsed liquid stream erosion. Similarly liquid quench thermal shock tests indicated that samples of thruster exposed catalyst exhibited a much lower resistance to breakup by the mechanism. These results, although limited in number, clearly indicate that thruster exposure can significantly degrade the ability of Shell 405 catalyst to resist breakup by a number of different mechanisms. These tests of used catalysts, however, were too limited in number to indicate what characteristics of thruster exposure was responsible for their loss of ability to resist breakup. An attempt was made to shed light on this complex question by examining samples of catalyst exposed to various controlled environments. Samples from a number of tests (void volume abrasion and liquid quench thermal shock) showed signs of an increase in particle mean crush strength indicating that the weaker particles were selectively removed in the original test. Samples after exposure to 600 seconds of steady state hot gases (thermal fatigue) did not show any signs of a loss in particle mean crush strength. In contrast, samples from two of three batches of fresh Shell 405 catalysts immersed in liquid hydrazine showed a decrease in particle mean crush strength. Limited tests were also made on the resistance to pulsed liquid erosion. Results indicated that samples of catalyst surviving "pop shocks" in excess of 1700 psi or 100 cycles of hot gas thermal cycling showed evidence of loss of resistance to pulsed liquid erosion. Although the results from these limited tests are not completely definitive, it is important to note that exposure to liquid hydrazine was the only environment from which surviving catalysts showed a decrease in mean crush strength. Thus, exposure to liquid hydrazine not only can directly cause particle breakup, but the survivors from such exposure also suffer a loss in crush strength which will make them more susceptible to break-up from pressure crushing forces.

• Comparison of Experimental and Analytical Results

In a number of areas both experimental and analytical modeling studies were carried out. An examination of the results of studies in these areas was made in order to assess the agreement between analytical modeling results and experimental measurements. The results of these tests between analytical modeling results and experimental results are summarized in Table 6-1. The agreement between modeling results and experimental results is outstanding. Particularly significant is that modeling results correctly predicted a number of physical results prior to actual experimental work being carried out, and that in many cases model calculations were made without the advantage of rigorously determined physical properties for actual Shell 405 catalyst granules. This excellent agreement between model results and experimental results in the complex hydrazine monopropellant thruster environment clearly demonstrate that catalyst breakup phenomena can indeed be successfully analytically modeled.

Table 6-1

Analytical Modeling Results Versus Experimental Results

<u>Test Number</u>	<u>Physical Effect Indicated By Analytical Model Results</u>	<u>Nature of Test</u>	<u>Comparison With Experimental Results</u>
1	Hot gas thermal shock would not be a major breakup mechanism.	Prediction	Prediction confirmed by thermal cycling data.
2	Liquid quench thermal shock would be a significant breakup mechanism	Prediction	Prediction confirmed by liquid quench data.
3	Smaller catalyst particles better able to withstand liquid quench thermal shock.	Prediction	Prediction confirmed by particle size effect in liquid quench data.
4	Under a dynamic pressure change, the bed would respond faster than pressure wave buildup.	Prediction	Prediction confirmed by "pop shock" data.
5	Catalyst particles in bed under static pressure forces will undergo crushing.	Confirmation	Model confirms effect and magnitude of fines to be expected.
6	Larger catalyst particles better able to withstand expose to liquid hydrazine at cold start temperatures.	Confirmation	Model confirmed U.T.R.L. data on the effect of catalyst particle size on breakage rate following exposure to liquid.
7	Active catalysts will not wet appreciably with liquid hydrazine, only inactive catalysts will wet.	Confirmation	Model confirmed U.T.R.L. data and observation on liquid wetting.
8	Time frame for catalyst to imbibe and react liquid hydrazine at low temperatures using results obtained from the actual Shell 405 pore size distribution rather than an assumed artificially large pore size.	Confirmation	Model confirms observed magnitude for cold start ignition delay times.

The analytical studies pinpointed a number of strength of material properties which influence the judgements made from calculations and which at present have only been indirectly determined for Shell 405 catalyst. These include tensile failure strength, multiaxis compressive failure strength and the Poisson ration.

In Table 6-2 is shown a summary of significant mechanism or factors along with the method(s) by which they were investigated. In Table 6-3 is shown a summary of insignificant mechanisms or factors and the method(s) by which they were investigated. The primary catalyst breakup mechanisms are, in general, associated with either pressure crushing forces or the influence of liquid hydrazine. Mechanisms in the pressure crushing area include the effects of steady-state gas flow ΔP , bed preload and differential thermal expansion and the effect of dynamic "pop shocks". The wide range of catalyst particle crush strength both on a batch to batch basis and on or within batch basis also can contribute to pressure crushing problems since the percent of very weak catalyst particles is strongly dependent on these factors. Mechanisms associated with the influence of liquid hydrazine include pulsed liquid stream erosion, liquid quench thermal shock and high internal particle pressures resulting from imbibed liquid. Erosion effects from solid particles present in the liquid hydrazine is also a possible significant mechanism but this must be confirmed experimentally. Another important factor in catalyst breakup is the deterioration as a result of thruster exposure of the ability of a fresh catalyst to resist the various breakup mechanisms. Our data to date indicates that liquid hydrazine exposure appears to be responsible for particle crush strength deterioration, however, the situation regarding how various environmental exposures effects the other important properties of the catalyst is not completely clear at present. The major secondary breakup mechanism is the possibility that catalyst in a voided bed will experience rapid motion and consequently experience significant particle to particle abrasion. Bed gas velocities are, in general, well above that required for incipient particle motion. However, this appears to be a necessary but not sufficient cause for particle motion, and at present the fluid dynamic criteria controlling potential particle motion in a voided bed are not defined. Our results also indicate that the effect of the various mechanisms on the magnitude of breakup can be controlled by adjusting reactor operating variables such as liquid injection velocities, bed temperature, bed gas linear velocity and pressure drop, bed preload and catalyst selection for the various sections of a thruster. It may also possible to mitigate the effects of thruster exposure on catalyst property deterioration or to reduce the probability that a void bed will experience rapid particle motion by controlling reactor operating variables, but this is not entirely clear at present. We feel that our results to date, and in particular the excellent agreement found between analytical and experimental results, clearly indicates that it is possible to develop a global scientific computer model that would interpret the results of all catalyst breakup studies and provide a fundamentally developed tool to assist thruster designers to achieve longer catalyst bed life.

Table 6-2

Summary of Significant Mechanisms or Factors

<u>Mechanism or Factor</u>	<u>Method Investigated</u>
<ul style="list-style-type: none"> ● Pressure Crushing <ul style="list-style-type: none"> - Effects in static situation of high ΔP from steady state gas flow, differential thermal expansion and bed preload. - "Pop shocks" in a dynamic situation. - Wide range of catalyst particle crush strengths both batch to batch and within batch. 	Experimental and Analytical Experimental Experimental
<ul style="list-style-type: none"> ● Corroboration of the deleterious effect of imbibed liquid producing a high internal particle pressure. 	Analytical
<ul style="list-style-type: none"> ● Deterioration of the ability of fresh catalyst to resist breakdown mechanisms after thruster exposure. <ul style="list-style-type: none"> - Liquid exposure reduces particle crush strength. - Resistance to liquid quench thermal shock and pulsed liquid erosion also effected. 	Experimental
<ul style="list-style-type: none"> ● Particles in rapid motion in a voided bed will suffer abrasion losses. 	Experimental
<ul style="list-style-type: none"> ● Pulsed liquid stream fluid dynamic erosion. 	Experimental
<ul style="list-style-type: none"> ● Thermal shock from liquid quench cooldown. 	Analytical and Experimental
<ul style="list-style-type: none"> ● Fluid dynamic erosion from solid particles in gas. 	Analytical (a)

(a) Requires experimental verification.

Table 6-3

Summary of Insignificant Mechanisms or Factors

<u>Mechanism or Factor</u>	<u>Method Investigated</u>
• Fluid dynamic erosion of particles by pure gas.	Experimental and Analytical
• Fluid dynamic erosion by liquid drops in gas.	Analytical
• Particle pore pressure gradients during rapid gas pressurization or depressurization (in the absence of liquid).	Analytical
• Transient effects per se in normal pressure buildup (must consider effect of pressure, however, as <u>static</u> pressure crushing).	Analytical
• Thermal shock from heating a particle with hot combustion gases.	Analytical
• Thermal fatigue of bed due to hot gas temperature cycling.	Experimental
• Thermal aging of bed from exposure to constant temperature hot gas.	Experimental
• Synergisms or interactions (no effects found to date beyond that expected from knowledge of individual mechanisms).	Experimental

7. REFERENCES

- (1) Adams, C.R. and Voge, H.H., "Aging of Silica Alumina Cracking Catalyst - Electron Microscope Studies," Journal of Physical Chemistry Vol. 61, p 722, 1957.
- (2) Baddour, R.F., et al., "The Palladium Catalyzed Carbon Monoxide Oxidation Catalyst Break-in Phenomenon," Journal of Physical Chemistry, Vol. 74, No. 8, April 16, 1970.
- (3) Bencsi, H.A., et al., "Determination of the Pore Volume of Solid Catalysts," Analytical Chemistry, Vol. 27, p 1963, 1955.
- (4) Bond, G.C., "Absorptive and Catalytic Properties of Small Metal Crystallites," 4th International Congress on Catalysis, Moscow, 6/23-29/68.
- (5) Brooks, C.S., "Characterization of Iridium Catalyst Surfaces by Gas Chemisorption," Journal of Colloid and Interface Science, Vol. Vol. 34, No. 3, November 1970.
- (6) Butt, J.B., "Thermal Conductivity of Porous Catalysts," AIChE Journal, Vol. II, p 106-12 Ja65.
- (7) Caldwell, A.D. and Calderbank, P.H., "Catalyst Dilution - A Means of Temperature Control in Packed Tubular Reactor," British Chem. Eng. IV, Vol. 14, No. 9, September 1969.
- (8) Carberry, J. J. and Goring, R.L., "Time-Dependent Pore-Mouth Poisoning of Catalysts," Journal of Catalysis 5, 529-543 (1966).
- (9) Carberry, J.J., "Heat and Mass Diffusional Intrusions in Catalytic Reactor Behavior," Catalysis Reviews, Vol. 3, p 61-91 (1969).
- (10) Cambell, J.S., "Influence of Catalyst Formulation and Poisoning on the Activity and Die-Off of Low Temperature Shift Catalysts," Ind. and Eng. Chem. Process Designs 9:588-95, 0 1970.
- (11) Chaplin, L.K., "Fundamental Stress-Strain Paths in Granular Materials Sheared with Small or No Volume Change," Proceedings of Sixth Int. Conference on Soil Mechanics, 1965.
- (12) Chu, C., "Effect of Adsorption on the Fouling of Catalyst Pellets," Industrial and Engineering Chemistry Fundamentals 7;p 507. August 1968.

- (13) Cusmano, J.A. and Low, J.D., *J. Catalysis*, p 798, 1970.
- (14) Dobkina, E.I., et al., "Determination of Wearability of Catalysts," *Kinetics and Catalysis*, Vol. 11 (3), p 771-4, 1970.
- (15) Emelianova, G.I. and Hassan, S.A., "About the Anomalous Character of Sintering of Supported Catalysts," 4th International Congress on Catalysis, Moscow, 6/23-29/68.
- (16) Ervin, M.A. and Luss, D., "Effect of Fouling of Adiabatic Packed Bed Reactors," *AIChE Journal* 16:979-84, November 1970.
- (17) Esso Research Report 3GE. 72, "Proposed Mechanism for Catalyst Break-Up in Cyclic Processes." (Unpublished)
- (18) Gloria, F., "Poisoning of Porous Catalyst Particles," *Industrial and Engineering Chemistry (Fundamentals)* 10 204-11 Ny 71.
- (19) Greer, H., "Vacuum Start Up of Reactors for Catalytic Decomposition of Hydrazine," *J. Spacecraft and Rockets*, Vol. 7, 522-8 (1970).
- (20) Griffith, R.M., "Silica and Alumina Powders Coherence and Strength of Composites," *Canadian Journal of Chemical Engineering* 44:111-16, April 1966.
- (21) Gwyn, J.E., "Particle Size Distribution Function and the Attrition of Cracking Catalysts," *AIChE Journal*, 15, 35, Ja 1969.
- (22) Harriott, P., "Diffusion Effects in the Preparation of Impregnated Catalysts," *Journal of Catalysis*, Vol. 14, 43-48 (1969).
- (23) Hasselman, D.P.H., "Relationship Between Macroscopic Shear Moduli and Micro-Mechanical Shear Stress," *Journal of American Ceramic Society*, Vol. 50 (6), p 331-2, 1967.
- (24) Hlorns, F.J. and Venables, J., "Controlled Fracture of Brittle Solids," *British Coal Utilization Research Association Monthly Bulletin*, Vol. XXVI, No. 3, March 1962.
- (25) Hughs, R. and Shethgar, V.R., "Regeneration of Silica-Alumina Catalyst Particles," *Journal Applied Chem. and Biotech.* 21, p 35, February 1971.
- (26) Huxtable, D.D., Capt. USAF, "Hydrazine Catalyst Evaluation," Technical Report AFRPL-TR-70-107, November 1970.

- (27) Ioffe, I.I., et al., "Fundamentals of the Theory of Chemical Reactor Reliability. III Methods of Calculating the Life of Industrial Catalysts," Chem. Tech., Vol. 23 (6), p 330-1, 1971.
- (28) Kehoe, J.P., "The Interactions of Inter- and Intrapphase Gradients," In a Diffusion Limited Exothermic Catalytic Reaction, AIChE Journal, Vol. 18, No. 2, p 347-55, March 1972.
- (29) Kenney, C.H. and Shah, Y.T., "Effectiveness Factors and Transient Behavior in Gas-Liquid Catalyst Systems," Chemical Engineering Science, Vol. 28, No. 1, p 325-28, January 1973.
- (30) Keston, A.S., "A Conceptual Model of Hydrazine Catalytic Reactor Washout Caused by Decomposition Product Poisoning and Pressure Build-Up," Paper in 1972 JANNAF Propulsion Meeting, CPIA No. 228, Vol. IV, December 1972.
- (31) Keston, A.S., "Integral Equation Method for Evaluating the Effects of Film and Pore Diffusion of Heat and Mass on Reaction Rates in Porous Catalyst Particles," AIChE Journal, Vol. 15, p 128, January 1969.
- (32) Keston, A.S., "Turbulent Diffusion of Heat and Mass in Catalytic Reactors for Hydrazine Decomposition," AIAA Paper 69-421, 1969.
- (33) Keston, A.S., "Analytical Study of Catalytic Reactors for Hydrazine Decomposition (V)," Hydrazine Monopropellant Technology Symposium, Johns Hopkins University, 1967.
- (34) Lee, J.C.M., "Stability of An Exothermic Reaction Inside a Catalytic Slab with External Transport Limitations," Industrial Engineering Chemistry Fundamentals 11: p 117-22, February 1972.
- (35) Levy, R.M., et al., "Effect of Thermal Aging on the Physical Properties of Activated Alumina," Industrial and Engineering Chemistry Product Research and Development, 7:217-20, S 1968.
- (36) Levy, R.M. and Bauer, D.S., "The Effect of Foreign Ions on the Stability of Activated Alumina," Journal of Catalysis, Vol. 9, p. 78-86, 1967.
- (37) McCullough, F., Jr., Engine Life Considerations Paper at 1972 JANNAF Propulsion Meeting, November 1972, CPIA Pub. No. 228, Vol. IV, December 1972.
- (38) Miller, M.R. and Wilhoyte, H.S., "Study of Catalyst Support Systems for Fume Abatement of Hydrocarbons," Air Pollution Control Association J, p 791, December 1967.
- (39) Mischke, R.A. and Smith, J.M., "Thermal Conductivity of Alumina Catalyst Pellets," Industrial Engineering Chemistry Fundamentals, Vol. 1, 288-92, 1962.

- (40) Morita, N. and Kumazawa, "The Effective Diffusion Coefficients in a Porous Catalyst Pellet," 5th Society of Chemical Engineering, Japan Autumn Meeting, Journal of Chemical Engineering, Japan, Vol. 5, No. 4, 375-80, December 1972.
- (41) Myers, C.G., et al., "Aging of Platinum Reforming Catalysts," Ind. and Eng. Chemistry, Vol. 53:299, April 1961.
- (42) Newkirk, A.E. and Mikie, D.W., "Thermal Decomposition of Rhodium, Iridium and Ruthenium Chlorides," Journal of Catalysis, Vol. 11, p 370-377 (1968).
- (43) Omata, H. and Brown, L.F., "The Dusty Gas Diffusion Equation in Catalyst Pores Smaller than 50Å. Radius," AIChE Journal, Vol. 18, No. 5, p 967-75, September 1972.
- (44) Osteen, S., "Significance of Pressure Gradients in Porous Materials," AIChE Journal, Vol. 11:439-45, May 1965.
- (45) Paranski¹, S.A., et al., "Evaluation of the Abrasion Resistance of Catalysts," Kinetics and Catalysis, Vol. 9, p 1072, 1968.
- (46) Physical Properties of the Platinum Metals, The Rare Metals Handbook.
- (47) Prater, C.D., "The Temperature Produced by Heat of Reaction in the Interior of Porous Particles," Chemical Engineering Science, Vol. 8, p 284-286, 1958.
- (48) Ramsen, J.H. and Hill, P.B., Industrial and Engineering Chemistry, Vol. 50, p 117-24, January 1958.
- (49) Rebinder, P.D., et al., "Mechanical Density in Porous Dispersion Bodies," Doklady Akad. Nauk, SSSR, Vol. 154 (3), p 695, 1964.
- (50) Resen, L., "Catalyst Erosion in Cat-Crackers Case Histories of Its Control," Oil and Gas Journal, Vol. 55, p 101, December 9, 1957; Vol. 61, 3 December 16, December 23, 1957; Vol. 56, p 106, January 6, 1958.
- (51) Reuschussel, A.M., et al., "Application of Scanning Electron Microscopy to the Study of the Morphology of Multicomponent Catalyst Systems," Journal of Materials Science, Vol. 4, No. 10, 885-9, 1969.
- (52) Roberts, J.E. and Souza, "The Compressibility of Sands," ASTM Proceedings, Vol. 58, p 1269, 1958.
- (53) Ruchenstein, E. and Petty, C.A., "On the Aging of Supported Metal Catalyst Due to Hot Spots," Chemical Engineering Science, Vol. 27, p 937, 1972.
- (54) Russell, A.S. and Cochran, C.N., "Surface Areas of Heated Alumina Hydrates," Industrial and Engineering Chemistry, Vol. 42 (1950).

- (55) Russell, A.S., "Alumina Properties," Technical Paper No. 10, Aluminum Company of America.
- (56) Sagara, M., "Effect of Non-isothermal Operation in Catalyst Fouling," AIChE Journal, Vol. 13, 1226-9, N 1961.
- (57) Sangiovanni, J. J. and Keston, A.S., "Study of Hydrazine Reactor Vacuum Heat Characteristics," United Aircraft Research Laboratories Report H910758, Contract WAS-7-696, December 1969.
- (58) Sangiovanni, J. J. and Keston, A.S., "Motion Picture Studies of the Startup Characteristics of Liquid Hydrazine Catalytic Reactors," Paper No. 71-702, AIAA/SAE 7th Propulsion Joint Specialist Conference, Salt Lake City, Utah, June 14-18, 1971.
- (59) Sayer, C.F., "The Decomposition of Hydrazine on Shell 405 Catalyst," AIAA Paper No. 70-606, 1970.
- (60) Shackner, H., "Structure and Activity of Platinum-Silica Catalysts Prepared by a Combustion Process," Journal of Applied Chemistry, Vol. 19, p 68-72, March 1969.
- (61) Shaw, G.Y. and Parsons, B.I., "Low Density Catalysts and Catalyst Supports II," Canadian Mines Branch of Research and Development Report R230, 1970.
- (62) Shchukin, E.D., "Mechanical Strength of Porous Disperse Bodies", Abh. Deut. Akad. Wiss. Berlin Kl. Chem. Geol. Biol., Vol. 5, p 89-91, 1968.
- (63) Shirasaki, T., et al., "Preparation of Catalyst and Support by Grinding," Kogyo Kagaku Zasshi, Vol. 9, No. 71, p 1313-8, 1968.
- (64) Shean-Liu, Li, "The Influence of Intraparticle Diffusion in Fixed Bed Catalytic Reactors," AIChE Journal, Vol. 16, No. 5, p 747, September 1970.
- (65) Sohn, H.Y., "On the Maximum Temperature Rise in Gas-Solid Reactions," AIChE Journal, Vol. 19, No. 1, p 191-3, January 1973.
- (66) Stumpf, H.C., et al., "Thermal Transportations of Aluminas and Alumina Hydrates," Industrial and Engineering Chemistry, Vol. 42, No. 7, July 1950.
- (67) Voge, H.H., Development of Catalyst for Monopropellant Hydrazine, Final Report, Contract WAS 7-97 Shell Development Company, Report No. S-13889, June 1963.
- (68) Wei, J., Chemical Engineering Science, Vol. 21, p 1171, 1966.
- (69) Williams, K.F. and Matthews, J.C., "Catalyst Activity and Performance of Stability Limited Fixed Bed Reactors," Industrial and Engineering Chemical Process Design 10, 483-9, October 1971.

- (70) Wolfe, S. Cr. "Catalyst Handbook, "Imperial Chemical Industries Limited, 1970, SBN 723401640, London.
- (71) Wood, S. E. and Bryant, J. T., "Decomposition of Hydrazine on Shell 405 Catalyst at High Pressure," Ind. Eng. Chemistry (Prod. Res. Dev.), Vol. 12, No. 2, 1973.
- (72) Fredrickson F. N. "Reaction Engine Module Test Evaluation," Report No. AFRPL-TR-72-44 AFRPL, USAF, Edwards, California July, 1972.
- (73) Neuton, N.C., Rice, P.R., Jr. and Huxtable, D. D., "Shell 405 Catalyst Improvement, Substrate Evaluation, Phase 1", July 1970 to April 1971, Report AFRPL-TR-71-81, AFRPL, USAF, Edwards, California, July 1972.
- (74) Fredrickson, F. N., "75-lbf. PBPS Monopropellant Engine Test and Evaluation", Report No. AFRP-TR-72-1, AFRPL, USAF, Edwards, California, June 1972.
- (75) Sayer, C.F. and Southern, G. R., "The Comparative Testing of the Shell 405, CNESRO-1 and RPE 72/1 Hydrazine Decomposition Catalysts" Ministry of Defense, Rocket Propulsion Establishment, Westcott Aylesburn, Buckinghamshire, England.
- (76) Ellison, M.F., and Frizell, D.P., and Meese, R.A., "Hydrazine Thrusters-Present Limitations and Possible Solutions" AIAA/SAE 9th Propulsion Conference, Las Vegas, Nevada, November 5-7, 1973.
- (77) Russi, M.S., "A Survey of Monopropellant Hydrazine Thruster Technology AIAA/SAE 9th Propulsion Conference Las Vegas, Nevada, November 1973, Paper No. 73-1263.
- (78) King, S.M., Max, P.C. and Taylor, D., "The Aerospace Corporation, Shell 405 Catalyst Evaluation Program Vol. I: Physical and Catalytic Properties", Report TR-0066 (5210-4) The Aerospace Corp., El Segundo, August 1969).
- (79) Shmitz, B., and Wilson, W. W., "Long-Life Monopropellant Hydrazine Engine Development Program", Final Report AFRPL TR-11-103, September, 1971.
- (80) Carlson, R.A., Blumenthal, J. L., Grassi, R. J., "Space Environment Operation of Experimental Hydrazine Reactors" Final Report No. 4715.3.68-27, Contract NAS7-520, July 1968.

- (81) Christopher, G. and Russell, S. "Effects of Hydrazine Contaminants on Catalyst Life", AIAA/SAE 9th Propulsion Conference, Las Vegas, November, 1973.
- (82) Moynihan, P.I., Bjorklund, R.A., "Performance Characterization Tests on Three Hydrazine Catalytic Thrusters" NASA Technical Report 32-1584.
- (83) Barclay, L.P., Capt., USAF "Transtage Catalyst Evaluation" AFRPL-TR-69-140, June, 1969.
- (84) Greer, H.G., "An Investigation of the First Pulse Characteristics of Monopropellant Hydrazine Reactors" Technical Report TR-0066 (5305)-1, July, 1961.
- (85) Traina, F. and Pernicone, N., 20th Int. Ind. Catal. Congr. (Milan 5/19-21/69) Chim Ind. (milan) 52 #1:1-12, Jan., 1970.
- (86) Papmahl, F. and Rose, H.F., Ind. Eng. Chem., Prod. Res. Development 8 #4:352-58, December, 1969.
- (87) Basmadjian, D., "Venting of High Pressure Fixed-Bed Catalytic Reactors", Canadian Journal of Chemical Engineering 42 #3:104-6, June, (1964).
- (88) Paranskii, S.A., Mechiedeva, et al., "The Evaluation of Catalyst Strength Under Condition of Attrition" Kinet. Katal 12 #2:473-79 (June 1971).
- (89) Smith, O.I. and Solomon, W.C., "Kinetics of Hydrazine Decomposition and Iridium and Alumina Supported Indium Catalysts" AFRPL-TR-73-59.
- (90) Petty, W. L., "Variation in Shell 405 Catalyst Physical Characteristics, Test Catalyst Preparation" AFRPL-TR-73-56 Final Report, May 72-May 73.
- (91) Beaver, E.R., Collier, C.L. and Murrell, C.R., ACS Pet. Div. Preprints 18, #4, 726 (1973).
- (92) Adams, A.R., Sartor, A.F. and Welch, J.G., Chemical Engineering Progress 71, 35 (1975).
- (93) Davies, O.L., "Statistical Methods in Research and Production," Chapter 6, Hafner Publishing Company, N.Y., 1958.
- (94) Cordfunke, E.H.P. and Meyer, G., Recueil Trav. Chim. 81, 495 (1962).
- (95) Cordfunke, E.H.P. and Meyer, G., Recueil Trav. Chim. 81, 670 (1962).
- (96) Alcoch, C.B., Platinum Metals Review, 5, (1961).
- (97) Alcoch, C.B. and Hooper, G.W., Proc. Royal Society, A254, 551 (1960).

- (99) Jortner, J., MDAC. Private communication.
- (100) Taylor, W. F., and Webber, W. T., Interim Report "External Catalyst Breakup Phenomena AFRPL-TR-75-44, September 1975.
- (101) Timoshenko, S. and Goodier, J. N., Theory of Elasticity. Second Edition. McGraw-Hill Book Company, New York, 1951.
- (102) Babel, H. W. and Sines, G., A Biaxial Failure Criterion for Porous Brittle Materials. Transactions of the ASME, Journal of Basic Engineering. Page 285-291. June 1968.
- (103) Schneider, P. J., Temperature Response Charts. John Wiley & Sons, New York, 1963.
- (104) Biot, M. A., Theory of Elasticity and Consolidation of a Porous Anisotropic Solid, Journal of Applied Physics, Volume 25, No. 2 February 1955.
- (105) Scott, R. R., Principles of Soil Mechanics, Adiston Wesley Publishing Company, Reading, Massachusetts, 1963.
- (106) Babcock, C. D., California Institute of Technology, Private Communication.
- (107) Love, G. H., Stress Produced in a Semi-Infinite Solid by Pressure on Part of the Boundary, Phil. Tran. A228, 1929.
- (108) Miller, R. J., Mechanics of Erosion Phase I, Defense Nuclear Agency, Washington, D. C., DNA 3446F-1, November 1974.
- (109) Kuenzly, J. D., "Study of Monopropellant for Electrothermal Thrusters", TRW Systems Group, Redondo Beach, California, Report 22409-6015-RU-00, June, 1974.
- (110) Marteney, P. J., and Kesten, A. S., "Internal Catalyst Breakup Phenomena, Technical Progress Reports", United Aircraft Research Laboratories, East Hartford, Connecticut, Contract FO4611-74-C-0031 (AFRPL), 1974-1975.
- (111) Brandt, H., A Study of the Speed of Sound in Porous Granular Media, Journal of Applied Mechanics, Vol. 22, No. 4, pp. 479-486, December 1955.
- (112) Fatt, I., Compressibility of a Sphere Pack Comparison of Theory and Experiment, Journal of Applied Mechanics, Vol. 24, No. 1, pp. 140-149, March 1957.
- (113) Hom-Yim Ko and Scott, R. R., Deformation of Sand in Hydrostatic Compression, Journal of Soil Mechanics and Foundation Division Proceedings of the American Society of Civil Engineers, pp. 137-156, May, 1967.

- (114) Scheidegger, A. E., The Physics of Flow Through Porous Media, University of Toronto Press, 1959.
- (115) Muscat, H., Physical Principles of Oil Production, McGraw-Hill Book Co., New York, 1949.
- (116) Amyx, J. W., D. M. Bass, and R. L. Whiting, Petroleum Reservoir Engineering - Physical Properties, McGraw-Hill Book Co., New York, 1960.
- (117) Rapoport, L. A. and W. J. Leas, Relative Permeability to Liquid in Gas-Liquid Systems, Trans. AIME, Vol. 192, 1951.
- (118) Leverett, M. C., Flow of Oil-Water Mixtures Through Unconsolidated Sands, Trans. AIME, 1939, p. 149.
- (119) Klinkenberg, L. J., The permeability of Porous Media to Liquids and Gases, Drilling and Production Practices, p. 200, American Petroleum Institute, 1941.
- (120) Recommended Practice for Determining Permeability of Porous Media, American Petroleum Institute, Division of Production, September 1952.
- (121) Brown, H. W., Capillary Pressure Investigations, Trans. AIME, 1951.
- (122) Leverett, M. C., Capillary Behavior in Porous Solids, Trans. AIME, Vol. 142, p. 152, 1941.
- (123) Rose, Walter, and Bruce, Evaluation of Capillary Characters in Petroleum Reservoir Rock, Trans. AIME, 1949.
- (124) Sangrovanni, J. J. and A. S. Kesten, Study of Hydrazine Reactor Vacuum Start Characteristics, United Aircraft Research Laboratories, Report H910758, December 1969.
- (125) Hoffman, R. J., W. T. Webber, et al., Plume Contamination Effects Prediction - The CONTAM Computer Program - Version II, AFRPL-TR-73-46, August 1973.
- (126) Tamura, Z. and Y. Tanasawa, Evaporation and Combustion of a Drop Contacting with a Hot Surface, Seventh Symposium (International) on Combustion, Butterworths, London, 1959.
- (127) Bernath, L., A Theory of Local-Boiling Burnout and its Application to Existing Data, Chem. Eng. Prog. Symposium Series 56, No. 30, 95-110, 1960.
- (128) Tong, L. S., Boiling Heat Transfer and Two-Phase Flow, John Wiley and Sons, 1965.

- (129) Nielson, J. H. and Gilchrist, A., "Erosion by a Stream of Solid Particles," *Wear*, 11 (1968), 111-122.
- (130) English, W. D. and Samuel, Jr., H. D., "Failure Mechanism of Attitude Control System Valve in Chlorine Pentafluoride Service, AFML-TR-71-94, McDonnell Douglas Corporation, July, 1971.
- (131) Rabinowicz, E., "Friction and Wear of Materials", John Wiley and Sons, New York, 1965.
- (132) Fancher, G. H., Lewis, J. A., and Barnes, K. B., "Some Physical Characteristics of Oil Sands", *Penn. State Coll. Bull.* 12, 1933.
- (133) Lapple, C. E. "Fluid and Particle Mechanics" University of Delaware Press, 1954, page 292.
- (134) Lowrison, G. C., "Crushing and Grinding--The Size Reduction of Solid Materials" CRC Press, Cleveland, Ohio, 1974, p. 76.
- (135) Hill, R., "The Mathematical Theory of Plasticity", Oxford The Clarendon Press, P. 317 (1950).
- (136) Hoffman, O., "The Brittle Strength of Orthotropic Materials," *J. Composite Materials*, Vol. 1, p. 200 (1967).
- (137) Goldenblat, I. I., Kopnov, V. A., "Strength of Glass-Reinforced Plastics in the Complex Stress State", *Mekhanika Polimerov*, Vol. 1, p. 70 (1965; English translation: *Polymer Mechanics*, Vol. 1, p. 54) 1966, pub. Faraday Press.
- (138) Ashkenazi, E. K., "Problems of the Anisotropy of Strength", *Mekanika Polimerov*, Vol. 1, p. 79 (1965; English translation: *Polymer Mechanics*, Vol. 1, p. 60 (1966), pub. Faraday Press.
- (139) Tsai, S. W., Wu, E. M., "A General Theory of Strength for Anisotropic Materials", *J. Composite Materials*, Vol. 5, January 1971, p. 58.
- (140) Priddy, T. G., "A Fracture Theory for Brittle Anisotropic Materials", Sandia Laboratories, November, 1971.
- (141) Mair, W. M., "Fracture Criteria for Cast Iron Under Biaxial Stress", *J. of Strain Analysis*, Vol. 3, No. 4, p. 254, (1968).
- (142) Miller, R. J., *Mechanics of Erosion-Phase 1*, Defense Nuclear Agency Report DNA 3446F-1, 13 November 1974.
- (143) Purcell, W. R., *Capillary Pressures--Their Measurement Using Mercury and the Calculation of Permeability Therefrom*, Trans. AIME, 1949.

- (144) Burdine, N. T., Gournay, L. S. and Reicherty, P.O., Pore Size Distribution of Reservoir Rocks, Trans. AIME, 1950.
- (145) Hassler, G. L., Rice, R. R. and Leeman, E. H., Investigations on the Recovery of Oil from Sandstones by Gas Drive, Trans. AIME, Vol. 118, p. 116, 1936.
- (146) Johnson, E. F., Bossler, D. P., and Naumann, V. O., Calculation of Relative Permeability from Displacement Experiments, J. of Pet. Tech. p. 61, (January, 1959).
- (147) Welge, H. J. and Bruce, W. A., The Restored State Method for Determination of Oil in Place and Connate Water, Drilling and Production Practices, American Petroleum Institute, 1947.
- (148) Buckley, S. E. and Leverett, M. C., Mechanism of Fluid Displacement in Sands, Trans. AIME. Vol. 146, p. 107, 1942.
- (149) Fayers, F. J. and Sheldon, J. W., The Effect of Capillary Pressure and Gravity on Two-Phase Flow in a Porous Medium, Petroleum Transactions, AIME, Vol. 216, 1959.
- (150) Kesten, A. S., Internal Catalyst Breakup Phenomena; Contract FO4611-74-C-0031, R&D Status Reports, United Aircraft Research Laboratory, 1975.
- (151) Moseley, V. A., et.al., Long Life Monopropellant Design Criteria, Contract FO4611-73-C-0044, R&D Status Reports, Bell Aerospace Company, 1974-75.

APPENDIX A

HSGET DATA ON THE EFFECT OF GAS EROSION
AT 250 FEET PER SECOND(a)

Fresh Shell 405 1/8" x 1/8" Cylinders

<u>Pellet</u>	<u>Initial</u> <u>Weight, grams</u>	<u>Final</u> <u>Weight, grams</u>	<u>Weight Change</u> <u>grams</u>
1	.04937	.04795	-.00142
2	.05055	.04857	-.00198
3	.04723	.04559	-.00164
4	.05288	.05116	-.00172
5	.04900	.04774	-.00126

Fresh Shell 405, 8-12 Mesh Particles

<u>Particle</u>	<u>Initial</u> <u>Weight, grams</u>	<u>Final</u> <u>Weight, grams</u>	<u>Weight Change</u> <u>grams</u>
1	.01295	.01337	+.00042
2	.02177	.02160	-.00017
3	.01253	.01234	-.00019
4	.01345	.01321	-.00024
5	.01761	.01684	-.00077

Fresh Shell 405, 14-18 Mesh Particles

<u>Particle</u>	<u>Initial</u> <u>Weight, grams</u>	<u>Final</u> <u>Weight, grams</u>	<u>Weight Change</u> <u>grams</u>
1	.00200	.00210	+.00010
2	.00363	.00360	-.00003
3	.00331	.00335	+.00004
4	.00241	.00233	-.00008
5	.00284	.00277	-.00007

Fresh Shell 405, 20-25 Mesh Particles

<u>Particle</u>	<u>Initial</u> <u>Weight, grams</u>	<u>Final</u> <u>Weight, grams</u>	<u>Weight Change</u> <u>grams</u>
1	.00104	.00107	+.00003
2	.00087	.00091	+.00004
3	.00079	.00091	+.00012
4	.00080	.00089	+.00009
5	.00108	.00112	+.00004

APPENDIX A (Cont'd.)

Fresh Shell 405, 25-30 Mesh Particles

<u>Particle</u>	<u>Initial Weight, grams</u>	<u>Final Weight, grams</u>	<u>Weight Change grams</u>
1	.00068	.00093	+.00025
2	.00080	.00085	+.00005
3	.00083	.00074	-.00009
4	.00099	.00090	-.00009
5	.00068	.00072	+.00004

Fresh Shell 405, 20-30 Mesh Particles

<u>Particle</u>	<u>Initial Weight, grams</u>	<u>Final Weight, grams</u>	<u>Weight Change grams</u>
1	.00058	.00079	+.00021
2	.00062	.00055	-.00007
3	.00098	.00101	+.00003
4	.00095	.00078	-.00017
5	.00048	.00050	+.00002

(a) Nitrogen flowing at 250 feet per second, 1700°F, specimens in preheated tube for 1 hour total. All catalyst specimens dried overnight in a vacuum oven at 110°C and 120 mm hg total pressure before weighing.

APPENDIX B

HSGET DATA ON THE EFFECT OF GAS EROSION
AT 110 FEET PER SECOND (a)

Fresh Shell 405 1/8" x 1/8" Cylinders

<u>Pellet</u>	<u>Initial weight,</u> <u>grams</u>	<u>Final weight,</u> <u>grams</u>	<u>Weight change,</u> <u>grams</u>
1	.05311	.05220	-.00091
2	.05103	.04975	-.00128
3	.05178	.05041	-.00137
4	.04986	.04810	-.00176
5	.05041	.04889	-.00151

Fresh Shell 405 14-18 Mesh Particles

<u>Particle</u>	<u>Initial weight,</u> <u>grams</u>	<u>Final weight,</u> <u>grams</u>	<u>Weight change,</u> <u>grams</u>
1	.00400	.00424	+.00024
2	.00652	.00675	+.00023
3	.00214	.00220	+.00006
4	.00491	.00503	+.00012
5	.00434	.00439	+.00005

Fresh Shell 405 25-30 Mesh Particles

<u>Particle</u>	<u>Initial weight,</u> <u>grams</u>	<u>Final weight,</u> <u>grams</u>	<u>Weight change,</u> <u>grams</u>
1	NA	NA	NA
2	.00058	.00066	+.00008
3	.00065	.00067	+.00002
4	.00055	.00070	+.00015
5	.00056	.00059	+.00003

(a) Nitrogen flowing at a superficial velocity of 110 feet per second, 1700°F, specimens in preheated tube for 1 hour total. All catalyst specimens dried overnight in a vacuum oven at 110°C and 120 mm Hg total pressure before weighing.

APPENDIX C

HSGET DATA ON THE EFFECT OF GAS EROSION
AT 50 FEET PER SECOND (a)

Fresh Shell 405 1/8" x 1/8" Cylinders

<u>Pellet</u>	<u>Initial weight, grams</u>	<u>Final weight, grams</u>	<u>Weight change, grams</u>
1	.04949	.04844	-.00105
2	.05002	.04826	-.00174
3	.04952	.04755	-.00197
4	.05015	.04824	-.00191
5	.05382	.05220	-.00162

Fresh Shell 405 25-30 Mesh Particles

<u>Particle</u>	<u>Initial weight, grams</u>	<u>Final weight, grams</u>	<u>Weight change, grams</u>
1	.00079	.00074	-.00005
2	.00067	.00075	+.00008
3	.00076	.00074	-.00002
4	.00105	.00102	-.00003
5	.00038	.00055	+.00017

- (a) Nitrogen flowing at a superficial velocity of 50 feet per second, 1700°F, specimens in preheated tube for 1 hour total. All catalyst specimens dried overnight in a vacuum oven at 110°C and 120 mm Hg total pressure before weighing.

APPENDIX D

ANALYSIS OF PERCENTAGE WEIGHT CHANGE RESULTS FROM GAS EROSION DATA IN HSGT

Gas Velocity	Fresh Shell 405 Catalyst	Percentage Change in Weight			
		Individual Rate	Mean	Standard Deviation	Standard Error
110 feet per second	1/8" x 1/8" Pellets	- 1.71	- 2.68	0.67	0.30
		- 2.51			
		- 2.64			
		- 3.53			
		- 3.02			
"	14-18 Mesh	+ 6.00	+ 3.18	1.79	0.80
		+ 3.53			
		+ 2.80			
		+ 2.44			
		+ 1.15			
"	25-30 Mesh	+13.80	+12.38	10.96	5.84
		+ 3.80			
		+27.30			
		+ 5.36			
50 feet per second	1/8" x 1/8" Pellets	- 2.12	- 3.28	0.75	0.33
		- 3.48			
		- 3.98			
		- 3.81			
		- 3.01			
"	25-30 Mesh	- 6.33	+ 8.96	21.18	9.47
		+11.94			
		- 2.63			
		- 2.86			
		+44.70			
250 feet per second	1/8" x 1/8" Cylinders	- 2.88	- 3.22	0.529	0.237
		- 3.94			
		- 3.40			
		- 3.26			
		- 2.57			
	8-12 Mesh	+ 3.24	- 1.04	2.75	1.23
		- 0.78			
		- 1.52			
		- 1.78			
		- 4.38			
	14-18 Mesh	+ 5.00	0.07	3.30	1.47
		- 0.83			
		+ 1.21			
		- 3.32			
		- 2.46			
		- 370 -			

APPENDIX D (Cont'd.)

<u>Gas Velocity</u>	<u>Fresh Shell 405 Catalyst</u>	<u>Percentage Change in Weight</u>			
		<u>Individual Rate</u>	<u>Mean</u>	<u>Standard Deviation</u>	<u>Standard Error</u>
20-25 Mesh		+ 2.88	7.52	5.42	2.42
		+ 4.59			
		+15.19			
		+11.25			
		+ 3.70			
25-30 Mesh		+36.76	5.79	19.08	8.53
		+ 6.25			
		-10.82			
		- 9.10			
		+ 5.88			
20-30 Mesh		+36.20	2.85	20.88	9.34
		-11.28			
		+ 3.07			
		-17.89			
		+ 4.17			

APPENDIX E

ANALYSIS OF VARIANCE(a) OF GAS FLUID DYNAMIC EROSION TEST RESULTS

A. Data:

Weight Change in 10^{-5} Grams

	Superficial Gas Velocity, ft/sec		
	50	110	250
1/8" x 1/8" Cylinders	-105	- 91	-142
	-174	-128	-198
	-197	-137	-164
	-191	-176	-172
	-162	-152	-126
25-30 Mesh Granules	- 5	+ 8	+ 25
	+ 8	+ 2	+ 5
	- 2	+ 15	- 9
	- 3	+ 3	- 9
	+ 17	(+7)	+ 4

B. ANOVA Results

<u>Variance Component</u>	<u>Sum of Squares</u>	<u>Degrees of Freedom</u>	<u>Mean Square</u>
Columns	1,559.267	2	779.633
Replicates	5,634.797	4	1,408.699
Columns x Replicates	1,722.400	8	215.300
Rows	188,972.000	1	188,972.000
Columns x Rows	870.066	2	435.033
Replicates x Rows	2,879.467	4	719.866
Columns x Replicates x Rows	3,404.933	8	425.616
TOTAL	205,042.800	29	

(a) See O.L. Davis, "Statistical Methods in Research and Production", Chapter 6, Hafner Publishing Company, New York, 1958.

APPENDIX F

EFFECT OF WATER CONTENT ON
PARTICLE CRUSHING STRENGTH

ITI Crush Strength Data on As-Is-Specimens

<u>Fresh Shell 405</u> <u>1/8" x 1/8" Cylinders</u>	<u>Fresh Shell 405,</u> <u>14-18 Mesh Granules</u>	<u>Harshaw Al 1602</u> <u>1/8" x 1/8" Cylinders</u>
32.75 lbs	2.80 lbs	25.20 lbs
30.75	2.97	24.10
39.70	1.00	23.50
25.80	1.60	29.10
27.95	1.62	25.00
39.07		21.90
43.12		31.60
38.20		24.80
27.85		21.90
38.62		39.20

ITI Crush Strength Data on Vacuum Oven Dried Specimens (a)

<u>Fresh Shell 405</u> <u>1/8" x 1/8" Cylinders</u> (b)	<u>Fresh Shell 405,</u> <u>14-18 Mesh Granules</u> (c)	<u>Harshaw Al 1602</u> <u>1/8" x 1/8" Cylinders</u> (d)
30.05 lbs	1.43 lbs	29.00 lbs
30.05	2.40	16.15
25.20	2.45	23.26
38.30	1.06	38.20
21.85	0.77	24.10
43.35	0.76	25.80
37.00	1.43	40.50
38.30	0.59	20.00
26.00	1.25	42.40
37.55	3.72	
45.10		
31.20		
46.85		
40.90		
33.00		

- (a) Dried in a vacuum oven overnight at 110°C and 120 mm Hg total pressure.
(b) Average weight loss was 6.04% from as is basis.
(c) Sample showed no average weight loss from as is basis.
(d) Average weight loss was 4.93% from as is basis.

APPENDIX F (Cont'd)

ITI Crush Strength Data on Water Saturated Specimens ^(a)

<u>Fresh Shell 405</u> <u>1/8" x 1/8" Cylinders</u> ^(b)	<u>Fresh Shell 405,</u> <u>14-18 Mesh Granules</u> ^(c)	<u>Harshaw A1 1602</u> <u>1/8" x 1/8" Cylinders</u> ^(d)
30.00 lbs	2.17 lbs	24.00 lbs
39.10	1.74	27.85
41.35	1.53	16.50
42.35	1.61	30.50
28.60	0.89	27.60
38.00	0.85	21.50
34.35	0.44	15.50
20.10	0.69	24.10
35.00	0.35	25.50
39.60	1.46	33.10
36.60		
45.50		
30.60		
32.60		
31.60		

(a) Saturated with water vapor at 80°F and 1 atm total pressure.

(b) Average weight gain was 1.39% from as is basis.

(c) Average weight gain was 12.6% from as is basis.

(d) Average weight gain was 2.59% from as is basis.

APPENDIX G

ITI CRUSH STRENGTH DATA ON FRESH SHELL 405 CATALYST

<u>8-12 Mesh</u>	<u>20-25 Mesh</u>	<u>25-30 Mesh</u>	<u>20-30 Mesh</u>
4.46 lbs	1.340 lbs	0.360 lbs	0.500 lbs
3.05	0.525	1.050	0.865
4.60	0.930	1.060	0.435
1.50	0.300	0.760	0.650
3.84	0.185	0.510	0.780
6.82	2.030	0.650	1.235
6.40	0.950	0.770	0.490
7.08	1.000	0.655	0.400
2.66	0.415	0.715	0.695
2.90	0.615	0.750	0.300
2.42	1.350	0.910	0.660
7.34	0.800	0.520	0.130
2.64	0.905	0.600	0.465
6.76	0.640	0.040	0.430
2.48	0.150	0.410	0.165
7.12	0.600	0.350	0.960
5.00	0.825	0.290	2.000
4.68	0.520	0.210	0.500
3.00	1.080	0.700	0.930
4.24	0.160	0.890	0.840
2.88	0.900	0.580	0.350
2.71	0.400	0.320	0.200
5.40	0.110	0.405	0.430
4.20	0.615	0.250	0.610
4.80	1.075	0.250	0.100

APPENDIX G (Cont'd)

ITI CRUSH STRENGTH DATA ON ALUMINA
SUPPORT BEFORE ATTRITION

<u>8-12 Mesh</u>	<u>14-18 Mesh</u>	<u>20-25 Mesh</u>	<u>25-30 Mesh</u>	<u>20-30 Mesh</u>
1.100 lbs	0.950 lbs	0.100 lbs	0.250 lbs	0.115 lbs
1.020	2.020	0.310	0.695	0.260
3.970	0.080	0.380	0.275	0.335
2.020	0.590	0.012	0.705	0.375
5.190	0.640	0.270	0.220	0.650
0.900	1.585	0.310	0.410	0.215
2.390	0.720	0.640	0.315	0.845
3.800	0.235	0.655	0.320	0.610
2.940	0.710	0.510	0.260	0.285
0.620	1.225	0.050	0.335	0.585
1.720	0.350	0.175	0.415	0.450
1.180	1.250	0.200	0.340	0.645
0.630	0.825	0.495	0.305	0.310
1.100	2.465	0.190	0.190	0.345
2.490	1.550	0.195	0.590	0.450
4.400	0.465	0.195	0.390	0.510
3.330	1.300	0.563	0.180	0.340
1.120	2.530	0.890	0.230	0.350
3.400	1.340	1.075	0.665	0.700
0.620	1.655	0.620	0.365	0.350
2.830	1.235	0.275	0.640	0.750
1.440	0.320	0.330	0.530	0.685
1.200	0.225	0.150	0.395	0.560
2.600	1.610	0.605	0.385	0.340
4.380	1.500	0.475	0.690	0.110

APPENDIX G (Cont'd)

ITI CRUSH STRENGTH DATA ON ALUMINA
SUPPORT AFTER 50% ATTRITION STEP

<u>8-12 Mesh</u>	<u>14-18 Mesh</u>	<u>20-25 Mesh</u>	<u>25-30 Mesh</u>	<u>20-30 Mesh</u>
3.680 lbs	1.915 lbs	0.410 lbs	0.415 lbs	0.485 lbs
2.220	3.345	0.565	0.335	0.260
2.190	2.240	0.600	0.450	0.515
5.050	2.735	0.390	0.950	0.430
4.560	0.730	0.575	0.610	0.625
0.900	0.170	0.085	0.615	0.195
4.425	1.580	0.615	0.485	0.500
3.660	2.310	1.315	0.445	0.345
3.575	1.740	0.300	0.190	0.250
3.410	1.970	1.240	0.300	0.610
4.910	1.150	0.420	0.550	0.150
2.950	3.100	1.410	0.170	0.110
4.875	1.110	1.195	1.020	0.550
3.565	2.830	0.615	1.155	0.260
2.630	2.550	0.360	0.160	0.200
2.715	1.035	1.650	0.275	1.015
2.560	2.580	0.440	0.560	0.625
2.665	1.360	0.290	0.690	0.325
1.680	2.510	0.775	0.345	1.660
3.015	0.775	0.800	0.340	0.290
3.900	2.325	0.720	0.565	0.555
4.500	2.310	0.825	0.270	0.800
0.850	1.230	0.930	0.810	1.005
2.400	0.460	0.550	0.315	0.020
2.170	2.400	0.815	0.560	0.360

APPENDIX H

ITI CRUSH STRENGTH DATA ON USED SHELL 405
CATALYST SAMPLES RECEIVED FROM TRW

<u>1/8" x 1/8"</u> <u>Cylinders (a)</u>	<u>14-18 Mesh</u> (b)	<u>18-20 Mesh</u> (c)	<u>18-20 Mesh</u> (d)
20.60 lbs	0.750 lbs	0.660 lbs	0.740 lbs
15.30	0.385	0.450	0.845
9.50	2.220	0.165	1.210
11.20	3.665	0.850	1.065
40.80	2.145	0.590	1.360
27.80	1.813	0.170	0.410
20.25	0.945	0.805	0.210
21.50	0.915	0.735	0.875
40.80	2.570	0.550	1.830
11.00	1.765		1.630

- (a) Detailed history not available, however, estimated at a few thousand seconds steady state operation.
- (b) Approximately 250 seconds of steady state firing over 51 cold starts.
- (c) Sample saw 84,000 pulses in 5 lbf thruster in November 1972. Sample from downstream end of bed.
- (d) Sample saw 210,000 pulses in 5 lbf thruster in August 1973. Sample from upper portion of bed near the injector.

APPENDIX H (Cont'd)

ITI Crush Strength Data on Used Shell 405 Catalyst From AFRPL (a)

<u>Sample S/N0001</u> <u>50% Attrited</u> <u>25-30 Mesh Size</u>	<u>Sample S/N0002</u> <u>90% Attrited</u> <u>25-30 Mesh Size</u>
0.26 lbs.	0.615 lbs.
0.73	0.555
0.68	0.965
0.475	0.84
0.37	0.31
0.45	1.22
0.665	0.10
0.44	0.75
0.39	0.86
0.11	1.97
0.15	0.76
0.81	0.765
0.38	0.36
0.585	0.71
0.13	1.195
0.18	1.19
0.50	0.365
0.435	0.74
0.58	0.935
0.39	0.78
0.125	0.985
0.485	0.78
0.16	0.77
0.26	1.015
0.37	0.625

(a) Used in a Marquardt 5 lbf thruster, 113,800 pulses,
2,680 seconds total time, 23 cold starts at approximately
40°F.

APPENDIX I

Detailed Crush Strength Measurements on TRW Samples From the "Pop Shock" Tests

Sample Identification	272- 292	292- 321	322- 354	356- 377	378- 386	100 cycles	600 sec. steady state
	0.405 lbs.	0.54 lbs.	0.69 lbs.	0.70 lbs.	0.33 lbs.	0.45 lbs.	0.335 lbs.
	0.29	0.175	0.50	0.235	0.475	0.215	0.295
	0.41	0.375	0.405	2.00	0.39	0.25	0.89
	0.58	1.025	0.66	0.895	0.48	0.89	0.31
	0.70	0.525	0.46	0.115	0.36	0.75	0.70
	0.925	0.54	0.85	0.595	0.385	0.70	0.57
	1.19	0.86	0.575	0.405	0.59	0.25	0.21
	0.96	0.675	0.42	0.44	0.61	0.195	0.56
	0.24	0.495	1.46	0.965	0.86	0.265	1.125
	0.16	0.50	0.39	0.31	0.12	0.935	0.56
	0.89	0.73	0.41	0.35	0.285	0.28	0.50
	0.215	0.43	0.435	1.25	0.39	0.765	0.15
	0.24	0.60	1.055	0.46	0.445	0.66	0.475
	0.16	0.59	0.43	0.845	0.94	0.43	0.415
	0.24	0.52	0.54	0.335	0.31	0.625	0.575
	0.65	0.76	0.295	0.775	0.54	0.305	1.33
	0.25	0.395	0.875	0.40	0.49	1.09	1.125
	0.69	0.355	0.45	0.66	1.06	0.37	0.405
	0.75	0.54	0.50	0.505	0.34	1.115	0.91
	0.66	0.54	0.55	0.32	0.025	1.32	0.725
	0.495	0.30	0.82	0.995	6.75	0.64	0.80
	0.565	0.405	0.425	0.645	0.65	0.195	0.65
	0.29	0.55	0.315	0.35	0.27	0.25	0.2
	0.32	0.50	0.765	0.45	0.41	0.355	0.25
	0.625	0.77	0.92	0.50	0.71	0.765	0.30

APPENDIX I (Cont'd)

**ITI Crush Strength Data on Samples of Catalysts
Used in the TRW Liquid Quench Thermal Shock (LQTS) Tests**

LQTS-1	LQTS-2	LQTS-3	LQTS-4	LQTS-5	LQTS-6	LQTS-7	LQTS-8
14-18 Mesh	14-18 Mesh	14-18 Mesh	14-18 Mesh	25-30 Mesh	25-30 Mesh	25-30 Mesh	25-30 Mesh
Fresh	Fresh	Fatigued	Fatigued	Fresh	Fresh	Fatigued	Fatigued
5 Cycles	25 Cycles	5 Cycles	25 Cycles	5 Cycles	25 Cycles	5 Cycles	25 Cycles
1.895 lbs.	1.16 lbs.	1.26 lbs.	1.66 lbs.	0.31 lbs.	0.22 lbs.	1.28 lbs.	0.76 lbs.
1.49	1.86	1.065	3.345	0.35	0.80	0.55	0.62
2.98	1.825	0.365	2.78	0.365	1.005	0.875	0.445
2.12	0.955	1.085	1.45	0.325	0.59	0.69	0.465
8.76	1.47	1.85	1.75	0.63	0.705	0.655	0.50
1.665	2.07	1.315	2.36	0.78	0.94	0.26	0.31
1.75	1.05	0.71	1.585	0.695	1.185	0.665	0.495
2.075	2.735	1.775	1.915	0.39	0.47	0.84	0.92
1.1	1.20	3.035	0.94	0.58	1.605	0.86	0.635
3.325	0.955	0.96	0.76	0.345	0.525	0.61	0.40
0.275	1.425	0.92	3.53	0.37	0.46	1.01	0.575
1.735	2.265	1.085	1.2	0.19	0.79	0.50	0.825
1.21	0.81	1.79	0.59	0.215	0.84	0.83	1.00
1.46	0.35	1.06	17.1	0.50	0.66	0.45	1.225
1.72	2.90	1.81	2.49	1.445	0.65	0.325	0.36
0.99	9.98	1.755	1.18	0.635	0.855	0.81	1.325
3.31	1.135	0.76	1.45	0.75	0.45	0.55	0.72
2.41	2.235	0.83	2.00	0.49	0.525	1.16	0.17
1.525	2.05	1.28	1.43	0.585	0.95	0.36	0.37
1.22	1.64	4.60	2.175	0.62	0.71	0.375	0.565
1.07	3.09	1.38	2.05	0.83	0.275	0.415	0.42
1.005	1.07	1.485	0.12	0.335	0.9	0.25	0.84
1.49	3.00	2.18	2.16	0.63	0.98	0.93	1.275
1.255	1.865	1.28	0.91	1.115	0.565	0.51	1.33
2.135	0.935	1.23	1.165	0.70	0.65	0.215	0.91

APPENDIX I (Cont'd)

ITI Crush Strength Data on Samples of Catalysts
Used in the TRW Void Volume Abrasion (VVA) Tests

<u>VVA-1</u> <u>14-18 Mesh</u> <u>10% Void</u>	<u>VVA-2</u> <u>14-18 Mesh</u> <u>20% Void</u>	<u>VVA-3</u> <u>25-30 Mesh</u> <u>10% Void</u>	<u>VVA-4</u> <u>25-30 Mesh</u> <u>20% Void</u>
0.365 lbs.	0.935 lbs.	0.675 lbs.	0.90 lbs.
0.80	0.81	0.54	1.00
2.10	2.135	0.96	0.51
1.50	0.98	0.775	0.53
1.635	2.605	1.315	0.585
2.07	2.04	0.165	0.285
4.30	2.36	0.56	0.91
1.35	1.115	0.83	0.40
1.27	4.605	0.41	0.80
1.635	1.335	0.45	0.325
1.11	4.58	0.185	0.62
1.94	0.64	0.725	0.69
2.905	1.785	1.16	2.27
1.16	1.255	0.86	1.095
2.26	2.105	0.095	0.73
0.91	2.85	0.77	0.10
1.55	1.46	0.965	0.48
1.585	2.70	1.11	1.805
1.05	2.45	0.295	1.145
1.015	2.075	0.36	0.91
1.66	1.185	0.415	0.325
2.30	1.18	0.99	0.57
2.26	3.07	0.505	0.41
0.56	0.715	0.87	0.34
1.855	1.14	0.85	0.88

APPENDIX J

Compressive Crushing of 8-12 Mesh Fresh Shell 405 Catalyst in PCMB (1/2" ID)

		Bed Pressure lbs/in ²				
Runs 96-100		25	50	100	200	300
Starting Wt. grams		2.604	2.6024	2.5872	2.5756	2.4316
On 12 Mesh	Grams	2.6024	2.5872	2.5756	2.4316	2.2591
	Wt. %	99.9	99.4	99.6	94.4	92.9
Through 12 Mesh	Grams	0.0006	0.0179	0.0164	0.1446	0.1669
	Wt. %	0.02	0.69	0.63	5.6	6.9
Material Balance %		99.9	100.1	100.2	100.0	99.8
Cumulative Wt. % Through 12 Mesh		0.02	0.71	1.34	6.94	13.84
On 14 Mesh	Grams		0.0149	0.0067	0.1118	0.0802
	Wt. %		0.57	0.26	4.3	3.3
Through 14 Mesh	Grams		0.0030	0.0097	0.0328	0.0867
	Wt. %		0.12	0.37	1.27	3.56
Material Balance %			99.7	100.6	100.2	99.5
Cumulative Wt. % Through 14 Mesh			0.12	0.49	1.76	5.32
On 18 Mesh	Grams			0.0034	0.0110	0.0521
	Wt. %			0.13	0.43	2.14
Through 18 Mesh	Grams			.0063	0.0218	0.0346
	Wt. %			0.24	0.85	1.4
Material Balance %				101.3	100.3	100.2
Cumulative Wt. % Through 18 Mesh				0.24	1.09	2.49
On 25 Mesh	Grams			0.0063	0.0064	0.0132
	Wt. %			0.24	0.25	0.54
Through 25 Mesh	Grams				0.0154	0.0214
	Wt. %				0.6	0.88
Material Balance %				101.5	99.6	101.6
Cumulative Wt. % Through 25 Mesh					0.6	1.48

APPENDIX J (Cont'd)

Compressive Crushing of 8-12 Mesh
Fresh Shell 405 Catalyst in PCMB (1/2" ID)

		Bed Pressure lbs/in ²				
		25	50	100	200	300
Runs 96-100						
On 30 Mesh	Grams				0.0050	0.0047
	Wt. %				0.19	0.19
Through 30 Mesh	Grams				0.0104	0.0167
	Wt. %				0.4	0.69
Material Balance %					99.6	100
Cumulative Wt. % Through 30 Mesh					0.4	1.09
On 35 Mesh	Grams				0.0030	0.0035
	Wt. %				0.12	0.0132
Through 35 Mesh	Grams	0.0006	0.0030		0.0074	0.0132
	Wt. %	0.02	0.12		0.29	0.54
Material Balance %		115.2	96.1		100.9	99.5
Cumulative Wt. % Through 35 Mesh		0.02	0.14		0.43	0.97
Overall Material Balance		99.94	100.1	100.18	100.02	99.59

APPENDIX J (Cont'd)

Compressive Crushing of 14-18 Mesh
Fresh Shell 405 Catalyst in PCMB (1/2" ID)

		Bed Pressure lbs/in ²				
		25	50	100	200	300
01-95						
Starting Weight		2.6001	2.5771	2.5608	2.5384	2.4904
On 18 Mesh	Grams	2.5771	2.5608	2.5384	2.4904	2.4281
	Wt. %	99.1	99.4	99.1	98.1	97.5
Through 18 Mesh	Grams	0.0130	0.0126	0.0187	0.0340	0.0692
	Wt. %	0.5	0.49	0.73	1.34	2.78
Material Balance %		99.6	99.8	99.8	99.4	100.3
Cumulative Wt. % Through 18 Mesh		0.5	0.99	1.72	3.06	5.84
On 25 Mesh	Grams	0.0107	0.0115	0.0130	0.0204	0.0386
	Wt. %	0.4	0.45	0.5	0.8	1.55
Through 25 Mesh	Grams	0.0023	0.0011	0.0057	0.0136	0.0305
	Wt. %	0.09	0.04	0.22	0.55	1.22
Material Balance %		100	0.49	100	99.9	99.8
Cumulative Wt. % Through 25 Mesh		0.09	0.58	0.8	1.35	2.57
On 30 Mesh	Grams			0.0007	0.0024	0.0077
	Wt. %			0.03	0.09	0.31
Through 30 Mesh	Grams			0.0050	0.0112	0.0228
	Wt. %			0.2	0.44	0.92
Material Balance %				101.2	97.4	100.4
Cumulative Wt. % Through 30 Mesh				0.2	0.64	1.56
On 35 Mesh	Grams				0.0025	0.0054
	Wt. %				0.1	0.23
Through 35 Mesh	Grams	0.0023	0.0011	0.0050	0.0087	0.0174
	Wt. %	0.09	0.04	0.2	0.34	0.7
Material Balance %		98.3	106.7	97.6	100.3	99.5
Cumulative Wt. % Through 35 Mesh		0.09	0.13	0.33	0.67	1.37
Overall Material Balance		99.62	99.86	99.36	99.45	100.27

APPENDIX J (Cont'd)

SEQUENTIAL COMPRESSIVE MINI-BED CRUSHING
OF 20-25 MESH FRESH SHELL 405

Series:	-----1-----				-----2-----		
Pressure lb/in ² :	<u>21.9</u>	<u>21.8</u>	<u>200</u>	<u>322</u>	<u>27.4</u>	<u>50</u>	<u>99</u>
Weight in Grams:							
Starting	.9050	.8662	.8414	.8132	.9226	.9080	.8949
On 25 Mesh	.8662	.8414	.8132	.5148	.9080	.8949	.8619
Through 25 Mesh	.0390	.0243	.0245	.2775	.0157	.0115	.0337
Wt. % Through 25 Mesh	4.31	2.81	2.91	34.12	1.70	1.27	3.77
Material Balance	100.9	99.9	99.6	97.4	100.1	99.8	100.0
Cumulative Wt. % Through 25 Mesh	4.31	7.12	10.03	44.15	1.70	2.97	6.74
On 30 Mesh	.0366	.0232	.0165	.0815	.0145	.0091	.0333
Through 30 Mesh	.0024	.0010	.0080	.1825	.0008	.0021	.0004
Wt. % Through 30 Mesh	0.27	0.12	0.95	22.44	0.51	0.23	0.04
Material Balance	100.0	99.8	100.0	95.1	97.5	97.4	100.0
Cumulative Wt. % Through 30 Mesh	0.27	0.39	1.34	23.78	0.51	0.74	0.78

APPENDIX J (Cont'd)

Compressive Crushing of 25-30 Mesh
Fresh Shell 405 Catalyst in PCMB

		Bed Pressure lbs/in ²				
		25	50	100	200	300
Runs 623-116						
Starting Wt. grams		1.005	0.9853	0.9788	0.9733	0.9651
On 30 Mesh	Grams	0.9853	0.9788	0.9733	0.9651	0.9648
	Wt. %	98.5	99.3	99.4	99.2	99.97
Through 30 Mesh	Grams	0.0110	0.0058	0.0042	0.0056	.0066
	Wt. %	1.10	0.59	0.43	0.58	0.70
Material Balance %		99.6	99.9	99.87	99.7	100.6
Cumulative Wt. % Through 30 Mesh		1.10	1.69	2.12	2.68	3.38
On 35 Mesh	Grams	0.0107	0.0052	0.0033	0.0040	0.0031
	Wt. %	1.1	0.53	0.34	0.41	0.32
Through 35 Mesh	Grams	0.0003	0.0006	0.0009	0.0016	0.0035
	Wt. %	0.03	0.06	0.09	0.16	0.36
Material Balance %		99.5	99.8	99.79	99.2	97.7
Cumulative Wt. % Through 35 Mesh		0.03	0.61	0.70	0.86	1.22
Overall Material		99.6	99.9	99.87	99.7	100.6

APPENDIX J (Cont'd)

SEQUENTIAL COMPRESSIVE MINI-BED CRUSHING
OF 25-30 MESH FRESH SHELL 405

Pressure lb/in ² :	<u>25</u>	<u>44.9</u>	<u>97.9</u>	<u>204</u>	<u>324</u>
Weight in Grams:					
Starting	.9257	.9218	.9227	.9193	.9122
On 30 Mesh	.9218	.9227	.9193	.9122	.8964
Through 30 Mesh	.0043	.0006	.0023	.0064	.0118
Weight % Through 30 Mesh	0.47	0.07	0.25	0.70	1.29
Material Balance	100.0	100.1	99.9	99.9	99.6
Cumulative Wt. % Through 30 Mesh	0.47	0.54	0.79	1.79	2.78

APPENDIX J (Cont'd)
Compressive Crushing of 20-30 Mesh
Fresh Shell 405 Catalyst in PCMB

		Bed Pressure lbs/in ²				
		25	50	100	200	300
Runs 623-111						
Starting Wt. grams		1.0003	0.9730	0.9368	0.9261	0.9181
On 30 Mesh	Grams	0.9730	0.9368	0.9261	0.9181	0.9028
	Wt. %	97.3	96.3	98.8	99.1	98.3
Through 30 Mesh	Grams	0.0241	0.0297	0.0105	0.0097	0.0122
	Wt. %	2.4	3.0	1.1	1.0	1.3
Material Balance %		99.7	99.3	99.9	100.2	99.7
Cumulative Wt. %						
Through 30 Mesh		2.4	5.4	6.5	7.5	8.8
On 30 Mesh	Grams	0.0235	0.0270	0.0098	0.0091	0.0109
	Wt. %	2.3	2.77	1.0	0.98	1.2
Through 30 Mesh	Grams	0.0006	0.0027	0.0007	0.0006	0.0013
	Wt. %	0.06	0.28	0.07	0.06	0.14
Material Balance %		100.4	101.7	101.9	104.7	102.2
Cumulative Wt. %		0.06	0.34	0.44	0.50	0.64
Overall Material Balance		99.7	99.3	99.9	100.2	99.7

APPENDIX K

Compressive Crushing of Used S/N001 50% Attrited 25 to 30 Mesh Shell 405 Catalyst in PCMB

		Bed Pressure lbs/in ²				
Runs 623-142		25	50	100	200	300
Starting Wt. grams		1.0004	0.9608	0.9231	0.9032	0.8523
On 30 Mesh	Grams	0.9608	0.9231	0.9032	0.8523	0.8324
	Wt. %	96.04	96.1	97.84	94.36	97.66
Through 30 Mesh	Grams	0.0381	0.0384	0.0195	0.0510	0.0193
	Wt. %	3.81	3.4	2.1	5.6	2.26
Material Balance %		99.85	100.0	99.96	100.0	99.93
Cumulative Wt. % Through 30 Mesh		3.81	7.21	9.31	14.91	17.17
On 35 Mesh	Grams	0.0368	0.0371	0.0183	0.0467	0.0151
	Wt. %	3.68	3.86	1.98	5.2	1.77
Through 35 Mesh	Grams	0.0013	0.0013	0.0012	0.0043	0.0042
	Wt. %	0.13	0.14	0.13	0.48	0.49
Material Balance %		99.85	100.1	99.96	100.0	99.93
Cumulative Wt. % Through 35 Mesh		0.13	0.27	0.40	0.88	1.37

APPENDIX K (Cont'd)

Compressive Crushing of Used S/N002 90% Attrited
25 to 30 Mesh Shell 405 Catalyst in PCMB

		Bed Pressure lbs/in ²				
Runs 623-147		25	50	100	200	300
Starting Weight, grams		1.0007	0.9104	0.8667	0.7988	0.7752
On 30 Mesh	Grams	0.9104	0.8667	0.7988	0.7752	0.7568
	Wt. %	90.98	95.2	92.16	97.0	97.86
Through 30 Mesh	Grams	0.0889	0.0437	0.0677	0.0240	0.0169
	Wt. %	8.86	4.8	7.8	3.0	2.2
Material Balance %		99.86	100.0	99.98	100.0	99.8
Cumulative Wt. % Through 30 Mesh		8.88	13.68	21.48	24.48	26.68
On 35 Mesh	Grams	0.0879	0.0437	0.0672	0.0231	0.0159
	Wt. %	8.78	4.8	7.8	2.9	2.0
Through 35 Mesh	Grams	0.0010	0	0.0005	0.0009	0.0010
	Wt. %	0.1	0	.06	0.11	0.13
Material Balance %		99.86	100.0	99.98	100.0	99.8
Cumulative Wt. % Through 35 Mesh		0.1	0.1	0.16	0.27	0.40

APPENDIX L

FRESH SHELL 405 PARTICLE FLUIDIZATION EXPERIMENTAL DATA

Minimum Inlet Distributor Superficial Velocity
For Particle Movement (a) Meters per Second

Pure Nitrogen			Pure Helium		
8-12 Mesh	14-18 Mesh	20-30 Mesh	8-12 Mesh	14-18 Mesh	20-30 Mesh
5.33	3.55	2.88	13.0	11.1	6.51
3.98	4.40	2.62	12.3	11.1	7.27
6.42	4.23	2.11	13.8	9.40	6.76
3.64	4.99	2.62	11.5	7.73	7.45
5.92	3.55	1.69	9.90	8.96	6.18
7.35	3.98	2.45	11.1	8.45	6.43
7.02	3.46	1.77	11.3	6.18	8.03
6.94	3.81	1.52	13.3	9.90	4.82
4.72	4.32	2.62	13.3	10.3	4.82
8.11	3.98	2.54	12.3	11.0	8.95

8-12 Mesh Fresh Shell 405		14-18 Mesh Fresh Shell 405		20-30 Mesh Fresh Shell 405	
Gas Comp. ZN ₂ (b)	Velocity Meters/Sec	Gas Comp. ZN ₂ (b)	Velocity Meters/Sec	Gas Comp. ZN ₂ (b)	Velocity Meters/Sec
86.9	5.59	78.8	4.40	55.2	2.45
88.2	6.43	75.6	3.46	66.7	2.54
87.5	6.09	60.4	4.05	76.0	2.21
81.1	7.61	65.8	3.46	50.0	4.06
92.3	5.50	61.4	3.72	46.7	2.54
85.3	6.34	59.6	3.97	55.8	3.64
87.7	6.17	44.3	5.92	68.6	2.96
85.5	6.42	58.3	4.06	92.0	2.12
74.4	6.93			58.7	3.89
81.4	7.26			63.2	3.22
26.0	11.8	37.9	5.56	16.7	2.02
18.1	7.01	30.3	6.42	45.4	1.52
25.6	3.63	30.2	3.63	26.7	1.27
16.4	10.3	19.2	2.79	14.7	4.31
18.0	7.52	13.1	5.15	36.4	1.86
27.5	5.82	23.1	3.30	32.1	2.37
17.6	8.61	30.2	3.63	21.7	3.89
29.0	3.21	21.4	3.55	34.8	3.89
24.5	3.80	31.0	2.45	32.1	2.37
20.3	5.82	25.7	2.96	41.2	2.88

(a) Minimum inlet distributor superficial velocity which results in any particle movement.

(b) Volume ZN₂ in a N₂-He blend.

APPENDIX M

ABRASION RESISTANCE IN PPARA

<u>Shell 405 Catalyst</u>	<u>Superficial Inlet Gas Velocity, V_0, ft/sec</u>	<u>Initial Catalyst Weight, grams</u>	<u>Final Catalyst Weight, grams (a)</u>
Fresh 8-12 mesh particles	250	6.1821	5.2799 (8-12 mesh) 0.3918 (12-14 mesh) 0.1894 (14-18 mesh) 0.0530 (18-25 mesh) 0.0166 (25-30 mesh) 0.0100 (30-35 mesh) 0.2414 (<35 mesh by difference)
Fresh 14-18 mesh particles	250	5.7887	4.8044 (14-18 mesh) 0.4527 (18-25 mesh) 0.0815 (25-30 mesh) 0.0533 (30-35 mesh) 0.3968 (<35 mesh by difference)
Fresh 20-30 mesh particles	250	5.4211	4.3682 (20-30 mesh) 0.3891 (30-35 mesh) 0.6638 (<35 mesh by difference)
Fresh 8-12 mesh particles	160	4.8426	4.6508 (8-12 mesh) 0.0880 (12-14 mesh) 0.0050 (14-18 mesh) 0.0 (18-35 mesh) 0.09880 (<35 mesh by difference)
Fresh 14-18 mesh particles	160	5.4898	5.3575 (14-18 mesh) 0.0410 (18-25 mesh) 0.0014 (25-30 mesh) 0.0 (30-35 mesh) 0.0899 (<35 mesh by difference)
Fresh 20-30 mesh particles	160	5.0562	4.7369 (20-30 mesh) 0.2300 (30-35 mesh) 0.0893 (<35 mesh by difference)

(a) After 2 hours exposure using N_2 .

APPENDIX N

PLPET DATA ON THE EFFECT OF LIQUID EROSION

- Fresh Shell 405 1/8" x 1/8" Cylinders at
100 Feet per Second and 8,200 Pulses

<u>Pellet</u>	<u>Initial Weight</u> <u>grams</u>	<u>Final Weight</u> <u>grams</u>	<u>Weight Change</u> <u>grams</u>
1	.05159	.05150	-.00009
2	.05122	.05105	-.00017
3	.05225	.05194	-.00031
4	.05025	.05012	-.00013
5	.05416	.05407	-.00009

- Fresh Shell 405 1/8" x 1/8" Cylinders at
100 Feet per Second and 100,000 Pulses

<u>Pellet</u>	<u>Initial Weight</u> <u>grams</u>	<u>Final Weight</u> <u>gram</u>	<u>Weight Change</u> <u>grams</u>
1	.04819	.04775	-.00044
2	.04930	.04891	-.00039
3	.04796	.04748	-.00048
4	.04899	.04854	-.00045
5	.05134	.05090	-.00044

- Fresh Shell 405 1/8" x 1/8" Cylinders at
100 Feet per Second and 500,000 Pulses

<u>Pellet</u>	<u>Initial Weight</u> <u>grams</u>	<u>Final Weight</u> <u>grams</u>	<u>Weight Change</u> <u>grams</u>
1	.05143	.05016	-.00127
2	.04995	.04989	-.00006
3	.04885	.04855	-.00030
4	.04947	.04940	-.00007
5	.05034	.04935	-.00099

APPENDIX N (Cont'd)

- Fresh Shell 405 1/8" x 1/8" Cylinders at
55 Feet per Second and 8,200 Pulses

<u>Pellet</u>	<u>Initial Weight</u> <u>grams</u>	<u>Final Weight</u> <u>grams</u>	<u>Weight Change</u> <u>grams</u>
1	.05204	.05201	-.00003
2	.04963	.04955	-.00008
3	.04684	.04675	-.00009
4	.04982	.04976	-.00006
5	.04998	.04995	-.00003

- Fresh Shell 405 1/8" x 1/8" Cylinders at
55 Feet per Second and 100,000 Pulses

<u>Pellet</u>	<u>Initial Weight</u> <u>grams</u>	<u>Final Weight</u> <u>grams</u>	<u>Weight Change</u> <u>grams</u>
1	.05111	.05126	+.00015
2	.04953	.04946	-.00007
3	.04996	.04976	-.00020
4	.05158	.05046	-.00112

- Fresh Shell 405 8 to 12 Mesh Granules at
100 Feet per Second and 8,200 Pulses

<u>Particle</u>	<u>Initial Weight</u> <u>grams</u>	<u>Final Weight</u> <u>grams</u>	<u>Weight Change</u> <u>grams</u>
1	.01383	.01378	-.00005
2	.01538	.01527	-.00011
3	.01418	.01409	-.00009
4	.02309	.02205	-.00104

APPENDIX N (Cont'd)

- Fresh Shell 405 8 to 12 Mesh Granules at 100 Feet per Second and 100,000 Pulses

<u>Particle</u>	<u>Initial Weight</u> <u>grams</u>	<u>Final Weight</u> <u>grams</u>	<u>Weight Change</u> <u>grams</u>
1	.02226	.02194	-.00032
2	.01696	.01674	-.00022
3	.01334	.01993	-.00034
4	.01334	.01318	-.00016
5	.01601	.01583	-.00018

- Fresh Shell 405 8 to 12 Mesh Granules at 55 Feet per Second and 8,200 Pulses

<u>Particle</u>	<u>Initial Weight</u> <u>grams</u>	<u>Final Weight</u> <u>grams</u>	<u>Weight Change</u> <u>grams</u>
1	.00865	.00864	-.00001
3	.01571	.01564	-.00007
4	.00816	.00818	+.00002
5	.01191	.01183	-.00008

- Fresh Shell 405 8 to 12 Mesh Granules at 55 Feet per Second and 100,000 Pulses

<u>Particle</u>	<u>Initial Weight</u> <u>grams</u>	<u>Final Weight</u> <u>grams</u>	<u>Weight Change</u> <u>grams</u>
1	.01448	.01438	-.00010
2	.02615	.02608	-.00007
3	.01959	.01940	-.00019
4	.01822	.01803	-.00019
5	.01211	.01199	-.00012

APPENDIX O

ANALYSIS OF PERCENTAGE WEIGHT CHANGE RESULTS
FROM PULSED LIQUID EROSION DATA IN PLPET

<u>Liquid Velocity feet per second</u>	<u>Number of Pulses</u>	<u>Fresh Shell 405 Catalyst</u>	<u>Percentage Change In Weight</u>		
			<u>Individual Change</u>	<u>Mean</u>	<u>Standard Deviation</u>
100	8,200	1/8" X 1/8" Cylinders	-0.17	-0.30	0.17
			-0.33		
			-0.59		
			-0.26		
			-0.17		
100	8,200	8-12 Mesh Particles	-0.36	-0.69	0.28
			-0.72		
			-0.63		
			-1.04		
100	100,000	1/8" X 1/8" Cylinders	-0.91	-0.90	0.08
			-0.79		
			-1.00		
			-0.92		
			-0.86		
100	100,000	8-12 Mesh	-1.44	-1.35	0.22
			-1.30		
			-1.68		
			-1.20		
			-1.12		

APPENDIX O (Cont'd)

<u>Liquid Velocity feet per second</u>	<u>Number of Pulses</u>	<u>Fresh Shell 405 Catalyst</u>	<u>Individual Change</u>	<u>Mean</u>	<u>Standard Deviation</u>
55	8,200	8 to 12 Mesh Granules	-0.12 -0.44 +0.24 -0.67	-0.25	0.40
55	8,200	1/8" x 1/8" Cylinders	-0.06 -0.16 -0.19 -0.12 -0.06	-0.12	0.06
55	100,000	1/8" x 1/8" Cylinders	+0.29 -0.14 -0.40 -2.17	-0.61	1.08
55	100,000	8 to 12 Mesh Granules	-0.69 -0.27 -0.97 -1.04 -0.99	-0.79	0.32
100	500,000	1/8" x 1/8" Cylinders	-2.47 -0.12 -0.61 -0.14 -1.97	-1.06	1.09

APPENDIX P

PLPET INDIVIDUAL DATA USED IN THE ANOVA

Number of Pulses	VELOCITY OF LIQUID RELATIVE TO PARTICAL				Row Means (Number of Pulse Effect)
	55 Feet per Second		100 Feet per Second		
	8-12 Mesh		8-12 Mesh		
	1/8" x 1/8" Cylinders	Granules	1/8" x 1/8" Cylinders	Granules	
8,200	.06	0.12	0.17	0.36	.339
	.16	0.44	0.33	0.72	
	.19	-0.24	0.59	0.63	
	.12	0.67	0.26	1.04	
	.06	(.25)	0.17	(.69)	
100,000	-.29	0.69	.91	1.44	.910
	.14	0.27	.79	1.30	
	.40	0.97	1.00	1.68	
	2.17	1.04	.92	1.20	
	(.61)	0.99	.86	1.12	
Column Means (Velocity Effect)	.441		.809		
Group Means (Catalyst Type Effect)		.481		0.769	

APPENDIX Q

PLPET Data On The Effect Of Liquid Erosion

- Fresh Shell 405 granules, 14-18 mesh,
at 100 feet per second and 100,000 Pulses

<u>Initial Weight,</u> <u>Grams</u>	<u>Final Weight,</u> <u>Grams</u>	<u>Weight Change,</u> <u>Grams</u>
.00302	.00294	-.00008
.00312	.00307	-.00005
.00459	.00454	0
.00623	.00617	-.00006
.00514	.00513	-.00001

- Air Force Rocket Propulsion Laboratory Sample of
Used Shell 405 granules, 14-18 mesh at 100 feet per
second and 100,000 Pulses

<u>Initial Weight,</u> <u>Grams</u>	<u>Final Weight,</u> <u>Grams</u>	<u>Weight Change,</u> <u>Grams</u>
.00274	.00272	-.00002
.00288	.00273	-.00015
.00374	.00365	-.00009
.00184	.00178	-.00006

- Rocket Research Corporation's sample of Used Shell
405 granules, 14-18 mesh at 100 feet per second
and 100,000 Pulses

<u>Initial Weight,</u> <u>Grams</u>	<u>Final Weight,</u> <u>Grams</u>	<u>Weight Change,</u> <u>Grams</u>
.00310	.00297	-.00013
.00212	.00210	-.00002
.00431	.00401	-.00030
.00472	.00302	-.00168 (a)
.00270	.00241	-.00029

- (a) Photomicrographs indicate part of pellet was broken
off during PLPET exposure.

APPENDIX Q (Cont'd)

- TRW sample of Used Shell 405 granules, 14-18 mesh,
at 100 feet per second and 100,000 Pulses

<u>Initial Weight,</u> <u>Grams</u>	<u>Final Weight,</u> <u>Grams</u>	<u>Weight Change</u> <u>Grams</u>
.00233	.00231	-.00002
.00351	.00180	-.00171 (a)
.00543	.00540	-.00003
.00372	.00361	-.00011
.00226	.00223	-.00003

- (a) Photomicrographs indicate part of pellet was broken off during PLPET exposure.

APPENDIX R

Analysis of Percentage Weight Change Results From Pulsed Liquid Erosion Data In PLPET

<u>Liquid Velocity</u> <u>feet per second</u>	<u>Number</u> <u>of Pulses</u>	<u>Catalyst</u>	<u>Percentage Change in Weight</u>		
			<u>Individual</u> <u>Change</u>	<u>Mean</u>	<u>Standard</u> <u>Deviation</u>
100	100,000	Fresh 14-18 mesh	- 2.65	- 1.08	1.08
			- 1.60		
			0		
			- 0.96		
			- 0.19		
100	100,000	Used 14-18 mesh sample from AF Rocket Propulsion Laboratory	- 0.73	- 2.90	1.86
			- 5.21		
			NA		
			- 2.41		
			- 3.46		
100	100,000	Used 14-18 mesh sample from Rocket Research Corp.	- 4.19	-11.68	13.84
			- 0.94		
			- 6.96		
			-35.59 (a)		
			-10.74		
100	100,000	Used 14-18 mesh sample from TRW	- 0.86	-10.88	21.17
			-48.72 (a)		
			- 0.55		
			- 2.96		
			- 1.33		

(a) Photomicrographs indicate part of pellet was broken off during PLPET exposure.

APPENDIX S

PLPET Liquid Erosion Tests With Used 14-18 Mesh Samples From TRW "Pop Shock" Apparatus (a)

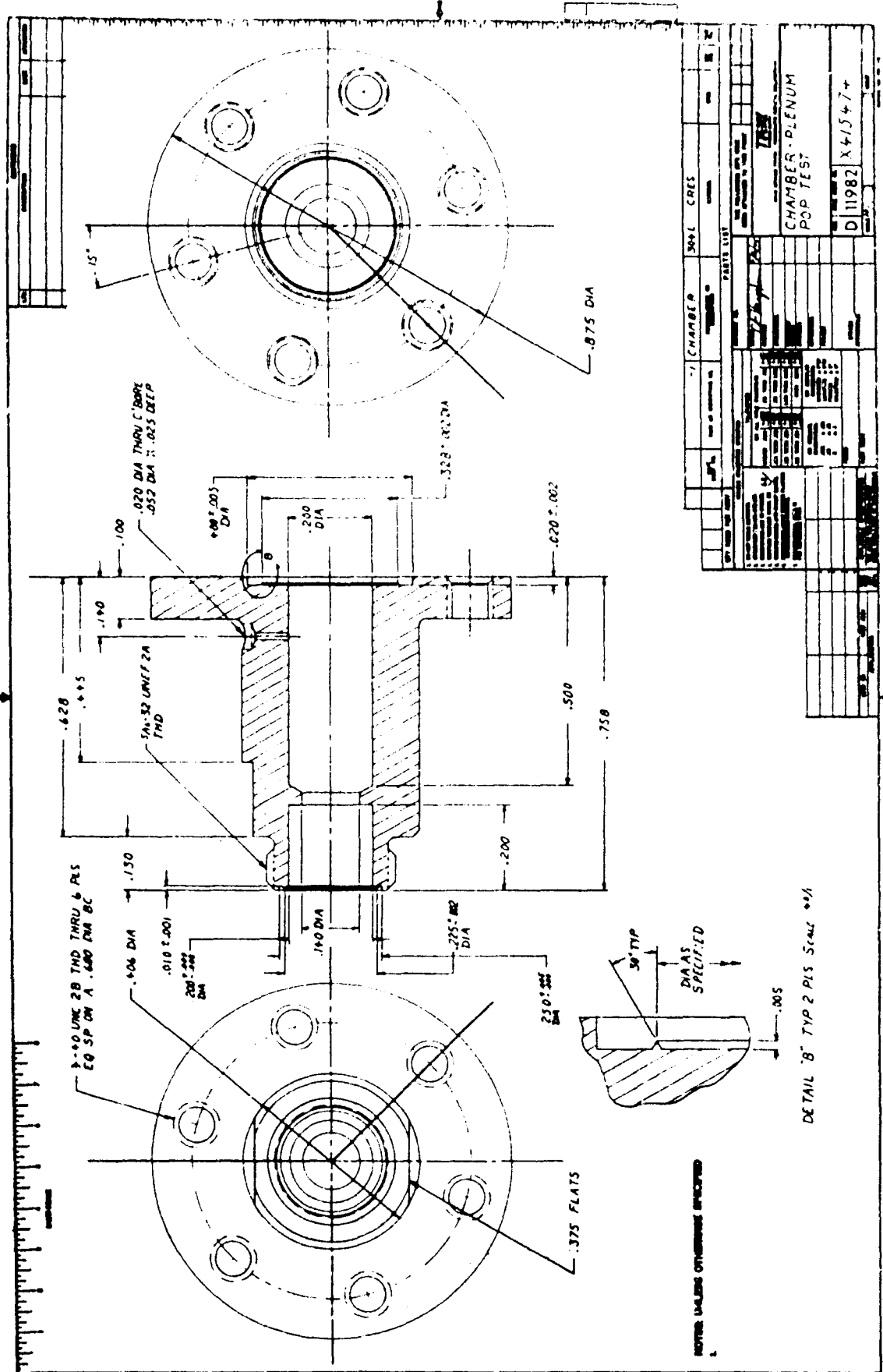
<u>TRW Identification</u>	<u>Initial Weights Grams</u>	<u>Final Weight, Grams</u>	<u>Weight Change, Grams</u>
41-52	.002585	.002565	-.000020
	.003496	.003471	-.000025
	.004199	.004190	-.000009
	.002454	.002425	-.000029
53-55	.005474	.005442	-.000032
	.005607	.005587	-.000020
	.003887	.003873	-.000014
105-107	.002854	.002837	-.000017
	.002293	.002240	-.000053
	.003972	.003677	-.000295 (particle broke)
	.003232	.003204	-.000038
108-125	.003167	.003118	-.000049
	.003545	.003505	-.000040
	.003708	.003611	-.000097
	.004334	.004274	-.000060
126-156	.002204	.002175	-.000029
	.002651	.002623	-.000028
	.003091	.003055	-.000036
	.002455	.002398	-.000057
100 cycles	.004217	.004168	-.000049
	.002120	.000863	-.001257 (particle broke)
	.004690	.004609	-.000081
	.003216	.003153	-.000063
60 seconds steady state	.003107	.003072	-.000035
	.002190	.002158	-.000032

(a) PLPET exposure to 100,000 pulses at 100 feet per second.

[illegible]

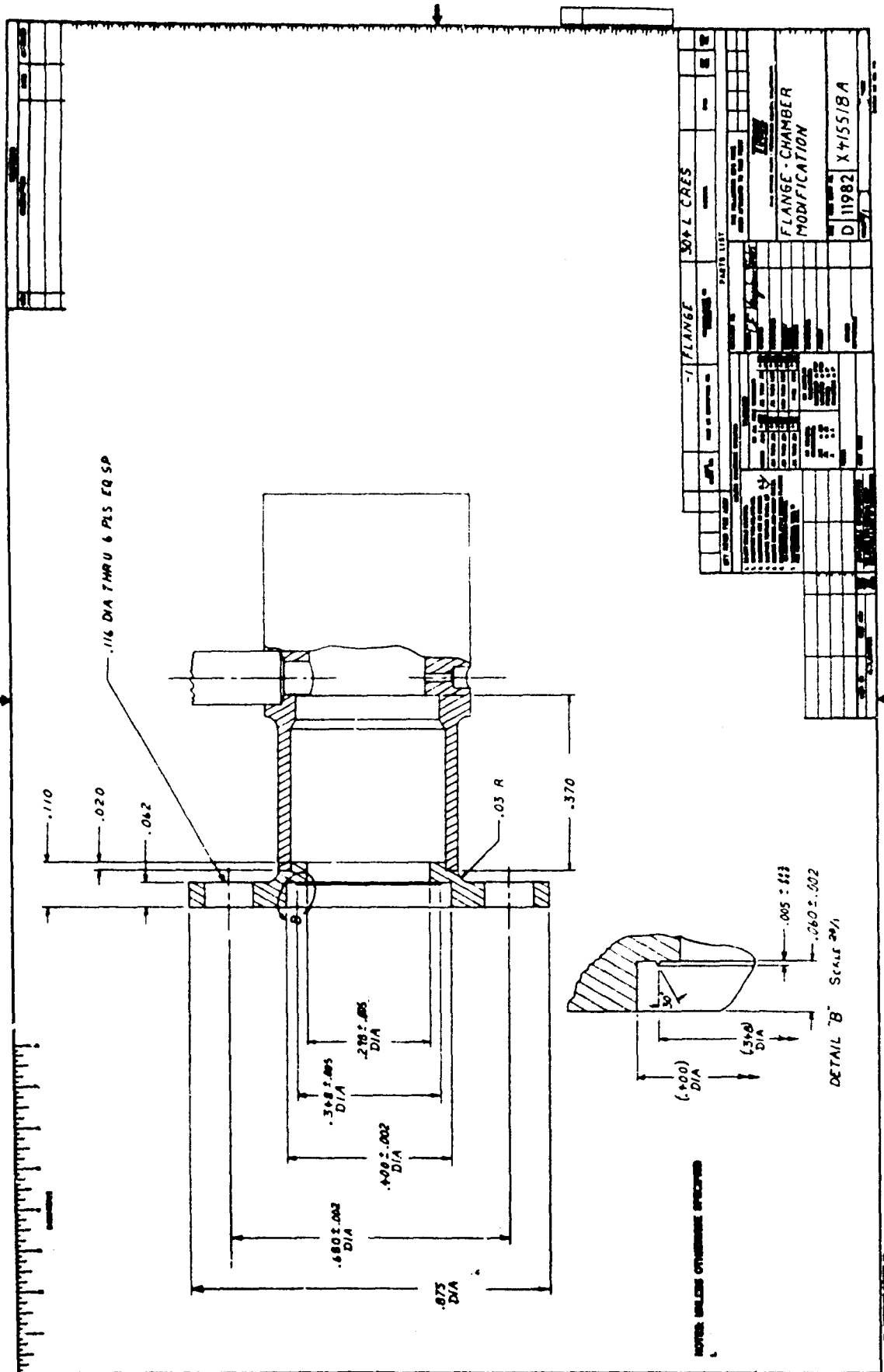
APPENDIX T (Cont'd)

LABORATORY REACTOR DRAWINGS



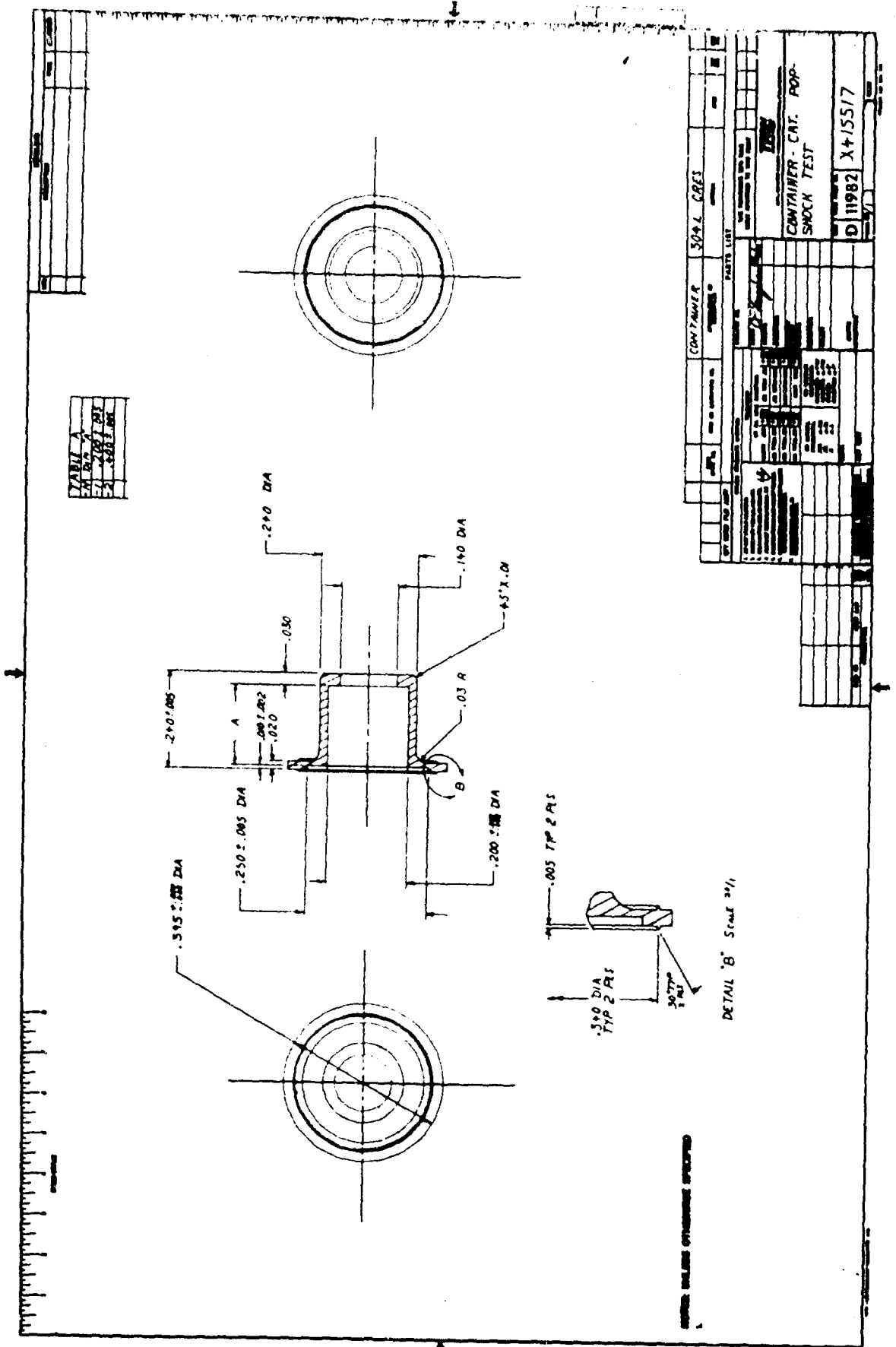
APPENDIX T (Cont'd)

LABORATORY REACTOR DRAWINGS

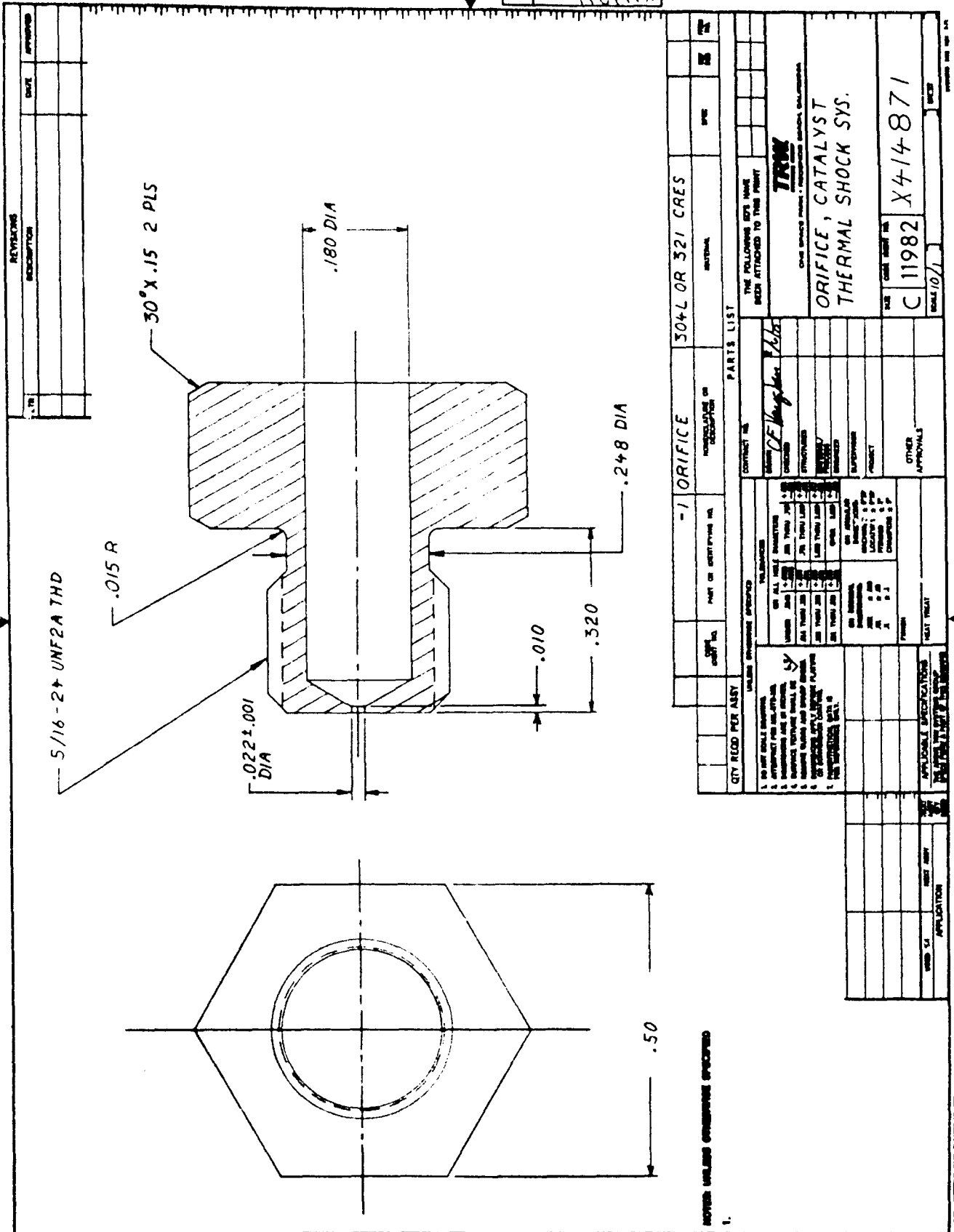


APPENDIX T (Cont'd)

LABORATORY REACTOR DRAWINGS



APPENDIX T (Cont'd) - LABORATORY REACTOR DRAWINGS



LABORATORY REACTOR DRAWINGS

- 409 -

APPENDIX U

SYSTEMS SAFETY STUDY

A preliminary system safety investigation was conducted as a means of developing safety criteria related to hydrazine propulsion systems. The purpose of this study was to provide the necessary guidelines to help minimize unintentional catastrophic failure of hydrazine propulsion system hardware and any resulting harm to uninvolved bystanders.

As a means of implementing this study, a typical ground test hydrazine propellant supply system was used as a baseline configuration. This system is shown in the following figure. The military standard of Reference 1 contains a list of 20 possible hazards that can be postulated for different types of systems. These hazards formed the basis for this study. These 20 potential hazards were condensed to 7 specific hazards that may be failure modes for a hydrazine system. Subsequent paragraphs describe the types of failure mechanisms together with a brief summary of the general precautions necessary to insure that they do not occur. The harmful effects of these failure modes are not discussed herein primarily because Reference 2 and other documents adequately cover the health hazards, fire and explosive conditions that can result from such failures.

Failure Mechanisms

Hydrazine propulsion systems are known to be highly reliable compared to other types of propulsion systems. Even with this high degree of reliability, catastrophic failure of hydrazine system hardware is possible. There are seven primary failure mechanisms that could occur within a hydrazine ground test system (flight systems also) that would produce catastrophic failure and a resulting hazard to personnel in the immediate area. The seven mechanisms are briefly discussed below:

- ● Over Pressurization

Typical of any propulsion system, exceeding the burst pressure of the system tanks and other components can result in catastrophic failure.

- ● Non-Compatible Materials of Construction

Certain materials of construction are not compatible with hydrazine and use of these materials would result in general corrosion, nitriding, stress crack corrosion and hydrogen embrittlement. All of these non-compatible conditions could result in catastrophic failure of hydrazine system components.

- ● Stagnant Areas in Reactor Feed Lines, Valve and Chamber

Hydrazine will thermally decompose in the temperature region at or above 300°F. If hydrazine is allowed to stay within a stagnant area of a reactor, it is possible that the thermal soak back from the reactor's combustion chamber can initiate decomposition of this stagnant fuel and a catastrophic failure may occur.

- Hydrazine Freeze/Thaw Cycle

Typical with any non-aqueous fluid, hydrazine will contract when frozen and expand again when re-converted to liquid. Feed line failures are possible, for example, if liquid hydrazine is added to a fixed line volume that contains contracted frozen hydrazine. When the frozen hydrazine thaws and expands, line rupture is possible if the line is isolated without any relief.

- System Leakage

Any leak condition can produce a health hazard and fire or excessive hazard to personnel in the immediate area.

- Contamination of Fuel and/or System Components

Contamination of hydrazine in the form of impurities (i.e. carbazic acid) can produce an increase in decomposition rate and a decrease in thermal stability. Carbazic acid can form either metal or hydrazinium salts which can be retained in the injector feed tubes and resulting in a reactor failure. System contamination with particulate matter can result in leak conditions in the event valves are impaired from closing properly.

- Component Failures

Tank, valves, regulator and reactor chamber design inadequacies can produce leakage and catastrophic failures.

Precautionary Techniques

Catastrophic failure of hydrazine propulsion system hardware can occur if proper design considerations, handling precautions and system redundancy are not followed.

- Proper Design Considerations

Most of the failure mechanisms previously described can be avoided by proper design of the system component hardware. A comprehensive understanding of hydrazine system design is mandatory and literature such as Reference 3 is available to provide the necessary design criteria.

- Proper Handling Precautions

All personnel involved with a hydrazine propulsion system should have a thorough understanding of the operational and safety aspects of hydrazine systems. Detail assembly, test and safety procedures should be employed wherever possible. Literature is available (Reference 2) to aid in establishing the proper handling procedures for hydrazine fuel.

- System Redundancy and Safety

Within practical limits, all hydrazine systems should contain redundant valving to minimize the chance of a failure. System safety can be enhanced by providing methods of isolating portions of the system in the event of a component failure. Pressure relief techniques should be employed in a system where an over-pressure condition can occur.

- Thermal Control

Perhaps the most important consideration relating to the prevention of catastrophic failures is that of thermal control. Every precaution must be taken to ensure that the hydrazine is maintained above +40°F and well below the threshold of thermal instability everywhere and within the transfer and storage system. Both active and passive means of thermal control must be employed as required to ensure that these requirements are met. Redundancy of thermal control systems should be employed to the maximum extent possible. The extreme need to maintain the hydrazine above freezing and well below the autodecomposition temperature everywhere in the system except for the combustion chamber cannot be overemphasized.

REFERENCES:

- (1) MIL-STD-882 dated July 15, 1969.
- (2) Handling & Storage of Liquid Propellants, DOD Document, dated January 1963.
- (3) AFRPL-TR-75-46, Design Handbook-Hydrazine Compatibility Design and Handling Criteria, December 1975.